Technische Universität München
TUM Fakultät für Medizin

Axo-Oligodendroglial Mechanisms of Paranodal Protein Sorting

Martina Arends

Vollständiger Abdruck der von der Fakultät für Medizin der Technischen Universität München zur Erlangung einer

Doktorin der Naturwissenschaften (Dr. rer. nat.)

genehmigten Dissertation.

Vorsitz:	Prof. Dr. Thomas Misgeld
Prüfer*innen der Dissertation:	1. Prof. Dr. Mikael Simons
	2. Prof. Dr. Ville R. I. Kaila

Die Dissertation wurde am 06.09.2022 bei der Technischen Universität München eingereicht und durch die Fakultät für Medizin am 13.12.2022 angenommen.

Abstract

Myelin, a specialized lipid membrane produced by oligodendrocytes in the central nervous system, is anchored to the axonal membrane with the help of different cell adhesion proteins. In this dissertation, we investigated how myelin adhesive proteins in the axonal membrane are redirected from myelin ensheathment sites to their functional position at paranodes. This dissertation focuses on the location and relocation of the axonal paranodal adhesion protein Caspr. We hypothesized that axonal ganglioside and oligodendroglial Mag interactions at internodes play a crucial role in the localization of Caspr and other paranodal adhesion proteins. These interactions would protrude the paranodal proteins from the internodal domain to their designated position.

In addition, we investigated the optic nerve ultrastructure of ganglioside null mice (ST3GAL5$^{-/-}$/ B4GALNT1$^{-/-}$) to evaluate the function of gangliosides during myelination further. We hypothesized that gangliosides provide a permissive surface in the axonal membrane, enabling myelination, and are hence crucial for myelination from early on. We applied a recently developed direct infusion (shotgun) lipidomics method to investigate the ganglioside content in the brains and optic nerves of these mice and wild type mice during development and in adulthood.

Our results indicate that internodal ganglioside-Mag interactions are not crucial but supportive for myelination and rather important for the maintenance and integrity of myelinated axons. Furthermore, the axonal myelin adhesion protein Caspr seems to interact with another unknown molecule on the oligodendroglial membrane. It probably accumulates Caspr at internodes before its relocation to paranodes. We found Nfascb (NFASC155) vital for Caspr localization to paranodes within this context.

Based on our results, we developed a model describing the function of myelin adhesion complexes during the wrapping process in more detail.

Zusammenfassung

Im Zentralen Nervensystem produzieren Oligodendrozyten Myelin, das mit Hilfe verschiedener Zelladhäsionsproteine an der axonalen Plasmamembran verankert ist. In dieser Dissertation haben wir untersucht, wie Myelinadhäsionsproteine in der axonalen Plasmamembran von einer zu myelinisierenden Stelle an ihre funktionalen Positionen an den Paranodien lokalisieren. Der Schwerpunkt dieser Dissertation liegt dabei auf der Verlagerung des axonalen paranodalen Adhäsionsproteins Caspr. Wir stellten die Hypothese auf, dass Interaktionen zwischen axonalen Gangliosiden und dem oligodendroglialen Mag-Protein an Internodien eine entscheidende Rolle bei der Lokalisation von Caspr und anderen paranodalen Proteinen spielen. Diese Interaktionen würden paranodale Proteine aus der internodalen Domäne an ihre vorgesehenen Positionen heraustreiben.

Darüber hinaus haben wir die Ultrastruktur des Sehnervs von Gangliosid-Null-Mäusen (*ST3GAL5*$^{-/-}$ / *B4GALNT1*$^{-/-}$) untersucht, um die Funktion der Ganglioside während der Myelinisierung besser zu beurteilen. Wir vermuteten, dass Ganglioside eine Oberfläche innerhalb der axonalen Membrane bilden, die Myelinisierung begünstigt und daher von Anfang an für die Myelinisierung entscheidend ist. Wir haben dazu u.a. eine kürzlich entwickelte (Shotgun)-Lipidomics Methode verwendet, um die Gangliosidkonzenzentration im Gehirn und in den Sehnerven dieser Mäuse und wildtyp-Mäusen während der Entwicklung und im adulten Stadium zu messen.

Unsere Ergebnisse deuten darauf hin, dass die Interaktion von Gangliosiden mit Mag die Myelinisierung unterstützt und die Integrität myelinisierter Axone aufrecht erhält. Außerdem scheint das axonale Myelinadhäsionsprotein Caspr mit einem bisher unbekannten Molekül auf der oligodendroglialen Membran zu interagieren. Dieses Molekül reichert Caspr möglicherweise an den Internodien an, bevor es an die Paranodien lokalisiert. In diesem Zusammenhang konnten wir zeigen, dass Nfascb (NFASC155) für die Lokalisierung von Caspr an die Paranodien entscheidend ist.

Auf der Grundlage unserer Ergebnisse haben wir ein Modell entwickelt, das die Funktionen der Myelinadhäsionskomplexe während der Wicklung des Myelins um die Axone detaillierter beschreibt.

Contents

List of Figures

List of Tables

List of Abbreviations

$^{-/-}$ gene knock out

$^{-/+}$ heterozygous gene

ANKG Ankyrin G

bp base pairs

BSA bovine serum albumin

°C degrees celsius

$CaCl_2$ calcium chloride

Cadm3 / **4** cell adhesion molecule 3 / 4

CAM cell adhesion molecule

CASPR / **2** contactin-associated protein / 2 in murine models and cell culture

Caspr / **2** contactin-associated protein / 2 in zebrafish

cds coding sequence

Cer ceramide

Chol cholesterol

CL cardiolipin

CNS central nervous system

CNTN / **1** / **2** contactin 1a / 1b / 2 in murine models and cell culture

Cntn / **1a** / **1b** / **2** contactin 1a / 1b / 2 in zebrafish

Cntnap1b contactin-associated Protein 1b

CRISPR clustered regularly interspaced short palindromic repeats

DAG diacylglycerol

DAPI 4',6-Diamidin-2-phenylindol

ddH_2O double destilled water

D.rerio Danio rerio

DMSO dimethyl sulfoxide

DNA deoxyribonucleic acid

dpf days post fertilization

DRM detergent-resistant membrane

E.coli Escherichia coli

EDTA ethylene-diamine-tetra-acetic acid

EM electron microscopy

ER endoplasmic reticulum

f femto

FBS fetal bovine serum

Fn fibronectin-like

FNIII fibronectin type III

Fum B1 Fumonisin B1 toxin

GFP green fluorescent protein

GalCer galactosylceramide

GlcCer glucosylceramide

GPI glycosylphosphatidylinositol

GSL glycosphingolipid

h hour(s)

HA influenza A virus hemagglutinin protein

het heterozygous

HexCer hexosylceramide

HMw high molecular weight

hPa hectopascal

HS herpes simplex virus protein

Ig immunoglobulin

kbp kilo base pairs

KCl potassium chloride

KO knock out

KH_2PO_4 potassium phosphate

K_v voltage-gated potassium

LacCer lactosylceramide

LB lysogeny broth

LMw low molecular weight

LPA lyso-phosphatidate

LPC lyso-phosphatidylcholine

LPE lyso-phosphatidylethanolamine

LPG lyso-phosphatidylglycerol

LPI lyso-phosphatidylinositol

LPS lyso-phosphatidylserine

M molar

MAG myelin-associated glycoprotein in murine models and cell culture

Mag myelin-associated glycoprotein in zebrafish

MBP myelin basic protein

MCS multiple cloning site

$MgCl_2$ magnesium chloride

$MgSO_4$ magnesium sulfate

µ micro **L** liter **M** molar **m** meter

m milli **L** liter **M** molar **s** seconds **m** meter

min minute(s)

Mpz myelin protein zero

mRNA messenger ribonucleic acid

n nano **L**liter **g** gram(s)

NA numerical aperture

Na_2HPO_4 sodium phosphate

NaCl sodium chloride

Na_v voltage-gated sodium

NFASC 155 / **186** Neurofascin / 155 / 186 in murine models and cell culture

Nfasc a / **b** neurofascin a / b in zebrafish

nt nucleotides

OCT optimum cutting temperature

OPC oligodendroglial precursor cell

p pico

PA phosphatidate

PBS phosphate-buffered saline

PC phosphatidylcholine

PCR polymerase chain reaction

PE phosphatidylethanolamine

PFA paraformaldehyde

PG phosphatidylglycerol

PI phosphatidylinositol

PLP proteolipid protein

PM palmitoylated

PNS periphal nervous system

preOL premyelinating oligodendrocyte

PS phosphatidylserine

psi pressure in pounds per square inch

PTU 1-phenyl 2-thiourea

Px postnatal day x

REZ restriction enzyme

RFLP restriction fragment length polymorphism

RFP red fluorescent protein

RNA ribonucleic acid

rpm rounds per minute

Siglec sialic acid-binding immunoglobulin-like lectin

SD standard deviation

sec second(s)

SM sphingomyelin

SP sphingolipid

Sulf sulfatide

TAE tris-acetate-edta

TAG triacylglycerol

TD-PCR touchdown PCR

TE tris-edta

TEM transmission electron microscope

TM transmembrane

U unit

V volt

wt wild type

YFP yellow fluorescent protein

Acknowledgements & Contributions

First and foremost, I would like to thank my supervisor, Prof. Mikael Simons, for giving me the opportunity to join his research group, to work on this dissertation, and for his guidance and feedback throughout the project.

I would like to extend my sincere thanks and appreciation to my mentors Prof. Ville Kaila and Dr. Leanne Godinho, for their support and encouragement throughout this dissertation.

I want to express my deepest gratitude to the members of the zebrafish core facility - Dr. Bettina Schmid, Dr. Frauke van Bebber, Alexander Hruscha, Roberto Rojas Rojas, and Sabine Schlink for their teaching, support, ideas, discussions, and the zebrafish care-taking.

This endeavor would not have been possible without Dr. Ioannis Alexopoulos, who taught me everything about light microscopy and *in vivo* imaging. Thank you for your patience and for sharing your expertise.

Special thanks to Dr. Sebastian Timmler and Dr. Minou Djannatian for the fruitful zebrafish collaboration as well as to Dr. Christian Klose for collaborating on the lipidomics project.

From the bottom of my heart, I would like to thank all Simons lab members, for your energy, understanding, and help throughout the last years. I will forever remember many special moments with every one of you - funny and tough ones, moments of despair, and encouraging ones. You created an energizing working atmosphere! Thank you very much! Thank you, Kerstin, for your unique sense of humor and your care packages.

I am incredibly grateful for my colleagues and friends who became an invaluable support for me - Mar and Lili.

En ganz besünnen Dank geiht na mien Famielje, de mi entraden muss un ünnerstütt hett, ofschons dat hör stuur fallen is to verstahn, worum as ik disse Pad gahn wull. Weest bedankt, dat ji mi röögt hebbt. Ik bün nu daan mit' School! Mit Lehren bün ik aver sinooit neet daan.

Andres, wees van Harten bedankt, dat du in disse heele Tied an mien Sied west büst, för dien Stöön un för dien Leev.

I am grateful for the help, fruitful discussions, and exchange of knowledge I experienced from so many people during this dissertation. This chapter also lists the contributions of colleagues with whom I had the pleasure of working and collaborating. A special "Thank you!" to you. Their contributions to this dissertation are listed by sections:

3.1.2: Dr. Minou Djannatian acquired and analyzed the initial data this thesis is based upon - the very initial Caspr-YFP localization experiments in spinal cord axons during the development of zebrafish larvae.

3.1.6: Dr. Sebastian Timmler stained for Caspr and Ankyrin staining in the wild type and *ST3GAL5*$^{-/-}$ *x B4GALNT1*$^{-/-}$ mouse spinal cord and analyzed the data.

3.1.6: Dr. Ioannis Alexopoulos wrote the macro for data analysis of membrane-anchored GFPs in the axonal membrane (full macro in Appendix VIII). The FRET experiment was also conducted together with him.

3.1.6: Dr. Minou Djannatian acquired the data of Caspr-YFP localization in spinal cord axons in Fum B1- treated zebrafish larvae.

3.2.3 and 3.2.4: M.Sc. Kerstin Karg handled and processed mouse samples for electron microscopy image acquisition, which she also conducted.

3.2.2 and 3.2.1: Lipidomic data were acquired in collaboration with Dr. Christian Klose from Lipotype GmbH, Dresden.

The experimental approach in Appendix I was developed together with M.Sc. Agata Rhomberg.

Illustrations were created with BioRender.com.

1 Introduction

1.1 Membrane Organization

Compartmentalization is a key to efficient processing of inter- and intracellular processes and the related communication. Lipid membranes play a crucial role in compartmentalization [Dowhan et al., 2008; Simons and Sampaio, 2011; Nelson and Cox, 2017]. They are necessary for cells and organelles to obtain and maintain their specific environment. For each cell type and organelle, the composition of proteins, lipids, and even sugar residues (=glycome) of some lipids in the membrane is different. The molecular membrane composition forms an identification attribute as unique as a fingerprint for each organelle, cell, and cell type.

Compared to other cell types, oligodendrocytes and Schwann cells have an enlarged lipid membrane surface. They produce myelin, a specialized lipid membrane that is the key to fast, saltatory nerve conduction as it insulates axons and leaves only nodes of Ranvier for neuronal signal conduction [Stadelmann et al., 2019; Nave and Werner, 2014]. Neurons also have particular lipid membrane components, such as specific glycolipids [Prinetti et al., 2000; Sonnino et al., 2007; Schnaar et al., 2014; Aureli et al., 2015]. Some of them are almost exclusively found in their membrane.

1.2 Myelin

Myelin is an extended lipid membrane wrapped around an axon in many bilayers [Chrast et al., 2011; Snaidero et al., 2014; Schmitt et al., 2015]. More than 70% of the dry weight of myelin is composed of lipids, with approximately 30% of them being glycosphingolipids (GSL), mainly galactosylceramide (GalCer) and sulfatide (Sulf) [Aggarwal et al., 2011; Schmitt et al., 2015; Poitelon et al., 2020]. Only less than 30% of the myelin dry weight makes up for proteins. Myelin was seen as a static structure, as an exception from the fluid mosaic model [Singer and Nicolson, 1972]. As for neurons, myelin damage was assumed to be irreversible. Nowadays, we know that myelin is a very dynamic and plastic structure, even in adulthood (Fig. 1) [Rivers et al., 2008; Nave and Werner, 2014; Hill et al., 2018; Hughes et al., 2018; Stadelmann et al., 2019; Bonetto et al., 2020] and the fluid mosaic model does indeed apply to myelin membranes as well [Yurlova et al., 2011]. In addition, oligodendrocytes have the potential to remyelinate damaged myelinated areas in the central nervous system (CNS) [Stadelmann et al., 2019].

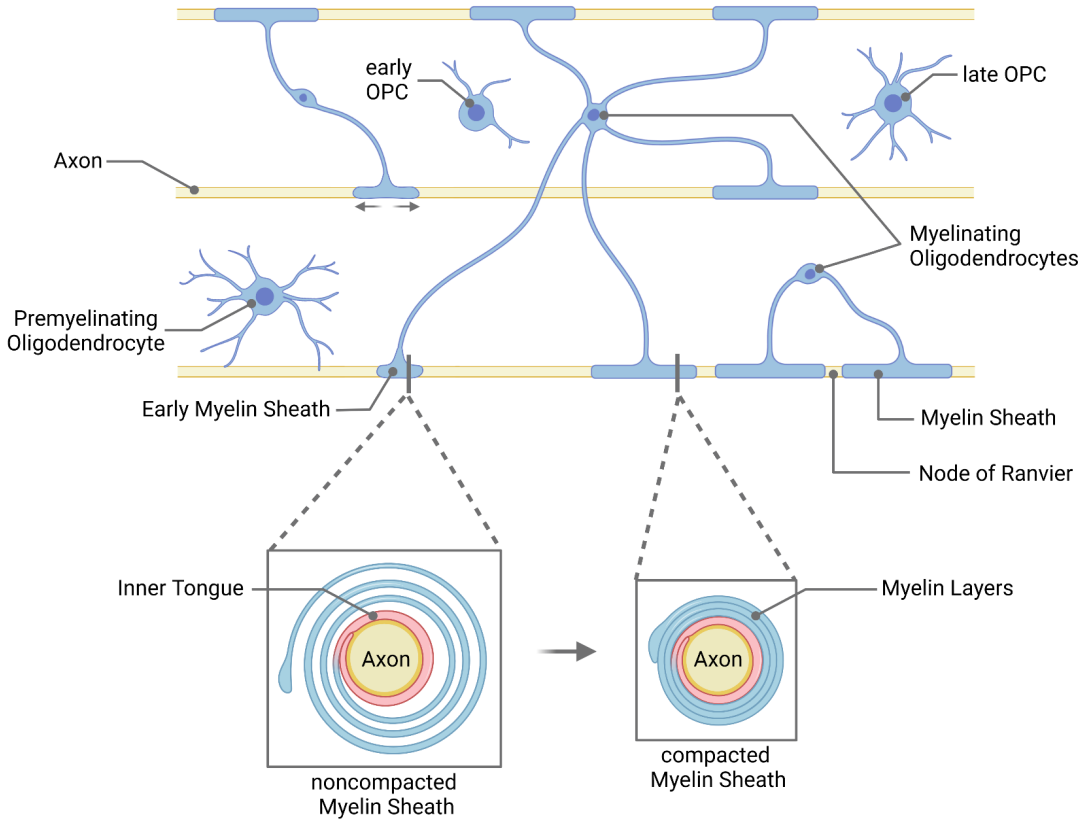

Figure 1: MYELIN IN THE CENTRAL NERVOUS SYSTEM During development in the CNS, early oligodendroglial precursor cells (OPC) surveil their environment to find appropriate space for myelination. They develop into late OPCs and premyelinating oligodendrocytes (preOL). If a preOL detects a cue for myelinating an axon, it extends a myelinating process to initiate myelination. The inner tongue constantly turns around the axon. Its internal actin cytoskeleton pushes itself forward underneath previously formed layers. This movement adds up layer by layer of myelin membrane. A myelin sheath also extends laterally. Myelin proteins compact the layers. Finally, single compacted myelin sheaths are separated by nodes of Ranvier.

Myelin is produced either by Schwann cells in the peripheral nervous system (PNS) or by oligodendrocytes in the CNS [Nave and Werner, 2014]. Oligodendrocyte precursor cells (OPC) extend

processes to surveil their environment, find appropriate axons and wrap their processes around them in several layers (Fig. 1) [Kirby et al., 2006; Czopka et al., 2013]. In contrast, Schwann cells enlarge their cell body to wrap it around a single axon in several layers. The convergent evolution of the two different cell types that basically have the same function indicates the importance of myelin for the evolutionary development of vertebrates by enabling faster recognition, action, and reaction [Nave and Werner, 2014]. Insulation of axons allows for faster signal propagation by saltatory conduction without enlarging the axonal diameter, which is limited by body size and oxygen availability (Fig. 2) [Zalc et al., 2008; Nave and Werner, 2014; Stassart et al., 2018].

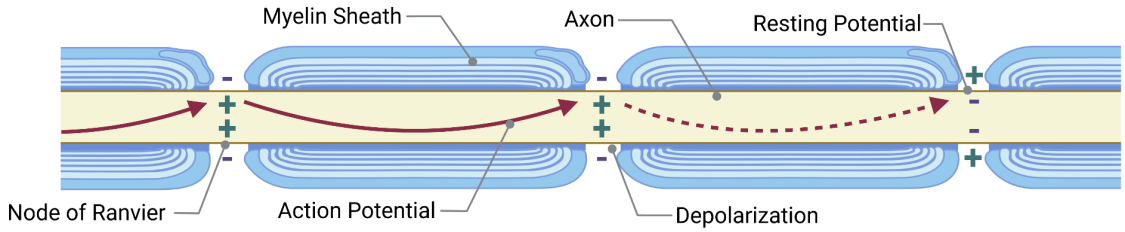

Figure 2: Signal Propagation in Myelinated Axons At resting state, axons have a negative membrane potential. An action potential briefly changes an axon's electric polarity into a positive membrane potential. Voltage-gated ion channels initiate this so-called depolarization. In myelinated axons, the depolarizing Na_v channels are solely located at the nodes of Ranvier.

Myelination terms the wrapping process of Schwann cells or oligodendrocyte processes around axons [Stadelmann et al., 2019]. Inappropriate myelination signals can cause retractions of oligodendrocyte processes, called myelin pruning [Czopka et al., 2013; Liu et al., 2013; Hughes and Appel, 2020]. Among many other positive and negative regulators, the axonal diameter and neuronal excitations provide cues for myelination [Demerens et al., 1996; Lee et al., 2012; Almeida et al., 2021]. Nevertheless, the mechanism of attracting or repelling oligodendrocyte processes and the molecules involved still remain not yet fully understood [Almeida, 2018].

Myelin layering in the central nervous system is achieved by the myelin inner tongue that continuously slides underneath a newly formed layer with permanent contact to the axonal membrane (Fig. 1 boxes) [Snaidero et al., 2014]. During this process, the myelin sheath also extends laterally along the axon. The actin cytoskeleton in the myelin inner tongue plays an important role in this process. A continuous buildup and breakdown of the actin filaments moves the inner tongue forward [Nawaz et al., 2015; Zuchero et al., 2015]. However, due to the repulsive nature of lipid membranes, the process of one membrane wrapping around another in several layers is unusual and needs strong adhesive forces to keep the myelin membrane in contact with the axonal membrane [Bakhti et al., 2013]. On the other hand, these forces need to be flexible enough to allow a constant movement of the inner tongue. The molecules involved in anchoring the two membranes at the early stages of myelination are yet unknown [Almeida, 2018].

In a next step compaction and elongation starts [Min et al., 2009; Aggarwal et al., 2013; Bakhti et al., 2013; Schmitt et al., 2015; Stadelmann et al., 2019]. Single myelin layers are glued together with the help of different proteins like Myelin Basic Protein (MBP). Other proteins and lipids like Myelin-Associated Glycoprotein (MAG), neurofascins (Nfasc), contactins (Cntn), and gangliosides help anchor the myelin sheath to the axonal membrane [Garcia and Zuchero, 2019; Rasband and Peles, 2021].

1.3 Axo-Oligodendroglial Adhesion Complexes in the CNS

A myelin sheath, either originating from Schwann cells (PNS) or oligodendrocytes (CNS), is tethered to the axonal membrane with the help of many cell adhesion molecules (CAM) [Quarles, 2007; Arancibia-Carcamo and Attwell, 2014; Schnaar, 2016; Fehmi et al., 2018; Faivre-Sarrailh, 2020; Rasband and Peles, 2021]. Different cell adhesion areas can be assigned for each myelin sheath either by structural features or signal transducing proteins and cell adhesion molecules that dominate each area. The outermost axo-glial adhesion areas, where terminal myelin loops are tethered to the axon, are called paranodes (Fig. 3). The Nfasc/Caspr/Cntn cell adhesion complexes dominate them. Paranodes are closest to the node of Ranvier, which consists of signal transducing Na_v channels. The adaxonal myelin wrap defines the innermost and biggest axo-glial adhesion area - the internode - which is dominated by MAG-ganglioside cell adhesion complexes. Finally, the areas between paranode and internode are called juxtaparanodes. Their distinct adhesion complexes are CNTN2-CASPR2 complexes, where neuronal CNTN2 interacts homophilic with oligodendroglial CNTN2. K_v channels cluster in juxtaparanodal areas. The axo-glial adhesion complexes form a fence-like structure, which disables molecules from diffusing and mixing freely between the different axonal areas. This ensures saltatory conduction as also Na_v and K_v channels are kept in place (compare Fig.2).

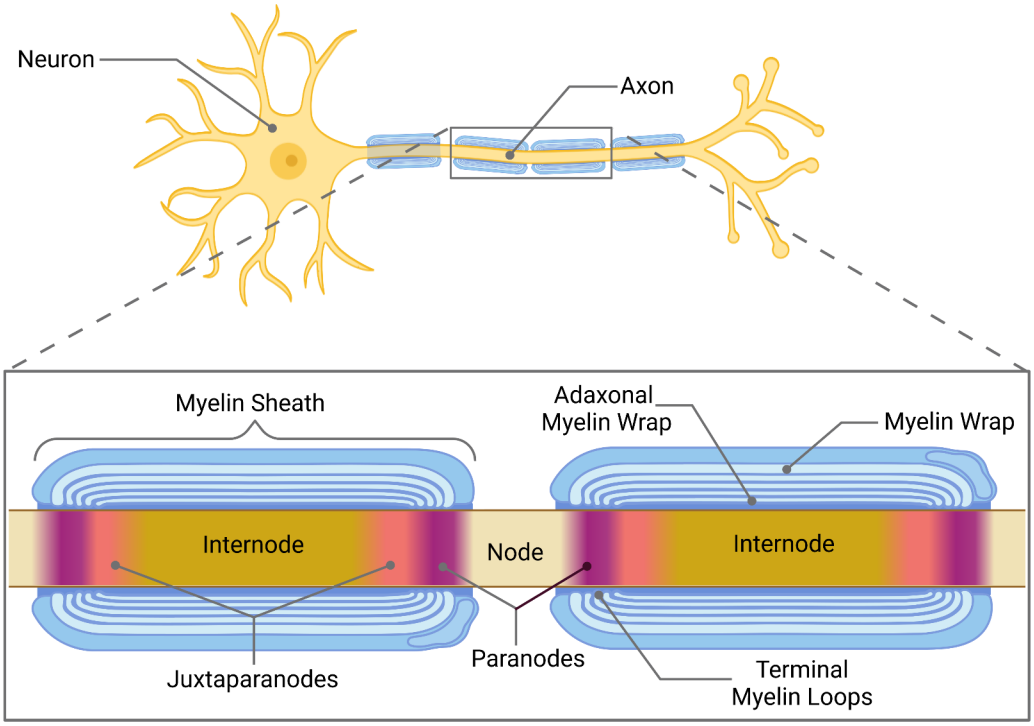

Figure 3: Axo-Glial Adhesion Areas Oligodendroglial processes wrap around axons forming a multi-layered myelin sheath. The wrap closest to the axon is called the adaxonal myelin wrap. Three different axo-glial adhesion areas can be distinguished by structure and dominating proteins: the Paranodes, the Juxtaparanodes, and the Internode.

1.3.1 Internodal Adhesion

The innermost axo-glial adhesion consists of different adhesion complexes. One of them is constituted by oligodendroglial Cell adhesion molecule 4 (Cadm4/SynCAM/Necl), which binds to axonal Cell adhesion molecule 3 (Cadm3) [Park et al., 2008; Zhu et al., 2013]. Besides a delay in the onset of myelination, deletion of Cadm4 (Necl-4 gene) or Cadm3 did not show a significantly changed pattern of myelination in the CNS, suggesting a compensatory axo-glial interaction complex [Elazar et al., 2019]. However, Cadm4 was shown to be beneficial for myelination. Another internodal adhesion complex - MAG interacting with gangliosides - seems beneficial for myelination as well [Quarles, 2007; Schnaar, 2016]. MAG is a myelin protein targeted to the axoglial membrane [Sternberger et al., 1979], the myelin membrane closest to the axon. Of the glycosphingolipid (GSL) family, the gangliosides GD1a and GT1b reside in the neuronal membrane [Ledeen, 1985; Posse de Chaves and Sipione, 2010]. MAG preferentially, but not only, interacts with them, thus anchoring the innermost myelin membrane layer to the axonal membrane (Fig. 4) [Yang et al., 1996b; Collins et al., 1997, 1999; Pronker et al., 2016]. The internodal adhesion areas sustain a fixed distance of approximately 10 nm between the axonal and the oligodendroglial membrane [Pronker et al., 2016].

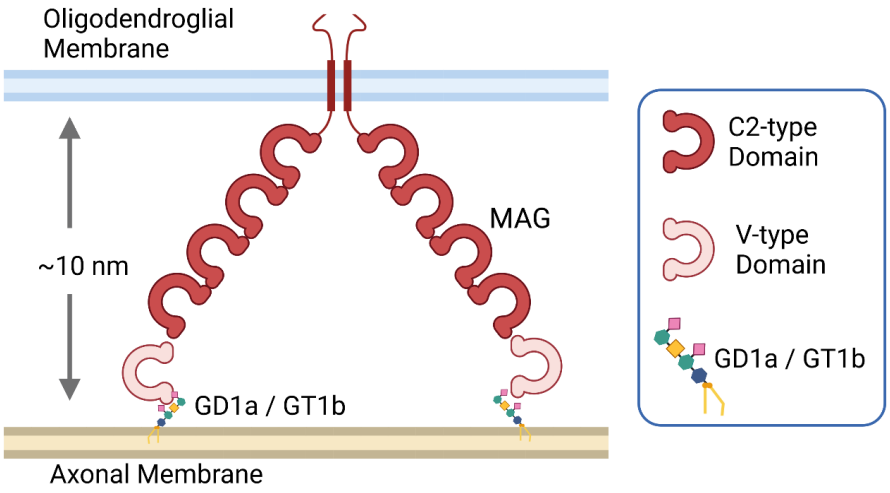

Figure 4: MAG-GANGLIOSIDE INTERACTION Mag consists of five Immunoglobulin (Ig)- like domains. The outermost V-type Ig domain binds to α2,3-linked sialic acid, which is present in the gangliosides GD1a and GT1b. They reside in the axonal membrane.

Myelin-Associated Glycoprotein: a Sialic-Acid Binding Protein

MAG belongs to the family of sialic acid-binding immunoglobulin-like lectins (Siglecs) [Kelm et al., 1994]. Siglecs are usually found on immune cells, where they are involved in *cis* and in *trans* cell-cell interactions [Siddiqui et al., 2019]. They are type I transmembrane proteins that consist of several immunoglobulin-like (Ig) domains [Kelm et al., 1994]. Their outermost Ig-like domain interacts with sialic acid-containing Glycosphingolipids (GSL) [Kelm et al., 1994; Pronker et al., 2016]. MAG is the only protein of this family that is expressed solely in the nervous system, more precisely on oligodendrocytes (as Siglec4) and Schwann cells (as Siglec4b) [Sutcliffe and Milner, 1984; Trapp, 1990; Quarles, 2007].

The extracellular domain of MAG consists of 5 Ig domains (Fig. 4). Four of the MAG Ig domains are C2-Ig domains, whereas the fifth, the N-terminal domain, is a V-type Ig domain [Trapp, 1990; Kelm et al., 1994]. The V-type Ig domain binds with high specificity to α2,3-linked sialic acid [Yang et al., 1996b; Collins et al., 1997; Vinson et al., 2001; Vyas et al., 2002; Pronker et al., 2016]. This structure is present on the neuronal gangliosides GD1a and GT1b and some sialic acid-containing oligosaccharides of glycoproteins [Yang et al., 1996b; Collins et al., 1997; Strenge et al., 1999; Vyas et al., 2002]. In total, the Ig domains have eight *N*-glycosylation sites, which cause a microheterogeneity of MAG [Kruse et al., 1984; Malfroy et al., 1985; Arquint et al., 1987; Lai et al., 1987; Salzer et al., 1987]. MAG's many glycosylation sites suggest a huge variety of binding partners, not only in *trans* but also in *cis* [Sedzik et al., 2015]. Structural analysis of MAG revealed its *cis* dimerization in the oligodendroglial membrane [Pronker et al., 2016].

Despite extensive research on the MAG protein, its exact functions remain not fully understood [Schwardt et al., 2015]. In oligodendrocytes, MAG is targeted to the axoglial membrane by the inclusion into galactolipid-rich microdomains [Sternberger et al., 1979; Poltorak et al., 1987; Bartsch et al., 1989; Trapp, 1990; DeBruin et al., 2005; Aureli et al., 2015]. Considering the variety of potential MAG interaction partners, *Mag*$^{-/-}$ mice were surprisingly normal [Montag et al., 1994]. Only subtle deficits, e.g., delayed onset of myelination, were discovered in the CNS. Based on these results and other studies, MAG was proposed to play an essential role in initiating myelination [Poltorak et al., 1987; Quarles, 2007]. Indeed, MAG was found on oligodendroglial processes before or during myelination [Bartsch et al., 1989; Trapp et al., 1989]. In addition, *Mag*$^{-/-}$ mice showed more unmyelinated axons in the optic nerve than wild type mice [Bartsch et al., 1997]. In contrast, another study reported slight behavioral deficits and periaxonal detachment of the myelin membrane in *Mag*$^{-/-}$ mice [Li et al., 1994]. Additionally, older *Mag*$^{-/-}$ mice developed axonal and myelin degeneration, hence suggesting a role of MAG in myelin maintenance rather than in myelin development [Fruttiger et al., 1995; Pan et al., 2005]. While MAG is probably essential for both processes, it was also identified to inhibit neurite outgrowth in the CNS, thus preventing the regeneration of injured axons [McKerracher et al., 1994; Mukhopadhyay et al., 1994]. A soluble form of MAG (dMAG), which consists of the entire extracellular part of MAG, is an even more potent inhibitor of neurite outgrowth [Tang et al., 1997, 2001]. Besides its extracellular activities with other molecules, a variety of intracellular interactions and its potential involvement in signal transducing processes have been reported for MAG (reviewed in [Quarles, 2007; Schnaar and Lopez, 2009]). In summary, the results of several studies cannot point out the exact function of MAG yet.

Gangliosides - Sialic Acid Containing Glycosphingolipids

The glycome and, as such, a big part of the fingerprint of brain cells like neurons and oligodendrocytes is unique. These cell types contain unusual high amounts of glycolipids like gangliosides and sulfatides [Schmitt et al., 2015; Olsen and Færgeman, 2017; Poitelon et al., 2020; Sipione et al., 2020]. With a fraction of 12% of the total lipid composition, gangliosides are considered highly enriched in the neuronal membrane. Besides, most sulfatides are found in cell membranes of myelinating glia.

Gangliosides were first discovered and isolated by Gunnar Blix and Ernst Klenk [Blix, 1936; Klenk,

1941]. Klenk purified sialic acid-containing GSLs and named them "Gangliosides" as he located them preferentially in glial cells [Schnaar, 2019; Klenk, 1942]. Since Klenk defined gangliosides "as a ceramide lipid in glycosidic linkage to a glycan (of any size and structure) that contains at least one sialic acid residue" [Klenk, 1941], a vast diversity of ganglioside subspecies (collected at www.lipidmaps.org [Fahy et al., 2005; Liebisch et al., 2020]) was discovered and their roles in different cellular processes determined. In the nervous system, Gangliosides were found to be involved in regulating receptor functions, neuronal survival, axonal regeneration, and in axon-myelin interactions [Olsen and Færgeman, 2017; Schnaar et al., 2014]. However, the exact roles of the specific ganglioside single species remain enigmatic. Studies on mouse models suggest that gangliosides can compensate for each other on single species level [Sturgill et al., 2012; Yamashita et al., 2003; Yoshikawa et al., 2009]. In addition, ganglioside detection methods were neither precise nor efficient, which made research on their exact functional roles even more challenging [Barrientos and Zhang, 2020].

Ganglioside synthesis is a developmentally regulated, region-dependent, and stepwise process [Desplats et al., 2007; Kolter et al., 2002; Kracun et al., 1992; Vanier et al., 1971]. A sphingoid base provides the core structure for synthesizing complex glycosphingolipids. Together with an *N*-acylated long-chain fatty acid amide it forms a ceramide backbone (Fig. 5, upper panel) [Posse de Chaves and Sipione, 2010; Olsen and Færgeman, 2017]. At the interface of the endoplasmic reticulum and the golgi apparatus, glycosylation of ceramide yields glucosylceramide (GlcCer) (Fig. 5) [Futerman and Pagano, 1991; Hirschberg et al., 1993; Ichikawa et al., 1996]. In the golgi apparatus, GlcCer is processed to lactosylceramide (LacCer), which serves as the metabolic substrate for synthesizing all GSL of the globo-, lacto-, ganglio- and asialo- series by stepwise addition of different sugar groups [Russo et al., 2018]. Sialic acid is the structure that confines gangliosides from other GSL [Klenk, 1942]. The simplest ganglioside species GM3 contains a single sialic acid [Kolter et al., 2002; Lahiri and Futerman, 2007]. The further development proceeds, the more complex gangliosides are being synthesized in the golgi apparatus and trans golgi network by adding glycans and sialic acids. Hence, existing simple molecules are extended and gain complexity and diversity. The majority of gangliosides in neurons are represented by four subspecies of the a- and b-series, GM1, GD1a, GD1b, and GT1b [Prinetti et al., 2000; Sonnino et al., 2007].

Studies on rat brains determined the ganglioside content and species during development [Yu et al., 1988; Saito and Sugiyama, 2002]. They reported an increase in ganglioside complexity during development. This developmental shift from simple to complex gangliosides was also observed in human brain studies [Vanier et al., 1971; Svennerholm et al., 1989; Kracun et al., 1992]. Interestingly, GD1a, GD1b, and GT1b were found before the onset of myelination [Irwin and Irwin, 1982; Svennerholm et al., 1989]. Caused by a drastic decrease of GM1 and GD1a, the total amount of gangliosides decreases during aging [Svennerholm et al., 1994; Kracun et al., 1992].

Together with sphingomyelin (SM) and cholesterol (Chol), GSL establish separate structures in the membrane (lipid rafts). They use hydrogen bonds to interact with neighboring ceramide hydroxyl groups and glycan head groups (*cis* interactions) [Olsen and Færgeman, 2017; Posse de

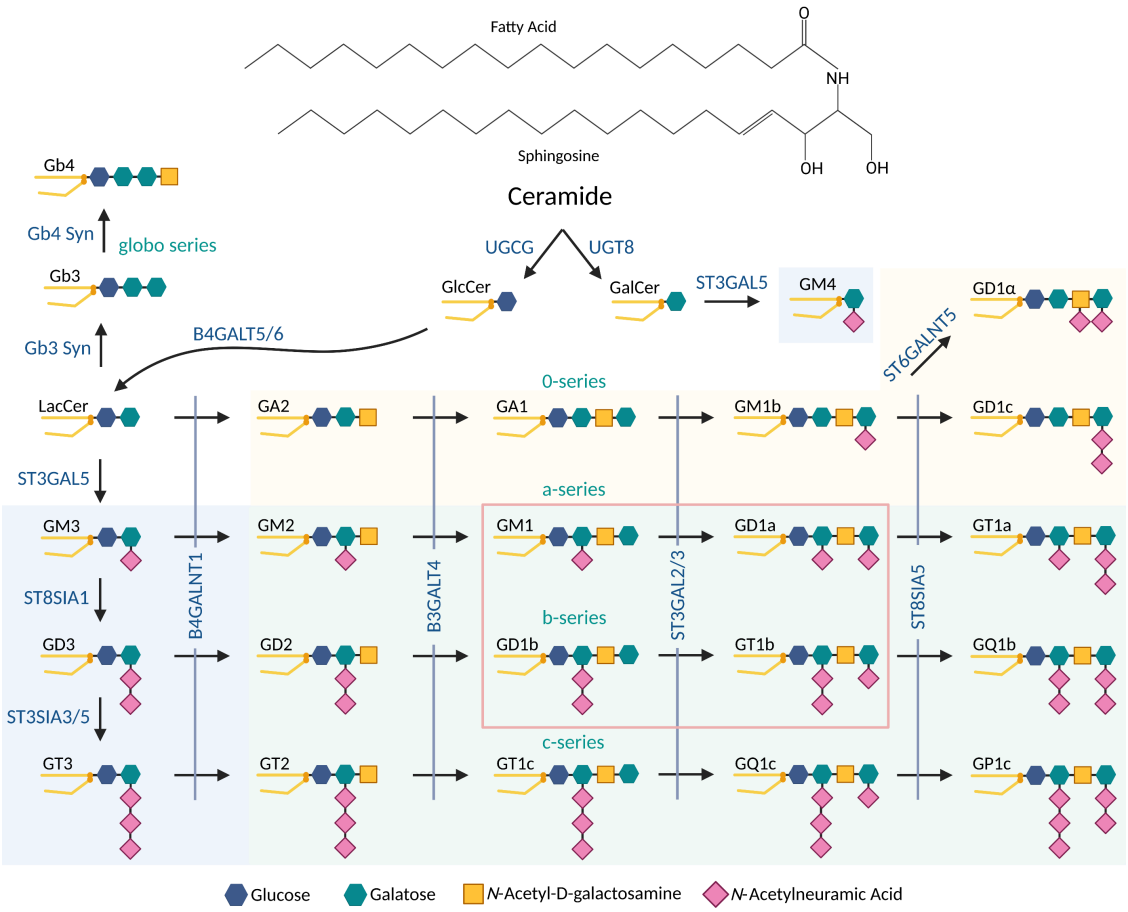

Figure 5: GANGLIOSIDE BIOYNTHESIS PATHWAY A sphingosine base and a fatty acid amide form a ceramide. Different ganglioside species are produced by stepwise addition of glucose, galactose, *N*-Acetyl-D-galactosamine and particularly *N*-Acetylneuramic Acid (sialic acid). Enzymes that catalyze the addition of sugar groups are written in dark blue. Blue shaded panel: gangliosides lacking in *St3gal5*$^{-/-}$ mice; yellow shaded panel: gangliosides lacking in *B4galnt1*$^{-/-}$ mice; green shaded panel: overlapping gangliosides lacking in double mutant mice; major brain gangliosides are encircled in red. 0-series gangliosides are also termed as asialo series gangliosides.

Chaves and Sipione, 2010; Simons and Gerl, 2010]. GSLs and SM consist of long and mostly unsaturated fatty acid carbon chains that allow for dense packing of these molecules. Thus, they enhance the formation of separate structures in the membrane, which are less fluid than loosely packed membrane structures consisting of shorter and polyunsaturated fatty acid chains [Piomelli et al., 2007]. These structures are detergent-resistant membranes (DRMs) [Piomelli et al., 2007], facilitate lipid-protein interactions [Posse de Chaves and Sipione, 2010] and enhance protein-protein interaction [Sonnino et al., 2007; Ichikawa et al., 2009].

The gangliosides GD1a and GT1b in the axonal membrane are specifically interacting in *trans* with MAG on the myelin membrane (see previous section for details) [Ledeen, 1985; Yang et al., 1996b; Collins et al., 1997; Strenge et al., 1999; Vyas et al., 2002].

Considering the vast diversity of enzymes for synthesizing a small proportion of specific lipids, the precise timing of synthesis during development and in confined areas, and their ability to compensate for the loss of specific species, the importance of gangliosides is probably underestimated and should be subject of intense investigations.

Mouse Models lacking Gangliosides

0-series Gangliosides only: *ST3GAL5*$^{-/-}$

The *ST3GAL5* gene encodes for GM3 synthase, which is involved in the first step of ganglioside synthesis (Fig. 5). It catalyzes the addition of sialic acid to LacCer and hence produces the first simple ganglioside GM3 [Sipione et al., 2020].

In two similar approaches, Yamashita et al. [2003] and Yoshikawa et al. [2009] generated mouse models lacking GM3 synthase by disrupting the *ST3GAL5* gene. *ST3GAL5*$^{-/-}$ mice were unexpectedly healthy. They did not show any neurological deficits nor axon-myelin impairment and developed normally, albeit they showed increased insulin sensitivity and were deaf by the loss of the organ of corti [Yamashita et al., 2003; Yoshikawa et al., 2009]. Thin-layer chromatography confirmed the lack of a-, b- and c-series gangliosides but showed increased concentrations of the 0-series gangliosides GM1b and GD1α [Schnaar et al., 2014; Yamashita et al., 2003; Yoshikawa et al., 2009]. Thus implicating a compensatory mechanism for a-, b- and 0- series gangliosides with equal efficiency in supporting axon-myelin interactions.

No Complex Gangliosides: *B4GALNT1*$^{-/-}$

The switch from simple to complex ganglioside synthesis is catalyzed by GM2/GD2 synthase (*N*-acetylgalactosaminyltransferase), which adds a sialic acid to GM3 and GD3 (Fig. 5) [Schnaar et al., 2014; Sipione et al., 2020]. The *B4GALNT1* gene encodes for GM2/GD2 synthase. Two different studies developed murine models with disrupted *B4GALNT1* gene, resulting in a lack of complex gangliosides and accumulation of GM3 and GD3 in brain and liver (Fig. 5) [Takamiya et al., 1996; Liu et al., 1999]. Young adult *B4GALNT1*$^{-/-}$ mice do not display phenotypic deficits nor any changes in nervous system anatomy, including the dendritic morphology, the spine density in the motor cortex and in the dentate granular cells, indicating that complex gangliosides are not necessary for early development of the nervous system [Takamiya et al., 1996; Liu et al., 1999; Dobrović et al., 2011]. However, results of subsequent studies indicate a deficit in axon-myelin interactions in *B4GALNT1*$^{-/-}$ mice and stress the requirement of complex gangliosides for optimal myelination. Starting from 10 weeks of age, they show a decrease in conduction velocity, which progresses with age [Takamiya et al., 1996; Susuki et al., 2007]. Ultrastructural analysis revealed paranodal deficits with enlarged and disorganized loops and Wallerian-like degeneration in the peripheral and central nervous system at 4-16 weeks [Sheikh et al., 1999; Ma et al., 2003; Susuki et al., 2007]. Consistent with the previous findings are behavioral deficits with difficulties in motor coordination and balance, hindlimb weakness, whole-body tremor, and hyperactivity in 6-12 months old *B4GALNT1*$^{-/-}$ mice [Chiavegatto et al., 2000; Pan et al., 2005].

Notably, Sheikh et al. [1999] showed a 43% lower expression of MAG in *B4GALNTt1*$^{-/-}$ mice compared to other myelin proteins even though the MAG mRNA is only slightly reduced (-18%). A further study reported phenotypic similarities in nervous system ultrastructure and behavior of *MAG*$^{-/-}$, *B4galnt1*$^{-/-}$ and double mutant mice [Pan et al., 2005]. Schafer et al. [2004] found Nfasc155 and Caspr associated with lipid rafts, thus probably providing paranodal stability. In contrast, Susuki et al. [2007] announced them to be less raft-associated in *B4galnt1*$^{-/-}$ mice suggesting lower paranodal stability within this genotype.

Ganglioside null: *ST3GAL5*$^{-/-}$ / *B4GALNT1*$^{-/-}$

Crossing *B4GALNT1*$^{-/-}$ with *ST3GAL5*$^{-/-}$ mice results in a loss of simple and complex gangliosides in double mutant mice (Fig. 5), while the amount of LacCer is increased [Yamashita et al., 2005b]. Double mutant mice were born healthy. However, these mice quickly developed a severe phenotype. They survived for only $\sim$1-3 months; their body and brain size and overall weight were significantly smaller and lower than wild type animals of the same age. Structural and ultrastructural analysis of 1.5- 3-month-old double mutant mice revealed white matter vacuolization in the cerebellum and spinal cord, axonal degeneration, and disorganized paranodes [Yamashita et al., 2005b]. Contrary to previous findings, the expression level of MAG in *B4GALNT1*$^{-/-}$ / *ST3GAL5*$^{-/-}$ mice was not significantly different from wild type mice, hinting toward a normal oligodendrocyte development [Sheikh et al., 1999; Yamashita et al., 2005b]. The nervous system failures of the double mutants are more severe than those of *B4GALNT1*$^{-/-}$ mice, once again stressing the role and importance of gangliosides in axon-myelin interactions [Yamashita et al., 2005b; Schnaar et al., 2014].

Other Mouse Models

ST8SIA1$^{-/-}$ mice do not synthesize GD1b and GT1b but instead GM1 and GD1a in high amounts. They do not show any alterations in axon-myelin interactions and appear normally developed and healthy [Kawai et al., 2001]. A double KO of *B4GALNT1* and *ST8SIA1* leads to premature death, primarily within six months.

In contrast, *ST3GAL2/3*$^{-/-}$ mice cannot synthesize the most complex gangliosides of all series. However, the major brain gangliosides GM1 and GD1b are still synthesized in low amounts, and the total amount of gangliosides in the brain did not change [Sturgill et al., 2012]. A reduction of GD1a and GT1b levels by 95% and protein sialylation by 50% leads to small, weak, and short-lived animals with deficits in hindlimb reflexes.

CGT$^{-/-}$ mice lack galactolipids (e.g., galactosylceramides and sulfatides) [Bosio et al., 1996; Coetzee et al., 1996; Bosio et al., 1998; Coetzee et al., 1998; Dupree et al., 1998]. Myelination occurs normally in these mice but seems unstable among the myelin wraps and not compacted. Myelin degenerates and affects the mouse behavior from 12-14 days onwards, leading to premature death after mostly 1-2 months. However, expression of CGT in oligodendrocytes only rescues the *CGT*$^{-/-}$ null phenotype, stressing the importance of galactolipids in oligodendrocytes [Zöller et al., 2005].

CST$^{-/-}$ mice lack sulfatides, which are predominantly found in myelinating cells [Honke et al., 2002; Ishibashi et al., 2002; McGonigal et al., 2019]. They develop normally but show age-related nervous system degeneration. Their phenotype indicates that sulfatides are important for myelin maintenance and the establishment of paranodes.

CST$^{-/-}$ *x B4GALNT1*$^{-/-}$ mice synthesize neither sulfatides nor complex gangliosides. They show disordered nodes and paranodes as well as axonal degeneration and premature death [McGonigal et al., 2019]. The authors of this study conclude that both sulfatides and b-series gangliosides are necessary to orchestrate the proper localization of the myelin adhesion proteins NFASC155 and MAG.

1.3.2 Paranodal Adhesion

Paranodal complexes adhere terminal myelin loops on both sides of a myelin sheath to the axon [Faivre-Sarrailh, 2020; Ghosh et al., 2018] (Fig. 3). On the axonal side, the paranodal adhesion complex consists of the GPI-anchored protein Contactin (CNTN, Cntn), which associates in *cis* with the transmembrane protein Contactin-associated protein (CASPR, Caspr) [Faivre-Sarrailh et al., 2000; Gollan et al., 2003]. CASPR/CNTN then interacts in *trans* with the oligodendroglial Neurofascin 155 (NFASC155, Nfascb), another transmembrane protein, thus tethering myelin loops to the axonal membrane [Charles et al., 2002; Sherman et al., 2005] (see Fig. 6C). Paranodal adhesion complexes establish a fixed distance of 6-8 nm between the axo-glial membranes in the CNS [Nans et al., 2011].

Intracellular interactions with Ankyrins and hence the axonal and glial cytoskeleton stabilize this adhesion [Chang et al., 2014; Davis et al., 1996; Zhang et al., 2013]. By forming a diffusion barrier, paranodal adhesion complexes segregate nodal Na_v-channels from juxtaparanodal K_v-channels in the axonal membrane, thus enabling saltatory signal transduction [Pedraza et al., 2001; Rasband et al., 2003; Rios et al., 2003]. A separation of the CASPR/CNTN complex and NFASC155 into lipid rafts probably promotes the formation and stability of paranodal adhesion complexes [Faivre-Sarrailh et al., 2000; Schafer et al., 2004; Susuki et al., 2007; Bonetto and Di Scala, 2019; McGonigal et al., 2019].

All three proteins mentioned above are strictly required to assemble paranodal adhesion complexes. The absence of either NFASC155, CNTN, or CASPR in mouse models results in disrupted paranodal adhesion complexes, intrusion of juxtaparanodal K_v-channels, and impaired nerve conduction. These phenotypes stress the mutual interdependence of each of the three proteins for the sustenance of saltatory conduction [Bhat et al., 2001; Boyle et al., 2001; Sherman et al., 2005; Pillai et al., 2009; Zonta et al., 2008]. Nevertheless, terminal myelin loops appear surprisingly normal without paranodal junctions.

Direct interaction of NFASC155 with CASPR has never been shown [Bonetto and Di Scala, 2019]. However, several studies detected co-localization of CASPR and NFASC155 [Pedraza et al., 2009; D'Este et al., 2017], while some studies observed interactions of NFASC155 with CNTN [Thaxton et al., 2010; Liu et al., 2011; Labasque et al., 2014].

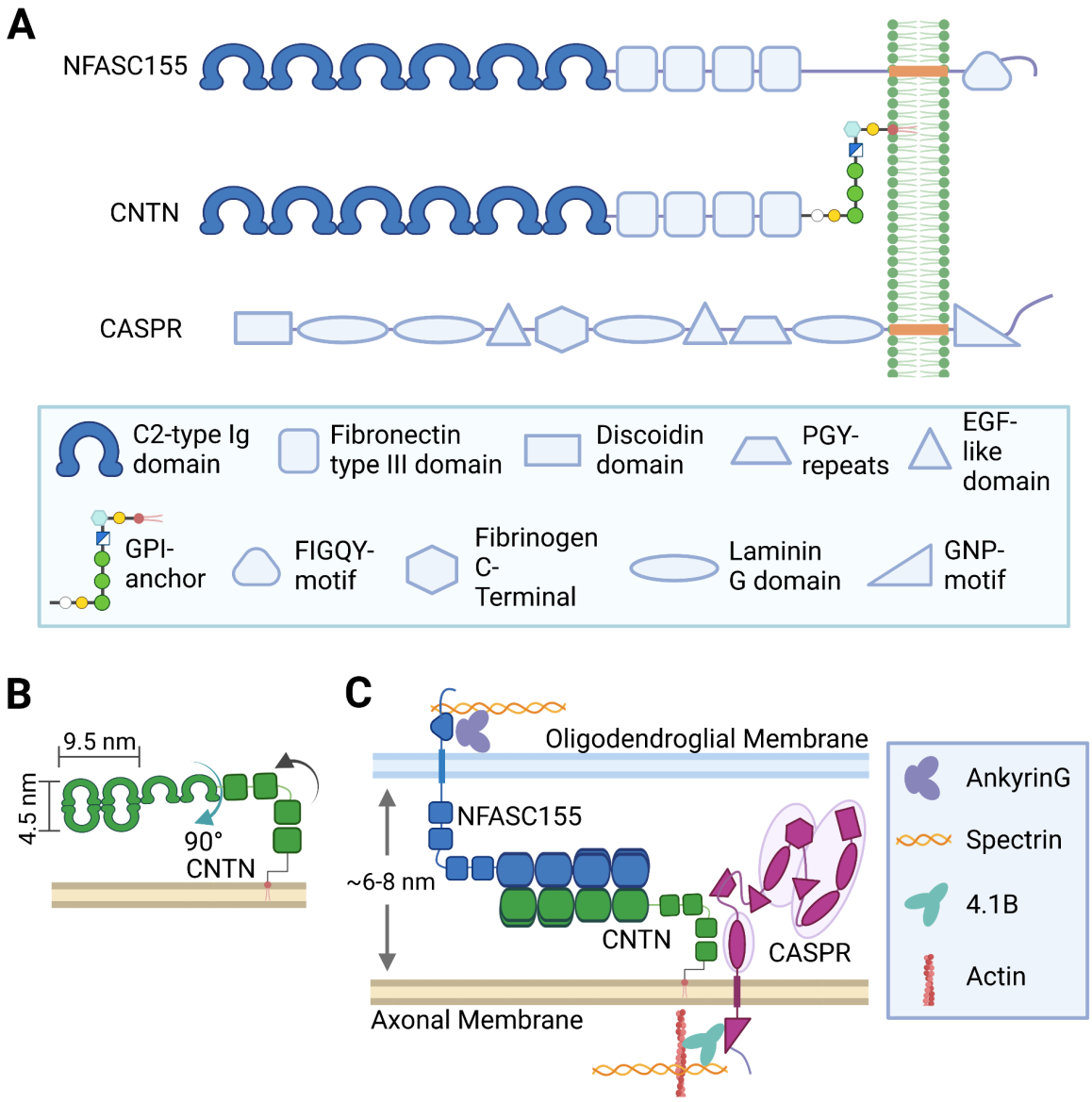

Figure 6: Proteins Forming the Paranodal Adhesion Complex A Structure of the proteins that form the paranodal adhesion complex. **B** The Ig1-Ig4 domains of NFASC155 and CNTN form a horseshoe-like structure, which has approximately a length of 9.5 nm, a width of 4.5 nm, and a thickness of 2.5 nm. The length of CNTN from the first fibronectin type III (FNIII) domain to the Ig3 domain would be 32 nm. By conformational bending after the second FNIII domain and a 90° rotation of the entire Ig domain, CNTN fits in the cleft. **C** Assumption for the formation of the paranodal adhesion complex in the paranodal cleft. CNTN and CASPR associate in the axonal membrane. CASPR is in contact with the axonal cytoskeleton via its transmembrane domain, while CNTN interacts with NFASC155. Considering its similar domain structure and the limited axo-glial space at paranodes, NFASC155 presumably shows the same protein conformation as CNTN. NFASC155 is associated with the oligodendroglial cytoskeleton.

Neurofascin

Neurofascin (NFASC, Nfasc) is a transmembrane cell adhesion protein that shares commonalities with the L1-group of the immunoglobulin superfamily [Volkmer et al., 1992; Davis et al., 1993; Holm et al., 1996]. The characteristic structure of this protein family consists of six immunoglobulin-like (Ig) domains, followed by four to five fibronectin-like (Fn) domains [Davis et al., 1993; Holm et al., 1996; Liu et al., 2011] (Fig. 6 A). Alternative splicing results in many different splice variants of NFASC [Hassel et al., 1997; Davis et al., 1993]. They differ structurally and by their cell expression, location, and function [Zonta et al., 2008; Kriebel et al., 2012].

The extracellular Ig1-Ig4 domains of NFASC form a horseshoe-like structure, where the Ig1-Ig2 domains fold back onto the Ig3-Ig4 domains [Liu et al., 2011] (Fig. 6 B). Liu et al. [2011] found that this conformation enables homophilic interactions of the Ig1-Ig2 domains with other NFASC155 proteins. However, Thaxton et al. [2010] discovered the Ig5-Ig6 domains in NFASC155 to be necessary for its interaction with CNTN, while Labasque et al. [2014] identified CNTN glycosylation sites necessary for NFASC155 interactions. Even though the interaction mechanism is not exactly clear, the interaction of oligodendroglial NFASC155 to CNTN of the axonal CASPR/CNTN complex eventually tethers the terminal myelin loops to the axonal membrane (Fig. 6 C) [Charles et al., 2002; Sherman et al., 2005]. The intracellular interaction of the NFASC155 FIGQY-motif with the oligodendroglial cytoskeleton via ankyrin G sustains the stabilization of this ternary complex [Chang et al., 2014; Tuvia et al., 1997; Ogawa et al., 2006; Pomicter et al., 2010]. Phosphorylation of the FIGQY motif regulates the interaction with ankyrin [Garver et al., 1997; Tuvia et al., 1997]. Interestingly, the amino acid sequence of NFASC contains a palmitoylated cysteine in its transmembrane domain [Ren and Bennett, 1998], which probably allows for association with lipid rafts during paranode formation and adds additional stability [Schafer et al., 2004].

The absence of the *Nfasc* gene in mice results in a wide distribution of nodal and paranodal proteins along the axon, the absence of paranodal junctions, and premature death at postnatal day 6 (P6) [Sherman et al., 2005; Zonta et al., 2008]. In contrast, the embryonic loss of only the mRNA splice variant NFASC155 is lethal at P17; these mice do not constitute paranodal adhesion complexes and show a lower signal conduction velocity [Pillai et al., 2009]. Adult ablation of *Nfasc155* leads to a progressive disorganization of axonal domains, while paranodal junctions become gradually undetectable. Surprisingly, terminal myelin loops appear hardly impaired. These mice show only some everted myelin loops and intrusions of other myelin sheath or Schwann cell processes [Sherman et al., 2005; Pillai et al., 2009]. Interestingly, in wild type mice, Pedraza et al. [2009] observed early axonal CASPR and glial NFASC155 accumulation at myelin ensheathment sites and its relocation to paranodes.

Caspr

Contactin-associated protein (CASPR, Caspr) is structurally similar to the Neurexin cell adhesion protein family and belongs to the subfamily of Neurexin-like proteins [Bellen et al., 1998; Menegoz et al., 1997; Peles et al., 1997].

The *Cntnap1* gene encodes for the transmembrane protein CASPR. [Peles et al., 1997; Menegoz et al., 1997]. It is part of the paranodal adhesion complex [Einheber et al., 1997; Menegoz

et al., 1997], where it associates 1:1 with Contactin on the axonal membrane (Fig. 6 B) [Peles et al., 1997; Rios et al., 2000; Bonnon et al., 2003]. This association starts in the endoplasmic reticulum (ER) and follows an N-glycan-dependent, Golgi-independent pathway to enter its final position at the axonal membrane [Faivre-Sarrailh et al., 2000; Rios et al., 2000; Bonnon et al., 2003]. CASPR's seemingly unique, extracellular PGY motif mediates this pathway [Bonnon et al., 2007]. It serves as an ER retention signal. Chaperoned by Contactin, the PGY motif changes conformation and allows the CASPR/CNTN complex to leave the ER. In the absence of CNTN, CASPR is chaperoned and glycosylated by calnexin and stays in the ER [Bonnon et al., 2003, 2007].

The absence of CASPR in murine models results in a lack of paranodal junctions and disorganized paranodal loops with neighboring myelin sheaths invading the paranodal area [Bhat et al., 2001]. K_V-channels intrude the paranode, leading to impaired signal conduction [Bhat et al., 2001; Gordon et al., 2014]. In addition, these mice are undersized and show tremor, ataxia, and motor paresis [Bhat et al., 2001].

However, the exact function of CASPR in the paranodal adhesion complex is not yet exactly clear. While CNTN seems to be the binding partner for NFASC155 [Thaxton et al., 2010; Liu et al., 2011; Labasque et al., 2014], CASPR's cytoplasmic domain is probably the key player in forming an axonal diffusion barrier for nodal proteins [Gollan et al., 2002; Horresh et al., 2010]. Via its FERM domain, Protein 4.1B can bind to CASPR's intracellular GNP motif, while it also links to the axonal actin/spectrin cytoskeleton [Chishti et al., 1998; Denisenko-Nehrbass et al., 2003; Buttermore et al., 2011; Einheber et al., 2013; Zhang et al., 2013] (Fig. 6 C). While the loss of Protein 4.1B disorganizes axonal domains and disrupts the axonal cytoskeleton at paranodes, the absence of spectrin does not affect paranodal junction formation [Buttermore et al., 2011; Einheber et al., 2013; Zhang et al., 2013; Faivre-Sarrailh, 2020]. A recent study found the interaction of 4.1B and CASPR necessary for longitudinal migration of myelin sheaths for nodal establishment [Brivio et al., 2017].

When CASPR was discovered, Einheber et al. [1997] also reported a diffuse localization of CASPR in unmyelinated axons. They suggested a CASPR relocation from the internode to the paranode during myelination. This hypothesis was confirmed by Eisenbach et al. [2009] and Pedraza et al. [2009], who discovered co-localization of CASPR and NFASC155 from the initial axo-glial contact until their final position at the paranodes of dorsal root ganglia and oligodendrocytes in co-cultures.

Contactin

Contactin, like NFASC155, belongs to the immunoglobulin superfamily [Gennarini et al., 1989; Reid et al., 1994]. Hence, CNTN follows the structure of NFASC155, having six Ig domains and four FNIII domains. However, instead of using a transmembrane domain, CNTN is tethered to the axonal membrane with a GPI-anchor (see Fig. 6 A). In contrast to CASPR, CNTN is expressed in both neurons and oligodendrocytes [Koch et al., 1997; Krämer et al., 1997; Çolakoğlu et al., 2014].

When CNTN is absent, CASPR stays in neuronal cell bodies, paranodal junctions are lacking, and CASPR, as well as NFASC155, are not detected at paranodes [Faivre-Sarrailh et al., 2000; Rios et al., 2000; Boyle et al., 2001; Bonnon et al., 2003]. Mice lacking *Cntn* are severely impaired. They show ataxic gait, defects in controlling voluntary movements, and abnormal cerebellar micro organization [Berglund et al., 1999]. The severity of these symptoms hints toward additional functions of CNTN besides paranodal adhesion, e.g., during development [Berglund et al., 1999; Lieberoth et al., 2009; Çolakoğlu et al., 2014]. However, in the paranodal adhesion complex, CNTN probably has two tasks: while it associates in *cis* with CASPR enabling it to leave the ER and take its position at the axonal membrane [Faivre-Sarrailh et al., 2000; Bonnon et al., 2003], CNTN also seems to interact in *trans* with NFASC155 on the oligodendroglial membrane [Thaxton et al., 2010; Liu et al., 2011; Labasque et al., 2014].

The 1:1 CASPR/CNTN complex includes low molecular weight (LMw) CNTN, which leaves the ER and travels to the axonal membrane in a Golgi-independent pathway, while free, high molecular weight (HMw) CNTN takes the Golgi-dependent route to the same destination [Bonnon et al., 2003]. The FNIII- domains and the GPI-anchor of CNTN are important for CASPR association, transport, and targeting [Faivre-Sarrailh et al., 2000]. One in vitro study pronounced that only HMw CNTN binds to glial NFASC155, while CASPR blocks the processing of LMw CNTN to HMw CNTN and thus inhibits NFASC155 binding [Gollan et al., 2003]. However, the results of this study were opposed by the finding that LMw CNTN associates with CASPR and selectively binds NFASC155, whereas HMw Cntn neither associates with CASPR nor interacts with NFASC155 [Bonnon et al., 2007]. Labasque et al. [2014] found a cluster of three Asparagine sites in the Ig5 domain of CNTN that needs to be *N*-glycosylated for functional interaction with NFASC155.

Freigang et al. [2000] unraveled the crystal structure of Axonin-1 (CNTN2), which is similar to CNTN in its structure. The Ig domains in their model form a horseshoe-like structure as described above for NFASC155. Because of the similarities of CNTN with CNTN2 and NFASC155, we assume that CNTN adopts the same protein structure. Considering the size of these proteins, as well as the distance between the terminal loops and the axonal membrane (6-8 nm) [Nans et al., 2011], an arrangement of the CNTN Ig domains in parallel with the axonal membrane (Fig. 6 B+C) seems likely. Crystallographic analysis of different contactins indeed implies a 90° foldable structure at the FNIII domains [Nikolaienko et al., 2016].

1.3.3 Juxtaparanodal Adhesion Complexes

The juxtaparanodal region is characterized by the presence of clustered $K_v$channels in the axonal membrane, which is necessary to maintain saltatory conduction. The association of CNTN2 and CASPR2 (sometimes referred to as TAG-1), a close relative to CASPR, [Poliak et al., 1999; Traka et al., 2003] clusters the $K_v$channels. However, CASPR2 contains a cytoplasmic PDZ binding domain, which is lacking in CASPR [Poliak et al., 1999]. This domain is probably involved in interactions with many different proteins, including axonal scaffolding proteins, but it is dispensable for $K_v$channel clustering [Horresh et al., 2008; Chen et al., 2015]. In contrast, CNTN2 is expressed in both oligodendrocytes and neurons and interacts *in trans* with itself, thus constituting another anchor for tethering the oligodendroglial membrane to the axon [Traka et al., 2003].

Denisenko-Nehrbass et al. [2003] reported that CASPR2, like CASPR, also interacts via its GNP motif with the axonal cytoskeleton protein 4.1B, probably only after CASPR2 reached its final position at the juxtaparanode. This was confirmed by Horresh et al. [2010], who found 4.1B necessary for $K_v$channel clustering. However, the mechanism responsible for $K_v$channel clustering is not yet fully understood (Pinatel and Faivre-Sarrailh [2021] wrote an extensive review).

1.4 Zebrafish

1.4.1 Zebrafish as Animal Model in Research

Research on genes that are functionally conserved among species has long been conducted on invertebrates like fruit flies (*Drosophila melanogaster*) or worms (*Caenorhabditis elegans*) [Lieschke and Currie, 2007]. Even though zebrafish (*Danio rerio*) were discovered in the 1960s as a model to study developmental and embryological processes, their breakthrough started only 20 years later [Davis et al., 2014]. Usually only applied to invertebrates, the adaptation of genetic techniques enabled the application and affordability of large-scale forward-genetic and chemical screens in a vertebrate animal model, the zebrafish [Lieschke and Currie, 2007; Davis et al., 2014; Early et al., 2018]. By far the most commonly used vertebrate animal model is the mouse (*mus musculus*) before other rodents [Robinson et al., 2019]. However, compared to rodents, zebrafish come with many unique advantages. Very pragmatically, the costs for the husbandry of the resistant, easy-to-breed zebrafish are much lower, while the progeny of a single, projectable zebrafish mating is much higher, allowing for a higher, easy-achievable sample size [Lieschke and Currie, 2007; Davis et al., 2014]. Additionally, the transparency of zebrafish larvae and their fast, *ex utero* development enable easy application of *in vivo* imaging techniques.

Being a young animal model system, research tools for zebrafish are not as advanced as for application in fruit flies or rodents [Ackerman and Monk, 2016; Davis et al., 2014]. However, the fast-growing zebrafish research community continues to adapt invertebrate and rodent-specific research tools and techniques like antibodies, cell lines, and genetic manipulation tools for zebrafish application. For example, when the discovery of CRISPR/Cas9 was announced in 2012 [Jinek et al., 2012], it was available in zebrafish only a few months later [Hruscha et al., 2013; Hwang et al., 2013], with the first tissue-specific CRISPR/Cas9 approaches being applicable only approximately 1.5 years later. [Ablain et al., 2015; Yin et al., 2015].

These advantages make zebrafish a sought-after animal model in developmental, cardiac, tumor and, with their enormous potential to regenerate axons in the CNS, for nervous system research [Becker and Becker, 2008; Feitsma and Cuppen, 2008; Vajn et al., 2013a; Davis et al., 2014]. However, the advantages of the zebrafish animal model come with a downside that makes targeting specific genes in reverse-genetic approaches challenging: Zebrafish are freshwater bony fish originating from South-East Asia. As such, they belong to the *Cyprinidae* family within the *Teleostei*. About 320 million years ago, a gene duplication in the common ancestor of all *Teleostei* developed a fish-specific whole genome duplication making it harder to knock out all versions of a specific gene [Vandepoele et al., 2004]. While zebrafish show the highest rates of genome duplication of all vertebrates, they have the lowest rates of alternatively spliced genes in all teleosts resulting in subfunctionalization of the duplicated genes [Lambert et al., 2014; Lu et al., 2012, 2010]. For example, in other vertebrates, the *Nfasc* gene encodes for NFASC155, NFASC186, and more versions by alternative splicing. The zebrafish homologs are Nfascb and Nfasca, each of which is encoded by its own gene. Nevertheless, the zebrafish genome shows 70% identity with the human genome [Howe et al., 2013; Davis et al., 2014]. In comparison, the mouse/human genome identity makes up for 80%.

1.4.2 Myelin(ation) in Zebrafish

The speed of *ex utero* development and the evolutionary conservation of myelin make zebrafish a perfect model to study myelination [Czopka, 2016]. In zebrafish, the first OPCs can be observed in the transparent larvae 48 hours after fertilization. After only 7 days, myelination is almost completed in zebrafish, whereas it takes approximately one entire month in mice [Sturrock, 1980; Brösamle and Halpern, 2002; Buckley et al., 2010; Czopka, 2016]. Mammals and zebrafish share myelin structure, ultrastructure, and composition characteristics, with many mammalian myelin proteins having homologs in zebrafish [Brösamle and Halpern, 2002; Preston and Macklin, 2015; de Bellard, 2016; Siems et al., 2021]. The evolutionary conservation of myelination from fish to mammals is also conveyed in its developmental pattern; OPCs originate from the same neural precursor cells. In addition, the same transcription factors regulate OPC and oligodendrocyte development [Kirby et al., 2006; Li et al., 2007; Ackerman and Monk, 2016; Czopka, 2016].

Compared to mammals, the myelin protein composition in zebrafish is expanded by the Zwilling, Claudin K, and 36K proteins, which are unique to teleosts [Preston and Macklin, 2015; Ackerman and Monk, 2016; Czopka, 2016; Siems et al., 2021]. Despite lacking sequence homologies, Zwilling-A and Zwilling-B share physiological features with mbp [Schaefer and Brösamle, 2009]. Claudin K is probably involved in forming axon-myelin junctions during nervous system myelination [Münzel et al., 2012]. The most abundant protein in the teleost CNS, 36K, was recently found to have a potential role in regulating oligodendrocyte differentiation via Notch signaling [Morris et al., 2004; Nagarajan et al., 2020]. The exact functions of the additional teleost-specific proteins are not yet fully revealed. However, they may support myelination in a poikilothermic environment to maintain membrane fluidity and myelin adhesion [Schaefer and Brösamle, 2009; Ackerman and Monk, 2016]. As there was no need for conserving these additional proteins with the evolution of homeothermy, they are not expressed in mammals anymore.

Mammals and zebrafish also share homologs of myelin proteins, which are involved in gluing and compacting single myelin membrane layers together, e.g., proteolipid protein (PLP), myelin basic protein (Mbp), and myelin protein zero (Mpz; P_0 in mammals) [Bai et al., 2011; Schweitzer et al., 2006; Nawaz et al., 2013; Siems et al., 2021]. While P_0 is restricted to the PNS in mammals, it is expressed in both the CNS and to a lower extent in the PNS of zebrafish [Bai et al., 2011].

Lately, *in vivo* imaging approaches in zebrafish revealed new insights into myelination dynamics. For example, Almeida et al. [2011] discovered that oligodendrocytes can adjust their myelination potential according to the presence of different caliber axons. Czopka et al. [2013] demonstrated that spinal cord oligodendrocytes myelinate within a time frame of only 5 hours, whereas a retraction of a single myelin sheath can take up to several days. Additionally, Liu et al. [2013] found that $\sim$28% of the nascent myelin sheath retract during the observed time course. They established the term "myelin pruning" for myelin sheath retractions. Auer et al. [2018] reported dynamic remyelination after ablation of myelin sheaths, either by elongating neighboring sheaths or newly formed myelin sheaths. Cunha et al. [2020] observed active phagocytosis of damaged myelin sheaths. The latest zebrafish-myelin research focuses on adaptive myelination by neuronal signals [Hines et al., 2015; Mensch et al., 2015; Koudelka et al., 2016; Baraban et al., 2018; Hughes and Appel, 2019; Almeida et al., 2021].

1.4.3 Axo-glial Adhesion Proteins in Zebrafish

Paranodal adhesion proteins are highly conserved among vertebrate species [Siems et al., 2021]. In zebrafish, Nfascb resembles the structure of NFASC155 of higher vertebrates and is located at paranodes [Djannatian et al., 2019]. Neurofascin is one example of the *teleostei* genome duplication. Its duplicated version Nfasca is homologous to NFASC186 and, like its higher vertebrate counterpart located in the axonal membrane at the nodes of Ranvier [Vagionitis et al., 2021]. A recent study found that Nfascb prevents oligodendroglial processes from myelinating neuronal cell bodies [Klingseisen et al., 2019]. Together with Caspr, Nfascb also supports myelin sheath growth. Recent data showed that zebrafish Nfasca in the axonal membrane indicates the future position of a node of ranvier before the onset of myelination [Vagionitis et al., 2021]. The teleost genome duplication affected not only Nfasc but also Cntn. It was also found duplicated and subfunctionalized in zebrafish as Cntn1a and Cntn1b [Haenisch et al., 2005]. While it is unclear whether one or both are expressed in oligodendrocytes and/or neurons, Cntn1a is expressed earlier in development than Cntn1b [Haenisch et al., 2005; Schweitzer et al., 2007]. One study reported Cntn1a to be located along the axon and at nodes of Ranvier [Koudelka et al., 2016]. In contrast, Cntn1b was found in axonal membranes as an interaction partner of Caspr and Nfascb at paranodes [Djannatian et al., 2019].

Siglec-4/MAG is a well-conserved protein among vertebrates [Lehmann et al., 2004; Siems et al., 2021]. Especially the sialic acid binding sites are highly conserved. Mag from fish was also shown to bind preferentially to α2,3 linked sialic acid, which is present in the gangliosides GD1a and GT1b. A loss of Mag in zebrafish leads to shorter myelin sheaths and less myelinated area [Djannatian et al., 2019]. Hence, we can assume that the Mag-ganglioside adhesion mechanism in zebrafish is similar to other vertebrates. Another internodal adhesion mechanism, which was described in murine models - oligodendroglial CADM4 interacting with axonal CADM proteins - has not been elucidated in zebrafish yet [Elazar et al., 2019]. However, Cadm4 has been described as a highly conserved adhesion protein in zebrafish myelin [Siems et al., 2021].

1.4.4 Gangliosides in Zebrafish

Only recently studies on the general zebrafish lipidome have been published. These include visualization of the glycerophospholipid content in zebrafish embryos during early development [Dueñas et al., 2017], observations of the changes in ceramide subspecies during development [Zhang et al., 2019] and investigations of lipidomic changes in the yolk [Fraher et al., 2016] and after exposure to stressors and toxins [Dreier et al., 2021].

However, the ganglioside lipidome in zebrafish remains remarkably obscure due to the challenges of GSL detection, especially in this species. One study used antibodies against the major brain gangliosides to reveal their localization in zebrafish, carp, and trout brains [Viljetić et al., 2012]. They found that GM1 was not present in zebrafish brains, whereas GT1b was the most abundant ganglioside type and similarly localized as in rodent brains. While GD1a was found in some fiber tracts of individual neurons, GD1b was located in neuronal cell bodies of different brain regions. Hence, they do not resemble the GD1a and GD1b localization of rodent brains. In contrast, a recent study used cholera toxin to visualize GM1 by light-sheet microscopy in zebrafish models of

lysosomal storage diseases (LSD) and found GM1 to be present in several neuronal fiber tracts [Cook et al., 2020]. However, to fully prove the absence of, e.g., GM1, the expression pattern and activity of enzymes for ganglioside synthesis need to be uncovered. A quick search in the zebrafish genome database (GRCz11) found two transcripts for the *St8sia1* gene and a single transcript for the *B3galt4* gene, both of which are involved in GM1 synthesis (compare Fig. 5). These genes showed high homology sequences to the same genes of higher vertebrates. This also holds true for *St3gal2* (one transcript) and *St3gal3* (two genes with one transcript each), which encode enzymes that synthesize other major brain gangliosides than GD1a and GT1b.

1.5 Aims of this Dissertation

Myelin enables faster cognition, action, and reaction compared to non-myelinated axons [Nave and Werner, 2014; Stassart et al., 2018; Stadelmann et al., 2019]. Nevertheless, myelin is also a target of different, in their majority auto-immune based diseases. A better understanding of the detailed mechanisms underlying myelination will support the search for new therapeutic targets and healing methods. With this dissertation, we aim to unravel details of the myelin adhesion and wrapping process.

Pedraza et al. [2009] showed that the axonal paranodal myelin adhesion protein CASPR first accumulates at myelin ensheathment sites and then relocates to paranodes. Indeed, in zebrafish experiments preceding this dissertation, we observed an accumulation of Caspr-YFP underneath a growing myelin sheath in the axonal membrane *in vivo*. While myelin sheaths grow larger and compact, Caspr relocates from the internode to the paranodes. Our observations raised the question about how and in which sequence of events paranodal adhesion proteins relocate to their functional position.

We aimed to develop a model which describes potential mechanisms driving the relocation of paranodal adhesion proteins (e.g., Caspr) from internodal accumulation to its establishment at the paranodes. It is likely that protein interactions drive the relocation. We took advantage of the zebrafish model as it allowed us to observe the relocation of paranodal proteins *in vivo*. By using genetically modified zebrafish, which lack potential oligodendroglial Caspr interaction partners, we investigated their influence on Caspr's localization. Pedraza et al. [2009] observed co-relocation of axonal CASPR and oligodendroglial NFASC155. Hence, we also focused on the role and the importance of Nfasc within the myelin wrapping process. In Fig. 7, we present a hypothetical model which illustrates the Caspr relocation during myelination and potential relocation mechanisms. This model served as a base for this dissertation.

Gangliosides are enriched in neuronal membranes [Schmitt et al., 2015; Olsen and Færgeman, 2017; Sipione et al., 2020]. We hypothesized that the interaction of gangliosides and Mag at myelin internodes [Yang et al., 1996b; Collins et al., 1997; Strenge et al., 1999; Vyas et al., 2002; Pronker et al., 2016] form a permissive surface in the axonal membrane, which supports myelin wrapping and protrudes paranodal proteins from the internodal area. We aimed to determine the importance of this interaction for the relocation of paranodal adhesion proteins. For that, we used zebrafish and ganglioside mutant mice (*ST3GAL5*$^{-/-}$ *B4GALNT1*$^{-/-}$).

Finally, we investigated the lipid composition, including gangliosides of the mouse brain and optic nerve samples, to search for potential compensation mechanisms for the lack of gangliosides at early stage myelin wrapping. We used the latest lipidomic approach, which our collaboration partner, lipotype, recently developed.

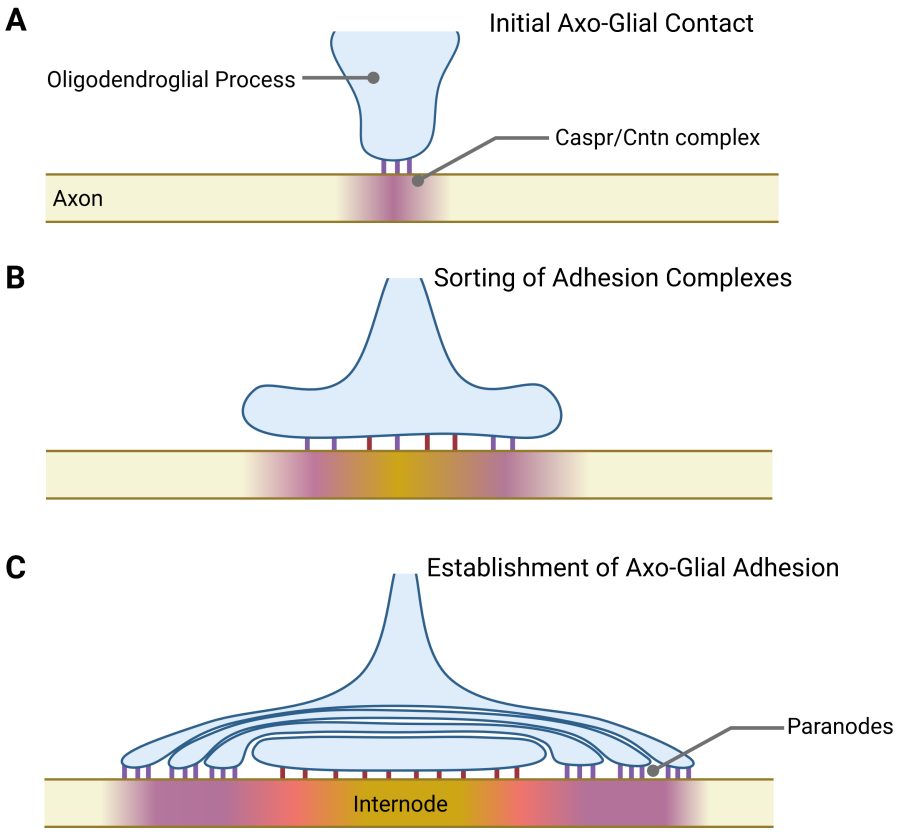

Figure 7: Hypothetical Model of a Paranodal Protein Sorting Mechanism A Our base model starts with the axo-glial contact, most likely initiated by oligodendroglial Nfascb, which interacts with the Caspr/Cntn complex. Caspr/Cntn accumulates upon oligodendroglial contact with the axonal membrane. **B** While the first myelin sheath grows around and along the axon, axonal membrane structures form, probably consisting of oligodendroglial Mag and axonal gangliosides. They start protruding proteins to their destined position, e.g., at the paranodes. **C** In the end, different axo-glial (adhesion) complexes define a fully grown myelin sheath with different adhesion areas.

2 Material and Methods

2.1 Material

2.1.1 Animal Lines and Husbandry

Zebrafish

All zebrafish procedures have been carried out with the approval and according to the regulations of the District Government of Upper Bavaria (project license AZ55.2-1-54-2532-157). Zebrafish were housed at the DZNE fish facility in Munich according to local animal welfare regulations. Transgenic and Knock-out (ko) Zebrafish lines used in this study were kindly shared by other labs or generated in previous studies. They are listed in Table 1.

Zebrafish Line	Source
Tg(Sox10:mRFP)	Kucenas et al. [2008], Almeida et al. [2011]
mag$^{-/-}$	Djannatian et al. [2019]
cntnap1b$^{+/-}$	Djannatian et al. [2019]
nfascb$^{+/-}$	Djannatian et al. [2019]
cntn1b$^{+/-}$	Djannatian et al. [2019]

Table 1: Zebrafish lines used in this dissertation.

Mouse

Mouse lines were obtained from Mutant Mouse Resource and Research Center (MMRRC by NIH). They are listed in Table 2.

Strain Name	MMRRC Stock Number	Source
B6;129S-St3gal5^{tm1Rlp}*/Mmmh*	000374-MU	Yamashita et al. [2003]
B6;129S-B4galnt1^{tm1Rlp}*/Mmmh*	000036-MU	Liu et al. [1999]
St3gal5xB4galnt1 double mutants	–	bred acc. to Yamashita et al. [2005b]

Table 2: Mouse lines used in this dissertation.

All mouse procedures have been carried out with approval and according to the regulations of the District Government of Upper Bavaria (project license AZ55.2-1-54-2532-157) Double mutant mice (St3gal5^{-}/ $^{-}$B4galnt1^{-}/ $^{-}$) were generated by KO/het crossbreeding (♂ St3gal5^{-}/ $^{-}$ B4galnt1^{-}/ $^{+}$) x (♀ St3gal5^{-}/ $^{+}$ B4galnt1^{-}/ $^{-}$). ♂ B4galnt1 $^{-}$/ $^{-}$ are sterile [Liu et al., 1999]. Mice were housed at the German Center for Neurodegenerative Diseases (DZNE) in Munich (single mutants) and the

Institute of Neuronal Cell Biology, Technical University Munich (double mutants) according to local animal welfare regulations. Double mutant litters were monitored for their burden every second day from P8 until P12 or P21, respectively.

2.1.2 Nucleotides

DNA gBlocks for Cloning

For faster cloning of new gene combinations, synthesized DNA sequences were ordered via DNA gblocks®. All DNA gBlocks® were obtained from Integrated DNA Technologies, Leuven, Belgium. They were inserted into plasmid multiple cloning sites via classic restriction enzyme digest and ligation or via Gibson assembly (see section 2.2.1). Their size varied from ∼900- ∼1200 bp. See Table 3 for gBlock names and details of their composition. How gene combinations were chosen and assembled is described in section 2.2.2. Sequences are listed in the attachment (see Appendix IX).

gBlock	Gene Combinations	Reference
GPI-GFP	GPI anchor signal sequence from D.rerio Cntn1a, anchoring extracellular GFP; connected with flexible linker	ensemble.org/ENSDARG00000045685, this dissertation
HA-TM-GFP	Transmembrane Domain from Influenza HA virus protein, anchoring extracellular GFP; connected with flexible linker	modified after Scheiffele et al. [1997]
Herpes-TM-GFP	Transmembrane Domain from Herpes simplex virus protein, anchoring extracellular GFP; connected with flexible linker	modified after Scheiffele et al. [1997]
PM-GFP	palmitoylation site, associates GFP with intracellular membrane	modified after Aicart-Ramos et al. [2011]
several-GFP_part1	single GFP with a rigid linker for construction of multiple GFPs in a row	this dissertation
several-GFP-Herpes-TM	single GFP with a rigid linker and the Herpes Transmembrane domain	this dissertation
several-GFP-GPI	single GFP with a rigid linker and the Cntn1b GPI anchor	this dissertation

Table 3: DNA gBlocks used for cloning. Sequences are listed in Appendix IX.

DNA Primers for Genotyping

For genotyping we used the primers that are listed in Table 4 in a PCR reaction (see section 2.2.1). They are listed in 5' - 3' direction. All primers were obtained from Sigma-Aldrich (Sigma-Aldrich Chemie GmbH, Munich, Germany).

Animal	Name	Sequence	Annealing Temp. in °C
Mouse	M374Mut.F	CAATAGATCTGACCCCTATGC	51
Mouse	M374Mut.R	TCGCCTTCTTGACGAGTTCTTCTG	51
Mouse	M374WT.F	AGCTCAGAGCTATGCTCAGGA	63
Mouse	M374WT.R	TACCACATCGAACTGGTTGAG	63
Mouse	L36-exon7 S	ACACGTGGAGCACTACTTCAT	64
Mouse	L36-exon8AS	AGGTCCAGGGGCGTCTTCT	64
Mouse	L36-neo AS	TGCAATCCATCTTGTTCAATG	64
Zebrafish	caspr fwd	CAAATACATGGTGCTGTACG	TD 66 (15x -1) + 51(22x)
Zebrafish	caspr rev	CCAACATTGTAAGCATAGACC	TD 66 (15x -1) + 51(22x)
Zebrafish	cntn1b fwd	CGTCTTTAAATTTTACCTTAAGTGCC	60
Zebrafish	cntn1b rev	TGCACTTTAACACAGATTAATGGAA	60
Zebrafish	nfascb fwd	AGAAGGCGGGGCTTAATATAAC	60
Zebrafish	nfascb rev	ATAAATGCAGTCTTGGTGAGCA	60
Zebrafish	mag fwd	CTCTTTCTCTAAACAGATGCAAGC	60
Zebrafish	mag rev	CGACAGAATTTTCATTGCTGG	60

Table 4: DNA Primers used for Genotyping.

DNA Plasmids for Use in Zebrafish

All plasmids used in this dissertation are listed in Table 5. They were solely used for cloning and expression in zebrafish. Plasmid maps are attached in Appendix X. All plasmids generated in this dissertation are available upon request.

Plasmid	Insert	Application	Source
pCS2FA-transposase	Tol2 Transposase	mRNA Synthesis	Kwan et al. [2007]
pDestTol2CG2	Backbone	Cloning	Kwan et al. [2007]
pDestTol2pACryGFP	Backbone	Cloning	Berger and Currie [2013]
pME_MCS	MCS	Cloning	Kwan et al. [2007]
p3E_polyA	SV40 polyA signal	Cloning	Kwan et al. [2007]
p5E_UAS	10x UAS	Cloning	Kwan et al. [2007]
pME_GPI-GFP	GPI-GFP	Cloning	this dissertation
pME_HA-TM-GFP	HA-TM-GFP	Cloning	this dissertation
pME_Herpes-TM-GFP	Herpes-TM-GFP	Cloning	this dissertation
pME_PM-GFP	PM-GFP	Cloning	this dissertation
pTol2CG2_-HuC:Gal4VP14	Gal4	Expression	Kwan et al. [2007]
pTol2CG2_UAS:GPI-GFP	10x UAS:GPI-GFP	Expression	this dissertation
pTol2CG2_UAS:HA-TM-GFP	10x UAS:HA-TM-GFP	Expression	this dissertation
pTol2CG2_UAS:HS-TM-GFP	10x UAS:HS-TM-GFP	Expression	this dissertation
pTol2CG2_UAS:PM-GFP	10x UAS:PM-GFP	Expression	this dissertation
pTol2CG2_UAS:Caspr-YFP	10x UAS:Caspr-YFP	Expression	cloned by Sebastian Timmler
pTol2CG2_UAS:Cntn1b	Cntn1b	Expression	cloned by Minou Djannatian, expression optimized in this dissertation

Table 5: DNA Plasmids used in this study. Plasmid maps can be found in Appendix X.

2.1.3 Chemicals

We obtained our general chemicals used in this dissertation from Sigma-Aldrich (Sigma-Aldrich Chemie GmbH, Munich, Germany), Merck (Merck KGaA, Darmstadt, Germany), or Carl Roth (Carl Roth GmbH & Co KG,Karlsruhe, Germany), unless stated otherwise (see Table 6).

Commercially available components

Important chemicals or chemicals obtained from other companies are listed in Table 6.

Component	Manufacturer	Cat No.
DAPI	Thermo Fisher Scientific, Germany	D1306
Epon Resin	SERVA Electrophoresis GmbH, Heidelberg, Germany	21045
HyClone Bovine Calf Serum (BCS)	Cytiva Europe GmbH, Freiburg, Germany	SH30073
DMSO, sterile	Cell Signaling Technology Inc., Danvers, USA	#12611
DNA Gel Loading Dye (6X)	Invitrogen™, ThermoFisher Scientific, Waltham, USA	R0611
FastStart Taq DNA Polymerase DNTPack	Roche, Grenzach-Wyhlen, Germany	
Fumonisin B1 from *Fusarium moniliforme*	Sigma-Aldrich, Munich, Germany	F1147
GelRed® Nucleic Acid Gel Stain	Biotium Inc., Fremont, USA	41003
GeneRuler 100bp and 1kb DNA ladder	Invitrogen™, ThermoFisher Scientific, Waltham, USA	SM0241, SM0311
25% Glutaraldehyde Aqueous Solution, EM grade	Electron Microscopy Sciences, Hatfield, USA	16200
Go Tag® DNA Polymerase	Promega GmbH, Walldorf, Germany	M3005
LR Clonase II Plus	Invitrogen™, ThermoFisher Scientific, Waltham, USA	11791020
NEB® 10-beta/stable Outgrowth Medium	New England Biolabs, Ipswich, USA	B9035S
SOC Outgrowth medium	New England Biolabs, Ipswich, USA	B9035
Nuclease free water (not DEPC treated)	Ambion/ Invitrogen™, ThermoFisher Scientific, Waltham, USA	AM9937

Tissue-Tek® O.C.T.™ Compound, Tissue embedding medium	Sakura Finetek Germany GmbH, Staufen, Germany	4583
16% Paraformaldehyde Aqueous Solution, EM grade	Electron Microscopy Sciences, Hatfield, USA	15710
Penicillin-Streptomycin	Gibco™, ThermoFisher Scientific, Waltham, USA	11548876
Pronase from *Streptomyces griseus*	Roche, Grenzach-Wyhlen, Germany	10165921001
ProLong™ Diamond Antifade Mountant	Invitrogen™, ThermoFisher Scientific, Waltham, USA	P36961
Proteinase K, recombinant, PCR Grade from *Pichia pastoris*	Roche, Grenzach-Wyhlen, Germany	
SeaKem LE Agarose	Lonza Inc., Rockland, USA	50000
T4 DNA Ligase	New England Biolabs, Ipswich, USA	M0202
0.25% Trypsin/EDTA	Gibco™, ThermoFisher Scientific, Waltham, USA	11580626
Tricaine (3-amino benzoic acidethylester)	provided by DZNE vet	
Ultra Pure™ Low Melting Point Agarose	ThermoFischer Scientific, Waltham, USA	16520050

Table 6: Chemicals used in this dissertation and the regarding suppliers.

Antibiotics

Different antibiotics adjusted to the plasmid resistances were used. Table 7 lists the antibiotics that were applied. The specific resistance of each plasmid can be found in the plasmid maps (Appendix X).

Antibiotic	**Solved in**	**Concentration [µg/µL]**
Ampicillin	ddH_2O	100
Kanamycin	ddH_2O	50
Chloramphenicol	Ethanol	35

Table 7: Antibiotics used for plasmid amplification in this dissertation.

Restriction Enzymes

For plasmid analysis, genotyping of CRISPR induced knock-out fish and cloning of plasmids with DNA gBlocks, different restriction enzymes were used in this dissertation (see Table 8). All restriction enzymes and the appropriate restriction enzyme buffers were obtained from New England Biolabs (NEB, Ipswich, MA, USA).

Restriction Enyme	Application	Cat No.
AciI	Nfascb/ Cntn1b Genotyping, RFLP Analysis	R0551S
BseRI	Cloning	R0581
HindIII	Mag Genotyping, RFLP Analysis	R0104S
KpnI	Cloning, Insertion check	R0142S
NcoI	Caspr Genotyping, RFLP Analysis	R0193S
NotI	Linearization for mRNA Synthesis	R3189S
PstI	Insertion check	R0140S
SacI	Cloning	R0156S

Table 8: Restriction Enzymes used in this dissertation.

Antibodies

To avoid unspecific binding and cross-reactivity of antibodies grown in mice with mouse tissue, samples were incubated in AffiniPure Fab fragment donkey anti-mouse IgG (Jackson ImmunoResearch, Cambridgeshire, UK) prior antibody staining.

We stained mouse spinal cord tissue with primary antibodies against CASPR (1:1000, mouse IgG1 anti-Caspr Antibody, clone K65/35, Merck, MABN69) and Ankyrin G (1:250, mouse IgG2a anti-Ankyrin-G, NeuroMab clone N106/36, UC Davis/NIH NeuroMab Facility).

We used goat anti-mouse IgG2a (alexa fluor 555, A21137) and goat anti-mouse IgG1 (alexa fluor 488, A21121) as secondary antibodies. All secondary antibodies were obtained from ThermoFisher Scientific, Waltham, USA.

Commercial Kits

Commercial kits used in this project are listed in Table 9.

Kit	Application	Manufacturer	Cat No.
Invisorb® Spin Plant Mini Kit	DNA Extraction	Invitek Molecular, Berlin, Germany	1037100300
mMESSAGE mMACHINE™ SP6 transcription kit	mRNA Synthesis	Invitrogen™, ThermoFisher Scientific, Waltham, USA	AM1340
NEBuilder® HiFi DNA Assembly Cloning Kit	Gibson Assemby Cloning	New England Biolabs, Ipswich, USA	E5520S
NucleoBond Xtra Midi Kit	medium scale DNA purification	Macherey-Nagel, Duren, Germany	740410
NucleoSpin Gel and PCR Clean-Up	Gel and Plasmid Clean-Up after REZ Digest	Macherey-Nagel, Düren, Germany	740609
NucleoSpin Plasmid Kit	small scale DNA purification	Macherey-Nagel, Düren, Germany	740588

Table 9: Commercial kits used in this dissertation.

2.1.4 Equipment and Consumables

General Consumables

Consumables were purchased from Falcon (Corning GmbH HQ, Wiesbaden, Germany), Eppendorf (Eppendorf AG, Hamburg, Germany), Sarstedt (Sarstedt AG & Co KG, Nümbrecht, Germany) and Brand (Brand GmbH + Co KG, Wertheim, Germany) unless stated otherwise.

General Equipment

Small general lab devices like vortex or microcentrifuges are not listed.

Equipment	Manufacturer
Centrifuge 5804 R	Eppendorf, Hamburg, Germany
Table-Top Centrifuge 5424 R	Eppendorf, Hamburg, Germany
Thermocycler Biometra TRio and Biometra TAdvanced	Analytik Jena, Jena, Germany
Mastercycler Nexus	Eppendorf, Hamburg, Germany
ThermoMixer C	Eppendorf, Hamburg, Germany
Nanodrop 2000 Spectrophotometer	ThermoFisher Scientific, Waltham, USA
ChemiDoc Imaging System XRS+	Bio-Rad, Hercules USA
SZ51 zoom-stereoscope (8x-40x magnification, KL 300 LED transmitted light)	Olympus, Hamburg, Germany
Nikon SMZ18 Stereomicroscope (0.75-13.5x magnification, Fluorescent filters for DAPI, GFP, RFP) & Nikon Intensilight C-HGFI	Nikon Instruments Europe BV, Amsterdam, Netherlands
UVP UV Benchtop Transilluminator	Analytik Jena, Jena, Germany
Thermo Scientific™ CryoStar™ NX70 Kryostat	Fisher Scientific GmbH, Schwerte, Germany
VWR INCU-Line® 68R Incubator	VWR International GmbH, Darmstdt, Germany
PerfectBlue Gelsystem, different sizes	VWR International GmbH, Darmstdt, Germany
PowerPac™Basic Power Supply	Bio-Rad, Hercules USA

Table 10: Necessary general equipment used in this dissertation.

Equipment for Zebrafish Embryo Microinjections

Zebrafish embryos were injected at one-cell stage using the equipment listed in Table 11.

Equipment	Manufacturer	Cat No.
Microinjector FemtoJet 4i	Eppendorf, Hamburg, Germany	5252000013
Stereomicroscope Stemi 2000-C Zeiss KL 1500 LCD transmitted light	Zeiss, Oberkochen, Germany	
Manual Manipulator	World Precision Instruments, Sarasota, USA	M3301R
Borosilicate Glass Capillaries with filament	World Precision Instruments, Sarasota, USA	1B120F-4
DMZ-Universal Electrode Puller	Zeitz-Instrumente GmbH, Munich, Germany	
Zebrafish Microinjection	World Precision Instruments, Sarasota, USA	Z-MOLDS
Microloader Tips	Eppendorf, Hamburg, Germany	5242956003
Forceps #5 Dumont	Fine Science Tools GmbH, Heidelberg, Germany	11252-30

Table 11: Equipment used for microinjecting zebrafish embryos at one-cell stage.

Equipment for Light Microscopy

The equipment listed in Table 12 was used for confocal imaging of either whole-mounted zebrafish larvae or for fixed mouse tissue.

Equipment	Manufacturer	Cat No.
29mm #1.5 cover glass	IBL Baustoff + Labor GmbH, Gerasdorf, Austria	220.100.012
Immersol W2010 water-immersion oil n_e=1.3339 (23℃)	Zeiss, Oberkochen, Germany	
ProLong™ Diamond Antifade Mountant	Invitrogen, ThermoFisher Scientific, Waltham, USA	P36961
High Precision Microscope Cover Glasses 24x50mm #1.5	Paul Marienfeld GmbH & Co. KG, Lauda-Königshofen, Germany	0107222
SuperFrost® Plus Microscope Slides, Menzel Gläser	ThermoFisher Scientific, Waltham, USA	15438060
Leica TCS SP8 confocal laser scanning microscope with automated moving stage, Lasers: 405nm, 488nm, 514nm, 552nm, Objectives: 10x 0.3 dry, 25x 0.95 water, 40x 1.1 water, 63x 1.4 oil	Leica Microsystems, Wetzlar, Germany	
The Cube & The Box temperature control system	Life Imaging Services, Basel, Switzerland	
Leica TCS SP5 confocal laser scanning microscope with automated moving stage, Lasers: 405nm, 488nm, 555nm, 647nm, Objectives: 10x 0.4 dry, 25x 0.95 water, 63x 1.3 glycerol	Leica Microsystems, Wetzlar, Germany	

Table 12: Equipment used for confocal imaging of Zebrafish larvae or Mouse tissue.

Equipment for Electron Microscopy

The equipment that is necessary for electron microscopy tissue preparation is listed in Table 13.

Equipment	Manufacturer	Cat No.
Merck Millex™Syringe Driven Filter Unit (0.22µm)	Merck KGaA, Darmstadt, Germany	SLGP033RS
Standard Razor Blade		
Forceps #5 Dumont	Fine Science Tools GmbH, Heidelberg, Germany	11252-30
Super Fine Paintbrushes		
Teabags		
Lynx Automated Tissue Processor	Electron Microscopy Sciences, Hatfield, USA	
Leica UC7 Ultramicrotome	Leica Microsystems, Wetzlar, Germany	
Ultra 35° Diamond Knife	Diatome, Switzerland	
JEOL JEM1400 plus TEM equipped with Ruby 8 Mpx CCD camera	JEOL (Germany) GmbH, Freising, Germany	

Table 13: Equipment used for Electron Microscopy on Mouse Optic Nerve Tissue.

Equipment for Lipidomics

The equipment that is necessary for tissue preparation is listed in Table 14. Samples were handed over to Lipotype GmbH for analysis. The equipment used during lipidomic anaylsis is described as detailed as possible in the methods part 2.2.7.

Equipment	Manufacturer	Cat No.
Grinding Borosilicate Glass Tissue Homogenizer, Tenbroek type, 2 mL and 7 mL,	VWR International GmbH, Darmstdt, Germany	432-1275 / 77

Table 14: Equipment used for tissue preparation prior lipidomic analysis with mass spectrometry .

2.1.5 Buffers and Solutions

Table 15 lists all buffers and the associated protocols used in this dissertation. Percentage indications of soluble materials are percentages by weight. For fluid materials, percentage indications are percent by volume. Tab water was filtered with a Milli-Q® Type 1 Ultrapure water system for use in buffers and solutions.

Name	**Protocol**
1% Agarose	1x TAE Buffer 1% Agarose (for molecular biology)
Cacodylate Buffer	0.4M sodium cacodylate in ddH_2O
Fish anesthetic Stock Solution (Tricaine)	400 mg 3-amino benzoic acidethylester 2.1 ml 1 M Tris (pH 9) 97.9 ml ddH_2O
Tissue Fixative for Electron Microscopy	4% of 25% Glutaraldehyde (EM grade) 5% of 16% Paraformaldehyde (EM grade) 2M $CaCl_2$ 0.4M Cacodylate Buffer in ddH_2O adjust pH to 7.4
Lysis Buffer for Fish samples	10% Tris EDTA Buffer 90% 17 mg/mL proteinase K in ddH_2O
PCR Pre-Mix	100 mM dATP, dGTP, dTTP, dCTP 5x Go Taq ® colorless reaction buffer in nuclease-free water
16% PFA Stock Solution	160 g PFA 1L 4x PBS stir and heat until PFA is dissolved (milky)
10x Phosphate-buffered Saline (PBS)	1,37M NaCl 27mM KCl 100mM Na_2HPO_4 100mM KH_2PO_4 pH was adjusted to 7.5
Pronase Stock Solution	20 mg/mL Pronase in E3 medium
50x PTU Stock Solution	10mM 1-phenyl-2-thiourea in dH_2O

Name	Protocol
50x TAE Buffer	2 M Tris (pH 7.6) 1 M acetic acid 50 mM EDTA (pH 8.0) in ddH_2O
Tris-EDTA Buffer (TE)	10 mM Tris pH 7.5 1 mM EDTA (pH 8.0) in ddH_2O pH was adjusted to 8.0

Table 15: Buffers, solutions and the associated protocols used in this study.

2.1.6 Media

Different media was used to grow either Zebrafish embryos or E.*coli*. Media is listed in Table 16.

Name	Protocol
E3 medium	5 mM NaCl 0,17 mM KCl 0,33 mM $CaCl_2$ 0,33 mM $MgSO_4$
LB Medium	1 % Bacto Tryptone 0,5% Yeast extract 17,25 mM NaCl in ddH_2O
LB Agar	1,5% Bacto Agar 1 % Bacto Tryptone 0,5% Yeast extract 17,25 mM NaCl in ddH_2O

Table 16: Media used for growing Zebrafish embryos or E.*coli*.

2.1.7 *E. coli* Strains

Due to the purpose of ccdB-survival or specific plasmid propagation during amplification, different E.coli chemically competent strains were used (see Table 17).

***E. coli* strain**	**Application**	**Manufacturer**	**Cat No.**
One Shot™ TOP10 Chemically Competent E.coli	basic plasmid propagation	Life Technologies, Carlsbad, CA, USA	C4040
One Shot™ *ccd*B Survival™ 2T1^{R} Competent Cells	propagation of plamids with ccdB survival gene	Life Technologies, Carlsbad, CA, USA	A10460
NEB® Stable Competent E.coli (High Efficiency)	propagation of plasmids that were assembled via Gibson Assembly	New England Biolabs, Ipswick, USA	C3040H

Table 17: Chemically Competent E.*Coli* used for transformation.

2.1.8 Software

Table 18 shows the software used in this study. A $*$ marks online available freeware. For some parts of image analysis, a Fiji macro written by Ioannis Alexopoulos was used (Appendix VIII).

Software	Application	Source
Adobe Illustator CS5.1	Illustrations, Graphics	Adobe Inc., San José, CA, USA
ApE (Vers. 2.0.49.10)$*$	DNA Analysis, Primer Design	https://ape-a-plasmid-editor.wikispaces.com
BioRender.com	Illustrations, Graphics	BioRender.com, Toronto, ON, Canada https://biorender.com/
chopchop$*$	Target selection	[Labun et al., 2019] https://chopchop.cbu.uib.no/
CLC Main Workbench	DNA Analysis, Cloning, Sequencing Analysis	QIAGEN Digital Insights, Hilden, Germany
GENEius Light$*$	Codon Optimization	Eurofins Genomics and BioLink https://geneius.de
Graphpad Prism 8 (Vers.8.4.1)	Statistics, Graphs	Graphpad Software Inc., San Diego, CA, USA
ImageJ/ Fiji 1.53c$*$	Image Analysis	Wayne Rasband, NIH, USA https://imagej.net/
Image Lab (V 5.2.1 build 11)	Gel Analysis	Bio-Rad Laboratories GmbH, Feldkirchen, Germany
Lipotype ZOOM	Lipidomic Analysis	Lipotype GmbH, Dresden, Germany
Microsoft Office 365 Excel	Data Analysis	Microsoft, Redmond, WA, USA
Microsoft Office Photo	Video Merging	Microsoft, Redmond, WA, USA
Nanodrop 2000/2000c	DNA quantification	NanoDrop Products, Wilmington, DE, USA
SignalP 4.1$*$	Signal Peptide Analysis	[Petersen et al., 2011] http://www.cbs.dtu.dk/services/SignalP/
SMART Protein Analysis$*$	Protein Domain Analysis	[Letunic and Bork, 2017] http://smart.embl.de

Table 18: Software used in this dissertation.

2.2 Methods

2.2.1 Molecular Biology

Restriction Enzyme Digest

For conventional cloning, entry vectors (pME-MCS) and DNA gBlocks (IDT, see Table 3) were digested using different restriction enzymes (see Table 8) for later 3' overhang or blunt end ligation for 1 h (hour) at 37 ℃. For gBlock digestion, a 20 µL reaction usually contained 100 ng gBlocks (diluted in ddH_2O), 10X CutSmart Buffer, 5-10 units of each restriction enzyme, and nuclease-free water. For entry vector digestion, a 50 µL digest usually contained 3 µg plasmid DNA (diluted in ddH_2O), 10X CutSmart Buffer, 30 units of each restriction enzyme, and nuclease-free water. Plasmid DNA bands were then separated via agarose gel electrophoresis.

Polymerase Chain Reaction

PCR was used for genotyping of zebrafish and mice. The exact procedure is described in the mouse (2.2.3) and zebrafish procedures 2.2.4.

Agarose Gel Electrophoresis

Agarose gel electrophoresis was used to separate, analyze and purify plasmids and for genotyping purposes. 1% agarose was dissolved in 1x TAE Buffer. The DNA intercalating dye Gel Red (Biotium Inc.) was added for visualization using only half of the amounts recommended by the manufacturer. Agarose was cast in a gel apparatus for polymerization (PerfectBlue Gel system, VWR). Desired amounts of PCR products or plasmids were mixed with 6x DNA Gel Loading Dye (ThermoFisher). Gel separation was performed at 125 volts (V) or 175 V for 60 minutes (min) (PowerPac^{TM}Basic Power Supply, Bio-Rad). A 100 bp or 1 kb DNA ladder (GeneRuler, Thermofisher Scientific) was used as a reference. DNA bands in the gel were visualized using ChemiDoc Imaging System XRS+ (BioRad) and the associated software (see Table 18). For cloning, digested plasmid and gBlock bands were visualized via ultraviolet light on a UVP UV Benchtop Transilluminator (Analytik Jena) and were then cut out using X-tracta^{TM} Gel Extractor Tool (Cat No. A2122, Promega).

DNA Clean-Up and Extraction from Gels

After electrophoresis and gel cutting, Plasmid DNA was extracted from agarose gels using the NucleoSpin Gel and PCR Clean-Up (Macherey-Nagel, Duren, Germany) according to the manufacturer's protocol (see Table 9). DNA gBlocks were directly cleaned up using the same kit. A 1:2 dilution of NTI buffer was used to make sure to get rid of small leftover DNA fragments.

DNA Ligation

DNA gBlocks were 3' overhang or blunt end ligated into the multiple cloning site of entry vectors (pME-MCS) using T4 DNA Ligase (NEB) in a molar ratio of 1:3 - 1:5 according to the manufacturer's protocol.

Gateway LR Reaction

In a single MultiSite Gateway LR reaction, promotor and desired genes were cloned into an expression vector (4 fragments in total) according to the manufacturer's protocol (LR Clonase II Plus, Invitrogen). In brief, 10 fmol of each entry vector (p5E_promotor, pME_gene-of-interest, and p3E_ployA) were mixed with 20 fmol of the expression vector (e.g., pDestTol2CG2). TE Buffer pH 8.0 was added to the vector mixture for a total reaction volume of 8 µL. After adding 2 µL Clonase II Plus, the reaction was incubated for 16-20 h at room temperature. The reaction was then deactivated with 1 µL Proteinase K for 10 minutes at 37℃.

Gibson Assembly

pME_2xGFP-TM was constructed using NEBuilder HiFi DNA Assembly kit (see Table 9) according to the manufacturer's protocol. In brief, two DNA gBlocks were designed, each containing one full GFP sequence plus 25 bp overhangs as linkers on both sides. The linkers mimicked the first and last bp of the following fragment or the pME-MCS multiple cloning site. pME-MCS was digested with SacI and KpnI (see Table 8) and cleaned up as described above. A reaction volume of 20 µL contained 0.1 pmol of each of the two gBlock fragments, 0.4 pmol of pME-MCS, 10 µL of NEBuilder HiFi DNA Assembly Master Mix, and nuclease-free water. The reaction was incubated at 50℃ for 15 min and then stored on ice or at -20℃ until transformation in NEB stable competent *E.coli* (see Table 17).

Transformation of *E.Coli*

Different Chemically Competent *E.Coli* strains were used for either plasmid amplification with ccdB survival or specific vector propagation (see Table 17). 2-4 µL plasmid solution were added to 25 µL competent cells. Cells were incubated for 30 min on ice and afterward heat-shocked at 42℃ for 35 seconds (sec) in a block heater (Eppendorf Thermomixer Compact). 250 µL Outgrowth medium (NEB) was added. *E.Coli* were incubated on ice for 2 min and then at 37℃ for 60-90 min while horizontally shaking at 300 rpm. *E.Coli* transformed with entry vectors were plated at volumes of 50 µL and 100 µL on LB agar plates containing the appropriate antibiotic (see Table 7). When destination vectors were transformed, the full volume of cells (pDestTol2) was plated. LB agar plates were then incubated overnight at 37℃. Colonies were picked and cultured for further amplification in 5 mL (Mini) or 100 mL (Midi) LB medium.

Plasmid DNA Isolation from *E.Coli*

For checking vector quality after cloning, bacterial colonies were cultured in 5 mL LB medium (25g/L) with appropriate antibiotic selection (see Table 7). Bacteria were grown at 37℃ overnight while constantly shaking at 200 rpm. The plasmids were isolated and purified with NucleoSpin Plasmid kit (see Table 9) according to the manufacturer's instructions.

For large-scale amplification, bacteria were inoculated in 100 mL LB medium with appropriate antibiotics (see Table 7) and incubated at 37℃ overnight while constantly shaking at 200 rpm. Bacteria were harvested by centrifugation (Centrifuge 5804R, Eppendorf) at maximum speed (3220xg) for 25 min at 4℃. Plasmids were isolated and purified with NucleoBond Xtra

Midi kit (see Table 9) according to manufacturer's instructions. Plasmid yields were determined using Nanodrop 2000/2000c (NanoDrop Products).

DNA Sequencing

DNA sequencing was performed by GATC Services/ eurofins Genomics (Ebersberg, Germany) via Surpreme Run Sanger Sequencing.

mRNA Synthesis

Zebrafish expression plasmids were co-injected with Transposase mRNA. The medaka fish *Tol2* transposon encodes for a transposase protein that catalyzes the insertion of DNA constructs that contain the end parts of the *Tol2* element by a simple cut-and-paste mechanism [Kawakami, 2007]. Hence, the insertion efficiency is highly increased by using transposase mRNA, together with *Tol2* containing plasmids.

Transposase mRNA was synthesized using the SP6 mMESSAGE mMACHINE® Kit (see Table 9). In brief, the pCS2FA-transposase plasmid was digested using NotI (see Table 8) as mentioned above. One 20 µL synthesis reaction contained 2x NTP/CAP, nuclease-free water, 10x reaction buffer, 1 µg linearised plasmid DNA, and 2 µL of enzyme. The reaction was mixed by gently flicking and briefly microcentrifuging the tube and then incubated at 37℃ for 2 h.

Synthesized RNA was precipitated using Lithium chloride. 30 µL nuclease-free water and 30 µL Lithium chloride precipitation solution were added and carefully as well as thoroughly mixed to stop the reaction. The reaction was chilled overnight at -20℃ and was then centrifuged at 4℃ for 15 min at maximum speed. The pellet was washed with 1 mL 70% ethanol and re-centrifuged at 4℃ for 15 min at maximum speed. The ethanol was carefully removed, and the pellet was re-suspended in nuclease-free water. After the concentration was determined, the mRNA was stored at -80℃ until further usage.

2.2.2 DNA gBlocks design of membrane-associated GFPs

We created a semi-artificial model system to investigate the influence of membrane-anchoring domains on the distribution of extra-axonal, membrane-associated proteins underneath a myelin sheath in zebrafish. For that, we used GFP, an inert protein that does not interact with other proteins. We designed three different GFP-versions by exchanging the membrane anchors. We used the transmembrane domain (TM) of the Influenza A virus hemagglutinin protein (HA-TM), the TM of the Herpes simplex virus protein (HS-TM), and the GPI-anchor of the axonal protein Cntn1a (*D. rerio*). The TMs differ in their lengths (HA-TM = 27aa, HS-TM = 23aa). As a control, we designed a palmitoylated GFP (PM-GFP) that attaches to the cytoplasmic axonal membrane.

HA-TM and HS-TM have been used in a previous study to investigate the association of transmembrane proteins with sphingolipid–cholesterol rafts in lipid membranes [Scheiffele et al., 1997]. They found the transmembrane-domain of wtHA to be the determining factor for raft association. The HS-TM version was not associated with lipid rafts. We used the corresponding DNA transmembrane sequence of the published HA-TM amino acid sequence (ILAIYATVAGSLSLAIMMAGISFWMCS), 5 amino acids of the luminal sequence (MGVYQ), and 9 amino acids of the cytoplasmic sequence (NGSLQCRICI). At the luminal end, a GFP sequence and the signal peptide of the HA protein were added with a flexible linker (GGGS) [Chen et al., 2013]. To clone these sequences into the middle entry vector, restriction sites for KpnI and SacI (see Table 8) were inserted at the ends of the sequence (Fig. 8). HS-TM was designed in a very similar fashion. We kept the described protein structure and only exchanged the transmembrane domain for HS-TM (WVGIGIGVLAAGVLVVTAI-VYVV), as it has been published [Scheiffele et al., 1997].

For generating a GPI-anchored GFP, we used the C-terminal GPI signal sequence of the nodal protein Cntn1a, added a GFP with the aforementioned flexible linker (GGGS), and the signal peptide of the paranodal protein Cntn1b. Relevant sequences were depicted from the zebrafish GRCz10 genome dataset, downloaded from `https://www.ensembl.org/` and analyzed using SMART and SignalP 4.1 (see Table 18).

We used the N-terminal myristoylation and palmitoylation (PM) sequence of the Lyn protein (MGCIKSKGKDSLSDDGVDLKT), which has been described before in subcellular trafficking routes [Sato et al., 2009; Aicart-Ramos et al., 2011], to generate a luminal, membrane-associated GFP. The GFP was attached again with the flexible GGGS linker.

To investigate if size-dependent molecular barriers play a role in sorting specific proteins underneath a myelin sheath, we designed a protein containing several GFPs in a row, linked together with rigid linkers(3x EAAAK) [Chen et al., 2013]. The corresponding gBlocks were designed in a modular manner. The design of the first gBlock resembled the above-mentioned HS-TM-GFP. A 25bp 5' overhang from pME-MCS for insertion via Gibson Assembly and a rigid instead of a flexible linker were added. The 3' end and the 5' end of the second gBlock overlap entirely with the rigid linker sequence. The second gBlock contained another GFP, with a 29 bp 3' pME-MCS overhang. In a Gibson Assembly reaction (see the previous section), these gBlocks were inserted into the pME-MCS vector to receive a PME_2xGFP-Herpes-TM sequence. The correct insertion of the gBlocks was checked via restriction enzyme digest and sequencing (see previous section).

All amino acid sequences were translated into DNA sequences with optimized codon usage for zebrafish using GENEius Light Software (see Table 18). Kozak sequences [Kozak, 1984] were added at the beginning of the open reading frame to optimize the start of transcription.

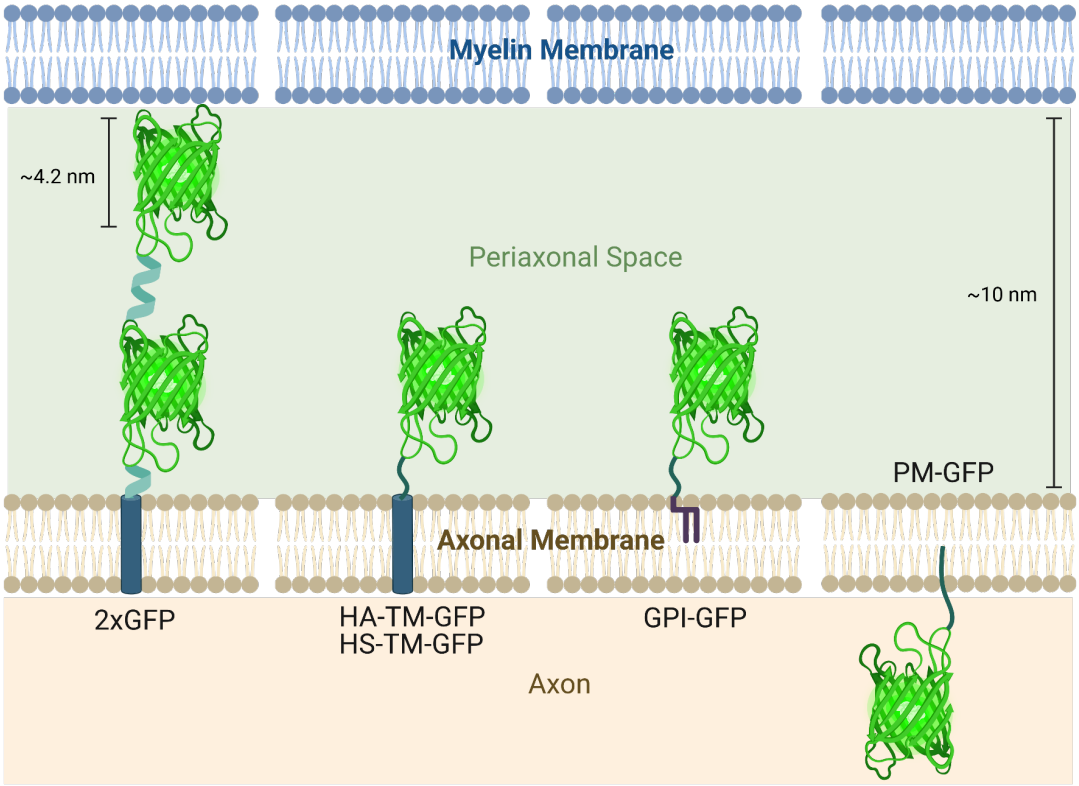

Figure 8: MEMBRANE-ASSOCIATED GFPS DNA gBlocks were designed to encode for the GFP constructs shown above. From left to right: Two GFPs are linked with rigid linkers, thus reaching a size of ∼10 nm, the length of the periaxonal space (2xGFP). HA- and HS-TM are designed similarly, with a flexible linker connecting their transmembrane domains with a single GFP, only differing in their transmembrane domains. Another single GFP is connected to a GPI anchor via a flexible linker (GPI-GFP). All of these GFP constructs face the periaxonal space. The only GFP facing the intracellular space of the axon is a myristoylated and palmitoylated GFP (PM-GFP).

2.2.3 Mouse Procedures

Mouse Perfusion

16% PFA stock solution was thawed, diluted with 1x PBS for a final concentration of 4% PFA, and filtered with a 500 mL Steritop filter (0.22 µm, Merck Millipore, Darmstadt, Germany) prior to perfusion. Mice were anesthetized with isoflurane and perfused with PBS only to remove blood cells from the tissue, then with 4% PFA in PBS, or PBS only (for Lipidomics and EM). The spinal columns, optic nerves, and brains were removed.

Tissue Preparation for EM

Mouse spinal columns and optic nerves were immersion fixed in EM tissue fixative for 24 h at 4℃. Samples were washed 3x and exchanged with 0.1 M Cacodylate buffer. The spinal cords were removed from the spinal columns and carefully cut with a razor blade. Cervical spinal cord tissue was kept at 4℃ until further processing.

Tissue Preparation for Lipidomic Analysis

For lipidomic analysis, mouse optic nerve and brain samples were snap frozen in liquid nitrogen and stored at -80℃ until further processing. Brain and optic nerve samples were weighed with a high precision analytical balance (Sartorius). Optic nerves of 3-5 animals were then pooled to reach the minimum volume of 300 µL with the minimum concentration of 5 mg/mL prior to homogenization. Samples were homogenized using a 1 mL or 2 mL Tenbroek grinding borosilicate glass tissue homogenizer (VWR) with ∼20-25 up and down movements. No tissue clumps were visible anymore. Samples were shipped to our collaborator on dry ice, Lipotype, for further analysis by mass spectrometry.

Immunohistochemistry

For immunohistochemistry, the spinal columns of P12 and P21 old mice were immersion fixed in 4% PFA in PBS overnight at 4℃ and soaked in 30% sucrose for 2 days for cryoprotection. The spinal cord was prepared from the spinal column, embedded in Tissue-Tek OCT compound, frozen on dry ice, and stored at -80℃. Longitudinal spinal cord sections (30 µm) were cut by cryostat (Leica) and stored free-floating in cryoprotective solution (25% ethylene glycol, 20% glycerol, in PBS) at -20℃ until further processing. Sections were transferred to PBS in 12 well plates and permeabilized with 0.2% Triton X-100 in PBS for 1h. To prevent unspecific binding, tissue sections were first blocked with donkey anti-mouse Fab fragments (Jackson ImmunoResearch) in PBS containing 0.2% Triton X-100 and then with blocking solution containing 2.5% Fetal Bovine Serum (FBS), 2.5% Bovine Serum Albumin (BSA) and 2.5% fish gelatin in PBS for 1h. Primary antibodies were diluted in blocking solution and applied overnight at 4℃. After washing the sections with 1x PBS, secondary antibodies, diluted in blocking solution (1:1000), were applied and incubated for 1h. Sections were rewashed, and DAPI was applied for 15 min. After final washing with 1x PBS and distilled water, the sections were mounted to glass slides with ProLong Diamond Antifade (ThermoFisher Scientific)and dried overnight. Unless stated otherwise, all steps were performed at room temperature.

Genotyping

Tissue lysis and DNA extraction were performed using the Invisorb® Spin Plant Mini Kit according to the manufacturer's protocol. Genotyping of the St3gal5 and B4galnt1 lines was performed in a standard PCR reaction with 1 µL of extracted DNA using the primers listed in Table 4 in a Biometra TRIO thermocycler and according to the following protocols for master mixes and thermocycler steps. PCR bands were analyzed on a 1% agarose gel after applying 125 or 175 V for 1 h.

St3gal5 PCR master mix:

component	concentration	µL/rxn
Roche FastStart Buffer with $MgCl_2$	10X	2
dNTPs	1.25 mM	3.2
Forward Primer (M374)	25 µM	0.3
Reverse Primer (M374)	25 µM	0.3
Roche FastStart *Taq*	5 U/µL	0.2
sterile ddH_2O		13

St3gal5 thermocycler protocol:

step	temperature	time
1	95 °C	3 min
2	94 °C	20 sec
3	63 °C (wt) 51 °C (mut)	30 sec
4	72 °C	30 sec
5	Repeat steps 2-4 34x	
6	72 °C	10 min
7	8 °C	hold

Band lengths of St3gal5 PCR products:
wild type: 337 bp
mutant: 250 bp

B4Galnt1 PCR master mix:

component	concentration	µL/rxn
Roche FastStart Buffer with $MgCl_2$	10X	2
dNTPs	1.25 mM	3.2
Forward Primer (L36)	25 µM	0.4
Reverse Primer (L36)	25 µM	0.4
Roche FastStart *Taq*	5 U/µL	0.2
sterile ddH_2O		12.8

B4Galnt1 thermocycler protocol:

step	temperature	time
1	94°C	10 min
2	94°C	1 min
3	64°C	30 sec
4	72°C	2 min
5	Repeat steps 2-4 44x	
6	72°C	7 min
7	8°C	hold

Band lengths of St3gal5 PCR products:
wild type: 600 bp
mutant: 300 bp

2.2.4 Zebrafish Procedures

Bleaching

Before raising embryos to adulthood in the fish facility, they were cleaned at 1 dpf to prevent the spreading of diseases in the facility. In a clean area with sanitised surfaces, egg lays bathed for 5 min. each in the following 5 different solutions at room temperature:

0.5 µL/mL bleach - ddH_2O - 0.5 µL/mL bleach - ddH_2O - ddH_2O.

Embryos were then kept in a clean petri dish and a clean, closed container at 28.5℃ until 5 dpf.

Fin Clips for Genotyping

To determine the genotype of each individual, biopsies were taken from fish by cutting a small part from the fin. For that, fish were anesthetized in 0.02% tricaine in tab water. After a small part of the fin was cut, the fish were kept single-wise in a small tank for recovery and until genotyping results were obtained.

Microinjecting Zebrafish Embryos

Microinjection needles were pulled from borosilicate glass capillaries with filament (1B120F-4, World Precision Instruments) using a DMZ needle puller (see Table 11). Zebrafish embryos were obtained by natural spawning about half an hour before injections. Shortly before injections, plasmids were diluted with ddH_2O and mixed with transposase mRNA to a final concentration of 25 ng/µL of both DNA and mRNA. Embryos were sorted into molds stamped into 1.75% hardened agarose in E3 medium in a petri dish. For transient expression or generation of a new line, embryos were injected with $\sim$1 nL injection mix using a Zeiss stereomicroscope (Stemi 2000) and a FemtoJet (Eppendorf) injection setup (settings: p_i=75-150 hPa, t_i=0.1 sec, p_c=15 hPa). Injected embryos were raised at 28.5℃ in E3 medium.

Fumonisin B1 Treatment

Fumonisin B1 (Fum B1) was dissolved in DMSO (Cell Signaling Technology Inc.) to a final concentration of 10 mM. After 1 dpf, we carefully removed the chorions from the embryos with fine forceps (Dumont #5, Fine Science Tools). 10 Embryos incubated in 1% Fum B1 10 mM or 1% DMSO only (control) in a 35 mm petri dish, sealed with parafilm to prevent evaporation, until 3-4 dpf.

Genotyping

For genotyping, anesthetized and methanol-fixed zebrafish embryos or fin clips were lysed in Tris-EDTA buffer (pH 8.0) and 1.7 mg/mL Proteinase K for 3-4 h at 55℃, following heat inactivation of Proteinase K. 1-2 µL lysate were used for PCR. We checked for restriction fragment length polymorphism (RFLP) by incubating PCR products for 1h at 37℃ (for restriction enzymes, see Table8). PCR products were analyzed after digestion on a 1% agarose gel after applying 125 or 175 V for 1 h.

In addition to the lysate, a standard PCR mix for zebrafish contained 15 µL of PCR Pre-Mix, 0.5 µL of forward and reverse primers (see Table 4) for a final concentration of 10 pmol\µL, and 0.2 µL GoTaq (Promega). The samples were then incubated as follows:

Lid temperature:	98 ℃		
1st Melting:	98 ℃	5 min	
Melting:	98 ℃	30 sec	
Annealing:	Table 4	30 sec	25-34 cycles
Elongation:	72 ℃	30 sec	
Finish:	72 ℃	5 min	

The thermocycler program for Cntnap1b zebrafish genotyping was optimized. A Touchdown PCR (TD) protocol with 15 additional cycles, where the annealing temperature starts at 66 ℃ and drops for 1 ℃ with every cycle, was added. This approach ensures better initial annealing of the primers. The program then proceeds with the above-described protocol.

Generation of Transgenic Zebrafish: HuCGal4;UAS:Caspr-YFP

For further investigations beyond the scope of this dissertation, a transgenic Caspr-YFP was established as part of this dissertation. For that, fish were co-injected with two plasmids (pTol2CG2_-Huc:Gal4 and pTol2CG2_UAS:CasprYFP) and transposase as described above. The F_0 generation was bleached and raised to adulthood. The burden load due to genetic modification was observed until 3 months. Via outcrossing the F_0 generation to wild type zebrafish, parental germ line transmission of the YFP signal intensity was checked by sorting under a confocal microscope. Males and females with the most efficient germ line transmission rate were inbred for the F_1 generation. Regarding development, burden, and efficiency checks, the F_1 generation was treated like the F_0 generation. For F_2 generation, males and females with the most efficient germ line transmission rate were outbred to wild type zebrafish.

2.2.5 Light Microscopy

Zebrafish

Zebrafish embryos were treated with 1x PTU (see Table 15) at 1 dpf to prevent the development of melanocytes which could cause autofluorescence during image acquisition. Embryos at 3 to 5 dpf were anesthetized with 0.5% tricaine and mounted laterally in 0.75 - 1% Ultra Pure ^{TM} low melting point agarose (ThermoFisher) on a glass bottom dish (# 1.5 cover glass, IBL).

Fish were imaged at a Leica TCS SP8 confocal laser scanning microscope with a motorized moving stage and climate chamber (28.5℃, The Box & The Cube), using a 1.1 NA 40× water immersion objective and 488, 514, and 552 nm lasers. Single images and z-stack tile scans (z-step = 0.28 - 0.48 µm) for quantification of internodal intensity and internodal vs. paranodal localization were acquired with optimized image format and pixel size according to the sampling theorem [Whittaker, 1915; Shannon, 1949; Goodman, 1996] using a hybrid detector in photon counting mode, 8-9x line accumulation and the pinhole at 1 airy unit. For Caspr-YFP localization experiments, all Caspr-YFP positive sheaths within a hemi-spinal cord were imaged.

For qualitative observations of Caspr-YFP localization during development in a region of interest, live imaging z-stacks tile scans (optimized image format) over time were acquired with a 40x water immersion objective (1.1 NA, using Immersol W2010 as immersion medium), a hybrid detector in photon counting mode, with 8x line accumulation, and a pinhole at 1 airy unit. Time intervals were set to 20 - 30 min. A bright field channel was acquired simultaneously to surveil the health status of the animals, capturing the transmitted laser light with a TL-photomultiplier.

All imaging data were acquired and stitched using the LAS X (v.3.5) software.

After imaging, larvae were sacrificed and genotyped if progeny from heterozygous incrosses was used.

Mouse

Mouse tissue was imaged at a Leica TCS SP5 confocal laser scanning microscope with a motorized moving stage, using a 1.3 NA 63x glycerol immersion objective and 405, 488, and 647 nm lasers. Single images and z-stack tile scans (optimized image format, z-step = 0.4 µm) were acquired using a TL-photomultiplier in photon counting mode, with 8x line accumulation and a pinhole at 1 airy unit.

All imaging data were acquired and stitched using the LAS X (v.3.5) software.

2.2.6 Transmission Electron Microscopy

Mouse optic nerves and spinal cords were prepared as described in section 2.2.3. Samples were then handed over to the Synergy Nanoscale Hub, the Electron Microscopy facility at DZNE Munich, where the samples were further processed and imaged according to the following protocol.

Samples were washed in 0.1 M sodium cacodylate buffer. After post-fixation in reduced osmium (2% osmium, 2.5% potassium ferrocyanide in 0.1 M cacodylate buffer), en bloc uranyl acetate (1% aqueous uranyl acetate) contrasting followed. Before embedding in epon resin (Serva), samples were dehydrated gradually in ethanol. Blocks were sectioned (50 nm), and the grids (Leica UC7 ultramicrotome) were contrasted by 1% uranyl acetate and Ultrostain (Leica). Images were acquired with a JEOL JEM1400 plus TEM equipped with a Ruby 8 Mpx CCD camera.

2.2.7 Lipidomics

Mouse brain and optic samples were prepared as described in section 2.2.3 and then shipped on dry ice to Lipotype GmbH, Dresden, for lipidomic analysis. They used a self-developed, brand-new method to analyze our samples' lipid and especially the ganglioside content. They describe the new analysis method as follows (as described in [Arends et al., 2022]):

Lipid Standard Titration

To estimate the sensitivity and linearity of the ganglioside analysis, Lipotype used lipid references from Matreya (Matreya LLC) or Avanti (Avanti Polar Lipids, Inc.). Being natural ganglioside extracts, these references contain a range of individual lipid species. For the necessary estimation, direct infusion mass spectrometry was used to identify the fraction of the most abundant species. Their concentration was then calculated based on the total concentration of the ganglioside mixture. The limits of detection and quantification were then calculated based on the concentration and intensity values of the most abundant lipid species in the mixture.

Lipid Extraction for Mass Spectrometry Lipidomics

The lipid analysis was done using a mass spectrometry-based approach described before [Sampaio et al., 2011]. 500 µg of tissue were used per sample, if not indicated otherwise. A two-step chloroform/ methanol protocol was used to extract the lipids from the samples [Ejsing et al., 2009]. Samples were spiked within Lipotype's internal lipid standard mixture containing: cardiolipin 16:1/15:0/ 15:0/15:0 (CL), ceramide 18:1;2/17:0 (Cer), diacylglycerol 17:0/17:0 (DAG), hexosylceramide 18:1;2/12:0 (HexCer), lyso-phosphatidate 17:0 (LPA), lyso- phosphatidylcholine 12:0 (LPC), lyso- phosphatidylethanolamine 17:1 (LPE), lyso- phosphatidylglycerol 17:1 (LPG), lyso-phosphatidylinositol 17:1 (LPI), lyso- phosphatidylserine 17:1 (LPS), phosphatidate 17:0/17:0 (PA), phosphatidylcholine 17:0/17:0 (PC), phosphatidylethanolamine 17:0/17:0 (PE), phosphatidylglycerol 17:0/17:0 (PG), phosphatidylinositol 16:0/16:0 (PI), phosphatidylserine 17:0/17:0 (PS), cholesterol ester 20:0 (CE), sphingomyelin 18:1;2/12:0;0 (SM), triacylglycerol 17:0/17:0/17:0 (TAG) and cholesterol D6 (Chol). The organic phase was transferred to an infusion plate and dried in a speed vacuum concentrator after extraction. The dry extract from the first step was re-suspended in 7.5 mM ammonium acetate in chloroform/ methanol/ propanol (1:2:4, V:V:V). The dry extract from the second step was re-suspended in 33% ethanol solution of methylamine in chloroform/ methanol (0.003:5:1; V:V:V). All liquid handling steps were performed using Hamilton Robotics STARlet robotic platform with the Anti Droplet Control feature for organic solvents pipetting.

MS Data Acquisition

Samples were analyzed by direct infusion on a QExactive mass spectrometer (Thermo Scientific) equipped with a TriVersa NanoMate ion source (Advion Biosciences). Samples were analyzed in positive and negative ion modes with a resolution of $R_{m/z=200}$=280000 for MS and $R_{m/z=200}$=17500 for MSMS experiments in a single acquisition. MSMS was triggered by an inclusion list encompassing corresponding MS mass ranges scanned in 1 Da increments [Surma et al., 2015]. MS and MSMS data were combined to monitor CE, DAG, and TAG ions as ammonium adducts; PC, PC O-, as acetate adducts; and CL, PA, PE, PE O-, PG, PI, and PS as deprotonated anions. MS only was used to monitor LPA, LPE, LPE O-, LPI, and LPS as deprotonated anions; Cer, HexCer,

SM, LPC, and LPC O- as acetate adducts and cholesterol as ammonium adduct of an acetylated derivative [Liebisch et al., 2006]. To control for technical variation, background signals, and sample carry-over, 6 blank and 6 reference samples were included in the analytical run and distributed evenly across the sample set, resulting in a blank and reference sample after every seventh study sample.

Lipidomic Analysis of Gangliosides

The gangliosides GM2, GM3, and GM4 were analyzed in the chloroform/methanol 2:1 (V:V) fraction, the second step of the two-step chloroform/methanol extraction procedure. Ganglioside classes GM1, GD1, GD2, GD3, GT1, GT2, GT3, and GQ1 were extracted from the remaining water phase of the second step. They were then subjected to purification using solid phase extraction (Thermo Scientific SOLA SPE plates, 10 mg/2 mL) [Senn et al., 1989]. The water phase was loaded on columns pre-washed with chloroform/methanol (2:1, V:V), methanol, and methanol/water (1:1, V:V); with the input flow through re-applied three times. Then, columns were washed with water, and the elution was carried out two times with methanol and one time with chloroform/methanol (1:1, V:V). Washing and elution steps were carried out using a vacuum manifold. Pooled eluates were dried in a speed vacuum concentrator and re-suspended in 33% ethanol solution of methylamine in chloroform/methanol (0.003:5:1; V:V:V). Ganglioside extracts were analyzed by direct infusion on a QExactive mass spectrometer (Thermo Scientific) equipped with a TriVersa NanoMate ion source (Advion Biosciences). Sample infusion was performed with a pressure p = 0.8 psi and voltage V = 0.95 V. Samples were analyzed in negative ion modes with a resolution of $R_{m/z=200}$ = 140,000; AGC target of 1e6; maximum injection time of 500 ms and 3 micro scans.

Data analysis and post-processing

Data were analyzed using in-house lipid identification software based on LipidXplorer [Herzog et al., 2011, 2012]. Data post-processing and normalization were performed using an in-house developed data management system. Only lipid identifications with a signal-to-noise ratio >5 and a signal intensity 5-fold higher than in corresponding blank samples were considered for further data analysis. Lipids were normalized to lipid class-specific internal standards. In the case of ganglioside classes for which no suitable lipid class-specific internal standards are available, spectral intensities were normalized to the internal standard GM1-D3 18:1;2/18:0;0, and the normalized intensities were further normalized to total lipid content (in pmol) of the sample.

2.2.8 Image Analysis

Electron Microscopy Analyses

The number of myelinated, unmyelinated, degenerated axons, vacuolization, and double myelination events in mouse optic nerve cross sections was manually counted using the ImageJ/Fiji cell counter tool. Five images (size 34 µm x 34 µm / image) per animal of at least three *ST3GAL5$^{-/+}$/ B4GALNT1$^{-/+}$ or ST3GAL5$^{-/-}$/B4GALNT1$^{-/-}$* mice were counted.

G ratios were calculated by dividing the axonal diameter by the diameter of the whole myelinated fiber. For that, axons and myelinated fibers were encircled in mouse optic nerve cross sections, and their area were measured using ImageJ/Fiji. Diameters were calculated from the area by $2 \times \sqrt{area \div \pi}$. 200 myelinated axons per animal of three *ST3GAL5$^{-/+}$/ B4GALNT1$^{-/+}$ or ST3GAL5$^{-/-}$/B4GALNT1$^{-/-}$* mice were measured.

The number of paranodal loops, detached paranodal loops, the length of paranodes and nodes, as well as the axonal diameter in mouse optic nerve longitudinal sections were counted and measured using ImageJ/Fiji. Every imaged paranode was counted in *ST3GAL5$^{-/+}$/ B4GALNT1$^{-/+}$ or ST3GAL5$^{-/-}$/B4GALNT1$^{-/-}$* mice.

CASPR Localization in Mouse Spinal Cord

Differences in the localization of paranodal proteins in the spinal cord of *ST3GAL5$^{-/+}$/ B4GALNT1$^{-/+}$ or ST3GAL5$^{-/-}$/B4GALNT1$^{-/-}$* mice were determined by manually counting the number of nodes per mm^2 in the spinal cord white matter using the ImageJ/Fiji cell counter tool. CASPR and Ankyrin G (ANKG) intensities were measured using the ImageJ/Fiji profile plot tool across paranodes (CASPR) flanking a node (ANKG) in a length of 10 µm. 5 events per genotype from 3 mice were randomly chosen for profile plot measurements.

Membrane-Associated Proteins in Zebrafish Spinal Cord

For experiments regarding the localization of membrane-associated proteins, intensities were measured on raw maximum projections (3-5 z-steps) of areas of interest. Intensities were measured in spinal cord neurons at myelinated areas and in the unmyelinated areas surrounding it, with a macro written by Ioannis Alexopoulos (see Appendix VIII) for ImageJ/Fiji. Axonal GFP intensities in myelinated areas were normalized to the intensities in unmyelinated areas.

Protein Localization in Zebrafish Spinal Cord

For Caspr-YFP localization experiments, a paranodal event was defined as precise paranodal localization when Caspr was localized at the edges of myelin sheaths. An overlay of YFP (Caspr) and RFP (myelin sheath) signal counted as an internodal event. For some experiments, overlay events were defined as internodal accumulation when the Caspr intensity was higher underneath a myelin sheath than in the surrounding area. When Caspr intensities under myelin sheaths were as high as in the surrounding area, this internodal event was counted as equally distributed. All events of a hemi spinal cord were counted. For measuring intensities across nodes of Ranvier (15 µm), the profile Plot tool of ImageJ/Fiji was used at a length of 15 µm. 5 events per fish from 3-4 fish were randomly chosen for profile plot measurements.

The sheath length of transgenic and Fum B1- treated zebrafish was measured using the ImageJ/Fiji measuring tool. All myelin sheaths within a hemi spinal cord of 3 animals were measured.

Movies were drift-corrected using the correct 3D drift plugin from ImageJ/Fiji whenever necessary and saved in single successions of different channels in RGB mode. Channel successions were then merged using the MS Office Photo app.

2.2.9 Statistics

General Comments

Acquired data were saved in MS Excel files. Data were then transferred and analyzed in Graphpad Prism 8 (see Table 18). All data were tested for Gaussian distribution. All graphs show mean $\pm$ SD.

Electron Microscopy Statistics

Differences in the amount of myelinated and unmyelinated axons between different genotypes and mouse optic nerve cross sections were tested using an unpaired t-test, two-sided. The same tests were applied to test for differences in the number of paranodal loops, detached paranodal loops, the length of paranodes and nodes, as well as the axonal diameter in mouse optic nerve longitudinal sections between different genotypes. The g ratios are presented as a simple linear regression model per axonal diameter.

CASPR Localization in Mouse Spinal Cord

Differences in the number of nodes per mm^2 between genotypes were tested using an unpaired t-test, two-sided.

Lipidomics

Data were downloaded from a web browser-based data visualization tool (LipotypeZoom), provided by our collaborator, Lipotype. Only results with > 1.5fold change and a p-value < 0.05 were selected for levels of lipid species as the percentage of the total lipid amount for each sample.

Statistical analysis was performed using GraphPad Prism 8.4.3 (GraphPad Software, Inc.). Two-way ANOVA followed by Tukey's post hoc test was used to compare the interactions between different genotypes or developmental stages. A p-value of < 0.05 was considered significant in all tests.

Membrane-Associated Proteins in Zebrafish Spinal Cord

Axonal GFP intensities in myelinated areas were tested for differences to one with one sample t-test, two-sided, or one-sample Wilcoxon test. No difference to one was interpreted as the same, less than one as lower, and more than one as higher intensities in myelinated and unmyelinated areas. Differences of HA-TM-GFP, HS-TM-GFP, and GPI-GFP to the control group PM-GFP were tested using one-way ANOVA with Sidak's multiple comparisons test. Differences between groups were tested with unpaired t-test, two-sided or Mann-Whitney test.

Caspr Localization in Zebrafish Spinal Cord

Differences in Caspr localization were tested with either one-way ANOVA with Tukey's multiple comparisons test, two-way ANOVA with Sidak's multiple comparisons test, or a simple unpaired t-test, two-sided.

Myelin Sheath Length in Transgenic Zebrafish

Differences in myelin sheath lengths across transgenic zebrafish were tested with the Kruskal-Wallis test, whereas differences between DMSO- and Fum B1-treated zebrafish were tested using Mann–Whitney U test, two-sided.

3 Results

3.1 Mechanisms of Paranodal Protein Sorting

3.1.1 Myelin Sheath Length Depends on Internodal and Paranodal Proteins

In a first approach to assess the importance of specific adhesion proteins that anchor myelin sheaths to axonal membranes, we examined how the myelin sheath length in the zebrafish spinal cord varies in animals that are mutant for some internodal and paranodal proteins compared to wild type zebrafish.

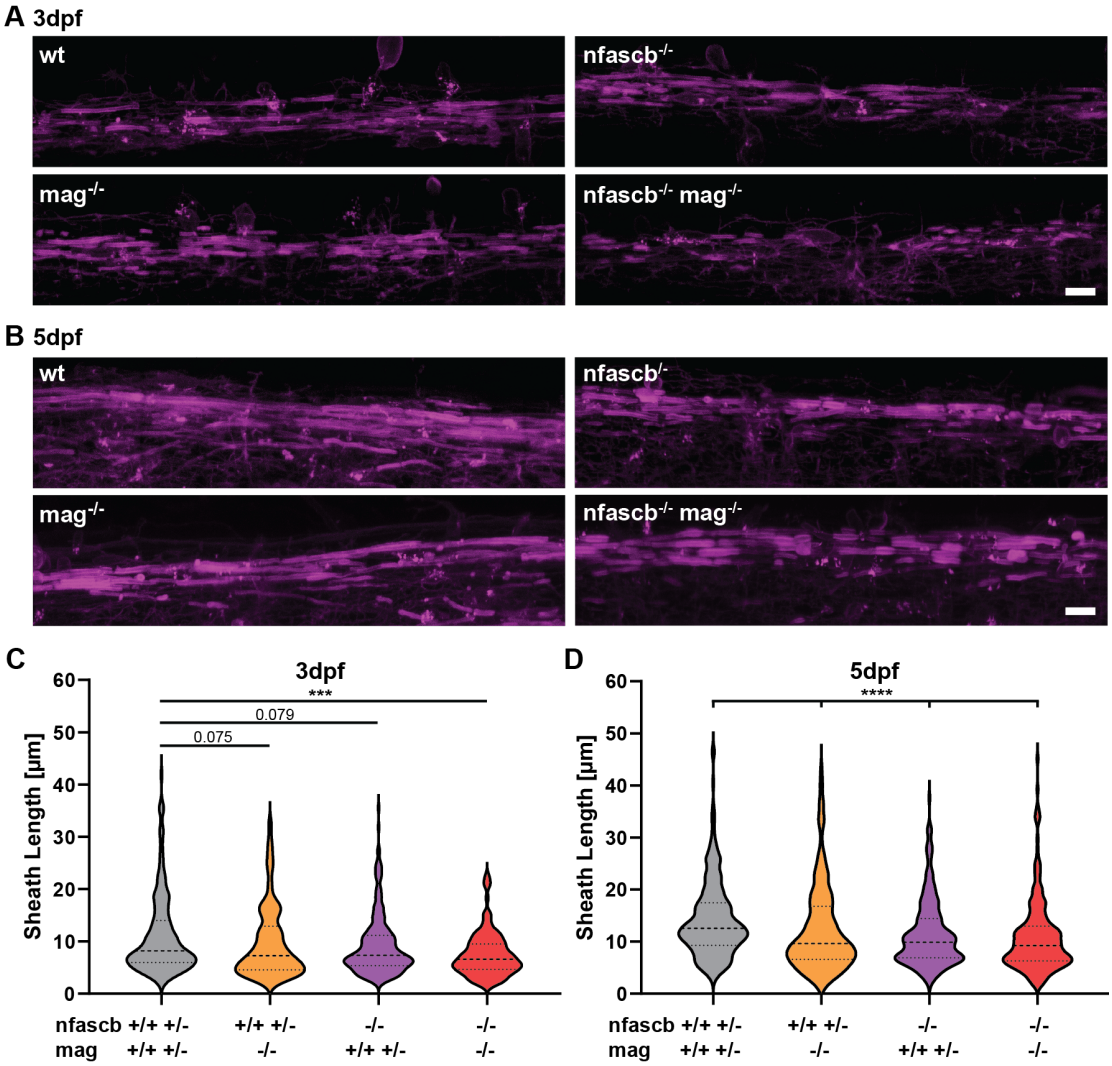

Figure 9: MYELIN SHEATHS LENGTH IN WILD TYPE, *mag*$^{-/-}$, *nfascb*$^{-/-}$ AND *nfascb*$^{-/-}$/*mag*$^{-/-}$ ZEBRAFISH Representative images show myelin sheaths in the zebrafish spinal cord in wild type, *mag*$^{-/-}$, *nfascb*$^{-/-}$ and *nfascb*$^{-/-}$/*mag*$^{-/-}$ animals at 3 dpf **A** and 5dpf **B**; Sheaths are visibly shorter in *nfascb*$^{-/-}$/*mag*$^{-/-}$. Violin plots display the distribution of sheath lengths of different genotypes at 3 dpf **C** and 5 dpf **D**; At 3 dpf, the myelin sheaths of all mutant animals were shorter than the sheaths of wild type and double heterozygous animals. However, only the sheaths of *nfascb*$^{-/-}$/*mag*$^{-/-}$ animals were significantly shorter (p=0.0001). At 5 dpf, sheaths of all genotypes were significantly shorter (p<0.0001) than the sheaths of wild type and double heterozygous animals. At both ages, there were no differences between other groups. The length of 120-300 sheaths from 3 animals per genotype and age were measured; Dotted lines represent median and quartiles; Differences were tested with the Kruskal-Wallis test. Scale bars = 10 µm.

Here, we used *mag*$^{-/-}$, *nfascb*$^{-/-}$ and *nfascb*$^{-/-}$/*mag*$^{-/-}$ double mutant animals. Additionally, the average myelin sheath length of *cntnap1b*$^{-/-}$, *cntn1b*$^{-/-}$, *mag*$^{-/-}$ and *cntn1b*$^{-/-}$/*mag*$^{-/-}$ or *caspr*$^{-/-}$/*mag*$^{-/-}$ double mutants are published in Djannatian et al. [2019].

We found the myelin sheath length reduced in *mag*$^{-/-}$ and *nfascb*$^{-/-}$ at 3 dpf. In single mutants, we observed a mean reduction of $\sim$2 µm length (wt: 11.03 µm $\pm$ 7.56 µm; *mag*$^{-/-}$: 9.7 µm $\pm$ 6.85 µm; *nfascb*$^{-/-}$: 9.13 µm $\pm$ 5.72 µm), which was not significantly different from the average sheath length in wild type animals (Fig. 9 A+C). However, when internodal as well as paranodal adhesion complexes are disturbed in *nfascb*$^{-/-}$/*mag*$^{-/-}$ double mutant animals, the myelin sheaths grow in average $\sim$4 µm shorter (7.5 µm $\pm$ 4.22 µm) than the myelin sheaths of wild type animals (p=0.0001).

At 5 dpf, all myelin sheaths of single and double mutants are significantly shorter by $\sim$2 µm on average than of wild type animals (wt: 14.19 µm $\pm$7.28 µm; *mag*$^{-/-}$: 12.37 µm $\pm$8.31 µm; *nfascb*$^{-/-}$: 11.45 µm $\pm$6.38 µm), Fig.9 B+D), while double mutant animals (*nfascb*$^{-/-}$/*mag*$^{-/-}$) grow the shortest myelin sheaths. They are, on average, about 4 µm shorter (10.89 µm $\pm$6.98 µm) than wild type myelin sheaths.

3.1.2 Caspr Relocates from the Internode to Paranodes

We made use of the several advantages of zebrafish as animal models, specifically of their fast central nervous system development and of the easy application of whole fish confocal time-lapse imaging. All experiments in this and some of the subsequent sections (3.1.3 - 3.1.7) were conducted by injecting pTol2CG2_HuC:gal4 and pTol2CG2_UAS:Caspr-YFP into Tg(Sox10:mRFP) one cell-stage zebrafish embryos. Hence, zebrafish overexpressed Caspr-YFP, the paranodal myelin anchoring protein in the axonal membrane of spinal cord neurons, while membrane-tagged RFP denotes oligodendrocytes with their processes and myelin sheaths.

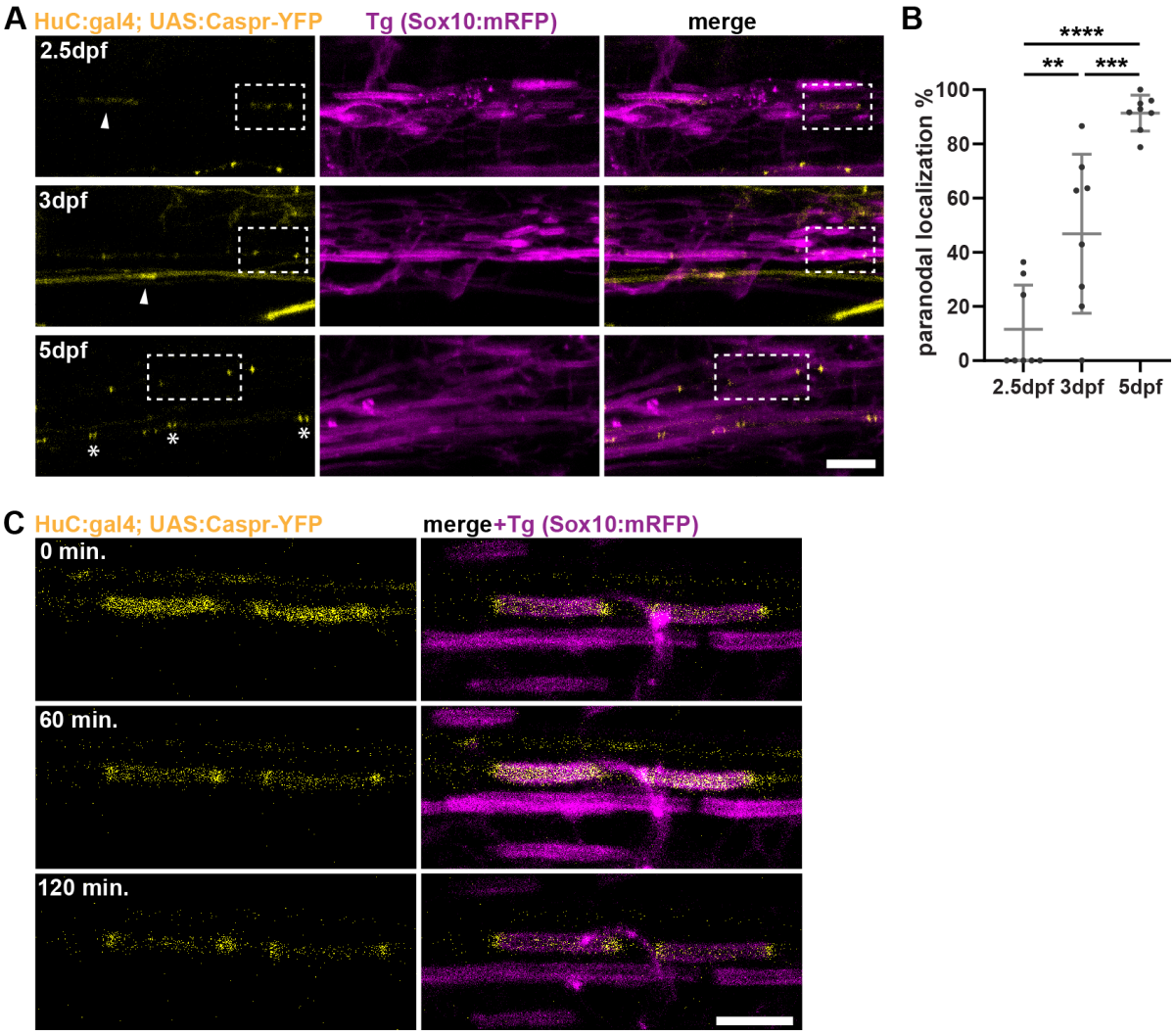

Figure 10: Caspr Relocation in the Zebrafish Spinal Cord A Images display axonal Caspr-YFP (yellow) localization underneath myelin sheaths (magenta) at 2.5 dpf, 3 dpf, and 5 dpf. Arrowheads point at internodal axonal Caspr-YFP accumulation, myelin sheath with axonal Caspr-YFP at paranodes are encircled, and asterisks show Caspr-YFP in paranodes close to nodes of Ranvier. Scale bar = 10µm **B** Graph displays ratio of paranodal to internodal Caspr-YFP accumulation. Differences were tested by one-way ANOVA with Tukey's multiple comparisons test; 2.5-3dpf p=0.005, 3-5 dpf p=0.0005, 2.5-5dpf p<0.0001. Every Caspr-YFP event in hemi spinal cords of 8 animals per age was counted **C** Time-lapse imaging shows Caspr-YFP relocation from internodal to paranodal within 2 h. Scale bar = 5 µm.

First, we observed the localization of Caspr-YFP during myelination. We followed Caspr-YFP in the axonal membrane during the development of the spinal cord to its final position at the paranodes of myelin sheaths from 2.5 dpf to 5 dpf. We expected to see Caspr-YFP distributing

equally along the axon, accumulating at the ends of myelin sheaths only at the stage of paranodal establishment.

In contrast to our expectation, we saw Caspr-YFP accumulating at myelin ensheathment sites at the early stages of myelination (Fig.10 A, arrowheads). At later stages of myelination, Caspr-YFP was mainly found at the ends of myelin sheaths, where we would expect the paranodes (Fig.10 A, encircled areas), thereby also forming the borders of nodes of Ranvier (Fig.10 A, asterisks). We determined the ratio of internodal and paranodal Caspr-YFP localization (Fig.10 B). At 2.5 dpf, Caspr was mainly found in internodes, confirming our observation of internodal accumulation at the early stages of myelination. At 3 dpf $\sim$50% of Caspr-YFP was located at paranodes (difference to 2.5 dpf: p=0.005), whereas at 5 dpf the majority of Caspr-YFP was found at the paranodes (difference to 2.5 dpf: p<0.0001 and to 3 dpf p=0.0005).

Time-lapse imaging revealed that Caspr-YFP first accumulates internodal and then relocates to the paranodes within a time frame of 2 h (Fig.10 C), leaving hardly any Caspr-YFP in the internodal area.

3.1.3 Caspr Accumulates Reversibly at Myelin Ensheathment Site upon Oligodendroglial Contact

We observed the distribution of Caspr-YFP within the axonal membrane even closer.

After we defined Caspr-YFP accumulation as an area with higher Caspr-YFP signal intensity than the surrounding axon's signal intensity, we observed many Caspr-YFP accumulation events at internodes (Fig. 11 A, arrowheads). We also found Caspr-YFP accumulating in the axon before the establishment of internodes but at the earliest possible point of axon-glia interaction - when a (premyelinating) oligodendrocyte process touches an axon (Fig. 11 A-C). Moreover, it seems that even a myelin sheath that is very close to an axon and thereby unintentionally touching it is sufficient for Caspr-YFP to accumulate at this site (Fig. 11 B, right panel).

While we observed the axo-glial interactions, we also saw myelin sheath retractions. Retractions have been described before [Czopka et al., 2013; Liu et al., 2013; Hughes and Appel, 2020]. We saw seemingly established myelin sheaths withdraw.

A representative time-lapse shows a retracting myelin sheath (Fig. 11 D, encircled), while a neighboring myelin sheath with established paranodes prolongates by $\sim$1 µm in the same time course. Caspr-YFP signal intensity varies during sheath retraction. While a single paranode is visible before the retraction starts, its signal intensity diminishes. There is no internodal Caspr-YFP accumulation visible in the course of myelin retraction.

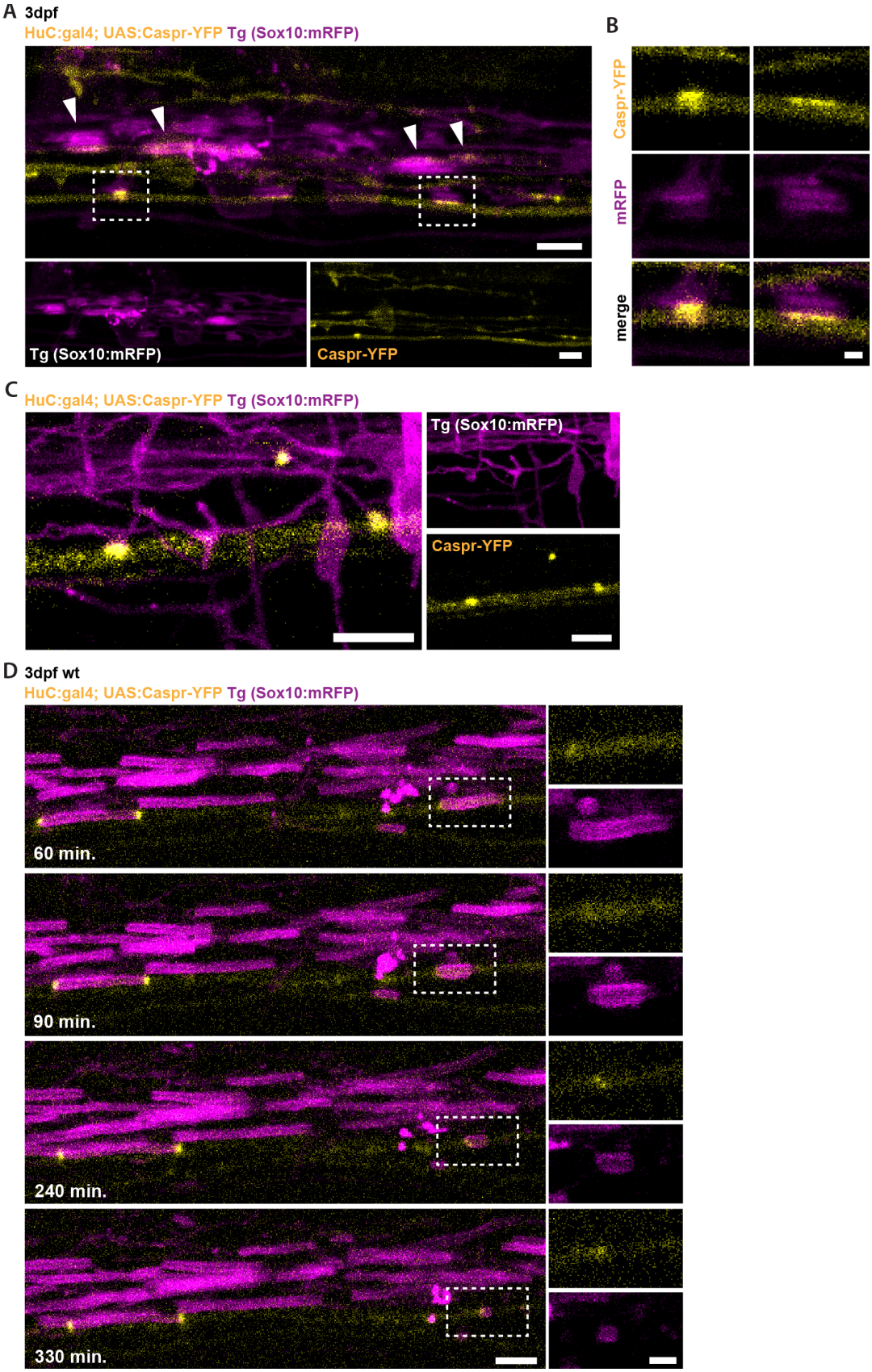

Figure 11: Early and Reversible Caspr Accumulation Images display axonal Caspr-YFP (yellow) localization underneath myelin sheaths (magenta) of zebrafish spinal cords **A** Axonal Caspr-YFP accumulates at internodes (arrowheads) and very early upon an oligodendrocyte process touching an axon (encircled) **B** Close-up of axonal Caspr-YFP accumulation upon oligodendroglial contact, Scale bar = 5µm **C** Axonal Caspr-YFP accumulation upon premyelinating oligodendrocyte contact **(A + C)** Scale bars = 1µm **D** Time-lapse shows Caspr-YFP dynamics during retraction of a myelin sheath. Scale bar = 5µm.

3.1.4 Caspr Accumulation and Relocation is timed precisely

After observing the early internodal accumulation of axonal Caspr-YFP, its relocation from the internode to paranodes, and its dynamics during myelin sheath retraction, we wanted to assess the dynamics of Caspr-YFP during the entire development *in vivo*. For that, we used time-lapse imaging with the above-described settings (see section 2.2.5).

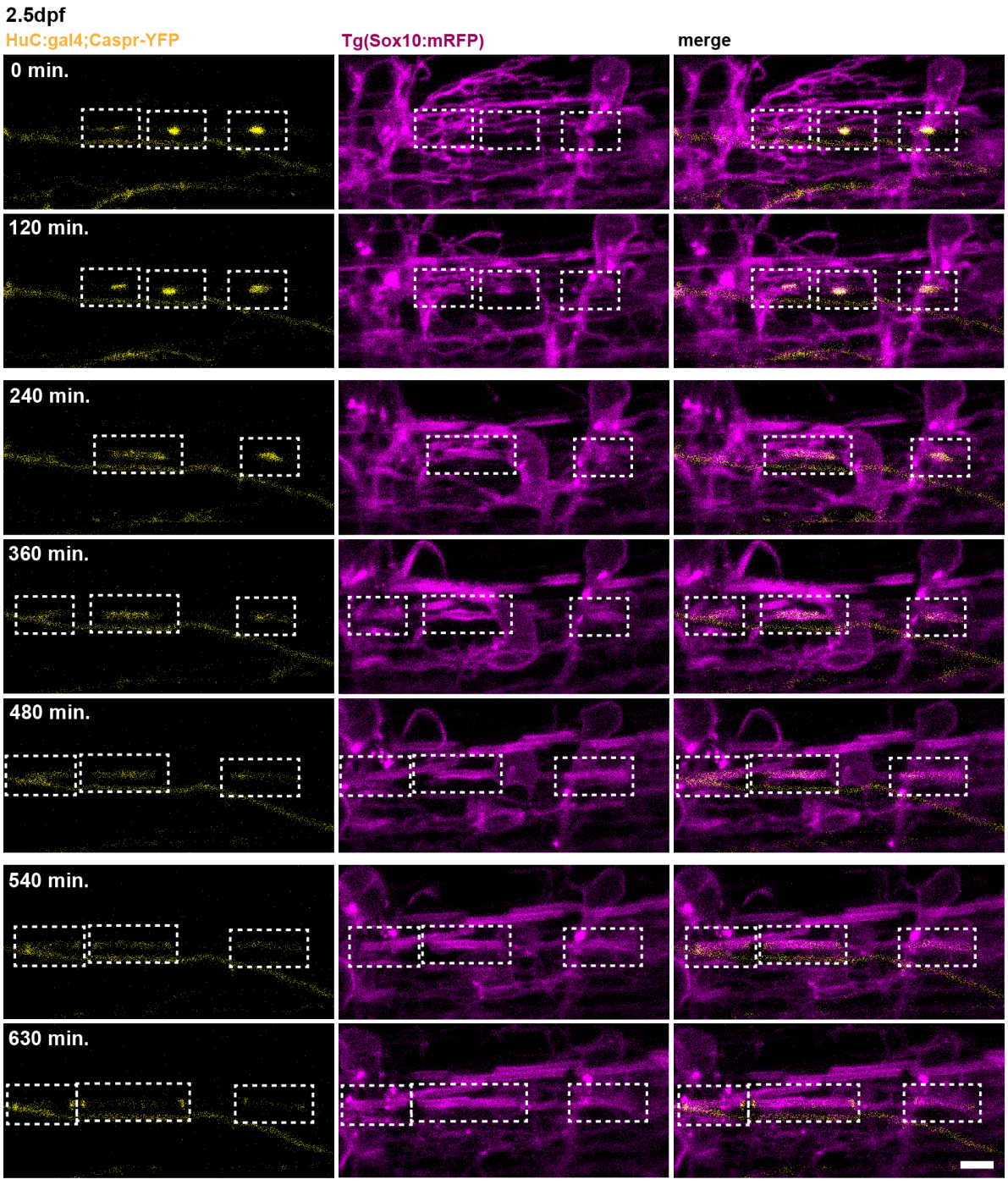

Figure 12: CASPR-YFP DYNAMICS AT INTERNODES AND PARANODES IN ZEBRAFISH SC AXONS Images show the dynamics of axonal Caspr-YFP (yellow) relocation underneath myelin sheaths of zebrafish spinal cords. Oligodendrocyte processes and myelin sheaths are labeled by Sox10-regulated mRFP (magenta). Caspr-YFP accumulates very early in the axon - when a premyelinating oligodendrocyte process touches an axon (see images at 0 - 120 min). Then it spreads internodal (240 - 480 min) and finally migrates to paranodes (540 - 630 min). The whole process takes about 10 h. Scale bar = 5 µm.

We then observed the Caspr-YFP dynamics from the earliest possible point of axon-glia interaction until the establishment of a myelin sheath (Fig. 12). It seems to take approximately 3 h until a premyelinating oligodendrocyte process, which is in contact with an axon, changes into a myelin sheath/ internodal structure. Axonal Caspr-YFP stays accumulated at the potential myelin ensheathment site during this time. Within the following 3 h, the Caspr-YFP accumulation spreads equally along the internode and stays underneath the myelin sheath. Then the axonal Caspr-YFP migrates to the paranodes. After approximately 10 h, the paranodes are fully established, and Caspr-YFP is precisely located at the paranodes. However, the myelin sheaths might still elongate laterally.

The complete process of Caspr-YFP relocation was only observed twice. Hence, a statistical analysis is not available.

3.1.5 Identifying the Caspr Accumulating Protein

The Oligodendroglial Adhesion Protein Nfascb accumulates at myelin sheath as well

The zebrafish version of the paranodal protein Neurofascin, Nfascb, has a similar structure and function as the mammalian Neurofascin, NFASC155. In concordance with the previous experiments, the following experiment aims at describing the localization dynamics of Nfascb during the development of the central nervous system. As Nfascb is the oligodendroglial counterpart to Caspr and probably its binding partner, localization dynamics were observed in oligodendroglial processes. We injected Sox10:gal4;UAS:Nfascb-GFP in one-cell stage zebrafish embryos with a Sox10:mRFP background and determined its localization in the spinal cord during development from 3 dpf to 5 dpf.

Notably, we found Nfascb-GFP accumulating at internodes, at the ends of myelin sheaths, and at paranodes flanking nodes of Ranvier at 4 dpf and 5dpf (encircled areas, Fig. 13 A). Time-lapse imaging showed that Nfascb-GFP relocates from internodes to paranodes within 2 hours (Fig. 13 B). These observations coincide with our observations on Caspr-YFP localization. The general expression efficiency of Nfascb-GFP was very low and could not be improved after several different approaches. Hence, the low sample size did not allow for a detailed quantification. In addition, our general experimental setting for zebrafish imaging does not allow the acquisition of more than two fluorescent channels at once. Therefore, axons were not labeled within this experimental setup, and a detailed analysis of the very early expression of Nfasc-GFP at potential myelin ensheathment sites was not possible.

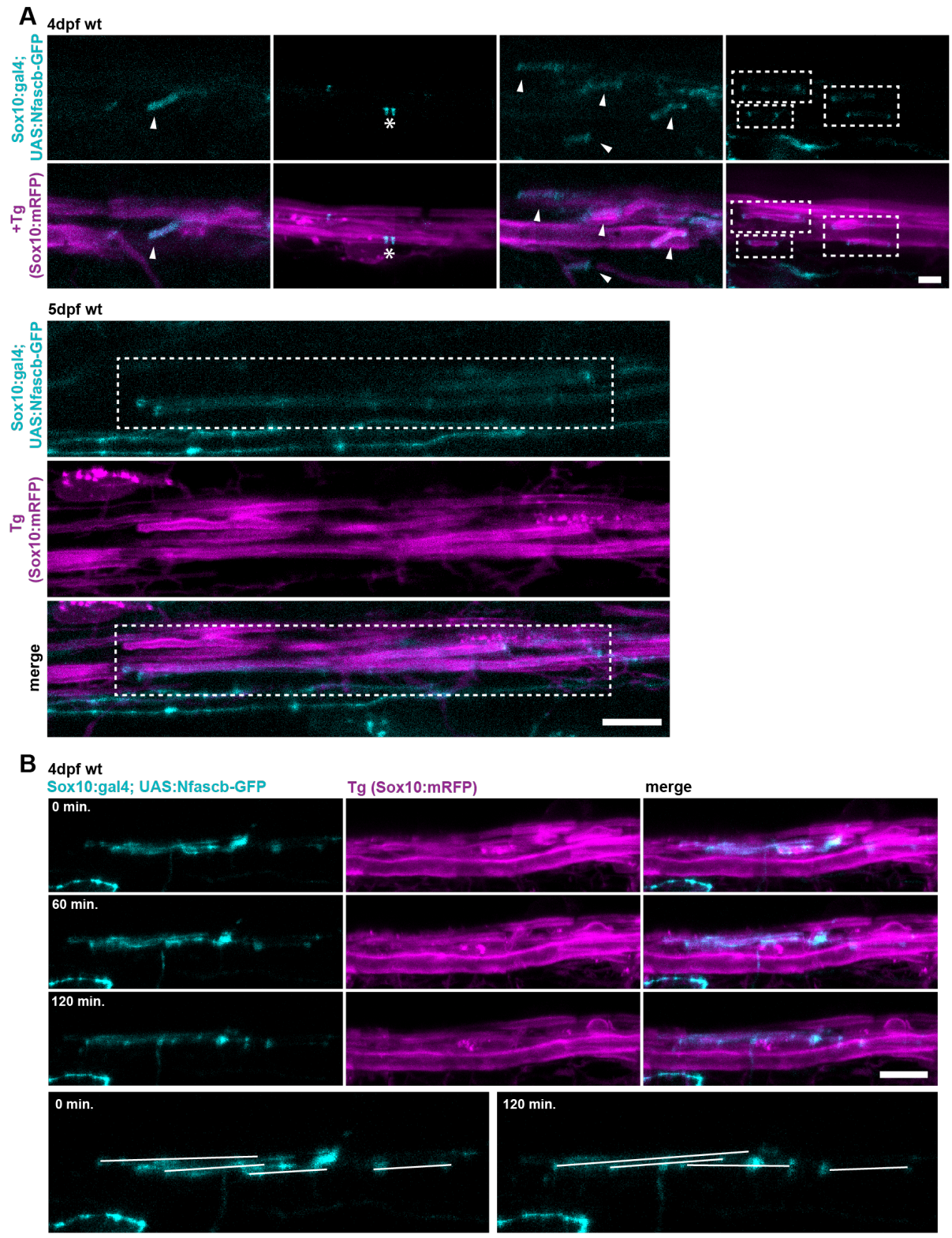

Figure 13: NFASCB LOCALIZATION DURING DEVELOPMENT Images show the distribution of oligodendroglial Nfascb-GFP (cyan) in spinal cord myelin sheaths (magenta) of Tg(Sox10:mRFP) zebrafish at 4 dpf and 5 dpf **A** Arrowheads indicate internodal accumulation, asterisks indicate nodes of Ranvier, and entire myelin sheaths with Nfasc at paranodes are encircled. Scale bars = 5 and 10 µm **B** 2 h time-lapse of oligodendroglial Nfascb-GFP relocating from internodes to paranodes. Lines indicate the direction of the myelin sheaths for a better overview. Scale bar = 10 µm.

In *nfascb*$^{-/-}$ *Zebrafish Caspr does not Locate Correctly to the Paranodes*

We used our previously described *nfascb*$^{-/-}$ zebrafish line [Djannatian et al., 2019] to prove Nfascb to be Caspr's initial binding partner. We investigated the Caspr localization in *nfascb*$^{-/-}$ zebrafish using Caspr-YFP again.

In wt and *nfascb*$^{+/-}$ animals, we observed the same internodal and paranodal Caspr-YFP distribution at 3 dpf and 5 dpf as described above (Fig. 14A + C). Caspr-YFP accumulates internodal and relocates to the paranodes during development. However, in 3 dpf *nfascb*$^{+/-}$ zebrafish, Caspr-YFP not only accumulates internodal, but it also stays internodal and does not relocate to the paranodes (Fig. 14 A-C). At 5 dpf, Caspr-YFP is still mainly located at internodes of *nfascb*$^{+/-}$ zebrafish. Hardly any relocation of Caspr-YFP was observed. A quantification to determine the ratio of internodal to paranodal Caspr-YFP localization points at internodal localization at 3 dpf and 5 dpf (p<0.0001, Fig. 14 C). Some Caspr-YFP events seemed to form paranodes in 5 dpf *nfascb*$^{-/-}$ animals.

However, these paranodes are characterized by a spread of Caspr-YFP (Fig. 14 B + D). For example, paranodes in wt animals are very densely packed with a width of $\sim$3 µm across two paranodes enclosing a node of Ranvier. In contrast, the width increases to $\sim$15 µm in *nfascb*$^{-/-}$ animals (Fig. 14 D + E). Caspr-YFP signal intensity measurements across these paranodes show two intensity maxima within a distance of $\sim$3 µm in wt animals, indicating a node flanked by paranodes (Fig. 14 E). In contrast, the signal intensity in *nfascb*$^{-/-}$ animals increases and decreases within a broader range of $\sim$5-7.5 µm per paranode without showing two intensity maxima as clearly defined as in wt animals. Notably, we found Caspr-YFP accumulating at the earliest stage of myelination, upon contact of an oligodendroglial process with the axon also in *nfascb*$^{-/-}$ zebrafish (Fig. 14 F).

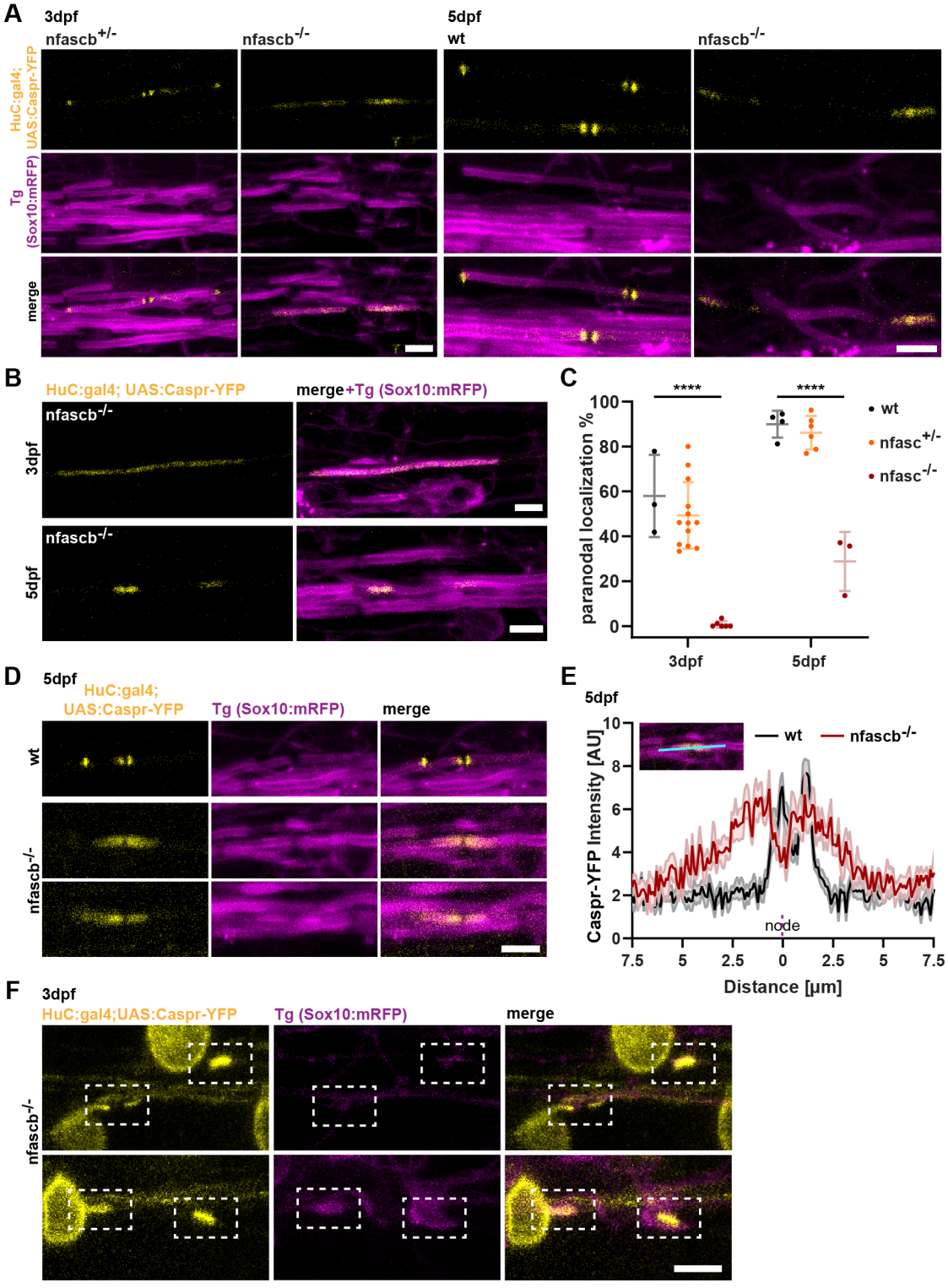

Figure 14: CASPR-YFP LOCALIZATION IN *nfascb*$^{-/-}$ ZEBRAFISH Images show the distribution of Caspr-YFP (yellow) underneath myelin sheaths (magenta) of spinal cord axons of wild type, *nfascb*$^{+/-}$ and *nfascb*$^{-/-}$ zebrafish at 3 dpf and 5dpf **A + B** In 3 dpf *nfascb*$^{-/-}$ zebrafish Caspr-YFP stays internodal, at 5 dpf as well. In some myelin sheaths, Caspr-YFP relocates and forms perturbed paranodes **C** Graph displays ratio of paranodal to internodal localisation of Caspr-YFP in *nfascb*$^{+/-}$ and *nfascb*$^{-/-}$ zebrafish at 3 dpf and 5 dpf. One dot represents the ratio of all Caspr-YFP events in a hemi-spinal cord of one animal. Differences (p<0.0001) were tested using a 2way ANOVA with Sidak's multiple comparisons test **D** Images show examples of typical, precisely located Caspr-YFP at paranodes in wt animals and enlarged paranodes in *nfascb*$^{-/-}$ animals at 5 dpf **E** Graph displays profile plots of Caspr-YFP intensity across paranodes bordering nodes of Ranvier in wt and *nfascb*$^{-/-}$ animals. Mean ± SEM of 7-9 events from ≥2 animals are shown. **F** Images show examples of Caspr-YFP accumulation in the axonal membrane of *nfascb*$^{-/-}$ animals upon contact with an oligodendrocyte process. All scale bars = 5 µm.

A Lack of Oligodendroglial Cntn1b does not Affect Axonal Caspr Localization

We also used our previously generated *cntn1b*$^{-/-}$ zebrafish line to test if oligodendroglial Cntn1b could potentially function as a Caspr attracting oligodendroglial protein and accumulate Caspr-YFP in the axonal membrane. Caspr-YFP was used as a marker again. To rescue Cntn1b expression in the neurons of our full-body mutant zebrafish, we additionally injected a UAS:cntn1b plasmid. Both plasmids were expressed under the control of the neuronal promoter HuC:gal4.

In the absence of Cntn1b in the oligodendrocytes of *cntn1b*$^{-/-}$ zebrafish we found Caspr-YFP accumulating internodal and relocating to paranodes as well (Fig. 15 A). We discovered no visible difference in Caspr-YFP localization between *cntn1b*$^{-/-}$ and wild type zebrafish. Quantification did not reveal a difference of Caspr-YFP localization in *cntn1b*$^{-/-}$ zebrafish compared to *cntn1b*$^{+/-}$ or wild type zebrafish, neither at 3 dpf nor at 5 dpf (Fig. 15 B). We also found axon-myelin overlaps that do not show any accumulation of Caspr-YFP at the internode or the paranodes (Fig. 23 B, arrowhead). As Caspr-YFP in these cases seemed to distribute in the same amounts everywhere along the axon, we defined these events as "equal distribution". The ratio of equal Caspr-YFP distribution underneath a myelin sheath usually ranged from 5-20% at 3 dpf to 10-20% at 5 dpf. We did not detect a difference in the different genotypes. However, we also detected early Caspr-YFP accumulation (Fig. 15 C).

We spotted Caspr-YFP expressing neurons in which the axons lacked Caspr-YFP. Instead, Caspr-YFP stayed in the neuronal cell body, probably due to the lack of Cntn1b expression. Previously, we described neuronal cell body myelination in full body *cntn1b*$^{-/-}$ zebrafish [Djannatian et al., 2019]. Here, we also found myelin sheath wrapping neuronal bodies in the absence of neuronal Cntn1b. Interestingly, the myelin sheaths touching the neuronal cell body also accumulate neuronal Caspr-YFP at the contact site of sheath and cell body (Fig. 15 D). This observation was not quantifiable.

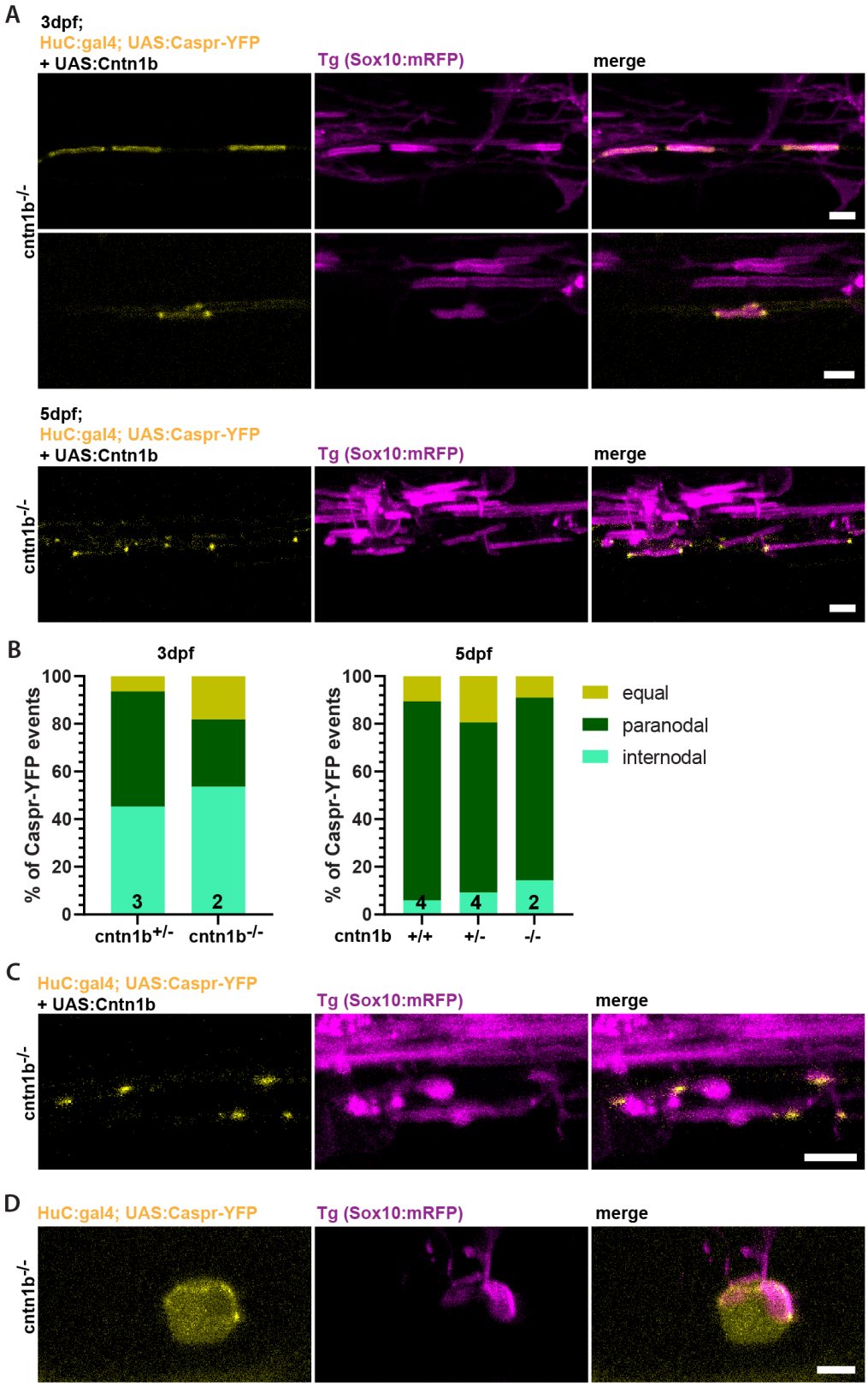

Figure 15: Caspr Localization in Neuronal *cntn1b*$^{-/-}$ Zebrafish Images show the distribution of Caspr-YFP (yellow) underneath myelin sheaths (magenta) of spinal cord axons in these zebrafish at 3 dpf and 5 dpf. **A** Caspr-YFP was found accumulated at internodes or relocated to paranodes in *cntn1b*$^{-/-}$ + neuronal Cntn1b rescue zebrafish **B** Graphs display the ratio of Caspr-YFP localization (internodal, paranodal, and equally distributed) in myelinated areas in these zebrafish. The numbers in the columns represent the number of sample replicates **C** Images show examples of Caspr-YFP accumulation in the axonal membrane of these zebrafish upon contact with an oligodendrocyte process **D** Cell body myelination of a *cntn1b*$^{-/-}$ neuron that did not express the rescuing Cntn1b. Caspr-YFP accumulates at the rim of the myelinating sheath. All scale bars = 5 µm.

3.1.6 The influence of Internodal Molecules on the Localization Dynamics of Paranodal Proteins

Caspr Locates Less to Paranodes in Ganglioside Null Mice

First, we wanted to estimate the influence of gangliosides on the distribution of paranodal myelin adhesion proteins. We immunolabeled longitudinal *ST3GAL5*$^{-/-}$/ *B4GALNT1*$^{-/-}$ double mutant mouse spinal cord sections at a stage where myelination is advanced but not yet completed (P21). These mice lack two genes necessary for synthesizing the majority of gangliosides (compare Fig. 5). Hence they are also referred to as ganglioside null mice. Their double heterozygous littermates *ST3GAL5*$^{+/-}$/ *B4GALNT1*$^{+/-}$ were used as control animals. We stained for Caspr as an indicator for paranodal protein localization and Ankyrin G as a marker for nodes Ranvier.

While we found Caspr perfectly located at the paranodes in *ST3GAL5*$^{+/-}$/ *B4GALNT1*$^{+/-}$ mice, it was less located at the paranodes in *ST3GAL5*$^{-/-}$/ *B4GALNT1*$^{-/-}$ mice (Fig.16 A + D), the nodes of Ranvier were also not as evident in these animals. We counted less nodes per mm^2 in ganglioside null mice (Fig.16 B). However, the difference was not significant (p=0.078). We measured Caspr intensities among a 10 µm long line across immunolabeled nodes and paranodes. The mean $\pm$SD profile plots show two intensity maxima and a drop in intensity between these maxima in *ST3GAL5*$^{+/-}$/ *B4GALNT1*$^{+/-}$ mice, indicating nodes flanked by paranodes (Fig.16 C). In comparison, in ganglioside null mice, intensity levels increase less from a higher bottom line and hardly show two maxima.

A profile plot of Caspr and Ankyrin G intensities across a single *ST3GAL5*$^{+/-}$/ *B4GALNT1*$^{+/-}$ node and the flanking paranodes shows two intensity maxima for Caspr, designating the paranodes, and one intensity maximum for Ankyrin G in between, indicating for the node (Fig.16 E). In ganglioside null mice, the Caspr staining hardly indicates the paranodes (Fig.16 A + D). However, the profile plot for Ankyrin G is not different from the control littermates, while Caspr intensity levels hardly increase and show a more diffuse distribution of Caspr (Fig.16 F).

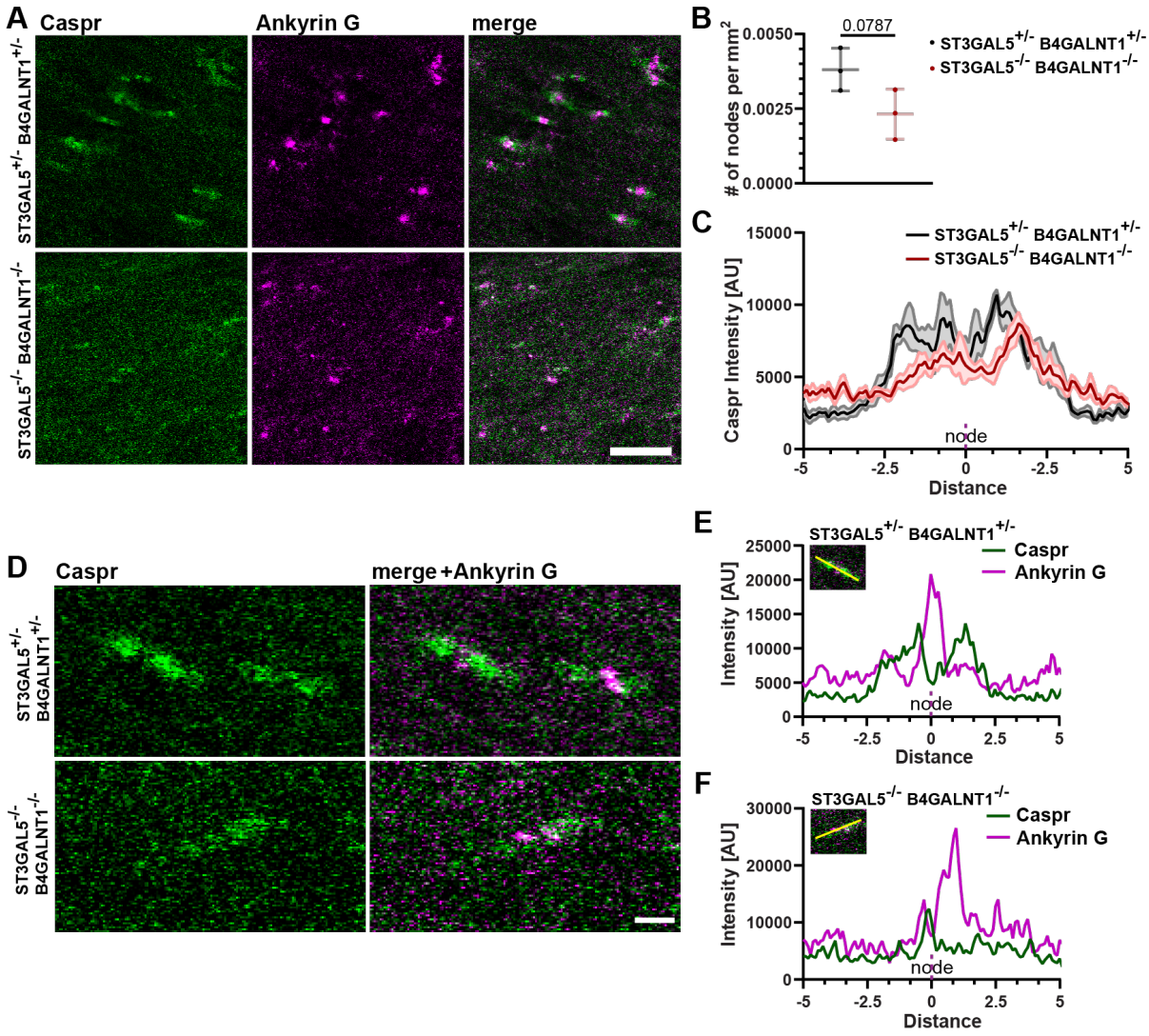

Figure 16: Immunofluorescent Staining of Longitudinal Ganglioside Null Mouse Spinal Cord Sections for Caspr and Ankyrin G Images of Caspr (green) and Ankyrin G (magenta) staining show Caspr localization at paranodes in *ST3GAL5*$^{-/-}$*/ B4GALNT1*$^{-/-}$ mice and in double heterozygous mice as control animals. **A** Compared to control animals, the paranodal localization of Caspr in the ganglioside null mice is not as precise. Ankyrin G marks the nodes of Ranvier. Scale bar = 10 µm **B** Graph displays the number of nodes per mm^2 in double mutant and double heterozygous zebrafish. Fewer nodes per mm^2 were counted in ganglioside null mice compared to their double heterozygous littermates, though the difference is not significant. Differences were tested using a two-tailed unpaired t-test (p=0.0787) **C** Images show profile plots of Caspr intensities across nodes in ganglioside null mice and double heterozygous littermates. While two peaks indicate the paranodes in the control animals, these peaks are not as visible in *ST3GAL5*$^{-/-}$*/ B4GALNT1*$^{-/-}$ mice. Mean ±SEM are shown. 5 paranodes per genotype were measured **D** Images show close-up of nodes and paranodes formed by Caspr and Ankyrin G in double heterozygous and *ST3GAL5*$^{-/-}$*/ B4GALNT1*$^{-/-}$. Scale bar = 2µm **E + F** Profile plots of Caspr and Ankyrin G intensities of single representative paranodes in control and double mutant animals.

Membrane-associated GFP is Depleted from Internodes

Next, we wanted to prove if the ganglioside-Mag interaction influences internodal membrane protein distribution *in vivo*. We made use of two main advantages of GFP. First, as a fluorescent protein, GFP can be visualized. Second, GFP is an inert protein. Thus, it does not interact with any other protein or molecule.

We designed GFPs that are attached to the external axonal membrane by two different transmembrane domains or a Glycosylphosphatidylinositol (GPI) anchor. The palmitoylation site of the Lyn protein was used to design a palmitoylated GFP. It attaches to the luminal axonal membrane and serves as a control. See section 2.2.2 for details on the fusion protein design. Our plasmids were injected into one-cell stage Tg(Sox10:mRFP) zebrafish embryos under the control of a UAS promoter, together with a HuC:gal4 plasmid for neuronal expression. The spinal cord of 3-4 dpf zebrafish larvae was imaged.

Compared to unmyelinated areas, we detected a lower signal intensity of all constructs located in the external axonal membrane (HS-TM-GFP, HA-TM-GFP, and GPI-GFP, Fig. 17 A) underneath myelin sheaths. In contrast, PM-GFP, the control construct located on the luminal axonal membrane, shows the same signal intensity underneath myelin sheaths and in unmyelinated areas.

Using a Fiji/ImageJ macro, the axonal GFP intensities in myelinated and unmyelinated areas were semi-automatically measured and quantified (Fig. 17 B, see Appendix VIII for the complete macro). The mean of all internodal intensity values was divided by the mean of all intensity values before and after the myelin sheath. If intensities in myelinated and unmyelinated axonal areas were the same, the output value would be 1. Intensities >1 would display internodal accumulation, while intensities <1 show internodal depletion of our construct.

The axonal GFP signal intensity underneath myelin sheaths is significantly lower than in unmyelinated areas for HS-TM-GFP (p=0.0009), HA-TM-GFP (p=0.0004) and GPI-anchored-GFP (p=0.029), while the intensity levels for our control, PM-GFP (p=0.775), are the same in both areas (Fig.17 C). Also, when compared among each other, the plasmids for extracellular axonal protein expression show a lower GFP signal intensity underneath myelin sheaths than the luminal axonal membrane-associated GFP (HA-TM-GFP: p=0.006; GPI-GFP: p=0.041). Only the intensity levels for HS-TM did not significantly differ from the control (p=0.075) but also showed the tendency to be lower.

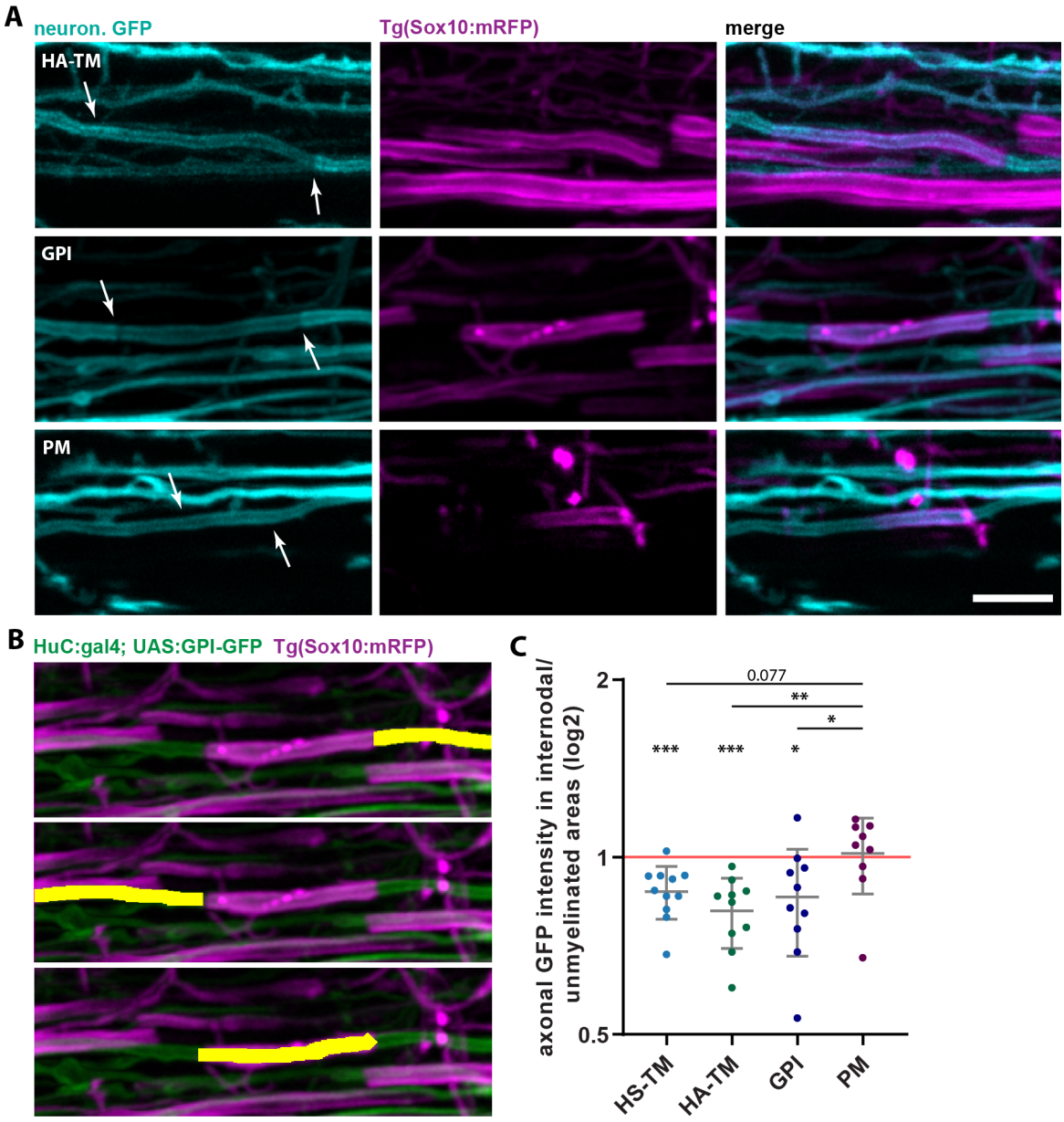

Figure 17: Internodal Membrane-Associated GFP in Zebrafish SC Axons A Images show the axonal expression of HA-TM-GFP, GPI-GFP, and PM-GFP (cyan) underneath myelin sheaths (magenta) in the zebrafish spinal cord. Oligodendroglial myelin sheaths are labeled with intracellular, membrane-tagged RFP. Arrows delineate the beginning and the end of myelin sheaths. The axonal GFP signal intensity of the extracellular GFP constructs is visibly lower underneath the myelin sheaths compared to unmyelinated areas. PM-GFP seems to be distributed equally along the axons. Scale bar = 5µm **B** Example of axon selection for semi-automated signal intensity measurements using a Fiji/ImageJ macro (see Appendix VIII) **C** Graph displays the GFP signal intensity ratio of myelinated (internodal) and unmyelinated areas. Mean $\pm$ SD is shown, tested for the difference to 1 by one sample t-test, two-sided; 1 = continuous distribution, <1 = internodal depletion, >1 = internodal accumulation; Differences of HS-TM, HA-TM, and GPI to control (PM) were tested with one-way ANOVA and Sidak's multiple comparisons; One dot represents mean of $\geq$3 measurements in one animal.

Depletion is not a Result of GFP Quenching

Even though our axonal GFP constructs are separated from the luminal oligodendroglial mRFP by at least one oligodendroglial lipid bilayer, we wanted to ensure that the observed internodal GFP depletion was not a result of GFP-quenching by mRFP. We used acceptor photobleaching, to detect if FRET between fluorophores occurs [Piston and Kremers, 2007]. After acceptor (mRFP) photobleaching, a higher GFP signal intensity indicates signal quenching.

Tg(Sox10:mRFP) zebrafish were injected as described above and imaged at 4 dpf with the usual settings (see section 2.2.5). Subsequently, we ablated the mRFP signal using 3 times more laser power with a 555 nm wavelength than usual for 70 sec (usual imaging time is in the ms range). Post ablation images of the same area were acquired with the same settings.

Photobleaching the mRFP fluorophore did not increase the GFP signal intensity visibly (Fig. 18 A). Also, quantification of the GFP signal intensity as described above, before and after photobleaching, did not show increasing but rather decreasing signal intensity (Fig. 18 B). Therefore, quenching of the extracellular axonal GFP intensity at the internode by the oligodendroglial mRFP does not occur.

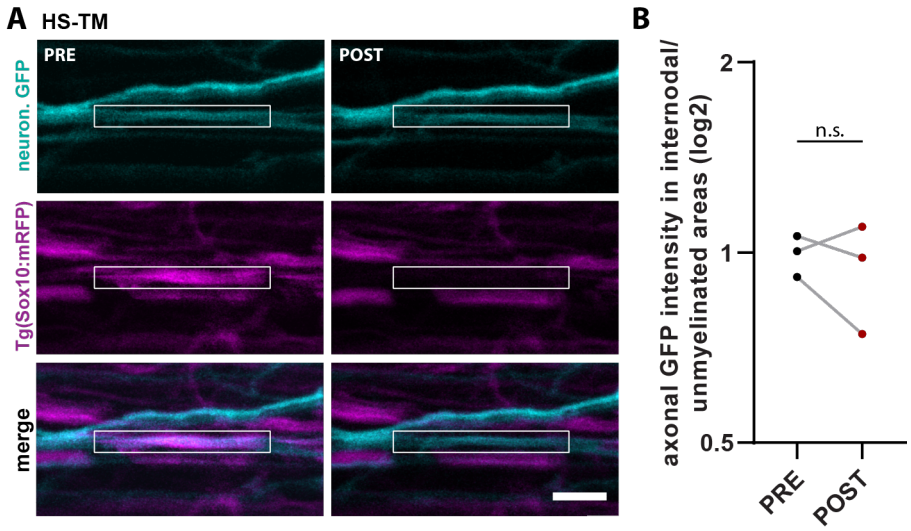

Figure 18: Membrane-Associated GFP Signal Intensity in Zebrafish Before and After Acceptor Photobleaching A Images show the axonal intensities of HS-TM-GFP (cyan) underneath myelin sheaths (magenta) in the zebrafish spinal cord before (PRE) and after (POST) photobleaching the oligodendroglial RFP signal. Scale bar = 5µm **B** Graph displays GFP signal intensity measurements before (PRE) and after (POST) photobleaching. Differences were tested with a paired t-test, two-tailed.

Sphingolipids have a Minor Role in Axonal Membrane Protein Distribution at Internodes

Next, we investigated the influence of either gangliosides or Mag on the distribution of internodal membrane proteins. We disturbed ganglioside synthesis pharmacologically by using Fumonisin B1 toxin (Fum B1) to block sphingolipid synthesis in zebrafish.

In brief, Tg(Sox10:mRFP) zebrafish larvae, injected with either GPI-GFP or HS-TM-GFP, were dechorionated and treated with 1% Fum B1 10 mM by adding it directly into the E3 medium at 1 dpf. After 2 days of incubation in Fum B1, the fish were imaged (at the age of 3 dpf). Control fish were treated with DMSO in the same amount and for the same time. Images were analyzed as described above.

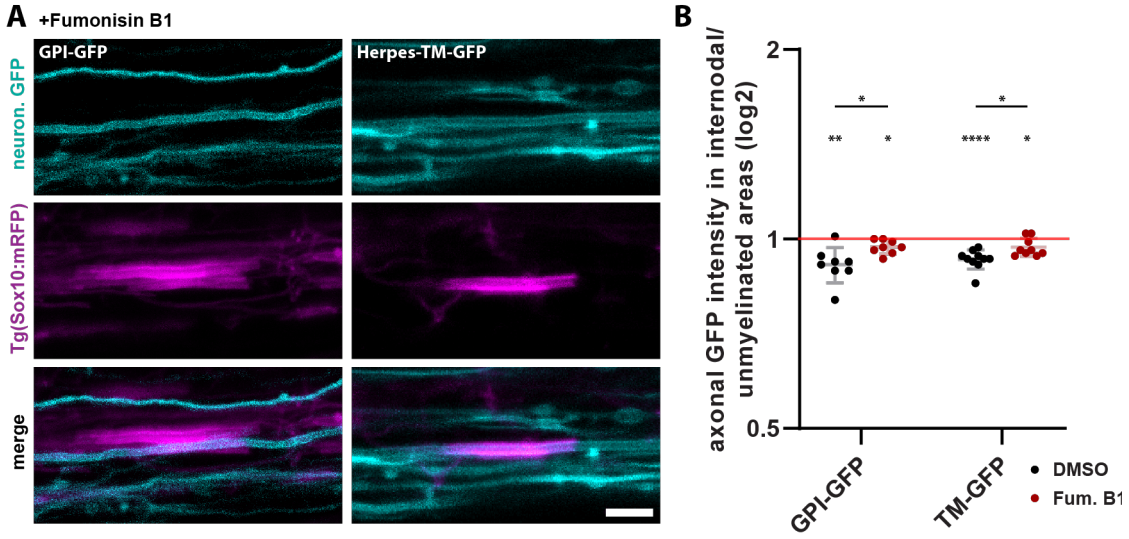

Figure 19: MEMBRANE-ASSOCIATED GFPS IN SPHINGOLIPID DEPLETED ZEBRAFISH A Images show the axonal expression of GPI-GFP and HS-TM-GFP (cyan) underneath myelin sheaths (magenta) in the spinal cord of zebrafish larvae treated with either Fum B1 to block sphingolipid synthesis or DMSO as a control; Scale bar = 5 µm **B** Graph displays the ratio of GFP signal intensities in myelinated and unmyelinated areas. GFP constructs are significantly depleted from myelinated areas in DMSO- and Fum B1-treated zebrafish, though Fum B1-treated zebrafish tend to show less depletion. Mean ± SD are shown; Tested for the difference to 1 by one sample t-test, two-sided, 1 = continuous distribution, <1 = internodal depletion, >1 = internodal accumulation; Differences between Fum B1- and DMSO-treated zebrafish were tested with unpaired t-test, two-tailed; One dot represents mean of ≥3 measurements in one animal.

Treating the zebrafish larvae with DMSO did not affect the internodal depletion of the constructs in spinal cord axons. In contrast, we hardly recognized any depletion in Fum B1-treated larvae (Fig. 19A). Quantification of axonal GFP signal intensities in myelinated and unmyelinated areas revealed a significant depletion of GPI-GFP and HS-TM-GFP in myelinated areas of spinal cord axons of DMSO-treated zebrafish larvae (GPI p=0.0034 and Herpes-TM p<0.0001) (Fig.19 B). However, the depletion of DMSO-treated zebrafish larvae is not as substantial (HS-TM mean 0.92 ± 0.032; GPI mean 0.91 ± 0.058) as in untreated zebrafish (wt HS-TM mean 0.87 ± 0.09; GPI mean 0.85 ± 0.17, compared with the previous experiment). Interestingly, in Fum B1-treated larvae, both GFP constructs are still significantly depleted (GPI p=0.013 and HS-TM p=0.022), though not as strong as in DMSO-treated zebrafish. Nevertheless, the difference in axonal GFP signal intensity in myelinated vs. unmyelinated areas between DMSO- and Fum B1-treated zebrafish is significant in both groups (GPI p=0.016 and HS-TM p=0.011).

Mag Influences Axonal Membrane Protein Distribution at Internodes

As described above, we injected the membrane-associated GFP plasmids into *mag*$^{-/-}$ zebrafish. Images were taken at 3-4 dpf, and axonal GFP signal intensities were quantified.

In *mag*$^{-/-}$ zebrafish, we did not observe a depletion of axonal GPI-anchored GFP nor of HS-TM-GFP in myelinated areas (Fig.20 A). Quantification revealed a significant internodal depletion of both constructs in *mag*$^{+/-}$ larvae (GPI $p<0.0001$, HS-TM $p=0.0016$), while we detected a continuous distribution of both constructs in *mag*$^{-/-}$ larvae (Fig.20 B). There is a significant difference in internodal axonal GFP signal intensity between *mag*$^{+/-}$ and *mag*$^{-/-}$ for GPI-anchored GFP ($p=0.0061$), while for HS-GFP, there is a trend for a difference ($p=0.16$).

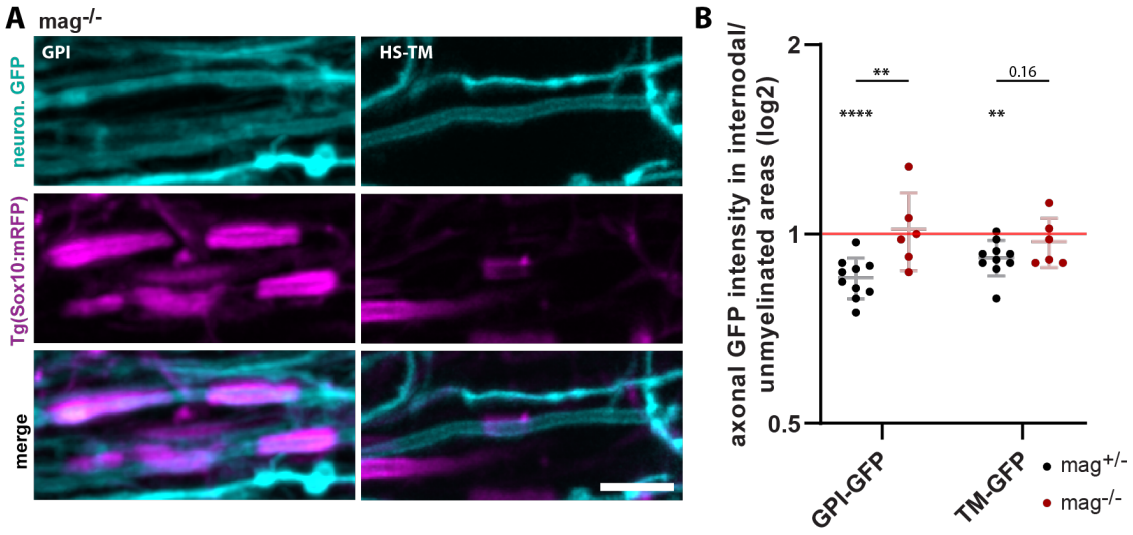

Figure 20: MEMBRANE-ASSOCIATED GFPS IN MAG$^{-/-}$ ZEBRAFISH A Images show the axonal expression of GPI-GFP and HS-TM-GFP (cyan) underneath myelin sheaths (magenta) in the spinal cord of *mag*$^{-/-}$ zebrafish; Scale bar = 5µm **B** Graph displays the ratio of GFP signal intensities in myelinated and unmyelinated areas. GFP constructs are significantly depleted from myelinated areas in *mag*$^{+/-}$ zebrafish but not in *mag*$^{-/-}$ animals. Mean $\pm$ SD are shown; Tested for the difference to 1 by one sample t-test, two-sided, 1 = continuous distribution, <1 = internodal depletion, >1 = internodal accumulation; Differences between *mag*$^{+/-}$ and *mag*$^{-/-}$ zebrafish were tested with unpaired t-test, two-tailed; one dot represents the mean of $\geq$3 measurements in one animal.

In Ganglioside Deficient Fish, Caspr Locates Less to Paranodes

We also depleted sphingolipid using Fum B1 in Caspr-YFP injected zebrafish larvae to observe the direct influence of sphingolipids on Caspr distribution. The axonal Caspr-YFP localization was studied at 3 dpf.

We observed a wild type typical ratio of axonal Caspr-YFP at internodes and paranodes in zebrafish larvae treated with DMSO (Fig. 21 A+B). In contrast, Caspr-YFP does not locate correctly to the paranodes in zebrafish treated with Fum B1 (Fig. 21 A). We found a few myelin sheaths where axonal Caspr-YFP entirely relocated to paranodes (arrowhead). However, at most myelin sheaths, Caspr-YFP stays partially (asterisk) or fully (arrow) internodal. This is also displayed in the ratio of paranodal to internodal localization (Fig. 21 B). In Fum B1-treated animals, Caspr-YFP stays significantly more often internodal (p=0.0124). Interestingly, measurements of myelin sheath length revealed slightly longer sheaths in Fum B1-treated animals (9.28µm ± 5.99µm) compared to DMSO-treated animals (10.97µm ± 7.71µm). The difference is not significant, though (p=0.08) (Fig.21 C+D).

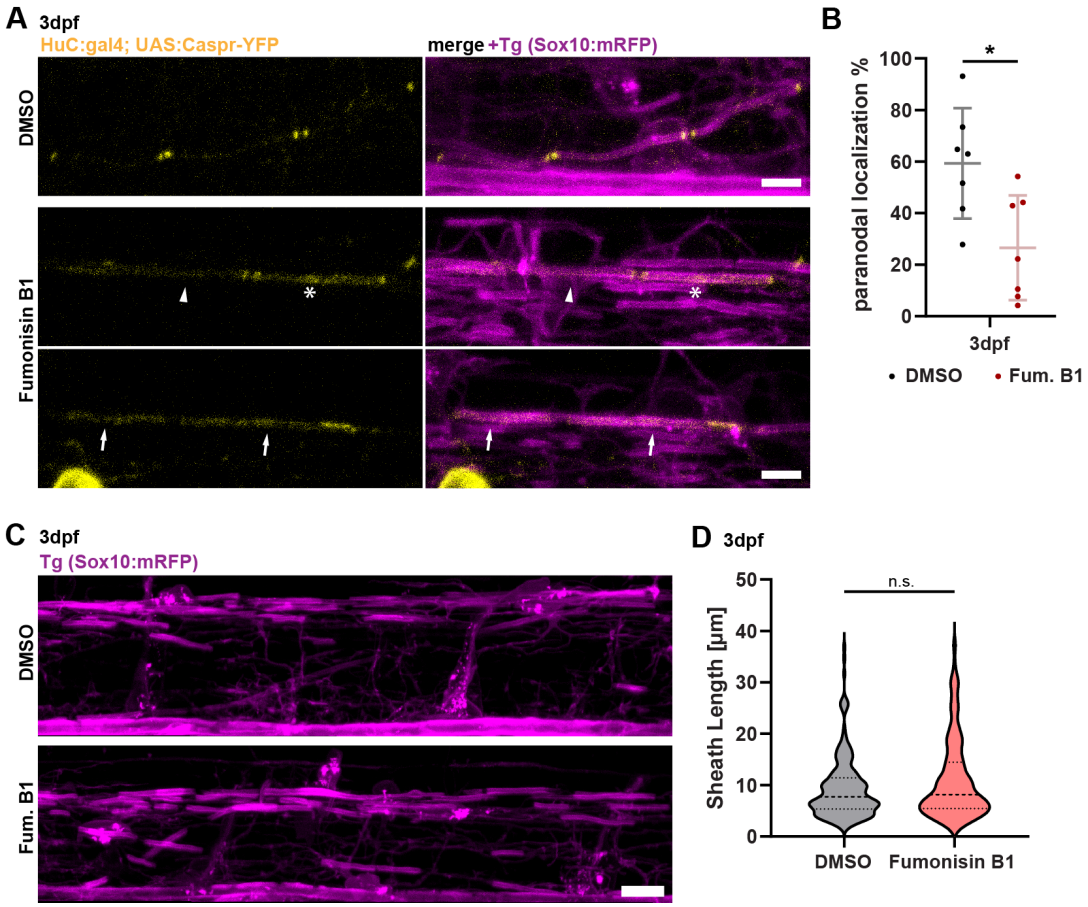

Figure 21: Caspr Localization in Sphingolipid Deficient Zebrafish Images show axonal Caspr-YFP-injected (yellow) zebrafish spinal cord myelin sheaths (magenta) treated with either DMSO or Fum B1 at 3 dpf **A** Caspr-YFP localization in DMSO-treated zebrafish resembles the wt Caspr-YFP localization, but it relocates less to paranodes in Fum B1-treated larvae **B** Graph displays the paranodal / internodal localization ratio of Caspr-YFP with less paranodal location in Fum B1-treated larvae (p=0.0124). One dot represents the mean ratio of all Caspr-YFP events in a hemi-spinal cord of one animal. Differences were tested with an unpaired t-test, two-tailed **C** Myelin sheaths of DMSO- or Fum B1-treated zebrafish do not show visible differences in length **D** Violin plot (>200 sheaths of 3 animals per treatment) shows a tendency for longer myelin sheaths in Fum B1-treated larvae compared to DMSO-treated larvae (p=0.08). Median ± quartiles are shown. Differences were tested with Mann Whitney test, two-tailed. Scale bars = 5 µm.

Caspr Locates Normally to Paranodes in *mag*$^{-/-}$ zebrafish

We injected our Caspr-YFP constructs into *mag*$^{-/-}$ embryos and did not find a difference in Caspr-YFP localization when Mag is depleted (Fig. 22 A+B). Like in wild type zebrafish, Caspr-YFP is mainly located at the internodes at 2.5 dpf, either at the internode or the paranodes at 3 dpf, and mainly at the paranodes at 5 dpf in *mag*$^{-/-}$ embryos (compare to section 3.1.2). Additionally, the paranodes appear healthy at all stages of myelination. However, there seems to be a slight delay in the relocation of Caspr-YFP to paranodes compared to wild type zebrafish at 5 dpf.

Interestingly, also in *mag*$^{-/-}$ zebrafish, Caspr-YFP accumulated at the earliest possible stage of myelination upon contact of an oligodendrocyte process with the axon (Fig. 22 C).

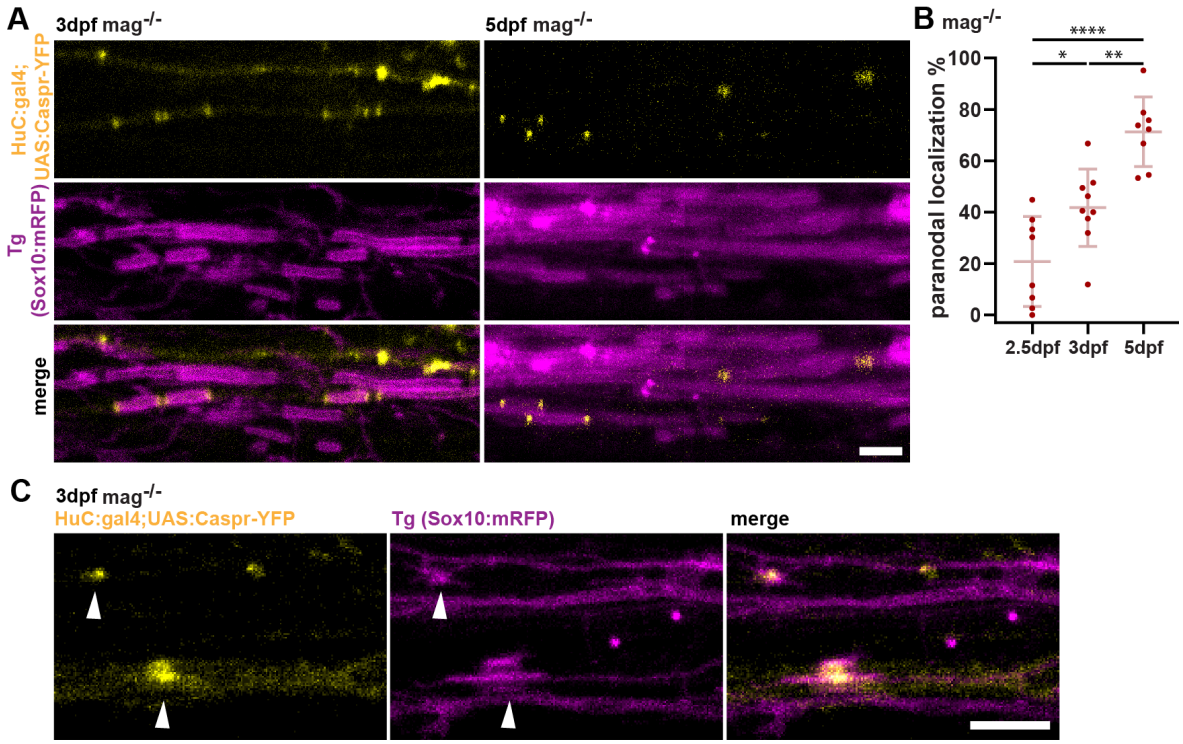

Figure 22: CASPR LOCALIZATION IN MAG$^{-/-}$ ZEBRAFISH A Axonal Caspr-YFP (yellow) localization at 3 dpf and 5 dpf underneath myelin sheaths (magenta) in the spinal cord of *mag*$^{-/-}$ zebrafish larvae. Like in wild type zebrafish, Caspr-YFP relocates to the paranodes, which have a normal appearance **B** Graph displays the paranodal to internodal localization ratio of axonal Caspr-YFP from 2.5 dpf to 5 dpf. Differences in localization of Caspr-YFP during development are significant: 2.5 dpf to 3 dpf p=0.027, 3 dpf to 5 dpf p=0.002, 2.5 dpf to 5 dpf p<0.0001. One dot represents the mean ratio of all Caspr-YFP events in a hemi-spinal cord of one animal. Differences were tested with one-way ANOVA with Tukey's multiple comparisons **C** Caspr-YFP accumulation upon contact of an oligodendrocyte process with an axon. Scale bars = 5 µm.

3.1.7 Oligodendroglial Adhesion Proteins are Necessary for the Relocation of Axonal Paranodal Adhesion Proteins

Finally, we investigated the localization of Caspr when proteins of both adhesion complexes - of the internodal and the paranodal complex - are lacking to elucidate the importance of the respective complex for the proper sorting of myelin adhesion proteins.

We crossbred *nfascb* $^{+/-}$ and *mag*$^{+/-}$ zebrafish to obtain double mutant zebrafish (*nfascb* $^{-/-}$/ *mag*$^{-/-}$) animals. Our breeding scheme generated 16 different genotypes, which we categorized into four different groups:

1. - double het / double wt / single het + single wt (*nfascb*$^{+/+\,/\,+/-}$/ *mag*$^{+/+\,/\,+/-}$)
2. - nfascb wt/het + mag KO (*nfascb*$^{+/+\,/\,+/-}$/ *mag*$^{-/-}$)
3. - nfascb KO + mag wt/ het (*nfascb*$^{-/-}$/ *mag*$^{+/+\,/\,+/-}$)
4. - double KO (*nfascb*$^{-/-}$/ *mag*$^{-/-}$)

We injected the Caspr-YFP plasmids again and evaluated its localization.

In animals of categories 1 and 2, Caspr-YFP relocated to normal appearing paranodes (Fig. 23 A+B) at 3 dpf and 5 dpf. These results confirm our previous results of Caspr-YFP localization in the spinal cord of wild type and *mag*$^{-/-}$ zebrafish. However, in animals of categories 3 and 4, Caspr-YFP hardly relocated to the paranodes but stayed internodal. These results resemble our previous results on *nfascb*$^{-/-}$ zebrafish (see section 3.1.5). Interestingly, quantification revealed an even stronger effect in double mutant zebrafish when compared to siblings of category 3. The Caspr-YFP distribution in all other categories aligns with our previous results (Fig. 23 C+D). We also checked for "equal distribution" events, where Caspr-YFP continuously spreads along the axon unaffected by myelination. At 3 dpf, we observed these events in the first three categories and less in double KO animals. However, at 5 dpf, most equal distributions were found in nfascb single KO zebrafish (category 3), some in double KO zebrafish (category 4), and only very few in category 1 and 2 zebrafish.

Like in *nfascb*$^{-/-}$ zebrafish, paranodes were not correctly established in double mutant zebrafish, neither at 3 dpf nor at 5 dpf (Fig. 24 A, upper panel + C). When Caspr-YFP was located at the paranodes in double mutant zebrafish, it showed a much larger spread indicating for a failure to condense the paranodal lamellae. Additionally, we detected different phenotypes of internodal Caspr-YFP events in *nfascb*$^{-/-}$/*mag*$^{-/-}$ animals. Besides the previously observed localization at the paranodes and the accumulation along the full length of a myelin sheath, we also saw Caspr-YFP accumulation concentrated in the middle of a myelin sheath (Fig. 24 A). This "internodal condensed" phenotype was mainly found at 3 dpf, hardly at 5 dpf (Fig. 24 C). Interestingly, the intensity maximum of the condensed Caspr-YFP accumulation coincides with the intensity maximum of the oligodendroglial mRFP (Fig. 24 D). The myelin sheath length of internodal accumulated or internodal condensed phenotypes is significantly shorter by $\sim$4 µm at 3 dpf (p=0.01 and p=0.02) and by $\sim$15 µm at 5 dpf (p<0.0001) than events with disturbed paranodal localization (Fig. 24 B). Also in *nfascb*$^{-/-}$/ *mag*$^{-/-}$ we found early accumulation of Caspr-YFP at myelin ensheathment sites (Fig. 24 E).

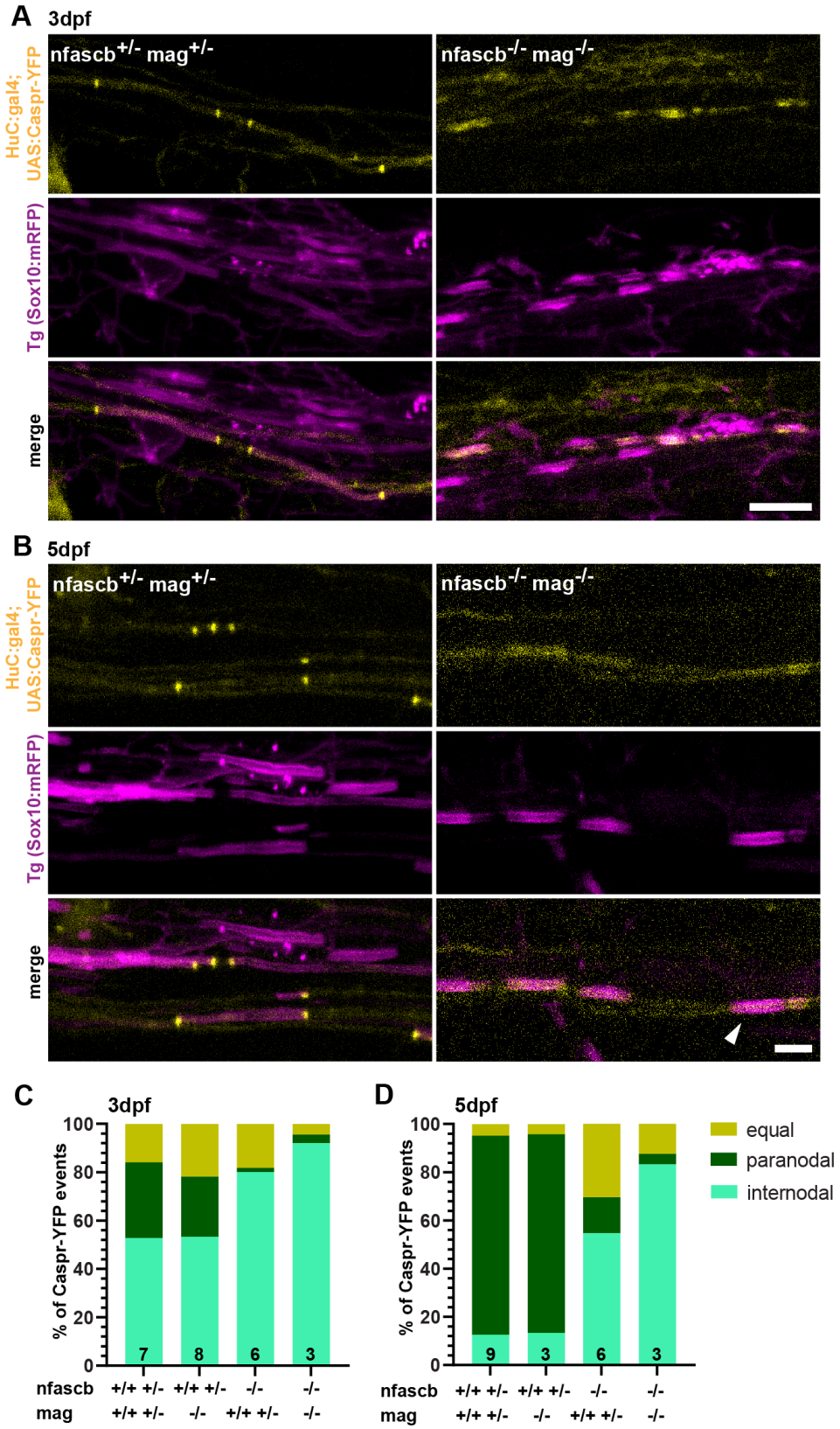

Figure 23: CASPR LOCALIZATION IN NFASCB$^{-/-}$/MAG$^{-/-}$ ZEBRAFISH - PART I Axonal Caspr-YFP (yellow) localization underneath myelin sheaths (magenta) at 3 dpf and 5 dpf in the spinal cord of *nfascb*$^{-/-}$*/mag*$^{-/-}$ or double heterozygous zebrafish larvae **A** Caspr-YFP can relocate to its allocated position at the paranodes in wild type and double heterozygous zebrafish. In contrast, it stays mainly internodal, under the myelin sheaths in zebrafish that lack both Nfasc and MAG at 3 dpf and **B** 5 dpf. Arrowhead points at equal distribution of Caspr under myelin sheath. **C** Graph displays the ratio of different Caspr-YFP events in myelinated areas with internodal and paranodal localization as well as equal Caspr-YFP distribution at 3 dpf and **D** 5 dpf. The numbers in the columns represent the number of sample replicates.

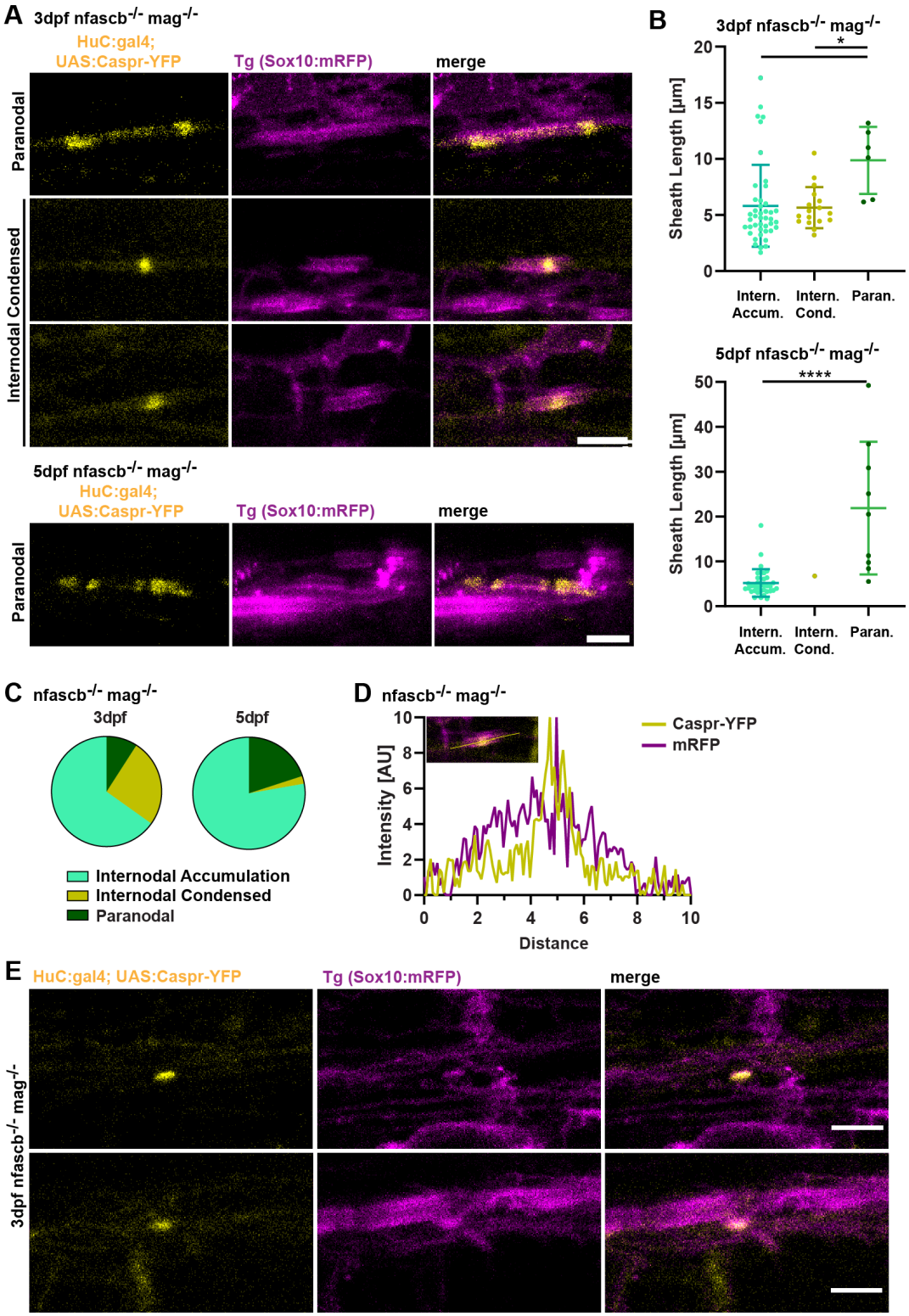

Figure 24: CASPR-YFP LOCALIZATION IN NFASCB$^{-/-}$/MAG$^{-/-}$ ZEBRAFISH - PART II A Specific phenotypes of Caspr-YFP (yellow) localization at 3 dpf and 5 dpf underneath myelin sheaths (magenta) in the spinal cord of *nfascb*$^{-/-}$/*mag*$^{-/-}$ zebrafish larvae. At 3 dpf, we observed enlarged paranodes. In addition, besides the usual internodal accumulation along the full length of a myelin sheath, Caspr-YFP concentrates in the middle of a myelin sheath - "internodal condensed", at some internodes **B** Graph displays the sheath lengths depending on sheath phenotype in *nfascb*$^{-/-}$/*mag*$^{-/-}$ zebrafish at 3 dpf and 5 dpf. Differences were tested with One-way ANOVA with Tukey's multiple comparisons test **C** Pie graphs display ratio of Paranodal, internodal accumulated and internodal condensed Caspr-YFP events in nfascb$^{-/-}$/mag$^{-/-}$ zebrafish at 3 dpf and 5 dpf. **D** Profile plot of Caspr-YFP and mRFP signal intensity across a single myelin sheath. The Caspr-YFP signal intensity peak coincides with the mRFP signal intensity peak **E** Caspr-YFP accumulation at axo-oligodendroglial contact sites - early accumulation. Scale bars = 5 µm.

3.2 Lipidomic and Ultrastructural Changes in Murine CNS Myelin

Most results of this section are also part of the publication "Ganglioside lipidomics of central nervous system myelination using direct infusion shotgun mass spectrometry; Arends et al.", which was submitted to "iScience (Cell press)".

3.2.1 Changes in the Murine Lipidome During Myelin Development

We applied a new direct infusion (shotgun) lipidomics approach developed by our collaborator Lipotype to detect and quantify gangliosides in mouse brain and optic nerve samples by mass spectrometry. To determine the lipidome of the brain and optic nerve of wild type mice during myelin development, we chose an early stage of myelination (P12), a stage at which myelination is almost completed (P21), and the adult stage (6 months), where myelination is fully completed. Internal standards were used to normalize the lipidomic data and determine the absolute quantity of the lipid species. For each lipid, the data were transformed to mol%. P21 and adult brain and optic nerve replicates cluster together in the principal component analyses (PCA), proving consistency as well as reproducibility of our data (Figs. 25 A and 26 A).

We determined the levels of gangliosides for each sample at P12, P21, and adult stage in brain and optic nerve samples (Figs. 25 B and 26 B). The lipidomic ganglioside data was normalized to a GM1 standard and total lipids for each sample. We found many different types of gangliosides in the mouse brain samples (Fig. 25 B). The usual major brain gangliosides GD1 and GT1 are the most abundant, even though their levels drop significantly from P12 to adult stage (*p*-values in Appendix VII). However, GD1 and GT1 subspecies of higher complexity by longer fatty acid carbon chains, more double bonds, and acetylation are rather synthesized at later stages in development. LacCer, the lipid species which all gangliosides derive from (compare Fig. 5), was not detected at any stage. The amounts of some low complex ganglioside species are higher at early (e.g., GD3, GD2, GT2) or later (e.g., GM3) stages in development.

In contrast, in optic nerve samples, we mainly detected the major brain gangliosides GM1, GD1, and GT1 (Fig. 26 B). GD1 is the most abundant ganglioside species in these samples, directly followed by GT1. Some of their subspecies decrease significantly from P12 to the adult stage, e.g., GD1 36:1;2 and GT1 36:1;2. In addition, the low complexity ganglioside GD3 was found at P12, whereas the globo-series ganglioside Gb3 was only discovered at the adult stage.

In general, ganglioside subspecies with shorter fatty acid carbon chains and a lower number of double bonds were preferentially detected at early stages. Vice versa, ganglioside subspecies with longer fatty acid carbon chains and a higher number of double bonds govern the later stages.

We also investigated the occurrence of other lipid species in the brain and optic nerve samples during myelin development (Figs. 25 C and 26 C). Within the group of glycerophospholipids, PC levels decrease significantly during development, while PE O- levels increase in both brain and optic nerve samples (*p*-values in Appendix VII). Cholesterol (Chol), hexosylceramide (HexCer),

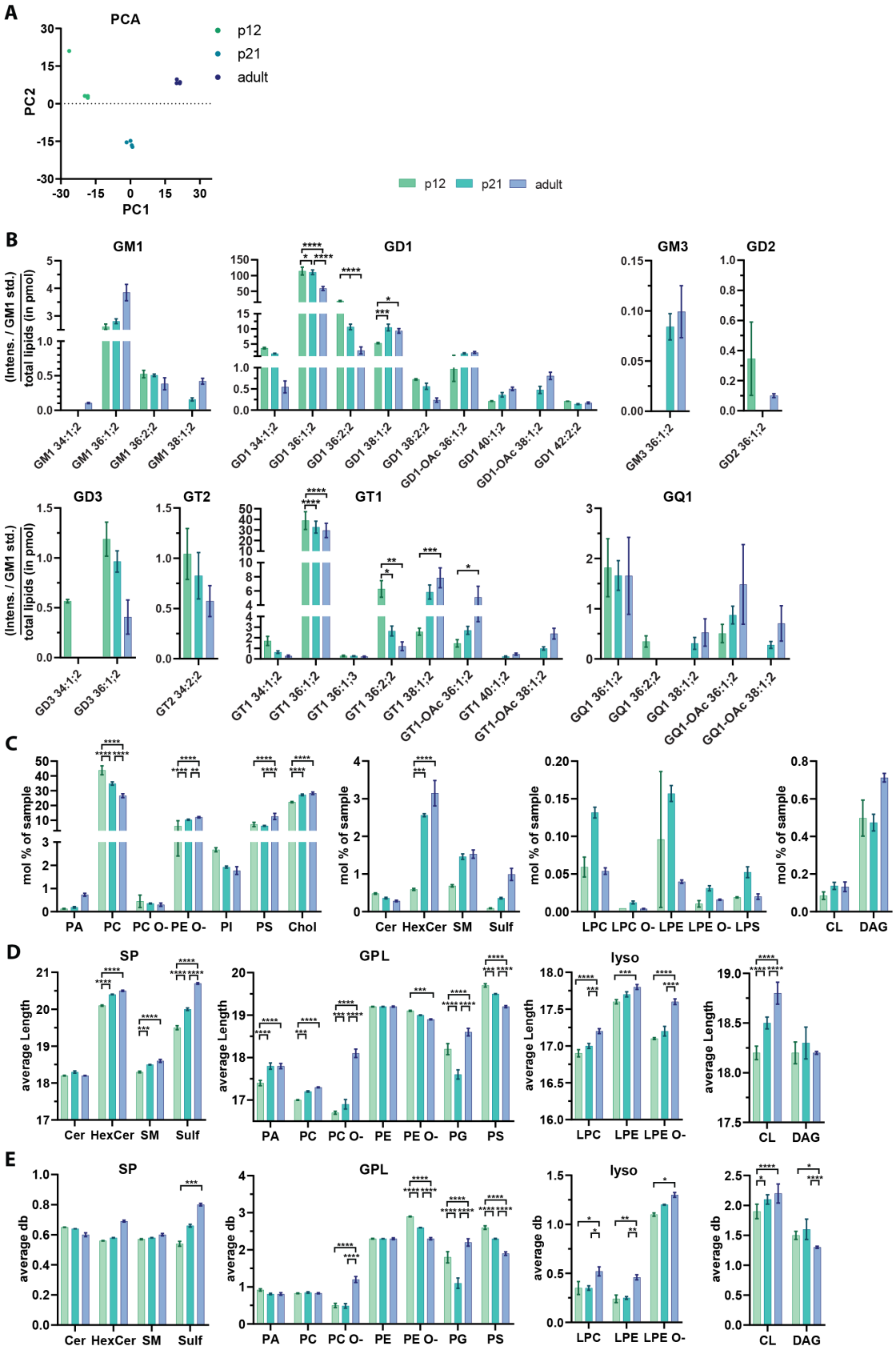

Figure 25: Lipid Composition in the Murine Brain During Development All graphs display lipidomic data of P12, P21, and adult stage mouse brain samples **A** PCA shows clustering of P21 and adult stage samples and a spread in both dimensions for P12 replicates. **B** Ganglioside composition of the above mentioned samples **C** General lipid composition grouped by lipid classes **D** Average length of fatty acid carbon chains grouped by lipid classes **E** The average number of double bonds grouped by lipid classes. Differences between the age groups were tested with Two-way ANOVA with additional Tukey's multiple comparisons test. All graphs represent mean ± SD.

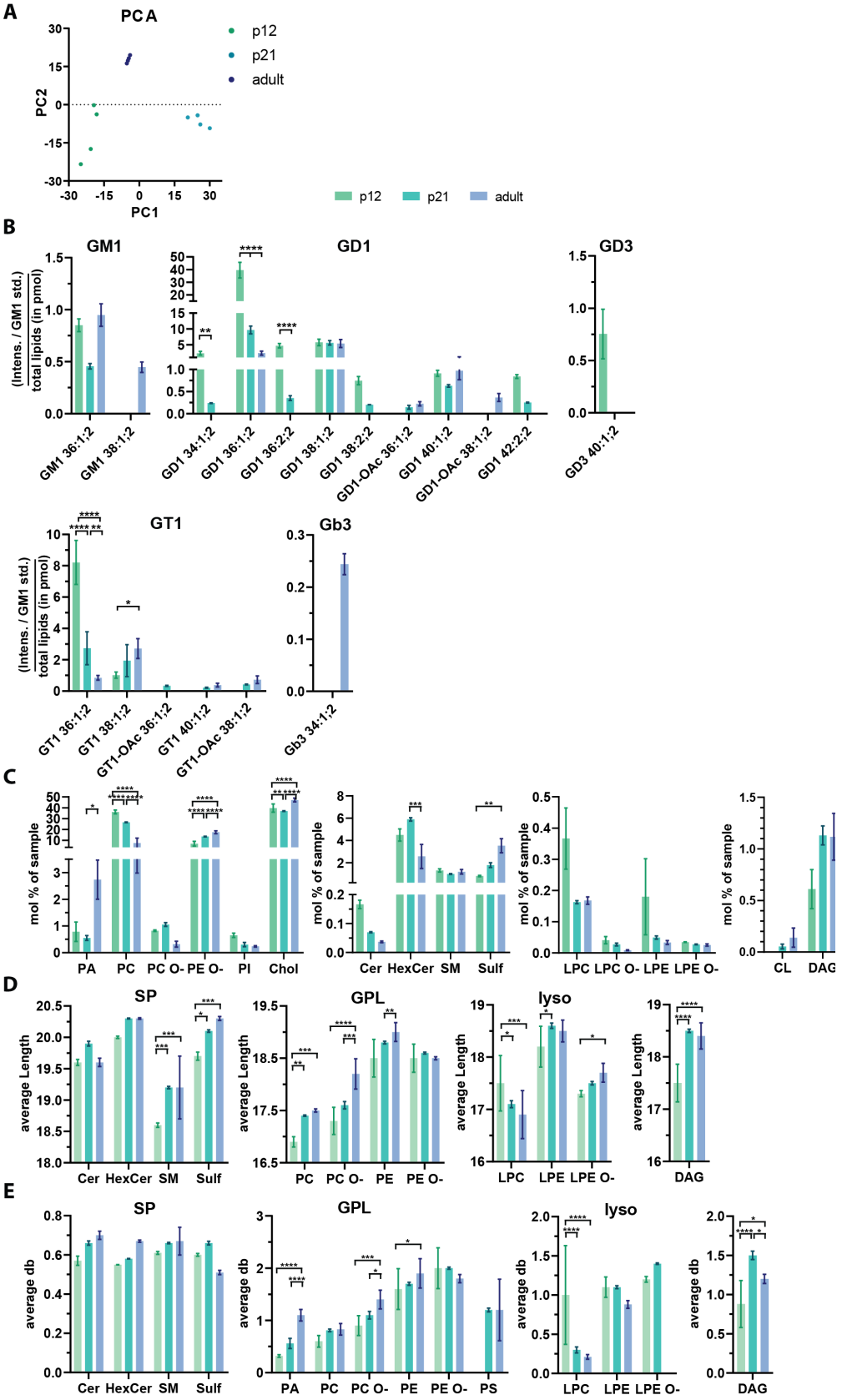

Figure 26: Lipid Composition in the Murine Optic Nerve During Development All graphs display lipidomic data of P12, P21, and adult stage mouse optic nerve samples **A** PCA shows P21 and adult stage samples clustering and a spread in both dimensions for P12 replicates **B** Ganglioside composition in optic nerves **C** General lipid composition grouped by lipid classes **D** Average length of fatty acid carbon chains grouped by lipid classes **E** The average number of double bonds grouped by lipid classes. Differences between the age groups were tested with Two-way ANOVA with additional Tukey's multiple comparisons test. All graphs represent mean ± SD.

and sulfatide (Sulf) levels increase until the adult stage, while Ceramide (Cer) levels decrease during development in both sample types. There is a general trend for all lyso-phospholipid levels to decrease during development, whereas cardiolipin (CL) and diacylglycerol (DAG) levels increase. Specifically in the optic nerve samples, PA levels increase significantly from P21 to the adult stage, whereas PS levels increase significantly during development in the brain samples.

The average length of the fatty acid carbon chain increases in general during development in both sample types, in some lipid species even significantly (Figs. 25 D and 26 D, *p*-values in Appendix VII). Only the average fatty acid carbon chains of PE O- and PS decrease significantly in length. In optic nerve samples only the fatty acid carbon chain length of LPC decreases significantly (Fig. 26 D).

For the average number of double bonds, there is no noticeable general trend throughout development in brain samples (Fig. 25 E). However, in optic nerve samples, the average number of double bonds increases generally during development. For some lipid species, the increase is significant (Fig. 26 E, *p*-values in Appendix VII).

3.2.2 Lipidome of Ganglioside Null Mice

We also analyzed the brain and optic nerve lipidome of ganglioside deficient mice (*ST3GAL5*$^{-/-}$/ *B4GALNT1*$^{-/-}$) in comparison to wild type mice and double heterozygous littermates at P21. Internal standards were used to normalize the lipidomic data and determine the absolute quantity of the lipid species. For each lipid, the data were transformed to mol%.

The PCAs of the brain and optic nerve replicates cluster in each group, proving consistency and reproducibility of our data (Figs. 27 A and 28 A). However, the data of the *ST3GAL5*$^{-/-}$/ *B4GALNT1*$^{-/-}$ spread slightly in both dimensions in the brain and optic nerve data set. Ganglioside null replicates are particularly segregated from wild type and double heterozygous PCA clusters.

Gangliosides were determined in wild type and *ST3GAL5*$^{+/-}$/ *B4GALNT1*$^{+/-}$ samples as intensities of the total lipid content normalized to a GM1 standard and total lipids for each sample. We found high levels of LacCer in ganglioside deficient mice, whereas no LacCer was detectable in wild type or *ST3GAL5*$^{+/-}$/ *B4GALNT1*$^{+/-}$ samples. Gangliosides GD2 and GT2 were detected only in brain samples of double heterozygous samples. The highest levels among all gangliosides were found within the group of GD1 and GT1. GD1 36:1;2, GD1 38:1;2, GT1 36:1;2, and GT1 38:1;2 were the most abundant ganglioside species in both brain and optic nerve samples (Figs. 27 B and 28 B). We also detected comparable low ganglioside levels in *ST3GAL5*$^{-/-}$/ *B4GALNT1*$^{-/-}$ samples among the GM1, GD1 and GD3 and species. Gb4, a member of the globo-series (compare Fig. 5), was detected in double ko brain samples only.

The general lipid composition is very similar across the different genotypes. We detected significant differences only among the glycerophospholipids in both brain and optic nerve samples (Figs. 27 C and 28 C, *p*-values in Appendix VII). Most differences were detected between wild type and double heterozygous replicates, e.g., PC showed lower amounts in the double heterozygous samples. In contrast, PS levels are increased in double heterozygous and *ST3GAL5*$^{-/-}$/ *B4GALNT1*$^{-/-}$ samples. The levels of lysophospholipids in double heterozygous and ganglioside deficient brain samples are decreased, albeit not significantly.

The lipid species' fatty acid carbon chain lengths are similar among the brain and optic nerve sample genotypes. In the brain samples, only PA, PC O-, LPE and DAG show significantly longer fatty acid carbon chains in double heterozygous and ganglioside null animals (Fig. 27 D, *p*-values in Appendix VII). In optic nerve samples, the fatty acid carbon chains increase only in double heterozygous and ganglioside null animals.

The average number of double bonds in the fatty acid carbon chains of all lipid species is similar among the different genotypes and samples (Figs. 27 E and 28 E, *p*-values in Appendix VII). Only PC O- and LPE show significantly more double bonds in their fatty acid chains in the brain samples in double heterozygous and ganglioside deficient samples. For the optic nerve samples, only DAG shows significantly fewer double bonds in its fatty acid chain.

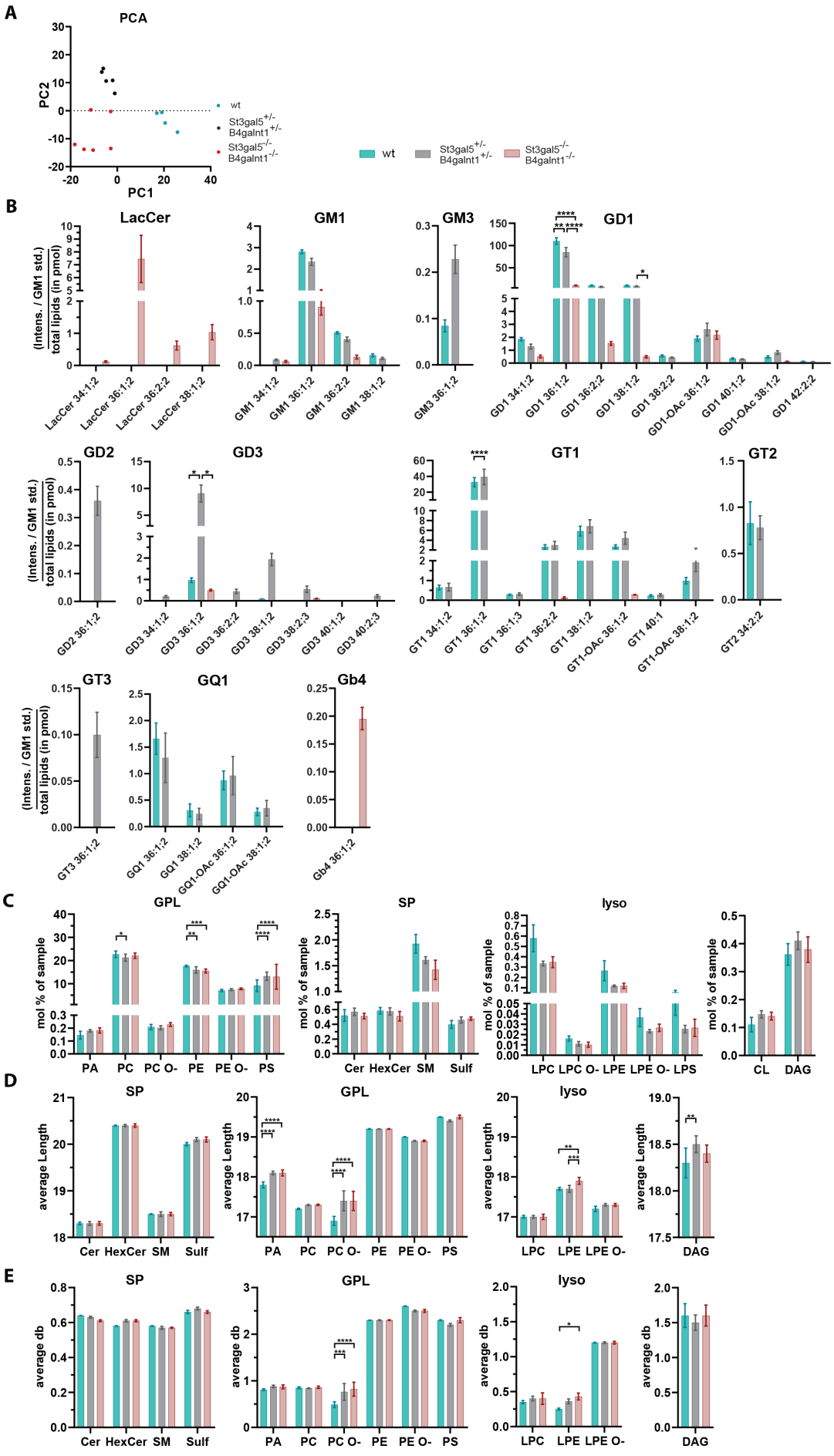

Figure 27: Brain Lipid Composition of P21 Ganglioside Null Mice (Caption next page).

Figure 27: BRAIN LIPID COMPOSITION OF P21 GANGLIOSIDE NULL MICE All graphs display the lipidomic data of *ST3GAL5/ B4GALNT1* double mutant, double het or wild type brain samples **A** PCA shows clustering of wild type and double heterozygous sample groups and a spread in both dimensions for *ST3GAL5*$^{-/-}$/ *B4GALNT1*$^{-/-}$ replicates. **B** Ganglioside composition **C** General lipid composition grouped by lipid classes **D** Average length of fatty acid carbon chains grouped by lipid classes **E** Average number of double bonds of lipids grouped by lipid classes Differences between the genotypes were tested with Two-way ANOVA with additional Tukey's multiple comparisons test. All graphs represent mean ± SD.

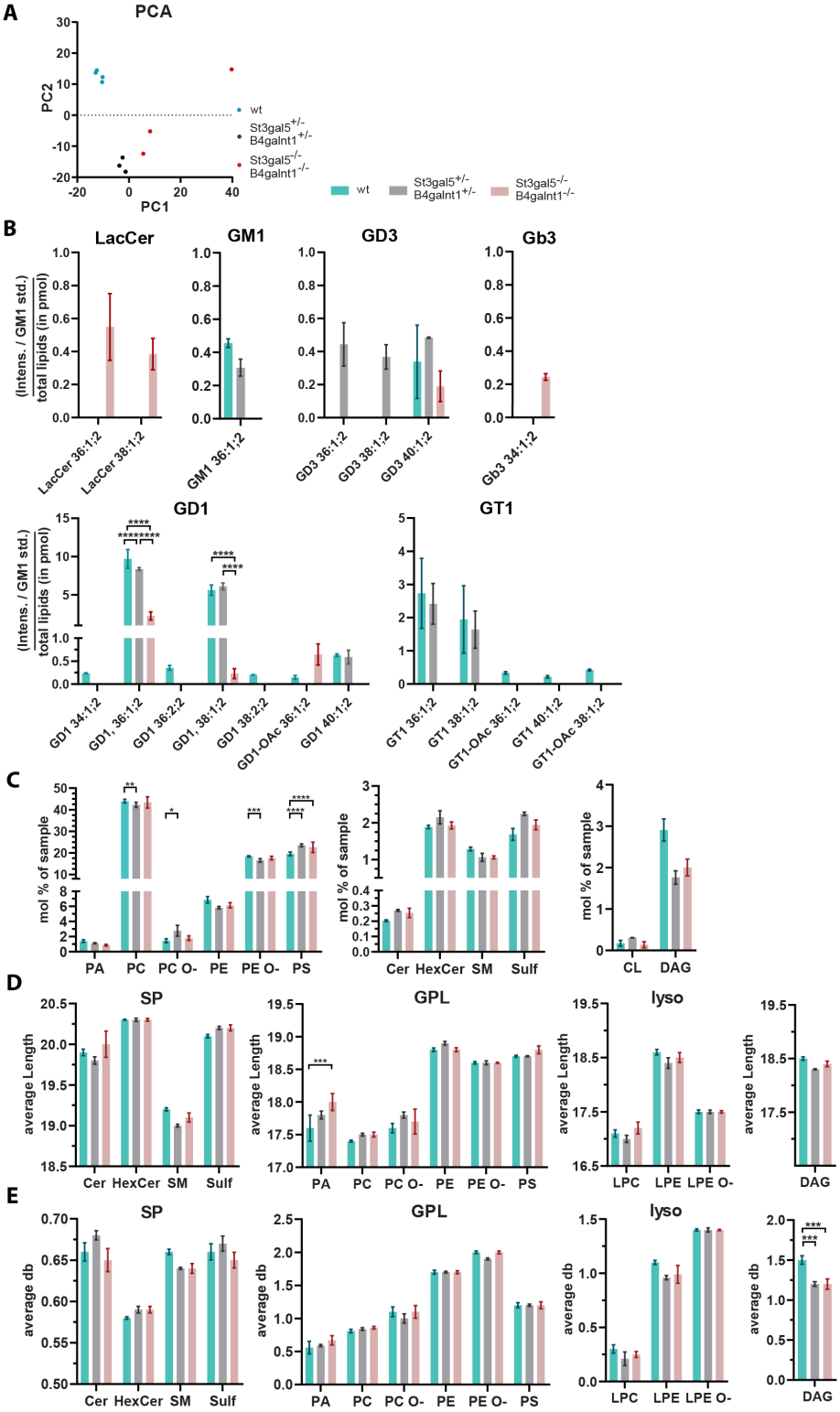

Figure 28: ON LIPID COMPOSITION OF P21 GANGLIOSIDE NULL MICE (Caption next page).

Figure 28: OPTIC NERVE LIPID COMPOSITION OF P21 GANGLIOSIDE NULL MICE All graphs display the lipidomic data of *ST3GAL5*$^{-/-}$ *B4GALNT1* double mutant, double het or wild type brain samples **A** PCA shows clustering of wild type and heterozygous groups and a spread in both dimensions for *ST3GAL5*$^{-/-}$/ *B4GALNT1*$^{-/-}$ replicates **B** Ganglioside composition **C** General lipid composition grouped by lipid classes **D** Average length of fatty acid carbon chains grouped by lipid classes **E** Average number of double bonds grouped by lipid classes. Differences between the genotypes were tested with Two-way ANOVA with additional Tukey's multiple comparisons test. All graphs represent mean $\pm$ SD.

3.2.3 Ultrastructural Analysis Reveals Vacuolization and Hypomyelination in Optic Nerve of Ganglioside Null Mice

We analyzed the myelin ultrastructure of murine *ST3GAL5*$^{-/-}$/*B4GALNT1*$^{-/-}$ optic nerve cross sections at an early stage of myelination (P12, see Appendix III for an image of a P12 *ST3GAL5*$^{-/-}$/*B4GALNT1*$^{-/-}$ phenotype) and a stage where myelination is almost completed (P21). Double heterozygous littermates served as control animals.

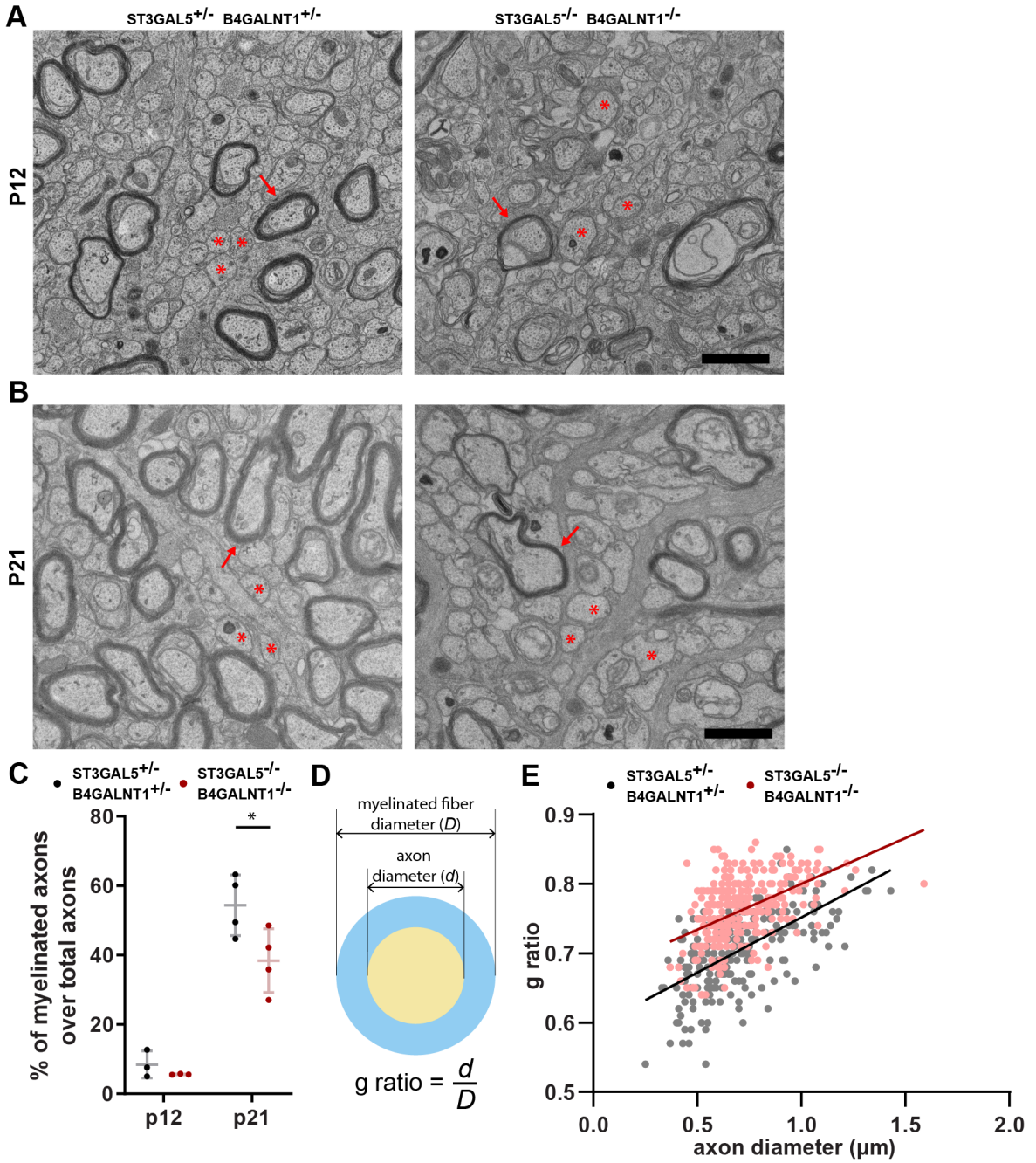

Figure 29: Ultrastructural Analysis of the Ganglioside Null Mouse Optic Nerve A Images show electron microscopy cross sections of the optic nerve of ganglioside heterozygous (left image) and ganglioside null mice (right image) at P12 and P21 (**B**) Arrows hint at examples for myelinated axons, asterisks mark examples for unmyelinated axons. Scale bars = 1 µM **C** Graph display the ratio of myelinated axons over total axons. Mean ± SD is shown. Differences between age groups were tested with unpaired t-test, two-sided. **D** The g ratio is calculated by dividing the axonal diameter by the diameter of the full myelinated fiber. **E** Measured g ratios in mouse optic nerves, Simple linear Regression.

In general, myelinated axons in *ST3GAL5*$^{-/-}$/ *B4GALNT1*$^{-/-}$ develop normally. Double myelination, outfoldings, or degenerated axons does not occur more often in ganglioside deficient mice (data not shown). In addition, we detected no difference in the ratio of unmyelinated to myelinated axons in optic nerve axons at P12 (Fig. 29 A-C). However, hypomyelination in ganglioside null mice was observed at P21. At this age it seems that less axons are myelinated and the myelin shaths appear thinner. Quantification showed that the number of myelinated axons in ganglioside null mice at P21 is indeed significantly reduced (p=0.045) compared to heterozygous littermates (Fig. 29 C-D).

We determined the myelin thickness by measuring the g ratio, which is the ratio of the axonal diameter and the diameter of the entire myelinated axon. At P21, we measured thinner myelin sheaths in ganglioside null mice (g-ratio=0.77) than in double heterozygous littermates (g-ratio=0.71) (Fig. 29E).

3.2.4 Ultrastructural Analysis Shows Slightly Disorganized Paranodes in the Optic Nerve of Ganglioside Null Mice

Previous studies reported disorganized paranodes in ganglioside null mice (Yamashita et al., 2005). However, these observations are based on qualitative results only. A quantitative analysis was lacking. We provide a quantitative analysis of paranodal deficits in *ST3GAL5*$^{-/-}$/*B4GALNT1*$^{-/-}$ mice compared to double heterozygous littermates.

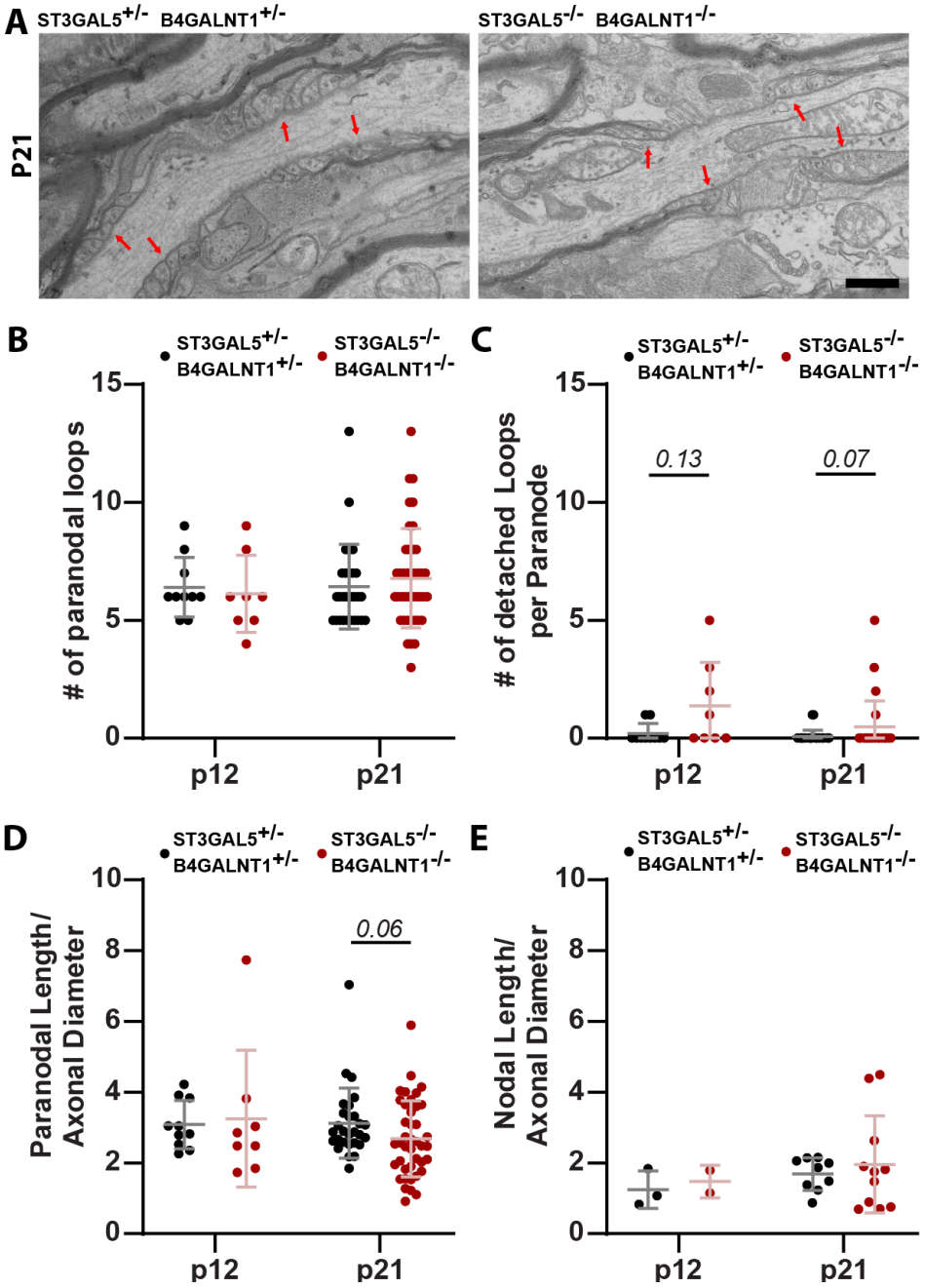

Figure 30: PARANODAL ULTRASTRUCTURE OF THE GANGLIOSIDE NULL MOUSE OPTIC NERVE A Longitudinal sections of the optic nerve of ganglioside het (left image) and ganglioside null mice (right image) at P21 show paranodes. Arrows hint at paranodal loops. Scale bar = 500 nm **B** Number of paranodal loops per paranode **C** Number of detached paranodal loops per paranode **D** Paranodal length divided by the axonal diameter **E** Nodal length divided by the axonal diameter. All graphs show mean ± SD. Differences between genotypes were tested with unpaired t-test, two-sided.

The majority of the paranodes in *ST3GAL5*$^{-/-}$/*B4GALNT1*$^{-/-}$ mouse optic nerves appeared healthy (Fig. 30 A). Nevertheless, there is a non-significant trend for more detached loops per paranode in double KO zebrafish (p=0.13 and p=0.07). We also measured a non-significant trend for a smaller paranodal length per axonal diameter at P21 within this genotype (p=0.06, Fig. 30 D). The nodal length per axonal diameter did not differ between the genotypes (Fig. 30 D). At P12, we found mostly hemi-nodes. Hence, a thorough analysis was not possible at this age.

4 Discussion

4.1 Paranodal Adhesion Proteins accumulate and Relocate to Paranodes During Myelination

Nfascb, Cntn (Cntn1b), and Caspr are part of the adhesion complexes that anchor myelin sheaths to axons at the paranodes. Another additional axo-oligodendroglial adhesion complex is established by the interaction of oligodendroglial Mag with axonal gangliosides, more precisely GD1a and GT1b. This complex is located at internodes.

In our previously published study, we proposed a model where adhesion complexes are necessary for the initiation of axo-glial interaction, the guidance of the myelin inner tongue around the axon, and the anchoring of the oligodendroglial paranodal loops to the axonal membrane [Djannatian et al., 2019]. However, it remained unclear how these molecules are exactly involved in the processes mentioned above and which proteins are involved at which time. This part of the thesis aimed to develop a model that exemplifies each molecule's location and function during myelination. Fig. 35 summarizes our model. We identified four different stages of adhesion protein relocation. Each stage is described and discussed in detail in the following section.

4.1.1 Stage 1: Caspr Accumulates upon Early Axo-Oligodendroglial Interaction

Zebrafish feature a fast-developing central nervous system, which can be observed by confocal time-lapse imaging. We took advantage of this animal model for our experiments. Using Caspr-YFP, we investigated the location dynamics of the paranodal adhesion protein Caspr during myelination.

We expected to see Caspr-YFP distributing equally along the axon, only accumulating upon establishment of paranodes. To our surprise, we observed axonal Caspr-YFP accumulating from the earliest possible stage of myelination, the first contact of an oligodendrocyte process with an axon. We further observed an accumulation of Caspr underneath developing myelin sheaths. Later in development, it relocates to its final position at the paranodes. This unexpected observation shows the involvement of a paranodal protein in the very initial axo-oligodendroglial interaction. However, while we observed *in vivo* Caspr accumulation and relocation in zebrafish for the first time, Eisenbach et al. [2009] reported it in cocultures of dorsal root ganglion neurons and oligodendrocytes. In line with this study, we did not observe intrinsic axonal Caspr accumulation before oligodendroglial contact. Hence, we suggest that tethering glial processes to the axonal membrane is Caspr's primary function. However, the necessity of recruiting/ adhesive factors on axonal membranes to initiate myelination remains questionable. Myelination in the absence of axonal molecules has been proven using nano- or microfibers and cultured oligodendrocytes,[Lee et al., 2012; Bechler et al., 2015]. However, we assume in accordance with Eisenbach et al. [2009] that an oligodendroglial counterpart interacting with Caspr is necessary for axonal Caspr accumulation.

It was previously reported that Caspr depends on Cntn to leave the endoplasmic reticulum and travel to the axonal membrane [Faivre-Sarrailh et al., 2000; Rios et al., 2000; Bonnon et al., 2003, 2007]. Therefore, we can assume that Caspr-YFP at axonal membranes is in contact with Cntn, forming the Caspr/Cntn complex. The most apparent early-stage oligodendroglial interaction partner to this axonal complex would have been Nfascb, as it was already shown to be the Caspr/Cntn interaction partner at paranodes [Charles et al., 2002; Sherman et al., 2005; Pillai et al., 2009; Eisenbach et al., 2009; Pedraza et al., 2009; Volkmer et al., 1998; Marcus and Popko, 2002]. Using a Nfascb-GFP construct expressed in oligodendrocytes, we observed a similar accumulation pattern at myelin sheaths *in vivo* as for Caspr-YFP. This result suggested an early interaction of oligodendroglial Nfascb with Caspr and an early establishment of the paranodal Nfascb/Caspr/Cntn adhesion complex. Unfortunately, Nfasc-GFP expression rates were low, and it was impossible to conduct quantitative analyses. We also did not observe Nfasc-GFP accumulation upon initial axon-oligodendroglial interaction (which does not disapprove of the existence).

Nevertheless, we were surprised to find Caspr accumulating at the earliest possible stage of myelination in *nfascb*$^{-/-}$ zebrafish. Thus, our results do not approve the results from Eisenbach et al. [2009] and Pedraza et al. [2009], who found that CASPR accumulation requires NFASC155 in murine cell cultures. However, it is in line with Gollan et al. [2003] who found the CASPR/CNTN1 complex not interacting with the extracellular domain of NFASC155. At least in zebrafish, another or an additional molecule is probably involved in the early accumulation of Caspr.

In case of inappropriate myelination, oligodendrocytes can retract their processes, even after interacting with the Caspr/Cntn complex [Czopka et al., 2013; Liu et al., 2013]. We observed retractions with a fluctuating Caspr-YFP signal intensity, where Caspr-YFP first accumulates and then diminishes until a small accumulation stays at the leftovers of a myelin sheath. Hence, the interaction of the unknown molecule on the oligodendrocyte process with the axonal Caspr/Cntn complex is presumably reversible. However, the observation of retraction dynamics is a side note of this thesis and was not investigated further. An engulfment of myelin by microglia should also be taken into consideration as a mechanism to remove improperly developed myelin sheaths [Hughes and Appel, 2020].

Another potential oligodendroglial candidate that could interact with the axonal Caspr/Cntn complex, suggested by Eisenbach et al. [2009] is oligodendroglial Cntn. Interestingly, CNTN1 is expressed not only in neurons but also in oligodendrocyte-lineage cells and found in insoluble myelin fractions [Koch et al., 1997; Krämer et al., 1997; Çolakoğlu et al., 2014]. Homophilic *in trans* interactions have been shown for CNTN2, which resembles the extracellular domain of CNTN1. Most likely axonal CNTN1 also interacts homophilic *in trans* with oligodendroglial CNTN1 [Freigang et al., 2000; Kunz et al., 2002]. However, in *cntn1b*$^{-/-}$ zebrafish with neuronal Cntn1b rescue, we observed early and internodal Caspr-YFP accumulation in axons again. This result is in line with Eisenbach et al. [2009], who observed CASPR clustering in axons that were in contact with CNTN1 lacking oligodendroglial processes. Therefore it is very likely that oligodendroglial Cntn does not accumulate axonal Caspr-YFP.

Our experiments in *cntn1b*$^{-/-}$ zebrafish not only excluded Cntn as a potential Caspr-YFP accumulating molecule, but we also confirmed the Cntn dependence of Caspr observed by Faivre-Sarrailh et al. [2000]; Rios et al. [2000]; Bonnon et al. [2003, 2007]. We observed Caspr being locked in some neuronal cell bodies, most likely in those where Cntn was absent due to mosaic expression of the neuronal Cntn1b rescue. Interestingly, a loss of Cntn in oligodendrocytes alone seems to allow for neuronal cell body myelination, which we also previously observed in full-body KO animals [Djannatian et al., 2019]. We even observed a Caspr accumulation line along the edges of myelin sheaths on the myelinated neuronal cell body. However, these observations need to be quantified for robust conclusions.

As no oligodendroglial molecule could be identified as the early Caspr/Cntn interaction partner, another known or unknown attraction molecule has to be found (Fig. 31). Eisenbach et al. [2009] propose that Nfasc155 is necessary but not sufficient for axonal Caspr clustering. The exact molecular interaction mechanism of Nfasc155 (Nfascb) with the Caspr/Cntn complex is not yet known. The unknown molecule either interacts with Nfasc155 (Nfascb) or hands axonal Caspr over to it.

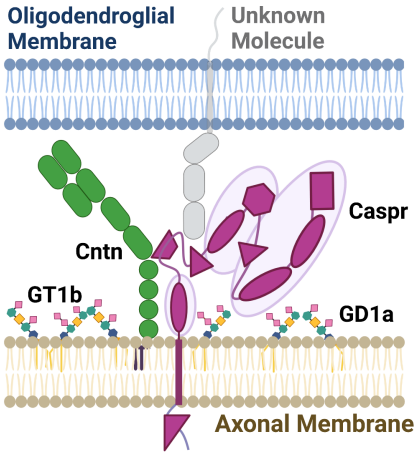

Figure 31: THE UNKNOWN CASPR ACCUMULATING MOLECULE A yet unknown oligodendroglial molecule attracts the Caspr/Cntn complex in the axonal membrane. Whether it interacts with Caspr or Cntn is not yet clear.

The myelin protein composition of zebrafish differs slightly from the mammalian one. Zebrafish have a few myelin proteins that are absent from mammalian myelin and vice versa [Siems et al., 2021]. At least some of these proteins are thought to maintain membrane fluidity of myelin in a poikilothermic environment [Schaefer and Brösamle, 2009; Ackerman and Monk, 2016]. In our experiments, one of these zebrafish-specific proteins may serve as an interaction partner for the Cntn/Caspr-YFP complex. Siems et al. [2021] provided a recent proteome profile of zebrafish myelin, from which potential candidates could be identified. However, the majority of the zebrafish myelin proteome (∼60%) is made up of unknown proteins. Experiments in rodent models and/or primary cell cultures are necessary to confirm early Caspr/Cntn accumulation, help identify a potential oligodendroglial interaction partner, and exclude the possibility that the Caspr accumulation that we observed is not restricted to zebrafish and initiated by a zebrafish-specific myelin protein.

However, as mentioned by Almeida [2018], our current knowledge of myelin adhesion proteins, especially in zebrafish, is not good enough to point directly at potential candidates as unknown oligodendroglial Caspr interaction partners.

We observed axonal Caspr-YFP accumulation from the first contact of oligodendroglial processes but could not identify an oligodendroglial interaction partner. More testing of potential candidates is necessary to identify the Caspr/Cntn accumulating molecule.

4.1.2 Stage 2: Mag-Ganglioside Interactions Deplete Extracellular Axonal Proteins

Gangliosides are enriched in neurons. They interact *in cis* with each other and *in trans* with oligodendroglial Mag, which is present at the myelin internode, forming a permissive surface (Fig. 32). We hypothesized that the interaction of axonal gangliosides with oligodendroglial Mag indirectly protrudes the Caspr/Cntn adhesion complex from its initial internodal position to its final position at the paranodes.

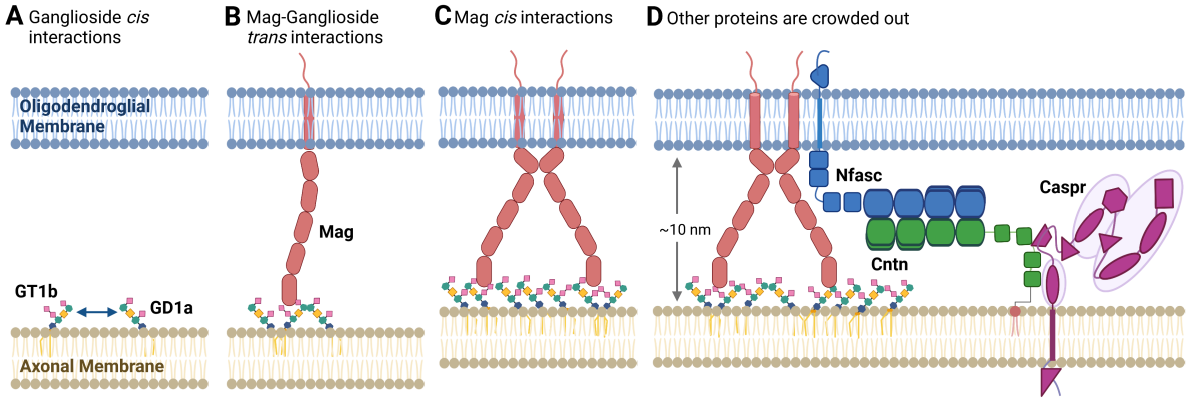

Figure 32: INTERNODAL MAG-GANGLIOSIDE INTERACTIONS A Gangliosides in the outer leaflet of the axonal lipid bilayer interact in *cis* with each other. **B** Oligodendroglial Mag interacts in *trans* with gangliosides. **C** Mag constitutes duplicates by *cis* interactions in the oligodendroglial membrane. **D** Mag and gangliosides form a permissive surface underneath a myelin sheath which excludes/ crowds out (paranodal) proteins from the internode.

We used specifically designed extracellular GFPs to observe their localization within the axonal membrane. GFPs by themselves are inert proteins [Jensen, 2012]. They do not interact with other molecules. Therefore, indirect forces within the axonal membrane would be necessary to move and relocate the GFPs. Extracellular attraction by oligodendroglial processes is excluded.

We found the extracellular, membrane-anchored GFPs depleted from the axonal membrane in myelinated areas. No external GFP construct accumulated in the internodal area, whether anchored to the membrane by a GPI-anchor or a transmembrane domain. The proteins were either excluded from the internodal area, or their entry into this area was indirectly blocked.

We then elucidated the localization of extracellular membrane-associated axonal GFPs in *mag*$^{-/-}$ or sphingolipid-depleted zebrafish. The extracellular GFPs entered the internodal area in *mag*$^{-/-}$ zebrafish, whereas they stayed slightly excluded from the internodal area when sphingolipids were lacking (Fig. 33). Therefore, Mag seems to be a more important factor within this structure than

sphingolipids. It seems possible that Mag crowds out the external GFPs from the internodal area simply by its size and location at the periaxonal oligodendroglial membrane.

Next, we investigated the localization of Caspr-YFP to paranodes in the absence of sphingolipids and Mag and found it less located to paranodes only in sphingolipid depleted zebrafish larvae (Fig. 34). For *Mag*$^{-/-}$ mice it was reported that Caspr did not locate well to the paranodes [Marcus et al., 2002]. However, contradictory to this study and our results on membrane-associated GFPs, we observed that Caspr-YFP relocates well from the internodal to the paranodal area in *mag*$^{-/-}$ zebrafish. Nevertheless, in the course of development, relocation to paranodes is slightly delayed compared to wild type zebrafish. This has already been reported in murine *Mag*$^{-/-}$ models [Montag et al., 1994], along with deficits in the CNS like axonal and myelin degeneration in adult *Mag*$^{-/-}$ mice [Li et al., 1994; Fruttiger et al., 1995]. However, considering the shorter myelin sheath length and the delay in development in *mag*$^{-/-}$ zebrafish, Mag seems supportive for myelination. In mice, MAG seems to have a more important role in the relocation of paranodal adhesion proteins. In contrast, the results on Caspr-YFP localization in sphingolipid-depleted zebrafish indicate that sphingolipids play an important role in the relocation of Caspr to paranodes.

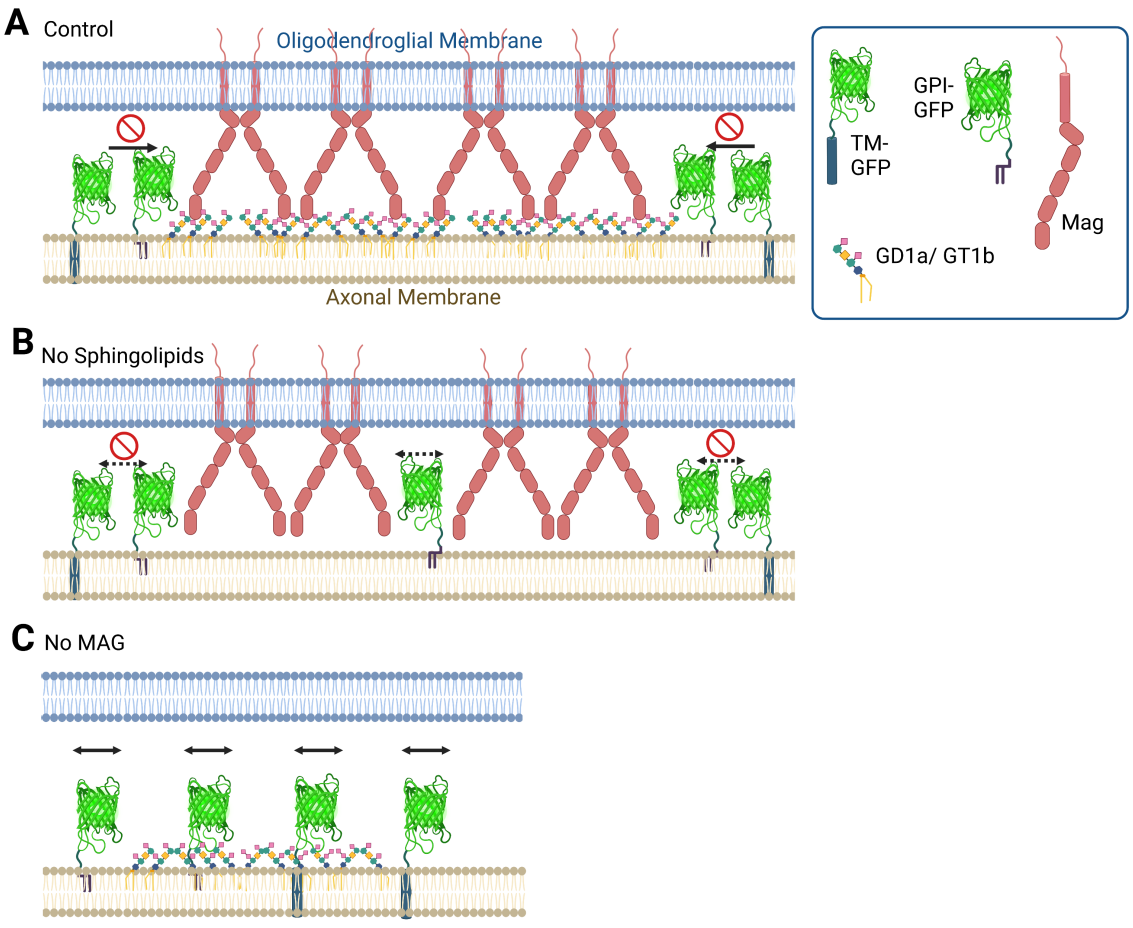

Figure 33: Summary of Results on Membrane-Associated GFP Localization in the Absence of Sphingolipids or Mag A Mag and Gangliosides form a structure underneath a myelin sheath which crowds out extracellular membrane-associated GFPs from entering the internode. **B** In the absence of sphingolipids, including gangliosides, extracellular membrane-associated GFPs enter the internodal area to a low extent. **C** In the absence of Mag, extracellular membrane-associated GFPs can enter the internodal area.

We confirmed our results in the murine animal model. In a ganglioside deficient mouse line, we found Caspr hardly detectable at paranodes hinting again towards gangliosides as a factor for Caspr relocalization.

GFPs that are extracellularly attached to the axonal membrane can enter the internodal area when Mag is absent, while the relocation of Caspr-YFP, which is a much larger protein, is unaffected. These results might seem contradictory at first glance. However, these two experiments are not comparable due to the nature of the used markers. The membrane-associated GFPs are inert, while Caspr-YFP interacts with oligodendroglial Nfascb, axonal Cntn, and probably with another yet unknown molecule, which lets Caspr accumulate internodal. These results additionally stress the need for an oligodendroglial Caspr interaction partner, which attracts and accumulates Caspr internodal.

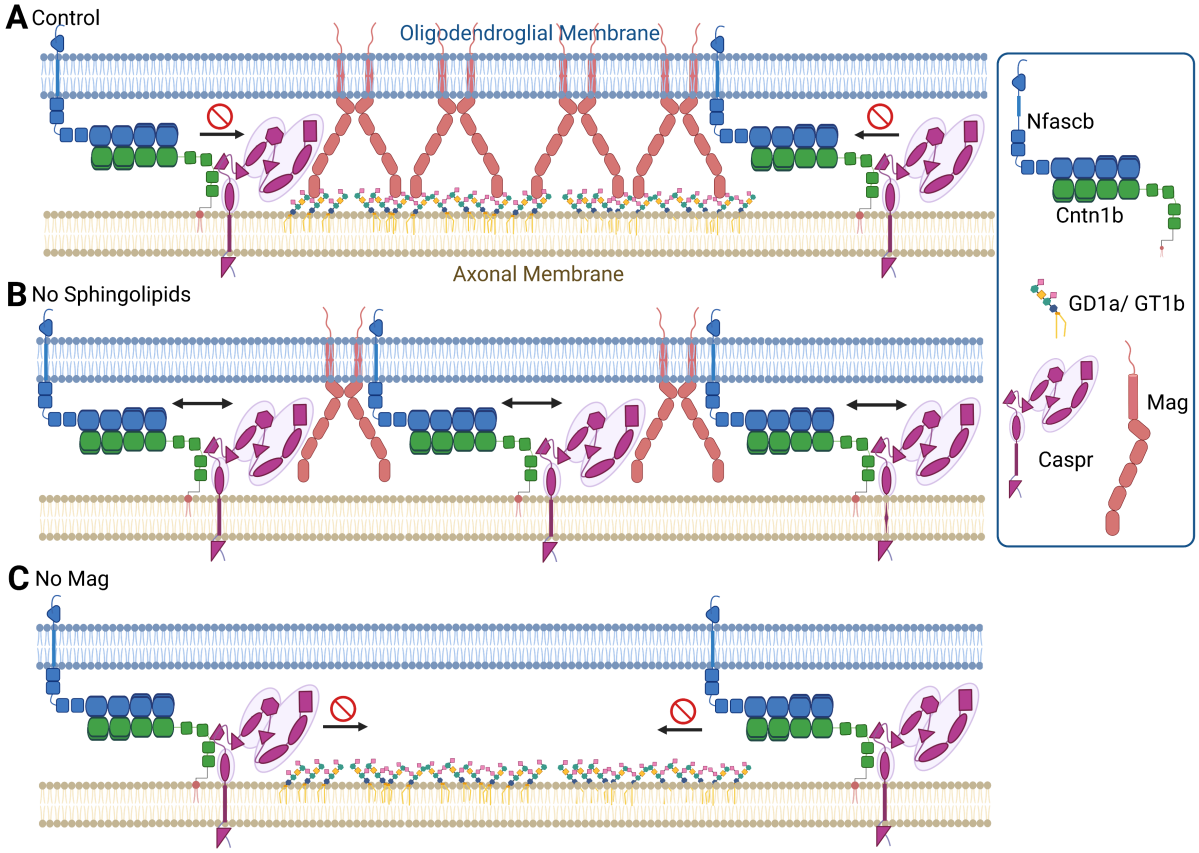

Figure 34: Summary of Results on Caspr-YFP Localization in the Absence of Sphingolipids or Mag A Mag and Gangliosides form a structure underneath a myelin sheath, thus excluding Caspr-YFP from entering the internodal area. **B** In the absence of sphingolipids, including gangliosides, some Caspr-YFPs can enter the internodal area. **C** In the absence of Mag, Caspr-YFP is still excluded internodal and relocated to paranodes.

4.1.3 Stage 3: Nfasc Relocates Caspr/Cntn to Paranodes

As our previous results uncovered that an additional molecule is involved in Caspr relocation, we investigated the role and importance of oligodendroglial Nfascb on Casor relocation in zebrafish.

In *nfascb*$^{-/-}$ zebrafish, we observed Caspr-YFP hardly relocating from internodes to paranodes. While we detected very few paranodes, they did not show proper, dense, and clearly defined

paranodal Caspr-YFP localization. In fact, the Caspr-YFP signal at paranodes in *nfascb*$^{-/-}$ zebrafish axons is spread in a large area. Considering the low amount of relocated Caspr-YFP and the incorrectly formed paranodes, Nfascb seems vital in relocating Caspr to paranodes. Our observation that Nfascb-GFP in the myelin membrane also relocates from the internode to paranodes further supports its role in Caspr/Cntn relocation. Additionally, previous studies confirmed our data, which indicate that Caspr and Nfasc coalesce before they relocate to the paranodes [Pedraza et al., 2009; Hivert et al., 2016; Eisenbach et al., 2009].

However, it is not clear how Nfascb (NFASC155) relocates the Caspr/Cntn complex to the paranodes. One possibility is the involvement of the oligodendroglial cytoskeleton for Nfascb relocation. Being transmembrane proteins, both NFASC186 and NFASC155 contain a FIGQY motif in their cytoplasmic domain [Ogawa et al., 2006; Pomicter et al., 2010], which interacts with Ankyrins [Bennett and Lorenzo, 2013]. The phosphorylation state of the FIGQY motif regulates its binding activity to ankyrin G for NFASC186 [Garver et al., 1997; Tuvia et al., 1997]. A similar mechanism can be assumed for NFASC155. Hence, the Nfascb/Caspr/Cntn relocation could be mediated via the actin cytoskeleton, as ankyrins interact with the actin cytoskeleton via spectrin binding as suggested by Ogawa et al. [2006] and Bennett and Lorenzo [2016]. As actin filament (de-) polymerization is the driving force for the wrapping movement of the myelin inner tongue [Nawaz et al., 2015], the actin cytoskeleton may also drive Nfascb/Caspr/Cntn to the edges of the myelin inner tongue. With the next wrap, this complex would be separated from the inner tongue and form a paranodal loop.

Another possible mechanism is similar to the *cis* ganglioside interaction in the axonal membrane. Myelin consists of a large amount of long fatty acid carbon chains containing galactosylceramides and sulfatides [Aggarwal et al., 2011], which were shown to self-aggregate in myelin membrane-mimicking GUVs [Yurlova et al., 2011]. We follow up with a suggestion from Marcus and Popko [2002] and propose that self-aggregation of myelin sphingolipids could form a rigid structure in the membrane at the tip of the oligodendroglial cell process, which also contains Nfascb. Indeed, Schafer et al. [2004] found NFASC155 in insoluble membrane fractions. While the myelin inner tongue moves forward, the lipid bilayer at its tip restructures, and the Nfasc/Caspr/Cntn adhesion complex, embedded in sphingolipids, is pushed passively to the edges of the myelin inner tongue. The next myelin wrap, like with the first above proposed mechanism, turns the edges of the myelin inner tongue into a paranodal loop with the paranodal adhesion complex already being in place. McGonigal et al. [2019] published a thorough study with mice incapable of synthesizing either sulfatides, gangliosides, some ganglioside species, or none of them. The most severe phenotype was described with severely disturbed paranodes, axonal degeneration, vacuolization, and reduced neuronal conduction velocity in mice that lacked sulfatides and gangliosides. Mice lacking gangliosides developed almost normal paranodes, while the phenotypes in between showed different levels of severity [McGonigal et al., 2019; Bonetto and Di Scala, 2019]. Their results hint at a potential regulation of Nfasc/Caspr/Cntn location and function by sphingolipids [McGonigal et al., 2019; Bonetto and Di Scala, 2019]. Whether they do this by directly interacting with these proteins or indirectly stabilizing them remains unclear.

In addition, we need to understand the exact interaction mechanism of Nfascb with the Caspr/Cntn complex. For example, which domains are involved in this contact [Schafer et al., 2004; Bonetto and Di Scala, 2019]? Our knowledge in this matter is limited because of the insolubility of the interaction complex - CASPR, CNTN, and NFASC155 were always found in co-fractions [Menon et al., 2003]. It is likely that NFASC155 interacts with CNTN and not directly with CASPR as a single study proposes [Thaxton et al., 2010]. Summing up, as Schafer et al. [2004] also already suggested, we propose that Nfascb (NFASC155) probably interacts with a yet unknown molecule. It is also possible that the unknown - probably also Caspr or Cntn attracting - molecule hands the Caspr/Cntn complex over to Nfascb.

Our data showed that Nfascb (NFASC155) relocates the Caspr/Cntn adhesion complex from the internode to the paranodes, anchoring the myelin membrane to the axon. The exact mechanism needs to be the subject of further investigations. However, this mechanism might need axonal facilitators - one of them being the earlier mentioned internodal Mag-ganglioside interactions.

4.1.4 Stage 4: Both Internodal and Paranodal Adhesion Complexes are Necessary for The Establishment of Paranodes

Finally, we also investigated the Caspr-YFP localization dynamics when both paranodal and internodal adhesion complexes are lacking. *Nfasc*$^{-/-}$*/mag*$^{-/-}$ double mutant zebrafish do not express the oligodendroglial adhesion proteins, which constitute paranodal and internodal adhesion complexes. We found that a lack of both complexes aggravates the previously observed inability of Caspr to relocate from the internode to the paranodes in *nfasc*$^{-/-}$ single mutant zebrafish. While we found Caspr-YFP relocation to paranodes only slightly delayed in *mag*$^{-/-}$ zebrafish, relocation was barely happening in *nfascb*$^{-/-}$ zebrafish. In double mutant zebrafish, Caspr-YFP relocated even less to paranodes. We also found that Caspr-YFP not only stayed accumulated at the internodes but also condensed in the middle of some developing myelin sheaths. This phenotype's axonal Caspr-YFP signal intensity peak coincides with an oligodendroglial mRFP signal intensity peak. Presumably, Caspr-YFP stays at the myelin inner tongue in double mutant zebrafish.

The internodal adhesion complex consisting of Mag and gangliosides may compensate to a low extent for the lack of Nfascb and crowd out Caspr-YFP to the paranodes. A removal of Mag then leads to a complete failure of the Caspr-YFP relocation mechanisms. Caspr stays internodal, very often supposedly at the myelin inner tongue.

Caspr (CASPR) is a transmembrane protein (Fig. 6 A) [Menegoz et al., 1997; Peles et al., 1997]. It interacts with the axonal cytoskeleton via its intracellular GNP domain and binding to protein 4.1B, a mediator for tethering membrane proteins to the cytoskeleton. Thus, Caspr arranges an axonal domain organization which enables saltatory conduction [Denisenko-Nehrbass et al., 2003; Buttermore et al., 2011; Einheber et al., 2013]. Summarizing our and previous results, it is likely that the paranodal adhesion complex is pushed and/or pulled to its functional position by oligodendroglial elements [Chang et al., 2014; McGonigal et al., 2019] as well as by the axonal cytoskeleton [Brivio et al., 2017]. However, as the paranodal connection to the oligodendroglial cytoskeleton gets lost with a lack of Nfascb, the axonal cytoskeleton's longitudinal push/pull mechanism is probably not strong enough to govern the establishment of paranodes. We observed

much shorter myelin sheaths in *nfasc*$^{-/-}$/*mag*$^{-/-}$ double mutant zebrafish within the phenotypic classes of internodal condensed or accumulated Caspr-YFP compared to those sheaths with unusual paranodes. Hence, the axonal cytoskeleton seems less critical for Caspr relocation than oligodendroglial factors.

These findings are in line with a study from Denisenko-Nehrbass et al. [2003]. They reported a regulated binding of protein 4.1B to CASPR2 only after it reached its final position at the juxtaparanode. Their results suggest a role for the axonal cytoskeleton in stabilizing paranodes, not in the localization of paranodal proteins. A potential oligodendroglial mechanism and our proposed internodal MAG-ganglioside interactions are probably the only Caspr/Cntn localization mechanisms.

4.2 Gangliosides Maintain the Integrity of Myelinated Fibers

The analysis of gangliosides and the investigation of their role in the nervous system is currently limited by the lack of suitable, easily applicable, and high-throughput methods. We analyzed the brain and optic nerve of ganglioside null mice by electron microscopy and used these mice to validate a newly developed shotgun lipidomics method.

4.2.1 Neurodegeneration in the *ST3GAL5*$^{-/-}$/ *B4GALNT1*$^{-/-}$ Mouse CNS at P21

Gangliosides, which are specifically enriched in neurons, are considered to be involved in axon-myelin interactions via *in trans* binding to Myelin-associated Glycoprotein (MAG) [Yang et al., 1996b; Collins et al., 1997; Vinson et al., 2001; Vyas et al., 2002; Pronker et al., 2016]. Previous studies on the CNS structure and ultrastructure showed white matter vacuolization in the cerebellum and the spinal cord of ganglioside null mice, axonal degeneration, and disorganized paranodes Yamashita et al. [2005b]. However, as Yamashita et al. [2005b] used 1.5-3 months old animals, it remains unclear if the reported deficits result from defective myelin generation or myelin degeneration. In optic nerves of 3-4 months old *B4GALNT1*$^{-/-}$ mice, Sheikh et al. [1999] found more unmyelinated and degenerated axons compared to wild type mice stating the need for gangliosides in myelin maintenance. Considering previous results on the CNS structure in *B4GALNT1*$^{-/-}$ and in ganglioside null mice and the fact that the optic nerve consists mainly of axons and oligodendrocytes, we expected to observe significant myelin defects in the ultrastructure of the optic nerve. We hypothesized that gangliosides provide a platform for the initial oligodendroglial attachment via MAG and are therefore necessary for myelination.

Unexpectedly, our ultrastructural analysis revealed no deficits in axon-myelin interactions at a very early stage of myelination (P12) in optic nerves of *ST3GAL5*$^{-/-}$/ *B4GALNT1*$^{-/-}$ mice. In contrast, when myelination progressed further (P21), we observed hypomyelination and a non-significant tendency for disorganized paranodes pointing towards a role for gangliosides in myelin maintenance as was previously described by Sheikh et al. [1999] for *B4GALNT1*$^{-/-}$ mice. At both time points, no myelination defects like outfoldings or double myelination were detected.

While disorganized paranodes in *ST3GAL5*$^{-/-}$/ *B4GALNT1*$^{-/-}$ mice have been observed in a previous study (Yamashita et al., 2005), hypomyelination was not reported. Also, a quantitative analysis of the electron microscopy output was lacking. In our quantitatively analyzed electron microscopy dataset, we compare the optic nerve of *ST3GAL5*$^{-/-}$/ *B4GALNT1*$^{-/-}$ mice to their double heterozygous littermates. A comparison to wild type animals might reveal more severe deficits as differences in the ganglioside lipidome (compare sections 3.2.2 and 4.2.3) of double heterozygous compared to wild type animals already suggest.

Nevertheless, our ultrastructural results conclude that gangliosides are of minor importance for myelin generation and rather prominent for myelin maintenance.

4.2.2 Developmental Shifts in Ganglioside Synthesis, Lipid Chain Lengths and Saturation

Using a new shotgun lipidomic approach developed by our collaborator lipotype, we followed ganglioside synthesis in wild type mouse brain and optic nerve during development. This new method is sensitive enough to detect gangliosides reliably in a small piece of tissue like a pool of optic nerves of P12 mice.

Gangliosides gain complexity during development [Kolter et al., 2002; Lahiri and Futerman, 2007; Russo et al., 2018]. The ganglioside class profile we obtained using a new shotgun lipidomics approach resembles ganglioside class profiles from other studies [Ikeda and Taguchi, 2010; Hájek et al., 2017; Wormwood Moser et al., 2021]. Our data confirm a shift from simple to complex gangliosides. Rather simple ganglioside species were detected at an early and intermediate stage of myelination. The more complex ganglioside species were rather prominent at the later stages of myelination. In contrast to the lipidomics data of the *ST3GAL5*$^{-/-}$/*B4GALNT1*$^{-/-}$ mice, we did not detect any LacCer at any stage as it was probably already processed into more complex gangliosides. In line with another study, we also did not detect any levels of GM2 and GD2 [Wormwood Moser et al., 2021]. Additionally, we found some levels of gangliosides subspecies with shorter fatty acid carbon chains and low saturation decrease, while the ones with longer chains and higher saturation levels increase, sometimes significantly (e.g., GD1 36:1;2 + GD1 38:1;2; GT1 36:1;2 + GT1 38:1;2).

In gangliosides and the general lipid composition, we observed an increased fatty acid carbon chain length during development from P12 to the adult stage. The saturation levels also increased among almost all lipid species. Together, chain length and saturation level determine the fluidity of a membrane, hinting toward a change in membrane fluidity during development [Posse de Chaves and Sipione, 2010].

Among the other lipid species, we found a non-significant decrease in ceramide levels, the precursor for complex glycosphingolipids [Kolter et al., 2002; Lahiri and Futerman, 2007; Russo et al., 2018], from early to later stages in development. As Sulfatides are part of oligodendroglial membranes [Aggarwal et al., 2011; Schmitt et al., 2015], we expected a substantial increase in sulfatide levels as myelination progresses. Indeed, we found increased levels of sulfatides in the optic nerve and brain samples during development but not substantial as expected. In addition, cholesterol levels also increased significantly during development in both sample types.

4.2.3 It Seems Impossible to Compensate for the Lack of Gangliosides

We further investigated the role of gangliosides in axon-myelin interactions. Considering the mild phenotype of ganglioside null mice when they are born, their distinct-severe individual phenotypes, and the surprisingly normal myelin ultrastructure in the optic nerve, we searched for potential compensation strategies on the lipidome level.

Interestingly, a principal component analysis (PCA) showed different clusters of *ST3GAL5*$^{-/-}$/*B4GALNT1*$^{-/-}$, double heterozygous and wild type replicates, indicating that differences in the lipidome probably occur already on the double heterozygous level. Our data confirm a lack of

gangliosides in the brain and the optic nerve of *ST3GAL5*$^{-/-}$/ *B4GALNT1*$^{-/-}$ mice. This is further supported by high levels of LacCer in the ganglioside null replicates. LacCer is the precursor of all gangliosides. Most likely, LacCer accumulates as further ganglioside synthesis is impossible. However, we still detected low to very low amounts of GM1, GD1, GD3, and GT1 in *ST3GAL5*$^{-/-}$/ *B4GALNT1*$^{-/-}$ brain and optic nerve replicates. Sturgill et al. [2012] reported low levels of GD1a and GT1b in *ST3GAL2/3*$^{-/-}$ mice and suggested the existence of other ST3GAL enzymes, which take over terminal sialylation to replace the lacking gangliosides at least to a low extent. In line with this study, a yet unknown enzyme of the *ST3GAL* family might explain the low levels of gangliosides that we detected in *ST3GAL5*$^{-/-}$/ *B4GALNT1*$^{-/-}$ mice. On the other hand, using thin-layer chromatography Yamashita et al. [2005a] showed similar signals deriving from sialylated neolactoseries glycosphingolipids. Our lipidomics approach does not distinguish between a- and b- series isomers. Hence, we cannot conclude which series is dominating in the CNS. Notably, we detected differences in ganglioside synthesis in double heterozygous brain samples, hinting at a weakened enzyme activity already within this genotype. A coping strategy on double heterozygous level seems to be an increase in GD3 36:1;2, GD3 38:1;2, and GT1 36:1;2 levels.

The lack of enzymes for ganglioside synthesis affects other lipids' synthesis and metabolic pathways, as decreased lysophospholipid and sphingolipids (SP) levels in double heterozygous and ganglioside null samples indicate. Significant differences in lipid species levels were only detected among some glycerophospholipids in double heterozygous and ganglioside null samples. However, the amplitude of these differences within individual lipid species is too small to be considered a potential compensating mechanism for the lack of gangliosides.

The average length of the fatty acid carbon chains and their saturation state between the different genotypes did not reveal differences, which would account for a compensation mechanism. Overall, the average length of the total amount of fatty acid carbon chains in brain samples was longer than in the optic nerve. Hence, in general, the membrane environment in the optic nerve seems to be more fluid than in the brain.

In general, a lack of gangliosides also affects the synthesis of other lipids, though slightly less than expected. As ganglioside synthesis fails to produce as many complex gangliosides as necessary to maintain development and cell membrane functionality, ganglioside null mice develop neurodegenerative symptoms, which increase in severity during development when more and more complex gangliosides are necessary.

4.3 Summary

4.3.1 The Mechanisms Behind Paranodal Protein Relocation During Myein Wrapping

Even after decades of research on myelination, its mechanism and molecular basis are not yet fully understood. This dissertation's results may help understand the molecular mechanisms behind the interaction of the myelin membrane with the axonal membrane.

We found the paranodal adhesion molecule Caspr accumulating in the axonal membrane upon contact with an oligodendroglial process. While a myelin sheath forms around and along the axon, Caspr stays accumulated at the internode and then relocates to its functional position at the paranodes at a later stage of myelination. Our results hint towards an additional oligodendroglial, yet unknown, molecule being involved in paranodal protein relocation at the early stages of myelin wrapping. Unfortunately, we did not identify this molecule. Its exact function and interaction partners still need to be determined as well. However, we found Nfascb to be vital for Caspr's relocation to the paranodes later in the wrapping process. An internodal structure consisting of oligodendroglial Mag and axonal gangliosides supports the Nfascb-mediated relocation.

With the results of this thesis, we would like to update our model of myelination, which we proposed in a previous publication [Djannatian et al., 2019]. The beginning of myelination is set by an oligodendroglial process contacting an axon (Fig. 35 A). The Caspr/Cntn complex accumulates in the axonal membrane at the contact site. We suspect an oligodendroglial interaction partner, which interacts with either Caspr or Cntn and which we did not identify at this stage. While the myelin sheath grows and occupies more space on the axonal membrane, more Caspr/Cntn complexes accumulate at the internode (Fig. 35 B). The axonal gangliosides GD1a and GT1b interact in *cis* with each other and in *trans* with oligodendroglial Mag, thus forming an internodal structure. The more this structure grows and the more space it takes, the more molecules are protruded from the internode. By now, at least some oligodendroglial Nfascb proteins interact with Caspr/Cntn complexes forming paranodal adhesion complexes. Yet unknown forces in the myelin membrane drive the paranodal adhesion complexes to the edges of the internode. The internodal structure supports the relocation. While it reorganizes the molecule content in the internode, the paranodal adhesion complexes are passively excluded from this area. With the first full myelin turn wrapped around an axon, the first paranodal loop is also established (Fig. 35 C). The paranodal adhesion complexes were already in place then. Each myelin turn around the axon establishes another paranodal loop, with the paranodal adhesion proteins already brought in place by the mechanisms described in B and C (Fig. 35 D). Ultimately, we can distinguish the internode from the juxtaparanode and paranode by their molecule content. The paranodal adhesion proteins form a fence-like structure in the axonal membrane. Nodal proteins cannot enter this area.

Three factors need to be clarified to unravel the complete mechanism of the paranodal protein relocation during myelin wrapping. First and foremost, we need to clarify the exact mechanism of Caspr/Cntn accumulation upon contact with an oligodendroglial process. For this purpose, we must identify the yet unknown oligodendroglial interaction partner of the Caspr/Cntn complex.

Second, we need to prove if Cntn and/or Caspr function as recognition molecules to start myelination. And finally, the relocation driving force of Nfascb and therefore the entire paranodal adhesion complex from the internode to paranodes needs to be deciphered.

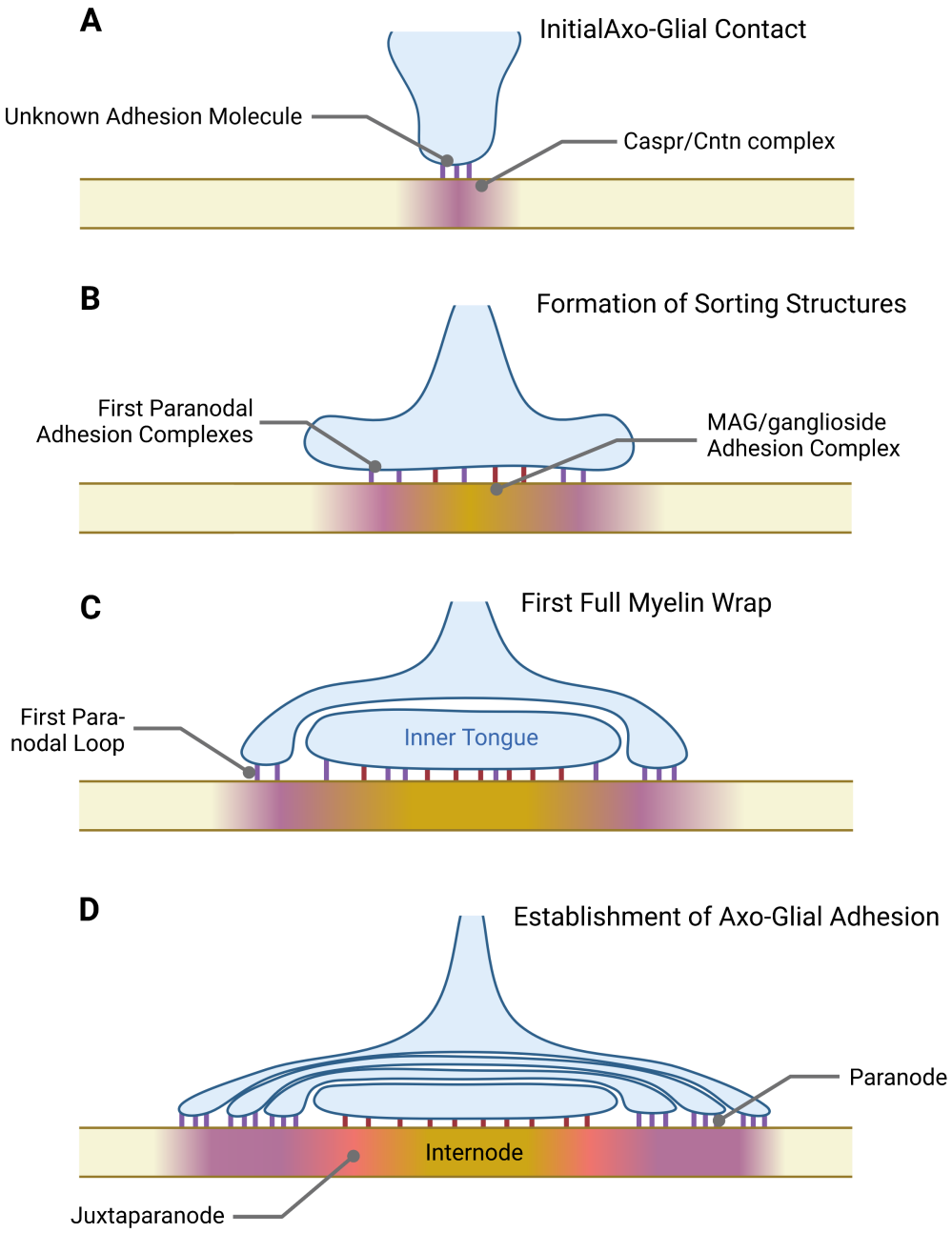

Figure 35: Final Model Summarizing Our Data for Paranodal Protein Sorting A The Caspr/Cntn complex accumulates upon attachment of an oligodendrocyte process at the axo-glial interaction site. It may be attracted by an unknown adhesion molecule in the oligodendroglial membrane. **B** While the oligodendrocyte process establishes a myelin sheath that wraps around the axon and also extends laterally, Mag and gangliosides start interacting *in cis* and *in trans*. Their interactions crowd out proteins like the Caspr/Cntn complex from this growing area and push them to the edges. Relocation of proteins is further enhanced by oligodendroglial Nfascb, which binds to the Caspr/Cntn complex and relocates this complex by a yet unknown mechanism. **C** After the first full myelin wrap, also the first paranodal loops are established, with the paranodal adhesion complexes already being in place. Internodal adhesion complexes stay at the inner tongue. **D** When the myelin sheath is finally established, we can define internodal, juxtaparanodal, and paranodal adhesion areas by molecule content.

4.3.2 The Role of Gangliosides in Myelination

The role and functions of gangliosides in the nervous system have always been challenging to seize. The structure of gangliosides does not allow to stain for them or analyze their exact content in tissues and cells. In addition, ganglioside synthesis involves many different enzymes, which can substitute for each other. This enzyme diversity is challenging for developing and breeding a ganglioside mutant animal line. Nevertheless, in the second part of this thesis, we investigated the role of gangliosides in myelination by using electron microscopy on optic nerve samples of ganglioside mutant mice (*ST3GAL5*$^{-/-}$/ *B4GALNT1*$^{-/-}$). Using a newly developed shotgun lipidomics method, we also analyzed the lipidome and the ganglioside content of brain and optic nerve samples of these mice to search for compensation strategies for the lack of gangliosides. In addition, we applied this new lipidomics method on wild type mouse brain and optic nerve samples to follow ganglioside synthesis during development.

We hypothesized that gangliosides in the axonal membrane provide a platform for myelination. Hence, we expected to observe myelin defects already from an early stage. In line with the observation that freshly born ganglioside null mice seem normal and only present with neurodegenerative symptoms with progressing development, our ultrastructural analysis detected hypomyelination only from a medium stage of myelination. We did not find any significant myelin deficit at early myelination. Our lipidomics approach detected a loss of gangliosides in *ST3GAL5*$^{-/-}$/ *B4GALNT1*$^{-/-}$ brain and optic nerve samples. However, low to very low levels of some complex gangliosides were still detected, to our surprise. We did not identify a clear compensation strategy for the lack of gangliosides at an early stage of myelination. Instead, gangliosides seem to play an essential role in myelin maintenance. Our lipidomic data on the ganglioside content during development confirmed a shift from simple to complex gangliosides, not only regarding ganglioside species but also ganglioside subspecies concerning their fatty acid carbon chain length and saturation levels.

Based on our results, we propose a crucial role for gangliosides in maintaining axon-myelin stability, not in the myelination process. By interaction with oligodendroglial MAG, axonal gangliosides are part of the internodal adhesion complex. This complex seems to be more involved in stabilizing the axon-myelin adhesion than in the active myelinating process.

Additionally, we present a sensitive, efficient and inexpensive mass spectrometry technique for ganglioside detection, developed by our collaborator lipotype, which can be used for high-throughput diagnostic applications. More details on this new shotgun lipidomics method are published in *"Ganglioside lipidomics of central nervous system myelination using direct infusion shotgun mass spectrometry; Arends et al."*, which was submitted to *"iScience (Cell press)"*.

Bibliography

Ablain, J., Durand, E. M., Yang, S., Zhou, Y., and Zon, L. I. (2015). A crispr/cas9 vector system for tissue-specific gene disruption in zebrafish. *Developmental cell*, 32(25752963):756–764.

Ackerman, S. D. and Monk, K. R. (2016). The scales and tales of myelination: using zebrafish and mouse to study myelinating glia. *Brain research*, 1641:79–91.

Aggarwal, S., Snaidero, N., Pähler, G., Frey, S., Sánchez, P., Zweckstetter, M., Janshoff, A., Schneider, A., Weil, M.-T., Schaap, I. A. T., Görlich, D., and Simons, M. (2013). Myelin membrane assembly is driven by a phase transition of myelin basic proteins into a cohesive protein meshwork. *PLoS biology*, 11:e1001577.

Aggarwal, S., Yurlova, L., and Simons, M. (2011). Central nervous system myelin: structure, synthesis and assembly. *Trends in cell biology*, 21:585–593.

Aicart-Ramos, C., Valero, R. A., and Rodriguez-Crespo, I. (2011). Protein palmitoylation and subcellular trafficking. *Biochimica et biophysica acta*, 1808:2981–2994.

Almeida, R. G. (2018). The rules of attraction in central nervous system myelination. *Frontiers in cellular neuroscience*, 12:367.

Almeida, R. G., Czopka, T., ffrench Constant, C., and Lyons, D. A. (2011). Individual axons regulate the myelinating potential of single oligodendrocytes in vivo. *Development*, 138(20):4443–4450.

Almeida, R. G., Williamson, J. M., Madden, M. E., Early, J. J., Voas, M. G., Talbot, W. S., Bianco, I. H., and Lyons, D. A. (2021). Myelination induces axonal hotspots of synaptic vesicle fusion that promote sheath growth. *Current biology : CB*, 31:3743–3754.e5.

Arancibia-Carcamo, I. L. and Attwell, D. (2014). The node of ranvier in cns pathology. *Acta neuropathologica*, 128(24913350):161–175.

Arends, M., Weber, M., Papan, C., Damm, M., Surma, M. A., Spiegel, C., Djannatian, M., Li, S., Connell, L., Johannes, L., Schifferer, M., Klose, C., and Simons, M. (2022). Ganglioside lipidomics of central nervous system myelination using direct infusion shotgun mass spectrometry. *in revision*.

Arquint, M., Roder, J., Chia, L. S., Down, J., Wilkinson, D., Bayley, H., Braun, P., and Dunn, R. (1987). Molecular cloning and primary structure of myelin-associated glycoprotein. *Proceedings of the National Academy of Sciences of the United States of America*, 84:600–604.

Auer, F., Vagionitis, S., and Czopka, T. (2018). Evidence for myelin sheath remodeling in the cns revealed by in vivo imaging. *Current biology : CB*, 28:549–559.e3.

Aureli, M., Grassi, S., Prioni, S., Sonnino, S., and Prinetti, A. (2015). Lipid membrane domains in the brain. *Biochimica et Biophysica Acta (BBA) - Molecular and Cell Biology of Lipids*, 1851(8):1006–1016.

Bai, Q., Sun, M., Stolz, D. B., and Burton, E. A. (2011). Major isoform of zebrafish p0 is a 23.5 kda myelin glycoprotein expressed in selected white matter tracts of the central nervous system. *Journal of Comparative Neurology*, 519(8):1580–1596.

Bakhti, M., Snaidero, N., Schneider, D., Aggarwal, S., Möbius, W., Janshoff, A., Eckhardt, M., Nave, K.-A., and Simons, M. (2013). Loss of electrostatic cell-surface repulsion mediates myelin membrane adhesion and compaction in the central nervous system. *Proc Natl Acad Sci USA*, 110(8):3143.

Baraban, M., Koudelka, S., and Lyons, D. A. (2018). Ca2+ activity signatures of myelin sheath formation and growth in vivo. *Nature neuroscience*, 21:19–23.

Barrientos, R. C. and Zhang, Q. (2020). Recent advances in the mass spectrometric analysis of glycosphingolipidome - a review. *Analytica chimica acta*, 1132(32980104):134–155.

Bartsch, S., Montag, D., Schachner, M., and Bartsch, U. (1997). Increased number of unmyelinated axons in optic nerves of adult mice deficient in the myelin-associated glycoprotein (mag). *Brain research*, 762:231–234.

Bartsch, U., Kirchhoff, F., and Schachner, M. (1989). Immunohistological localization of the adhesion molecules l1, n-cam, and mag in the developing and adult optic nerve of mice. *Journal of Comparative Neurology*, 284(3):451–462.

Bechler, M. E., Byrne, L., and Ffrench-Constant, C. (2015). Cns myelin sheath lengths are an intrinsic property of oligodendrocytes. *Current biology : CB*, 25:2411–2416.

Becker, C. G. and Becker, T. (2008). Adult zebrafish as a model for successful central nervous system regeneration. *Restorative neurology and neuroscience*, 26:71–80.

Bellen, H. J., Lu, Y., Beckstead, R., and Bhat, M. A. (1998). Neurexin iv, caspr and paranodin–novel members of the neurexin family: encounters of axons and glia. *Trends in neurosciences*, 21:444–449.

Bennett, V. and Lorenzo, D. N. (2013). Spectrin- and ankyrin-based membrane domains and the evolution of vertebrates. *Current topics in membranes*, 72:1–37.

Bennett, V. and Lorenzo, D. N. (2016). An adaptable spectrin/ankyrin-based mechanism for long-range organization of plasma membranes in vertebrate tissues. *Current topics in membranes*, 77:143–184.

Berger, J. and Currie, P. D. (2013). 503unc, a small and muscle-specific zebrafish promoter. *genesis*, 51(6):443–447.

Berglund, E. O., Murai, K. K., Fredette, B., Sekerková, G., Marturano, B., Weber, L., Mugnaini, E., and Ranscht, B. (1999). Ataxia and abnormal cerebellar microorganization in mice with ablated contactin gene expression. *Neuron*, 24:739–750.

Bhat, M. A., Rios, J. C., Lu, Y., Garcia-Fresco, G. P., Ching, W., St Martin, M., Li, J., Einheber, S., Chesler, M., Rosenbluth, J., Salzer, J. L., and Bellen, H. J. (2001). Axon-glia interactions and the domain organization of myelinated axons requires neurexin iv/caspr/paranodin. *Neuron*, 30:369–383.

Blix, G. (1936). Über die kohlenhydratgruppen des submaxillarismucins. *Hoppe-Seyler´s Zeitschrift Für Physiologische Chemie*, 240(1-2):43–54.

Bonetto, G. and Di Scala, C. (2019). Importance of lipids for nervous system integrity: Cooperation between gangliosides and sulfatides in myelin stability. *The Journal of neuroscience : the official journal of the Society for Neuroscience*, 39:6218–6220.

Bonetto, G., Kamen, Y., Evans, K. A., and Káradóttir, R. T. (2020). Unraveling myelin plasticity. *Frontiers in Cellular Neuroscience*, 14:156.

Bonnon, C., Bel, C., Goutebroze, L., Maigret, B., Girault, J.-A., and Faivre-Sarrailh, C. (2007). Pgy repeats and n-glycans govern the trafficking of paranodin and its selective association with contactin and neurofascin-155. *Molecular biology of the cell*, 18:229–241.

Bonnon, C., Goutebroze, L., Denisenko-Nehrbass, N., Girault, J.-A., and Faivre-Sarrailh, C. (2003). The paranodal complex of f3/contactin and caspr/paranodin traffics to the cell surface via a non-conventional pathway. *The Journal of biological chemistry*, 278:48339–48347.

Bosio, A., Binczek, E., Haupt, W. F., and Stoffel, W. (1998). Composition and biophysical properties of myelin lipid define the neurological defects in galactocerebroside- and sulfatide-deficient mice. *Journal of neurochemistry*, 70:308–315.

Bosio, A., Binczek, E., and Stoffel, W. (1996). Functional breakdown of the lipid bilayer of the myelin membrane in central and peripheral nervous system by disrupted galactocerebroside synthesis. *Proceedings of the National Academy of Sciences of the United States of America*, 93:13280–13285.

Boyle, M. E. T., Berglund, E. O., Murai, K. K., Weber, L., Peles, E., and Ranscht, B. (2001). Contactin orchestrates assembly of the septate-like junctions at the paranode in myelinated peripheral nerve. *Neuron*, 30(2):385–397.

Brivio, V., Faivre-Sarrailh, C., Peles, E., Sherman, D. L., and Brophy, P. J. (2017). Assembly of cns nodes of ranvier in myelinated nerves is promoted by the axon cytoskeleton. *Current biology : CB*, 27:1068–1073.

Brösamle, C. and Halpern, M. E. (2002). Characterization of myelination in the developing zebrafish. *Glia*, 39(1):47–57.

Buckley, C. E., Marguerie, A., Alderton, W. K., and Franklin, R. J. M. (2010). Temporal dynamics of myelination in the zebrafish spinal cord. *Glia*, 58:802–812.

Buttermore, E. D., Dupree, J. L., Cheng, J., An, X., Tessarollo, L., and Bhat, M. A. (2011). The cytoskeletal adaptor protein band 4.1b is required for the maintenance of paranodal axoglial septate junctions in myelinated axons. *Journal of Neuroscience*, 31(22):8013–8024.

Chang, K.-J., Zollinger, D. R., Susuki, K., Sherman, D. L., Makara, M. A., Brophy, P. J., Cooper, E. C., Bennett, V., Mohler, P. J., and Rasband, M. N. (2014). Glial ankyrins facilitate paranodal axoglial junction assembly. *Nature neuroscience*, 17:1673–1681.

Charles, P., Tait, S., Faivre-Sarrailh, C., Barbin, G., Gunn-Moore, F., Denisenko-Nehrbass, N., Guennoc, A.-M., Girault, J.-A., Brophy, P. J., and Lubetzki, C. (2002). Neurofascin is a glial receptor for the paranodin/caspr-contactin axonal complex at the axoglial junction. *Current biology : CB*, 12:217–220.

Chen, N., Koopmans, F., Gordon, A., Paliukhovich, I., Klaassen, R. V., van der Schors, R. C., Peles, E., Verhage, M., Smit, A. B., and Li, K. W. (2015). Interaction proteomics of canonical caspr2 (cntnap2) reveals the presence of two caspr2 isoforms with overlapping interactomes. *Biochimica et biophysica acta*, 1854:827–833.

Chen, X., Zaro, J. L., and Shen, W.-C. (2013). Fusion protein linkers: property, design and functionality. *Advanced drug delivery reviews*, 65:1357–1369.

Chiavegatto, S., Sun, J., Nelson, R. J., and Schnaar, R. L. (2000). A functional role for complex gangliosides: motor deficits in gm2/gd2 synthase knockout mice. *Experimental neurology*, 166:227–234.

Chishti, A. H., Kim, A. C., Marfatia, S. M., Lutchman, M., Hanspal, M., Jindal, H., Liu, S. C., Low, P. S., Rouleau, G. A., Mohandas, N., Chasis, J. A., Conboy, J. G., Gascard, P., Takakuwa, Y., Huang, S. C., Benz, E. J., Bretscher, A., Fehon, R. G., Gusella, J. F., Ramesh, V., Solomon, F., Marchesi, V. T., Tsukita, S., Tsukita, S., and Hoover, K. B. (1998). The ferm domain: a unique module involved in the linkage of cytoplasmic proteins to the membrane. *Trends in biochemical sciences*, 23:281–282.

Chrast, R., Saher, G., Nave, K.-A., and Verheijen, M. H. G. (2011). Lipid metabolism in myelinating glial cells: lessons from human inherited disorders and mouse models. *Journal of Lipid Research*, 52(3):419–434.

Coetzee, T., Dupree, J. L., and Popko, B. (1998). Demyelination and altered expression of myelin-associated glycoprotein isoforms in the central nervous system of galactolipid-deficient mice. *Journal of neuroscience research*, 54:613–622.

Coetzee, T., Fujita, N., Dupree, J., Shi, R., Blight, A., Suzuki, K., Suzuki, K., and Popko, B. (1996). Myelination in the absence of galactocerebroside and sulfatide: normal structure with abnormal function and regional instability. *Cell*, 86:209–219.

Collins, B. E., Ito, H., Sawada, N., Ishida, H., Kiso, M., and Schnaar, R. L. (1999). Enhanced binding of the neural siglecs, myelin-associated glycoprotein and schwann cell myelin protein, to chol-1 (alpha-series) gangliosides and novel sulfated chol-1 analogs. *The Journal of biological chemistry*, 274:37637–37643.

Collins, B. E., Yang, L. J., Mukhopadhyay, G., Filbin, M. T., Kiso, M., Hasegawa, A., and Schnaar, R. L. (1997). Sialic acid specificity of myelin-associated glycoprotein binding. *The Journal of biological chemistry*, 272:1248–1255.

Cook, S. R., Bladen, C., Smith, J., Maguire, E., Copner, J., Fenn, G. D., Wager, K., Waller-Evans, H., and Lloyd-Evans, E. (2020). Visualisation of cholesterol and ganglioside gm1 in zebrafish models of niemann-pick type c disease and smith-lemli-opitz syndrome using light sheet microscopy. *Histochemistry and cell biology*, 154:565–578.

Cunha, M. I., Su, M., Cantuti-Castelvetri, L., Müller, S. A., Schifferer, M., Djannatian, M., Alexopoulos, I., van der Meer, F., Winkler, A., van Ham, T. J., Schmid, B., Lichtenthaler, S. F., Stadelmann, C., and Simons, M. (2020). Pro-inflammatory activation following demyelination is required for myelin clearance and oligodendrogenesis. *J Exp Med*, 217(5).

Czopka, T. (2016). Insights into mechanisms of central nervous system myelination using zebrafish. *Glia*, 64(3):333–349.

Czopka, T., ffrench Constant, C., and Lyons, D. (2013). Individual oligodendrocytes have only a few hours in which to generate new myelin sheaths in vivo. *Developmental Cell*, 25(6):599–609.

Davis, E. E., Frangakis, S., and Katsanis, N. (2014). Interpreting human genetic variation with in vivo zebrafish assays. *Biochimica et biophysica acta*, 1842:1960–1970.

Davis, J. Q., Lambert, S., and Bennett, V. (1996). Molecular composition of the node of ranvier: identification of ankyrin-binding cell adhesion molecules neurofascin (mucin+/third fniii domain-) and nrcam at nodal axon segments. *The Journal of cell biology*, 135:1355–1367.

Davis, J. Q., McLaughlin, T., and Bennett, V. (1993). Ankyrin-binding proteins related to nervous system cell adhesion molecules: candidates to provide transmembrane and intercellular connections in adult brain. *Journal of Cell Biology*, 121(1):121–133.

de Bellard, M. E. (2016). Myelin in cartilaginous fish. *Brain research*, 1641(26776480):34–42.

DeBruin, L. S., Haines, J. D., Wellhauser, L. A., Radeva, G., Schonmann, V., Bienzle, D., and Harauz, G. (2005). Developmental partitioning of myelin basic protein into membrane microdomains. *J. Neurosci. Res.*, 80(2):211–225.

Demerens, C., Stankoff, B., Logak, M., Anglade, P., Allinquant, B., Couraud, F., Zalc, B., and Lubetzki, C. (1996). Induction of myelination in the central nervous system by electrical activity. *Proc Natl Acad Sci USA*, 93(18):9887.

Denisenko-Nehrbass, N., Oguievetskaia, K., Goutebroze, L., Galvez, T., Yamakawa, H., Ohara, O., Carnaud, M., and Girault, J.-A. (2003). Protein 4.1b associates with both caspr/paranodin and caspr2 at paranodes and juxtaparanodes of myelinated fibres. *The European journal of neuroscience*, 17:411–416.

Desplats, P. A., Denny, C. A., Kass, K. E., Gilmartin, T., Head, S. R., Sutcliffe, J. G., Seyfried, T. N., and Thomas, E. A. (2007). Glycolipid and ganglioside metabolism imbalances in huntington's disease. *Neurobiology of disease*, 27:265–277.

D'Este, E., Kamin, D., Balzarotti, F., and Hell, S. W. (2017). Ultrastructural anatomy of nodes of ranvier in the peripheral nervous system as revealed by sted microscopy. *Proceedings of the National Academy of Sciences of the United States of America*, 114:E191–E199.

Djannatian, M., Timmler, S., Arends, M., Luckner, M., Weil, M.-T., Alexopoulos, I., Snaidero, N., Schmid, B., Misgeld, T., Möbius, W., Schifferer, M., Peles, E., and Simons, M. (2019). Two adhesive systems cooperatively regulate axon ensheathment and myelin growth in the cns. *Nature communications*, 10:4794.

Dobrović, B., Ćurić, G., Petanjek, Z., and Heffer, M. (2011). Dendritic morphology and spine density is not altered in motor cortex and dentate granular cells in mice lacking the ganglioside biosynthetic gene b4galnt1 - a quantitative golgi cox study. *Collegium antropologicum*, 35 Suppl 1:25–30.

Dowhan, W., Bogdanov, M., Mileykovskaya, E., Vance, D. E., and Vance, J. E. (Dowhan2008). Chapter 1 - functional roles of lipids in membranes. In *Biochemistry of Lipids, Lipoproteins and Membranes (Fifth Edition)*, pages 1–37. Elsevier, San Diego.

Dreier, D. A., Nouri, M.-Z., Denslow, N. D., and Martyniuk, C. J. (2021). Lipidomics reveals multiple stressor effects (temperature × mitochondrial toxicant) in the zebrafish embryo toxicity test. *Chemosphere*, 264:128472.

Dueñas, M. E., Essner, J. J., and Lee, Y. J. (2017). 3d maldi mass spectrometry imaging of a single cell: Spatial mapping of lipids in the embryonic development of zebrafish. *Scientific reports*, 7:14946.

Dupree, J. L., Coetzee, T., Suzuki, K., and Popko, B. (1998). Myelin abnormalities in mice deficient in galactocerebroside and sulfatide. *Journal of neurocytology*, 27:649–659.

Early, J. J., Cole, K. L., Williamson, J. M., Swire, M., Kamadurai, H., Muskavitch, M., and Lyons, D. A. (2018). An automated high-resolution in vivo screen in zebrafish to identify chemical regulators of myelination. *eLife*, 7(29979149):e35136.

Einheber, S., Meng, X., Rubin, M., Lam, I., Mohandas, N., An, X., Shrager, P., Kissil, J., Maurel, P., and Salzer, J. L. (2013). The 4.1b cytoskeletal protein regulates the domain organization and sheath thickness of myelinated axons. *Glia*, 61:240–253.

Einheber, S., Zanazzi, G., Ching, W., Scherer, S., Milner, T. A., Peles, E., and Salzer, J. L. (1997). The axonal membrane protein caspr, a homologue of neurexin iv, is a component of the septate-like paranodal junctions that assemble during myelination. *The Journal of cell biology*, 139:1495–1506.

Eisenbach, M., Kartvelishvily, E., Eshed-Eisenbach, Y., Watkins, T., Sorensen, A., Thomson, C., Ranscht, B., Barnett, S. C., Brophy, P., and Peles, E. (2009). Differential clustering of caspr by oligodendrocytes and schwann cells. *Journal of neuroscience research*, 87:3492–3501.

Ejsing, C. S., Sampaio, J. L., Surendranath, V., Duchoslav, E., Ekroos, K., Klemm, R. W., Simons, K., and Shevchenko, A. (2009). Global analysis of the yeast lipidome by quantitative shotgun mass spectrometry. *Proceedings of the National Academy of Sciences of the United States of America*, 106:2136–2141.

Elazar, N., Vainshtein, A., Golan, N., Vijayaragavan, B., Schaeren-Wiemers, N., Eshed-Eisenbach, Y., and Peles, E. (2019). Axoglial adhesion by cadm4 regulates cns myelination. *Neuron*, 101(2):224–231.e5.

Fahy, E., Subramaniam, S., Brown, H. A., Glass, C. K., Merrill, A. H., Murphy, R. C., Raetz, C. R. H., Russell, D. W., Seyama, Y., Shaw, W., Shimizu, T., Spener, F., van Meer, G., VanNieuwenhze, M. S., White, S. H., Witztum, J. L., and Dennis, E. A. (2005). A comprehensive classification system for lipids. *Journal of lipid research*, 46:839–861.

Faivre-Sarrailh, C. (2020). Molecular organization and function of vertebrate septate-like junctions. *Biochimica et Biophysica Acta (BBA) - Biomembranes*, 1862(5):183211.

Faivre-Sarrailh, C., Gauthier, F., Denisenko-Nehrbass, N., Le Bivic, A., Rougon, G., and Girault, J. A. (2000). The glycosylphosphatidyl inositol-anchored adhesion molecule f3/contactin is required for surface transport of paranodin/contactin-associated protein (caspr). *The Journal of cell biology*, 149:491–502.

Fehmi, J., Scherer, S. S., Willison, H. J., and Rinaldi, S. (2018). Nodes, paranodes and neuropathies. *Journal of Neurology, Neurosurgery & Psychiatry*, 89(1):61–71.

Feitsma, H. and Cuppen, E. (2008). Zebrafish as a cancer model. *Mol Cancer Res*, 6(5):685.

Fraher, D., Sanigorski, A., Mellett, N. A., Meikle, P. J., Sinclair, A. J., and Gibert, Y. (2016). Zebrafish embryonic lipidomic analysis reveals that the yolk cell is metabolically active in processing lipid. *Cell reports*, 14:1317–1329.

Freigang, J., Proba, K., Leder, L., Diederichs, K., Sonderegger, P., and Welte, W. (2000). The crystal structure of the ligand binding module of axonin-1/tag-1 suggests a zipper mechanism for neural cell adhesion. *Cell*, 101(4):425–433.

Fruttiger, M., Montag, D., Schachner, M., and Martini, R. (1995). Crucial role for the myelin-associated glycoprotein in the maintenance of axon-myelin integrity. *The European journal of neuroscience*, 7:511–515.

Futerman, A. H. and Pagano, R. E. (1991). Determination of the intracellular sites and topology of glucosylceramide synthesis in rat liver. *The Biochemical journal*, 280 (Pt 2):295–302.

Garcia, M. A. and Zuchero, J. B. (2019). Anchors away: Glia-neuron adhesion regulates myelin targeting and growth. *Developmental Cell*, 51(6):659–661.

Garver, T. D., Ren, Q., Tuvia, S., and Bennett, V. (1997). Tyrosine Phosphorylation at a Site Highly Conserved in the L1 Family of Cell Adhesion Molecules Abolishes Ankyrin Binding and Increases Lateral Mobility of Neurofascin. *Journal of Cell Biology*, 137(3):703–714.

Gennarini, G., Rougon, G., Vitiello, F., Corsi, P., Di Benedetta, C., and Goridis, C. (1989). Identification and cdna cloning of a new member of the l2/hnk-1 family of neural surface glycoproteins. *Journal of neuroscience research*, 22:1–12.

Ghosh, A., Sherman, D. L., and Brophy, P. J. (2018). The axonal cytoskeleton and the assembly of nodes of ranvier. *The Neuroscientist : a review journal bringing neurobiology, neurology and psychiatry*, 24:104–110.

Gollan, L., Sabanay, H., Poliak, S., Berglund, E. O., Ranscht, B., and Peles, E. (2002). Retention of a cell adhesion complex at the paranodal junction requires the cytoplasmic region of caspr. *The Journal of cell biology*, 157:1247–1256.

Gollan, L., Salomon, D., Salzer, J. L., and Peles, E. (2003). Caspr regulates the processing of contactin and inhibits its binding to neurofascin. *The Journal of cell biology*, 163:1213–1218.

Goodman, J. W. (1996). *Introduction to Fourier Optics 2nd*. McGraw-Hill.

Gordon, A., Adamsky, K., Vainshtein, A., Frechter, S., Dupree, J. L., Rosenbluth, J., and Peles, E. (2014). Caspr and caspr2 are required for both radial and longitudinal organization of myelinated axons. *Journal of Neuroscience*, 34(45):14820–14826.

Haenisch, C., Diekmann, H., Klinger, M., Gennarini, G., Kuwada, J. Y., and Stuermer, C. A. O. (2005). The neuronal growth and regeneration associated cntn1 (f3/f11/contactin) gene is duplicated in fish: expression during development and retinal axon regeneration. *Molecular and cellular neurosciences*, 28:361–374.

Hassel, B., Rathjen, F. G., and Volkmer, H. (1997). Organization of the neurofascin gene and analysis of developmentally regulated alternative splicing. *The Journal of biological chemistry*, 272:28742–28749.

Herzog, R., Schuhmann, K., Schwudke, D., Sampaio, J. L., Bornstein, S. R., Schroeder, M., and Shevchenko, A. (2012). Lipidxplorer: a software for consensual cross-platform lipidomics. *PloS one*, 7:e29851.

Herzog, R., Schwudke, D., Schuhmann, K., Sampaio, J. L., Bornstein, S. R., Schroeder, M., and Shevchenko, A. (2011). A novel informatics concept for high-throughput shotgun lipidomics based on the molecular fragmentation query language. *Genome biology*, 12:R8.

Hill, R. A., Li, A. M., and Grutzendler, J. (2018). Lifelong cortical myelin plasticity and age-related degeneration in the live mammalian brain. *Nature Neuroscience*, 21(5):683–695.

Hines, J. H., Ravanelli, A. M., Schwindt, R., Scott, E. K., and Appel, B. (2015). Neuronal activity biases axon selection for myelination in vivo. *Nature neuroscience*, 18:683–689.

Hirschberg, K., Rodger, J., and Futerman, A. H. (1993). The long-chain sphingoid base of sphingolipids is acylated at the cytosolic surface of the endoplasmic reticulum in rat liver. *The Biochemical journal*, 290 (Pt 3):751–757.

Hivert, B., Pinatel, D., Labasque, M., Tricaud, N., Goutebroze, L., and Faivre-Sarrailh, C. (2016). Assembly of juxtaparanodes in myelinating drg culture: Differential clustering of the kv1/caspr2 complex and scaffolding protein 4.1b. *Glia*, 64:840–852.

Hájek, R., Jirásko, R., Lísa, M., Cífková, E., and Holčapek, M. (2017). Hydrophilic interaction liquid chromatography-mass spectrometry characterization of gangliosides in biological samples. *Analytical chemistry*, 89:12425–12432.

Holm, J., Hillenbrand, R., Steuber, V., Bartsch, U., Moos, M., Lübbert, H., Montag, D., and Schachner, M. (1996). Structural features of a close homologue of l1 (chl1) in the mouse: A new member of the l1 family of neural recognition molecules. *European Journal of Neuroscience*, 8(8):1613–1629.

Honke, K., Hirahara, Y., Dupree, J., Suzuki, K., Popko, B., Fukushima, K., Fukushima, J., Nagasawa, T., Yoshida, N., Wada, Y., and Taniguchi, N. (2002). Paranodal junction formation and spermatogenesis require sulfoglycolipids. *Proceedings of the National Academy of Sciences of the United States of America*, 99:4227–4232.

Horresh, I., Bar, V., Kissil, J. L., and Peles, E. (2010). Organization of myelinated axons by caspr and caspr2 requires the cytoskeletal adapter protein 4.1b. *Journal of Neuroscience*, 30(7):2480–2489.

Horresh, I., Poliak, S., Grant, S., Bredt, D., Rasband, M. N., and Peles, E. (2008). Multiple molecular interactions determine the clustering of caspr2 and kv1 channels in myelinated axons. *J. Neurosci.*, 28(52):14213.

Howe, K., Clark, M. D., Torroja, C. F., Torrance, J., Berthelot, C., Muffato, M., Collins, J. E., Humphray, S., McLaren, K., Matthews, L., McLaren, S., Sealy, I., Caccamo, M., Churcher, C., Scott, C., Barrett, J. C., Koch, R., Rauch, G.-J., White, S., Chow, W., Kilian, B., Quintais, L. T., Guerra-Assunção, J. A., Zhou, Y., Gu, Y., Yen, J., Vogel, J.-H., Eyre, T., Redmond, S., Banerjee, R., Chi, J., Fu, B., Langley, E., Maguire, S. F., Laird, G. K., Lloyd, D., Kenyon, E., Donaldson, S., Sehra, H., Almeida-King, J., Loveland, J., Trevanion, S., Jones, M., Quail, M., Willey, D., Hunt, A., Burton, J., Sims, S., McLay, K., Plumb, B., Davis, J., Clee, C., Oliver, K., Clark, R., Riddle, C., Elliot, D., Eliott, D., Threadgold, G., Harden, G., Ware, D., Begum, S., Mortimore, B., Mortimer, B., Kerry, G., Heath, P., Phillimore, B., Tracey, A., Corby, N., Dunn, M., Johnson, C., Wood, J., Clark, S., Pelan, S., Griffiths, G., Smith, M., Glithero, R., Howden, P., Barker, N., Lloyd, C., Stevens, C., Harley, J., Holt, K., Panagiotidis, G., Lovell, J., Beasley, H., Henderson, C., Gordon, D., Auger, K., Wright, D., Collins, J., Raisen, C., Dyer, L., Leung, K., Robertson, L., Ambridge, K., Leongamornlert, D., McGuire, S., Gilderthorp, R., Griffiths, C., Manthravadi, D., Nichol, S., Barker, G., Whitehead, S., Kay, M., Brown, J., Murnane, C., Gray, E., Humphries, M., Sycamore, N., Barker, D., Saunders, D., Wallis, J., Babbage, A., Hammond, S., Mashreghi-Mohammadi, M., Barr, L., Martin, S., Wray, P., Ellington, A., Matthews, N., Ellwood, M., Woodmansey, R., Clark, G., Cooper, J. D., Cooper, J., Tromans, A., Grafham, D., Skuce, C., Pandian, R., Andrews, R., Harrison, E., Kimberley, A., Garnett, J., Fosker, N., Hall, R., Garner, P., Kelly, D., Bird, C., Palmer, S., Gehring, I., Berger, A., Dooley, C. M., Ersan-Ürün, Z., Eser, C., Geiger, H., Geisler, M., Karotki, L., Kirn, A., Konantz, J., Konantz, M., Oberländer, M., Rudolph-Geiger, S., Teucke, M., Lanz, C., Raddatz, G., Osoegawa, K., Zhu, B., Rapp, A., Widaa, S., Langford, C., Yang, F., Schuster, S. C., Carter, N. P., Harrow, J., Ning, Z., Herrero, J., Searle, S. M. J., Enright, A., Geisler, R., Plasterk, R. H. A., Lee, C., Westerfield, M., de Jong, P. J., Zon, L. I., Postlethwait,

J. H., Nüsslein-Volhard, C., Hubbard, T. J. P., Roest Crollius, H., Rogers, J., and Stemple, D. L. (2013). The zebrafish reference genome sequence and its relationship to the human genome. *Nature*, 496:498–503.

Hruscha, A., Krawitz, P., Rechenberg, A., Heinrich, V., Hecht, J., Haass, C., and Schmid, B. (2013). Efficient crispr/cas9 genome editing with low off-target effects in zebrafish. *Development*, 140(24):4982–4987.

Hughes, A. N. and Appel, B. (2019). Oligodendrocytes express synaptic proteins that modulate myelin sheath formation. *Nature communications*, 10:4125.

Hughes, A. N. and Appel, B. (2020). Microglia phagocytose myelin sheaths to modify developmental myelination. *Nature Neuroscience*, 23(9):1055–1066.

Hughes, E. G., Orthmann-Murphy, J. L., Langseth, A. J., and Bergles, D. E. (2018). Myelin remodeling through experience-dependent oligodendrogenesis in the adult somatosensory cortex. *Nature Neuroscience*, 21(5):696–706.

Hwang, W. Y., Fu, Y., Reyon, D., Maeder, M. L., Tsai, S. Q., Sander, J. D., Peterson, R. T., Yeh, J.-R. J., and Joung, J. K. (2013). Efficient genome editing in zebrafish using a crispr-cas system. *Nature biotechnology*, 31(23360964):227–229.

Ichikawa, N., Iwabuchi, K., Kurihara, H., Ishii, K., Kobayashi, T., Sasaki, T., Hattori, N., Mizuno, Y., Hozumi, K., Yamada, Y., and Arikawa-Hirasawa, E. (2009). Binding of laminin-1 to monosialoganglioside gm1 in lipid rafts is crucial for neurite outgrowth. *Journal of cell science*, 122:289–299.

Ichikawa, S., Sakiyama, H., Suzuki, G., Hidari, K. I., and Hirabayashi, Y. (1996). Expression cloning of a cdna for human ceramide glucosyltransferase that catalyzes the first glycosylation step of glycosphingolipid synthesis. *Proceedings of the National Academy of Sciences*, 93(10):4638–4643.

Ikeda, K. and Taguchi, R. (2010). Highly sensitive localization analysis of gangliosides and sulfatides including structural isomers in mouse cerebellum sections by combination of laser microdissection and hydrophilic interaction liquid chromatography/electrospray ionization mass spectrometry with theoretically expanded multiple reaction monitoring. *Rapid communications in mass spectrometry : RCM*, 24:2957–2965.

Irwin, L. N. and Irwin, C. C. (1982). Developmental changes and regional variation in the ganglioside composition of the rat hippocampus. *Developmental Brain Research*, 4(4):481–485.

Ishibashi, T., Dupree, J. L., Ikenaka, K., Hirahara, Y., Honke, K., Peles, E., Popko, B., Suzuki, K., Nishino, H., and Baba, H. (2002). A myelin galactolipid, sulfatide, is essential for maintenance of ion channels on myelinated axon but not essential for initial cluster formation. *Journal of Neuroscience*, 22(15):6507–6514.

Jensen, E. C. (2012). Use of fluorescent probes: their effect on cell biology and limitations. *Anatomical record (Hoboken, N.J. : 2007)*, 295:2031–2036.

Jinek, M., Chylinski, K., Fonfara, I., Hauer, M., Doudna, J. A., and Charpentier, E. (2012). A programmable dual-rna-guided dna endonuclease in adaptive bacterial immunity. *Science (New York, N.Y.)*, 337(22745249):816–821.

Kawai, H., Allende, M. L., Wada, R., Kono, M., Sango, K., Deng, C., Miyakawa, T., Crawley, J. N., Werth, N., Bierfreund, U., Sandhoff, K., and Proia, R. L. (2001). Mice expressing only monosialoganglioside gm3 exhibit lethal audiogenic seizures*. *Journal of Biological Chemistry*, 276(10):6885–6888.

Kawakami, K. (2007). Tol2: a versatile gene transfer vector in vertebrates. *Genome Biology*, 8(1):S7.

Kelm, S., Pelz, A., Schauer, R., Filbin, M. T., Tang, S., de Bellard, M.-E., Schnaar, R. L., Mahoney, J. A., Hartnell, A., Bradfield, P., and Crocker, P. R. (1994). Sialoadhesin, myelin-associated glycoprotein and cd22 define a new family of sialic acid-dependent adhesion molecules of the immunoglobulin superfamily. *Current Biology*, 4(11):965–972.

Kirby, B. B., Takada, N., Latimer, A. J., Shin, J., Carney, T. J., Kelsh, R. N., and Appel, B. (2006). In vivo time-lapse imaging shows dynamic oligodendrocyte progenitor behavior during zebrafish development. *Nature neuroscience*, 9:1506–1511.

Klenk, E. (1941). Neuraminsäure, das spaltprodukt eines neuen gehirnlipoids. *Hoppe-Seyler´s Zeitschrift Für Physiologische Chemie*, 268(1-2):50–58.

Klenk, E. (1942). Über die ganglioside, eine neue gruppe von zuckerhaltigen gehirnlipoiden. *Hoppe-Seyler´s Zeitschrift Für Physiologische Chemie*, 273(1-2):76–86.

Klingseisen, A., Ristoiu, A.-M., Kegel, L., Sherman, D. L., Rubio-Brotons, M., Almeida, R. G., Koudelka, S., Benito-Kwiecinski, S. K., Poole, R. J., Brophy, P. J., and Lyons, D. A. (2019). Oligodendrocyte neurofascin independently regulates both myelin targeting and sheath growth in the cns. *Developmental cell*, 51:730–744.e6.

Koch, T., Brugger, T., Bach, A., Gennarini, G., and Trotter, J. (1997). Expression of the immunoglobulin superfamily cell adhesion molecule f3 by oligodendrocyte-lineage cells. *Glia*, 19:199–212.

Kolter, T., Proia, R. L., and Sandhoff, K. (2002). Combinatorial ganglioside biosynthesis. *The Journal of biological chemistry*, 277:25859–25862.

Kotani, M., Ozawa, H., Kawashima, I., Ando, S., and Tai, T. (1992). Generation of one set of monoclonal antibodies specific for a-pathway ganglio-series gangliosides. *Biochimica et biophysica acta*, 1117:97–103.

Kotani, M., Terashima, T., and Tai, T. (1995). Developmental changes of ganglioside expressions in postnatal rat cerebellar cortex. *Brain research*, 700:40–58.

Koudelka, S., Voas, M. G., Almeida, R. G., Baraban, M., Soetaert, J., Meyer, M. P., Talbot, W. S., and Lyons, D. A. (2016). Individual neuronal subtypes exhibit diversity in cns myelination mediated by synaptic vesicle release. *Current biology : CB*, 26:1447–1455.

Kozak, M. (1984). Point mutations close to the aug initiator codon affect the efficiency of translation of rat preproinsulin in vivo. *Nature*, 308(5956):241–246.

Kracun, I., Rosner, H., Drnovsek, V., Vukelic, Z., Cosovic, C., Trbojevic-Cepe, M., and Kubat, M. (1992). Gangliosides in the human brain development and aging. *Neurochemistry international*, 20:421–431.

Kriebel, M., Wuchter, J., Trinks, S., and Volkmer, H. (2012). Neurofascin: A switch between neuronal plasticity and stability. *The International Journal of Biochemistry & Cell Biology*, 44(5):694–697.

Krämer, E.-M., Koch, T., Niehaus, A., and Trotter, J. (1997). Oligodendrocytes direct glycosyl phosphatidylinositol-anchored proteins to the myelin sheath in glycosphingolipid-rich complexes*. *Journal of Biological Chemistry*, 272(14):8937–8945.

Kruse, J., Mailhammer, R., Wernecke, H., Faissner, A., Sommer, I., Goridis, C., and Schachner, M. (1984). Neural cell adhesion molecules and myelin-associated glycoprotein share a common carbohydrate moiety recognized by monoclonal antibodies l2 and hnk-1. *Nature*, 311:153–155.

Kucenas, S., Takada, N., Park, H.-C., Woodruff, E., Broadie, K., and Appel, B. (2008). Cns-derived glia ensheath peripheral nerves and mediate motor root development. *Nature neuroscience*, 11:143–151.

Kunz, B., Lierheimer, R., Rader, C., Spirig, M., Ziegler, U., and Sonderegger, P. (2002). Axonin-1/tag-1 mediates cell-cell adhesion by a cis-assisted trans-interaction. *The Journal of biological chemistry*, 277:4551–4557.

Kwan, K. M., Fujimoto, E., Grabher, C., Mangum, B. D., Hardy, M. E., Campbell, D. S., Parant, J. M., Yost, H. J., Kanki, J. P., and Chien, C.-B. (2007). The tol2kit: A multisite gateway-based construction kit for tol2 transposon transgenesis constructs. *Developmental Dynamics*, 236(11):3088–3099.

Labasque, M., Hivert, B., Nogales-Gadea, G., Querol, L., Illa, I., and Faivre-Sarrailh, C. (2014). Specific contactin n-glycans are implicated in neurofascin binding and autoimmune targeting in peripheral neuropathies. *The Journal of biological chemistry*, 289:7907–7918.

Labun, K., Montague, T. G., Krause, M., Torres Cleuren, Y. N., Tjeldnes, H., and Valen, E. (2019). Chopchop v3: expanding the crispr web toolbox beyond genome editing. *Nucleic acids research*, 47:W171–W174.

Lahiri, S. and Futerman, A. (2007). The metabolism and function of sphingolipids and glycosphingolipids. *Cellular and Molecular Life Sciences*, 64:2270–2284.

Lai, C., Brow, M. A., Nave, K. A., Noronha, A. B., Quarles, R. H., Bloom, F. E., Milner, R. J., and Sutcliffe, J. G. (1987). Two forms of 1b236/myelin-associated glycoprotein, a cell adhesion molecule for postnatal neural development, are produced by alternative splicing. *Proceedings of the National Academy of Sciences of the United States of America*, 84:4337–4341.

Lambert, M. J., Olsen, K. G., and Cooper, C. D. (2014). Gene duplication followed by exon structure divergence substitutes for alternative splicing in zebrafish. *Gene*, 546:271–276.

Ledeen, R. (1985). Gangliosides of the neuron. *Trends in Neurosciences*, 8:169–174.

Lee, S., Leach, M. K., Redmond, S. A., Chong, S. Y. C., Mellon, S. H., Tuck, S. J., Feng, Z.-Q., Corey, J. M., and Chan, J. R. (2012). A culture system to study oligodendrocyte myelination processes using engineered nanofibers. *Nature methods*, 9:917–922.

Lehmann, F., Gäthje, H., Kelm, S., and Dietz, F. (2004). Evolution of sialic acid-binding proteins: molecular cloning and expression of fish siglec-4. *Glycobiology*, 14:959–968.

Letunic, I. and Bork, P. (2017). 20 years of the smart protein domain annotation resource. *Nucleic Acids Research*, 46(D1):D493–D496.

Li, C., Tropak, M. B., Gerlai, R., Clapoff, S., Abramow-Newerly, W., Trapp, B., Peterson, A., and Roder, J. (1994). Myelination in the absence of myelin-associated glycoprotein. *Nature*, 369(6483):747–750.

Li, H., Lu, Y., Smith, H. K., and Richardson, W. D. (2007). Olig1 and sox10 interact synergistically to drive myelin basic protein transcription in oligodendrocytes. *J. Neurosci.*, 27(52):14375.

Lieberoth, A., Splittstoesser, F., Katagihallimath, N., Jakovcevski, I., Loers, G., Ranscht, B., Karagogeos, D., Schachner, M., and Kleene, R. (2009). Lewis(x) and alpha2,3-sialyl glycans and their receptors tag-1, contactin, and l1 mediate cd24-dependent neurite outgrowth. *The Journal of neuroscience : the official journal of the Society for Neuroscience*, 29:6677–6690.

Liebisch, G., Binder, M., Schifferer, R., Langmann, T., Schulz, B., and Schmitz, G. (2006). High throughput quantification of cholesterol and cholesteryl ester by electrospray ionization tandem mass spectrometry (esi-ms/ms). *Biochimica et biophysica acta*, 1761:121–128.

Liebisch, G., Fahy, E., Aoki, J., Dennis, E. A., Durand, T., Ejsing, C. S., Fedorova, M., Feussner, I., Griffiths, W. J., Köfeler, H., Merrill, A. H., Murphy, R. C., O'Donnell, V. B., Oskolkova, O., Subramaniam, S., Wakelam, M. J. O., and Spener, F. (2020). Update on lipid maps classification, nomenclature, and shorthand notation for ms-derived lipid structures. *Journal of lipid research*, 61:1539–1555.

Lieschke, G. J. and Currie, P. D. (2007). Animal models of human disease: zebrafish swim into view. *Nature reviews. Genetics*, 8:353–367.

Liu, H., Focia, P. J., and He, X. (2011). Homophilic adhesion mechanism of neurofascin, a member of the l1 family of neural cell adhesion molecules. *The Journal of biological chemistry*, 286:797–805.

Liu, P., Du, J.-l., and He, C. (2013). Developmental pruning of early-stage myelin segments during cns myelination in vivo. *Cell Research*, 23(7):962–964.

Liu, Y., Wada, R., Kawai, H., Sango, K., Deng, C., Tai, T., McDonald, M. P., Araujo, K., Crawley, J. N., Bierfreund, U., Sandhoff, K., Suzuki, K., and Proia, R. L. (1999). A genetic model of substrate deprivation therapy for a glycosphingolipid storage disorder. *The Journal of Clinical Investigation*, 103(4):497–505.

Lu, J., Peatman, E., Tang, H., Lewis, J., and Liu, Z. (2012). Profiling of gene duplication patterns of sequenced teleost genomes: evidence for rapid lineage-specific genome expansion mediated by recent tandem duplications. *BMC Genomics*, 13(1):246.

Lu, J., Peatman, E., Wang, W., Yang, Q., Abernathy, J., Wang, S., Kucuktas, H., and Liu, Z. (2010). Alternative splicing in teleost fish genomes: same-species and cross-species analysis and comparisons. *Molecular Genetics and Genomics*, 283(6):531–539.

Ma, Q., Kobayashi, M., Sugiura, M., Ozaki, N., Nishio, K., Shiraishi, Y., Furukawa, K., Furukawa, K., and Sugiura, Y. (2003). Morphological study of disordered myelination and the degeneration of nerve fibers in the spinal cord of mice lacking complex gangliosides. *Archives of Histology and Cytology*, 66(1):37–44.

Malfroy, B., Bakhit, C., Bloom, F. E., Sutcliffe, J. G., and Milner, R. J. (1985). Brain-specific polypeptide 1b236 exists in multiple molecular forms. *Proceedings of the National Academy of Sciences of the United States of America*, 82:2009–2013.

Marcus, J., Dupree, J. L., and Popko, B. (2002). Myelin-associated glycoprotein and myelin galactolipids stabilize developing axo-glial interactions. *The Journal of cell biology*, 156:567–577.

Marcus, J. and Popko, B. (2002). Galactolipids are molecular determinants of myelin development and axo–glial organization. *Biochimica et Biophysica Acta (BBA) - General Subjects*, 1573(3):406–413. Developmental Glycobiology.

McGonigal, R., Barrie, J. A., Yao, D., McLaughlin, M., Cunningham, M. E., Rowan, E. G., and Willison, H. J. (2019). Glial sulfatides and neuronal complex gangliosides are functionally interdependent in maintaining myelinating axon integrity. *Journal of Neuroscience*, 39(1):63–77.

McKerracher, L., David, S., Jackson, D., Kottis, V., Dunn, R., and Braun, P. (1994). Identification of myelin-associated glycoprotein as a major myelin-derived inhibitor of neurite growth. *Neuron*, 13(4):805–811.

Menegoz, M., Gaspar, P., Le Bert, M., Galvez, T., Burgaya, F., Palfrey, C., Ezan, P., Arnos, F., and Girault, J. A. (1997). Paranodin, a glycoprotein of neuronal paranodal membranes. *Neuron*, 19:319–331.

Menon, K., Rasband, M. N., Taylor, C. M., Brophy, P., Bansal, R., and Pfeiffer, S. E. (2003). The myelin–axolemmal complex: biochemical dissection and the role of galactosphingolipids. *Journal of Neurochemistry*, 87(4):995–1009.

Mensch, S., Baraban, M., Almeida, R., Czopka, T., Ausborn, J., El Manira, A., and Lyons, D. A. (2015). Synaptic vesicle release regulates myelin sheath number of individual oligodendrocytes in vivo. *Nature Neuroscience*, 18(25849985):628–630.

Min, Y., Kristiansen, K., Boggs, J. M., Husted, C., Zasadzinski, J. A., and Israelachvili, J. (2009). Interaction forces and adhesion of supported myelin lipid bilayers modulated by myelin basic protein. *Proceedings of the National Academy of Sciences of the United States of America*, 106:3154–3159.

Münzel, E. J., Schaefer, K., Obirei, B., Kremmer, E., Burton, E. A., Kuscha, V., Becker, C. G., Brösamle, C., Williams, A., and Becker, T. (2012). Claudin k is specifically expressed in cells that form myelin during development of the nervous system and regeneration of the optic nerve in adult zebrafish. *Glia*, 60(2):253–270.

Montag, D., Giese, K. P., Bartsch, U., Martini, R., Lang, Y., Blüthmann, H., Karthigasan, J., Kirschner, D. A., Wintergerst, E. S., Nave, K.-A., Zielasek, J., Toyka, K. V., Lipp, H.-P., and Schachner, M. (1994). Mice deficient for the glycoprotein show subtle abnormalities in myelin. *Neuron*, 13(1):229–246.

Morris, J. K., Willard, B. B., Yin, X., Jeserich, G., Kinter, M., and Trapp, B. D. (2004). The 36k protein of zebrafish cns myelin is a short-chain dehydrogenase. *Glia*, 45(4):378–391.

Mukhopadhyay, G., Doherty, P., Walsh, F. S., Crocker, P. R., and Filbin, M. T. (1994). A novel role for myelin-associated glycoprotein as an inhibitor of axonal regeneration. *Neuron*, 13(3):757–767.

Nagarajan, B., Harder, A., Japp, A., Häberlein, F., Mingardo, E., Kleinert, H., Yilmaz, z., Zoons, A., Rau, B., Christ, A., Kubitscheck, U., Eiberger, B., Sandhoff, R., Eckhardt, M., Hartmann, D., and Odermatt, B. (2020). Cns myelin protein 36k regulates oligodendrocyte differentiation through notch. *Glia*, 68(3):509–527.

Nans, A., Einheber, S., Salzer, J. L., and Stokes, D. L. (2011). Electron tomography of paranodal septate-like junctions and the associated axonal and glial cytoskeletons in the central nervous system. *Journal of Neuroscience Research*, 89(3):310–319.

Nave, K.-A. and Werner, H. B. (2014). Myelination of the nervous system: Mechanisms and functions. *Annu. Rev. Cell Dev. Biol.*, 30(1):503–533.

Nawaz, S., Schweitzer, J., Jahn, O., and Werner, H. B. (2013). Molecular evolution of myelin basic protein, an abundant structural myelin component. *Glia*, 61(8):1364–1377.

Nawaz, S., Sánchez, P., Schmitt, S., Snaidero, N., Mitkovski, M., Velte, C., Brückner, B. R., Alexopoulos, I., Czopka, T., Jung, S. Y., Rhee, J. S., Janshoff, A., Witke, W., Schaap, I. A. T., Lyons, D. A., and Simons, M. (2015). Actin filament turnover drives leading edge growth during myelin sheath formation in the central nervous system. *Developmental cell*, 34:139–151.

Nelson, D. L. and Cox, M. M. (2017). *Lehninger Principles of Biochemistry, 7h Edition*. 7th edition edition.

Nikolaienko, R. M., Hammel, M., Dubreuil, V., Zalmai, R., Hall, D. R., Mehzabeen, N., Karuppan, S. J., Harroch, S., Stella, S. L., and Bouyain, S. (2016). Structural basis for interactions between

contactin family members and protein-tyrosine phosphatase receptor type g in neural tissues. *The Journal of biological chemistry*, 291:21335–21349.

Ogawa, Y., Schafer, D. P., Horresh, I., Bar, V., Hales, K., Yang, Y., Susuki, K., Peles, E., Stankewich, M. C., and Rasband, M. N. (2006). Spectrins and ankyrinb constitute a specialized paranodal cytoskeleton. *The Journal of neuroscience : the official journal of the Society for Neuroscience*, 26:5230–5239.

Çolakoğlu, G., Bergstrom-Tyrberg, U., Berglund, E. O., and Ranscht, B. (2014). Contactin-1 regulates myelination and nodal/paranodal domain organization in the central nervous system. *Proceedings of the National Academy of Sciences of the United States of America*, 111:E394–E403.

Olsen, A. S. B. and Færgeman, N. J. (2017). Sphingolipids: membrane microdomains in brain development, function and neurological diseases. *Open biology*, 7.

Ormö, M., Cubitt, A. B., Kallio, K., Gross, L. A., Tsien, R. Y., and Remington, S. J. (1996). Crystal structure of the aequorea victoria green fluorescent protein. *Science (New York, N.Y.)*, 273:1392–1395.

Ozawa, H., Kotani, M., Kawashima, I., and Tai, T. (1992). Generation of one set of monoclonal antibodies specific for b-pathway ganglio-series gangliosides. *Biochimica et biophysica acta*, 1123:184–190.

Pan, B., Fromholt, S. E., Hess, E. J., Crawford, T. O., Griffin, J. W., Sheikh, K. A., and Schnaar, R. L. (2005). Myelin-associated glycoprotein and complementary axonal ligands, gangliosides, mediate axon stability in the cns and pns: Neuropathology and behavioral deficits in single- and double-null mice. *Experimental Neurology*, 195(1):208–217.

Park, J., Liu, B., Chen, T., Li, H., Hu, X., Gao, J., Zhu, Y., Zhu, Q., Qiang, B., Yuan, J., Peng, X., and Qiu, M. (2008). Disruption of nectin-like cell adhesion molecule leads to delayed axonal myelination in the cns. *J. Neurosci.*, 28(48):12815.

Pedraza, L., Huang, J. K., and Colman, D. (2009). Disposition of axonal caspr with respect to glial cell membranes: Implications for the process of myelination. *Journal of neuroscience research*, 87:3480–3491.

Pedraza, L., Huang, J. K., and Colman, D. R. (2001). Organizing principles of the axoglial apparatus. *Neuron*, 30:335–344.

Peles, E., Nativ, M., Lustig, M., Grumet, M., Schilling, J., Martinez, R., Plowman, G. D., and Schlessinger, J. (1997). Identification of a novel contactin-associated transmembrane receptor with multiple domains implicated in protein-protein interactions. *The EMBO journal*, 16:978–988.

Petersen, T. N., Brunak, S., von Heijne, G., and Nielsen, H. (2011). Signalp 4.0: discriminating signal peptides from transmembrane regions. *Nature Methods*, 8(10):785–786.

Pillai, A. M., Thaxton, C., Pribisko, A. L., Cheng, J.-G., Dupree, J. L., and Bhat, M. A. (2009). Spatiotemporal ablation of myelinating glia-specific neurofascin (nfasc nf155) in mice reveals gradual loss of paranodal axoglial junctions and concomitant disorganization of axonal domains. *Journal of neuroscience research*, 87:1773–1793.

Pinatel, D. and Faivre-Sarrailh, C. (2021). Assembly and function of the juxtaparanodal kv1 complex in health and disease. *Life*, 11(1).

Piomelli, D., Astarita, G., and Rapaka, R. (2007). A neuroscientist's guide to lipidomics. *Nature reviews. Neuroscience*, 8:743–754.

Piston, D. W. and Kremers, G.-J. (2007). Fluorescent protein fret: the good, the bad and the ugly. *Trends in Biochemical Sciences*, 32(9):407–414.

Poitelon, Y., Kopec, A. M., and Belin, S. (2020). Myelin fat facts: An overview of lipids and fatty acid metabolism. *Cells*, 9(4).

Poliak, S., Gollan, L., Martinez, R., Custer, A., Einheber, S., Salzer, J. L., Trimmer, J. S., Shrager, P., and Peles, E. (1999). Caspr2, a new member of the neurexin superfamily, is localized at the juxtaparanodes of myelinated axons and associates with k+ channels. *Neuron*, 24(4):1037–1047.

Poltorak, M., Sadoul, R., Keilhauer, G., Landa, C., Fahrig, T., and Schachner, M. (1987). Myelin-associated glycoprotein, a member of the l2/hnk-1 family of neural cell adhesion molecules, is involved in neuron-oligodendrocyte and oligodendrocyte-oligodendrocyte interaction. *The Journal of cell biology*, 105:1893–1899.

Pomicter, A. D., Shroff, S. M., Fuss, B., Sato-Bigbee, C., Brophy, P. J., Rasband, M. N., Bhat, M. A., and Dupree, J. L. (2010). Novel forms of neurofascin 155 in the central nervous system: alterations in paranodal disruption models and multiple sclerosis. *Brain : a journal of neurology*, 133:389–405.

Posse de Chaves, E. and Sipione, S. (2010). Sphingolipids and gangliosides of the nervous system in membrane function and dysfunction. *FEBS letters*, 584:1748–1759.

Preston, M. A. and Macklin, W. B. (2015). Zebrafish as a model to investigate cns myelination. *Glia*, 63(2):177–193.

Prinetti, A., Chigorno, V., Tettamanti, G., and Sonnino, S. (2000). Sphingolipid-enriched membrane domains from rat cerebellar granule cells differentiated in culture. a compositional study. *The Journal of biological chemistry*, 275:11658–11665.

Pronker, M. F., Lemstra, S., Snijder, J., Heck, A. J. R., Thies-Weesie, D. M. E., Pasterkamp, R. J., and Janssen, B. J. C. (2016). Structural basis of myelin-associated glycoprotein adhesion and signalling. *Nature communications*, 7:13584.

Quarles, R. H. (2007). Myelin-associated glycoprotein (mag): past, present and beyond. *Journal of neurochemistry*, 100:1431–1448.

Rasband, M. N. and Peles, E. (2021). Mechanisms of node of ranvier assembly. *Nature Reviews Neuroscience*, 22(1):7–20.

Rasband, M. N., Taylor, C. M., and Bansal, R. (2003). Paranodal transverse bands are required for maintenance but not initiation of nav1.6 sodium channel clustering in cns optic nerve axons. *Glia*, 44(2):173–182.

Reid, R. A., Bronson, D. D., Young, K. M., and Hemperly, J. J. (1994). Identification and characterization of the human cell adhesion molecule contactin. *Brain research. Molecular brain research*, 21:1–8.

Ren, Q. and Bennett, V. (1998). Palmitoylation of neurofascin at a site in the membrane-spanning domain highly conserved among the l1 family of cell adhesion molecules. *Journal of Neurochemistry*, 70(5):1839–1849.

Rios, J. C., Melendez-Vasquez, C. V., Einheber, S., Lustig, M., Grumet, M., Hemperly, J., Peles, E., and Salzer, J. L. (2000). Contactin-associated protein (caspr) and contactin form a complex that is targeted to the paranodal junctions during myelination. *The Journal of neuroscience : the official journal of the Society for Neuroscience*, 20:8354–8364.

Rios, J. C., Rubin, M., St Martin, M., Downey, R. T., Einheber, S., Rosenbluth, J., Levinson, S. R., Bhat, M., and Salzer, J. L. (2003). Paranodal interactions regulate expression of sodium channel subtypes and provide a diffusion barrier for the node of ranvier. *The Journal of neuroscience : the official journal of the Society for Neuroscience*, 23:7001–7011.

Rivers, L. E., Young, K. M., Rizzi, M., Jamen, F., Psachoulia, K., Wade, A., Kessaris, N., and Richardson, W. D. (2008). Pdgfra/ng2 glia generate myelinating oligodendrocytes and piriform projection neurons in adult mice. *Nature Neuroscience*, 11(12):1392–1401.

Robinson, N. B., Krieger, K., Khan, F. M., Huffman, W., Chang, M., Naik, A., Yongle, R., Hameed, I., Krieger, K., Girardi, L. N., and Gaudino, M. (2019). The current state of animal models in research: A review. *International Journal of Surgery*, 72:9–13.

Russo, D., Capolupo, L., Loomba, J. S., Sticco, L., and D'Angelo, G. (2018). Glycosphingolipid metabolism in cell fate specification. *Journal of cell science*, 131.

Saito, M. and Sugiyama, K. (2002). Characterization of nuclear gangliosides in rat brain: concentration, composition, and developmental changes. *Archives of biochemistry and biophysics*, 398:153–159.

Salzer, J. L., Holmes, W. P., and Colman, D. R. (1987). The amino acid sequences of the myelin-associated glycoproteins: homology to the immunoglobulin gene superfamily. *The Journal of cell biology*, 104:957–965.

Sampaio, J. L., Gerl, M. J., Klose, C., Ejsing, C. S., Beug, H., Simons, K., and Shevchenko, A. (2011). Membrane lipidome of an epithelial cell line. *Proceedings of the National Academy of Sciences of the United States of America*, 108:1903–1907.

Sato, I., Obata, Y., Kasahara, K., Nakayama, Y., Fukumoto, Y., Yamasaki, T., Yokoyama, K. K., Saito, T., and Yamaguchi, N. (2009). Differential trafficking of Src, Lyn, Yes and Fyn is specified by the state of palmitoylation in the SH4 domain. *Journal of Cell Science*, 122(7):965–975.

Schaefer, K. and Brösamle, C. (2009). Zwilling-a and -b, two related myelin proteins of teleosts, which originate from a single bicistronic transcript. *Molecular biology and evolution*, 26:495–499.

Schafer, D. P., Bansal, R., Hedstrom, K. L., Pfeiffer, S. E., and Rasband, M. N. (2004). Does paranode formation and maintenance require partitioning of neurofascin 155 into lipid rafts? *The Journal of neuroscience : the official journal of the Society for Neuroscience*, 24:3176–3185.

Scheiffele, P., Roth, M. G., and Simons, K. (1997). Interaction of influenza virus haemagglutinin with sphingolipid-cholesterol membrane domains via its transmembrane domain. *The EMBO journal*, 16:5501–5508.

Schmitt, S., Castelvetri, L. C., and Simons, M. (2015). Metabolism and functions of lipids in myelin. *Biochimica et biophysica acta*, 1851:999–1005.

Schnaar, R. L. (2016). Gangliosides of the vertebrate nervous system. *Journal of molecular biology*, 428(27261254):3325–3336.

Schnaar, R. L. (2019). The biology of gangliosides. *Advances in carbohydrate chemistry and biochemistry*, 76:113–148.

Schnaar, R. L., Gerardy-Schahn, R., and Hildebrandt, H. (2014). Sialic acids in the brain: gangliosides and polysialic acid in nervous system development, stability, disease, and regeneration. *Physiological reviews*, 94:461–518.

Schnaar, R. L. and Lopez, P. H. (2009). Myelin-associated glycoprotein and its axonal receptors. *Journal of Neuroscience Research*, 87(15):3267–3276.

Schwardt, O., Kelm, S., and Ernst, B. (2015). Siglec-4 (mag) antagonists: From the natural carbohydrate epitope to glycomimetics. *Topics in current chemistry*, 367:151–200.

Schweitzer, J., Becker, T., Schachner, M., Nave, K.-A., and Werner, H. (2006). Evolution of myelin proteolipid proteins: gene duplication in teleosts and expression pattern divergence. *Molecular and cellular neurosciences*, 31:161–177.

Schweitzer, J., Gimnopoulos, D., Lieberoth, B. C., Pogoda, H.-M., Feldner, J., Ebert, A., Schachner, M., Becker, T., and Becker, C. G. (2007). Contactin1a expression is associated with oligodendrocyte differentiation and axonal regeneration in the central nervous system of zebrafish. *Molecular and Cellular Neuroscience*, 35(2):194–207.

Sedzik, J., Jastrzebski, J. P., and Grandis, M. (2015). Glycans of myelin proteins. *Journal of neuroscience research*, 93:1–18.

Senn, H. J., Orth, M., Fitzke, E., Wieland, H., and Gerok, W. (1989). Gangliosides in normal human serum. concentration, pattern and transport by lipoproteins. *European journal of biochemistry*, 181:657–662.

Shannon, C. (1949). Communication in the presence of noise. *Proceedings of the IRE*, 37(1):10–21.

Sheikh, K. A., Sun, J., Liu, Y., Kawai, H., Crawford, T. O., Proia, R. L., Griffin, J. W., and Schnaar, R. L. (1999). Mice lacking complex gangliosides develop wallerian degeneration and myelination defects. *Proceedings of the National Academy of Sciences*, 96(13):7532–7537.

Sherman, D. L., Tait, S., Melrose, S., Johnson, R., Zonta, B., Court, F. A., Macklin, W. B., Meek, S., Smith, A. J. H., Cottrell, D. F., and Brophy, P. J. (2005). Neurofascins are required to establish axonal domains for saltatory conduction. *Neuron*, 48:737–742.

Siddiqui, S. S., Matar, R., Merheb, M., Hodeify, R., Vazhappilly, C. G., Marton, J., Shamsuddin, S. A., and Al Zouabi, H. (2019). Siglecs in brain function and neurological disorders. *Cells*, 8.

Siems, S. B., Jahn, O., Hoodless, L. J., Jung, R. B., Hesse, D., Möbius, W., Czopka, T., and Werner, H. B. (2021). Proteome profile of myelin in the zebrafish brain. *Frontiers in Cell and Developmental Biology*, 9:678.

Simons, K. and Gerl, M. J. (2010). Revitalizing membrane rafts: new tools and insights. *Nature reviews. Molecular cell biology*, 11:688–699.

Simons, K. and Sampaio, J. L. (2011). Membrane organization and lipid rafts. *Cold Spring Harbor perspectives in biology*, 3:a004697.

Singer, S. J. and Nicolson, G. L. (1972). The fluid mosaic model of the structure of cell membranes. *Science (New York, N.Y.)*, 175:720–731.

Sipione, S., Monyror, J., Galleguillos, D., Steinberg, N., and Kadam, V. (2020). Gangliosides in the brain: Physiology, pathophysiology and therapeutic applications. *Frontiers in Neuroscience*, 14:1004.

Snaidero, N., Möbius, W., Czopka, T., Hekking, L. P., Mathisen, C., Verkleij, D., Goebbels, S., Edgar, J., Merkler, D., Lyons, D., Nave, K.-A., and Simons, M. (2014). Myelin membrane wrapping of cns axons by pi(3,4,5)p3-dependent polarized growth at the inner tongue. *Cell*, 156(1):277–290.

Sonnino, S., Mauri, L., Chigorno, V., and Prinetti, A. (2007). Gangliosides as components of lipid membrane domains. *Glycobiology*, 17:1R–13R.

Stadelmann, C., Timmler, S., Barrantes-Freer, A., and Simons, M. (2019). Myelin in the central nervous system: Structure, function, and pathology. *Physiological Reviews*, 99(3):1381–1431.

Stassart, R. M., Möbius, W., Nave, K.-A., and Edgar, J. M. (2018). The axon-myelin unit in development and degenerative disease. *Frontiers in neuroscience*, 12(30050403):467–467.

Sternberger, N. H., Quarles, R. H., Itoyama, Y., and Webster, H. D. (1979). Myelin-associated glycoprotein demonstrated immunocytochemically in myelin and myelin-forming cells of developing rat. *Proceedings of the National Academy of Sciences of the United States of America*, 76(3):1510–1514.

Strenge, K., Schauer, R., and Kelm, S. (1999). Binding partners for the myelin-associated glycoprotein of n2a neuroblastoma cells. *FEBS Letters*, 444(1):59–64.

Sturgill, E. R., Aoki, K., Lopez, P. H. H., Colacurcio, D., Vajn, K., Lorenzini, I., Majić, S., Yang, W. H., Heffer, M., Tiemeyer, M., Marth, J. D., and Schnaar, R. L. (2012). Biosynthesis of the major brain gangliosides gd1a and gt1b. *Glycobiology*, 22:1289–1301.

Sturrock, R. R. (1980). Myelination of the mouse corpus callosum. *Neuropathology and applied neurobiology*, 6:415–420.

Surma, M. A., Herzog, R., Vasilj, A., Klose, C., Christinat, N., Morin-Rivron, D., Simons, K., Masoodi, M., and Sampaio, J. L. (2015). An automated shotgun lipidomics platform for high throughput, comprehensive, and quantitative analysis of blood plasma intact lipids. *European journal of lipid science and technology : EJLST*, 117:1540–1549.

Susuki, K., Baba, H., Tohyama, K., Kanai, K., Kuwabara, S., Hirata, K., Furukawa, K., Furukawa, K., Rasband, M. N., and Yuki, N. (2007). Gangliosides contribute to stability of paranodal junctions and ion channel clusters in myelinated nerve fibers. *Glia*, 55:746–757.

Sutcliffe, J. and Milner, R. J. (1984). Brain specific gene expression. *Trends in Biochemical Sciences*, 9(3):95 – 99.

Svennerholm, L., Boström, K., Fredman, P., Månsson, J. E., Rosengren, B., and Rynmark, B. M. (1989). Human brain gangliosides: developmental changes from early fetal stage to advanced age. *Biochimica et biophysica acta*, 1005:109–117.

Svennerholm, L., Boström, K., Jungbjer, B., and Olsson, L. (1994). Membrane lipids of adult human brain: Lipid composition of frontal and temporal lobe in subjects of age 20 to 100 years. *Journal of Neurochemistry*, 63(5):1802–1811.

Takamiya, K., Yamamoto, A., Furukawa, K., Yamashiro, S., Shin, M., Okada, M., Fukumoto, S., Haraguchi, M., Takeda, N., Fujimura, K., Sakae, M., Kishikawa, M., Shiku, H., Furukawa, K., and Aizawa, S. (1996). Mice with disrupted gm2/gd2 synthase gene lack complex gangliosides but exhibit only subtle defects in their nervous system. *Proceedings of the National Academy of Sciences*, 93(20):10662–10667.

Tang, S., Qiu, J., Nikulina, E., and Filbin, M. T. (2001). Soluble myelin-associated glycoprotein released from damaged white matter inhibits axonal regeneration. *Molecular and Cellular Neuroscience*, 18(3):259–269.

Tang, S., Woodhall, R. W., Shen, Y. J., deBellard, M. E., Saffell, J. L., Doherty, P., Walsh, F. S., and Filbin, M. T. (1997). Soluble myelin-associated glycoprotein (mag) foundin vivoinhibits axonal regeneration. *Molecular and Cellular Neuroscience*, 9(5):333–346.

Thaxton, C., Pillai, A. M., Pribisko, A. L., Labasque, M., Dupree, J. L., Faivre-Sarrailh, C., and Bhat, M. A. (2010). In vivo deletion of immunoglobulin domains 5 and 6 in neurofascin (nfasc) reveals domain-specific requirements in myelinated axons. *The Journal of neuroscience : the official journal of the Society for Neuroscience*, 30:4868–4876.

Traka, M., Goutebroze, L., Denisenko, N., Bessa, M., Nifli, A., Havaki, S., Iwakura, Y., Fukamauchi, F., Watanabe, K., Soliven, B., Girault, J.-A., and Karagogeos, D. (2003). Association of tag-1 with caspr2 is essential for the molecular organization of juxtaparanodal regions of myelinated fibers. *J Cell Biol*, 162(6):1161–1172.

Trapp, B. D. (1990). Myelin-associated glycoprotein location and potential functionsa. *Annals of the New York Academy of Sciences*, 605(1):29–43.

Trapp, B. D., Andrews, S. B., Cootauco, C., and Quarles, R. (1989). The myelin-associated glycoprotein is enriched in multivesicular bodies and periaxonal membranes of actively myelinating oligodendrocytes. *Journal of Cell Biology*, 109(5):2417–2426.

Tuvia, S., Garver, T. D., and Bennett, V. (1997). The phosphorylation state of the figqy tyrosine of neurofascin determines ankyrin-binding activity and patterns of cell segregation. *Proceedings of the National Academy of Sciences of the United States of America*, 94:12957–12962.

Vagionitis, S., Auer, F., Xiao, Y., Almeida, R. G., Lyons, D. A., and Czopka, T. (2021). Clusters of neuronal neurofascin prefigure node of ranvier position along single axons. *bioRxiv*.

Vajn, K., Plunkett, J. A., Tapanes-Castillo, A., and Oudega, M. (2013a). Axonal regeneration after spinal cord injury in zebrafish and mammals: differences, similarities, translation. *Neuroscience bulletin*, 29:402–410.

Vajn, K., Viljetić, B., Degmečić, I. V., Schnaar, R. L., and Heffer, M. (2013b). Differential distribution of major brain gangliosides in the adult mouse central nervous system. *PloS one*, 8:e75720.

Vandepoele, K., Vos, W., Taylor, J., Meyer, A., and Van de Peer, Y. (2004). Major events in the genome evolution of vertebrates: paranome age and size differs considerably between fishes and land vertebrates. *Proceedings of the National Academy of Sciences of the United States of America*, 101:1638–43.

Vanier, M. T., Holm, M., Ohman, R., and Svennerholm, L. (1971). Developmental profiles of gangliosides in human and rat brain. *Journal of neurochemistry*, 18:581–592.

Viljetić, B., Labak, I., Majić, S., Stambuk, A., and Heffer, M. (2012). Distribution of mono-, di- and trisialo gangliosides in the brain of actinopterygian fishes. *Biochimica et biophysica acta*, 1820:1437–1443.

Vinson, M., Strijbos, P. J., Rowles, A., Facci, L., Moore, S. E., Simmons, D. L., and Walsh, F. S. (2001). Myelin-associated glycoprotein interacts with ganglioside gt1b: A mechanism for neurite outgrowth inhibition*. *Journal of Biological Chemistry*, 276(23):20280–20285.

Volkmer, H., Hassel, B., Wolff, J. M., Frank, R., and Rathjen, F. G. (1992). Structure of the axonal surface recognition molecule neurofascin and its relationship to a neural subgroup of the immunoglobulin superfamily. *The Journal of cell biology*, 118:149–161.

Volkmer, H., Zacharias, U., Nörenberg, U., and Rathjen, F. G. (1998). Dissection of Complex Molecular Interactions of Neurofascin with Axonin-1, F11, and Tenascin-R, Which Promote Attachment and Neurite Formation of Tectal Cells . *Journal of Cell Biology*, 142(4):1083–1093.

Vyas, A. A., Patel, H. V., Fromholt, S. E., Heffer-Lauc, M., Vyas, K. A., Dang, J., Schachner, M., and Schnaar, R. L. (2002). Gangliosides are functional nerve cell ligands for myelin-associated glycoprotein (mag), an inhibitor of nerve regeneration. *Proceedings of the National Academy of Sciences*, 99(12):8412–8417.

Whittaker, E. T. (1915). On the functions which are represented by the expansions of the interpolation-theory. *Proceedings of the Royal Society of Edinburgh*, 35:181–194.

Wormwood Moser, K. L., Van Aken, G., DeBord, D., Hatcher, N. G., Maxon, L., Sherman, M., Yao, L., and Ekroos, K. (2021). High-defined quantitative snapshots of the ganglioside lipidome using high resolution ion mobility slim assisted shotgun lipidomics. *Analytica chimica acta*, 1146:77–87.

Yamashita, T., Allende, M. L., Kalkofen, D. N., Werth, N., Sandhoff, K., and Proia, R. L. (2005a). Conditional loxp-flanked glucosylceramide synthase allele controlling glycosphingolipid synthesis. *genesis*, 43(4):175–180.

Yamashita, T., Hashiramoto, A., Haluzik, M., Mizukami, H., Beck, S., Norton, A., Kono, M., Tsuji, S., Daniotti, J. L., Werth, N., Sandhoff, R., Sandhoff, K., and Proia, R. L. (2003). Enhanced insulin sensitivity in mice lacking ganglioside gm3. *Proceedings of the National Academy of Sciences*, 100(6):3445–3449.

Yamashita, T., Wada, R., Sasaki, T., Deng, C., Bierfreund, U., Sandhoff, K., and Proia, R. L. (1999). A vital role for glycosphingolipid synthesis during development and differentiation. *Proceedings of the National Academy of Sciences of the United States of America*, 96:9142–9147.

Yamashita, T., Wu, Y.-P., Sandhoff, R., Werth, N., Mizukami, H., Ellis, J. M., Dupree, J. L., Geyer, R., Sandhoff, K., and Proia, R. L. (2005b). Interruption of ganglioside synthesis produces central nervous system degeneration and altered axon–glial interactions. *Proceedings of the National Academy of Sciences*, 102(8):2725–2730.

Yang, F., Moss, L. G., and Phillips, G. N. (1996a). The molecular structure of green fluorescent protein. *Nature biotechnology*, 14:1246–1251.

Yang, L. J., Zeller, C. B., Shaper, N. L., Kiso, M., Hasegawa, A., Shapiro, R. E., and Schnaar, R. L. (1996b). Gangliosides are neuronal ligands for myelin-associated glycoprotein. *Proceedings of the National Academy of Sciences of the United States of America*, 93:814–818.

Yin, L., Maddison, L. A., Li, M., Kara, N., LaFave, M. C., Varshney, G. K., Burgess, S. M., Patton, J. G., and Chen, W. (2015). Multiplex conditional mutagenesis using transgenic expression of cas9 and sgrnas. *Genetics*, 200(25855067):431–441.

Yoshikawa, M., Go, S., Takasaki, K., Kakazu, Y., Ohashi, M., Nagafuku, M., Kabayama, K., Sekimoto, J., Suzuki, S.-i., Takaiwa, K., Kimitsuki, T., Matsumoto, N., Komune, S., Kamei, D., Saito, M., Fujiwara, M., Iwasaki, K., and Inokuchi, J.-i. (2009). Mice lacking ganglioside gm3 synthase exhibit complete hearing loss due to selective degeneration of the organ of corti. *Proceedings of the National Academy of Sciences*, 106(23):9483–9488.

Yu, R. K., Macala, L. J., Taki, T., Weinfield, H. M., and Yu, F. S. (1988). Developmental changes in ganglioside composition and synthesis in embryonic rat brain. *Journal of neurochemistry*, 50:1825–1829.

Yurlova, L., Kahya, N., Aggarwal, S., Kaiser, H.-J., Chiantia, S., Bakhti, M., Pewzner-Jung, Y., Ben-David, O., Futerman, A. H., Brügger, B., and Simons, M. (2011). Self-segregation of myelin membrane lipids in model membranes. *Biophysical journal*, 101:2713–2720.

Zalc, B., Goujet, D., and Colman, D. (2008). The origin of the myelination program in vertebrates. *Current Biology*, 18(12):R511–R512.

Zhang, C., Susuki, K., Zollinger, D. R., Dupree, J. L., and Rasband, M. N. (2013). Membrane domain organization of myelinated axons requires βII spectrin. *The Journal of cell biology*, 203:437–443.

Zhang, T., Trauger, S. A., Vidoudez, C., Doane, K. P., Pluimer, B. R., and Peterson, R. T. (2019). Parallel reaction monitoring reveals structure-specific ceramide alterations in the zebrafish. *Scientific reports*, 9:19939.

Zhu, Y., Li, H., Li, K., Zhao, X., An, T., Hu, X., Park, J., Huang, H., Bin, Y., Qiang, B., Yuan, J., Peng, X., and Qiu, M. (2013). Necl-4/syncam-4 is expressed in myelinating oligodendrocytes but not required for axonal myelination. *PLOS ONE*, 8(5):e64264.

Zöller, I., Büssow, H., Gieselmann, V., and Eckhardt, M. (2005). Oligodendrocyte-specific ceramide galactosyltransferase (cgt) expression phenotypically rescues cgt-deficient mice and demonstrates that cgt activity does not limit brain galactosylceramide level. *Glia*, 52:190–198.

Zonta, B., Tait, S., Melrose, S., Anderson, H., Harroch, S., Higginson, J., Sherman, D. L., and Brophy, P. J. (2008). Glial and neuronal isoforms of neurofascin have distinct roles in the assembly of nodes of ranvier in the central nervous system. *The Journal of cell biology*, 181:1169–1177.

Zuchero, J. B., Fu, M.-M., Sloan, S. A., Ibrahim, A., Olson, A., Zaremba, A., Dugas, J. C., Wienbar, S., Caprariello, A. V., Kantor, C., Leonoudakis, D., Leonoudakus, D., Lariosa-Willingham, K., Kronenberg, G., Gertz, K., Soderling, S. H., Miller, R. H., and Barres, B. A. (2015). Cns myelin wrapping is driven by actin disassembly. *Developmental cell*, 34:152–167.

Appendix

I An Experimental Approach for Detection of Oligodendroglial Caspr Interaction Partners

The results of this dissertation found Caspr-YFP accumulating at the earliest phase of myelination - upon contact of the oligodendroglial membrane with the axonal membrane. Thus, our results hint toward an unknown protein on the oligodendroglial membrane, which interacts with Caspr on the axonal membrane at the initial contact of the two membranes. We tested Nfascb, Cntn1b, and MAG as potential candidates. However, none of these three proteins interact with Caspr from the oligodendroglial side.

This section suggests an experiment to find the "Mister X" on the oligodendroglial membrane. Instead of reversely testing different proteins by genetic modifications, we suggest using a forward screening using a newly generated HuC:Gal4;UAS:Caspr-YFP zebrafish line (Fig. 36).

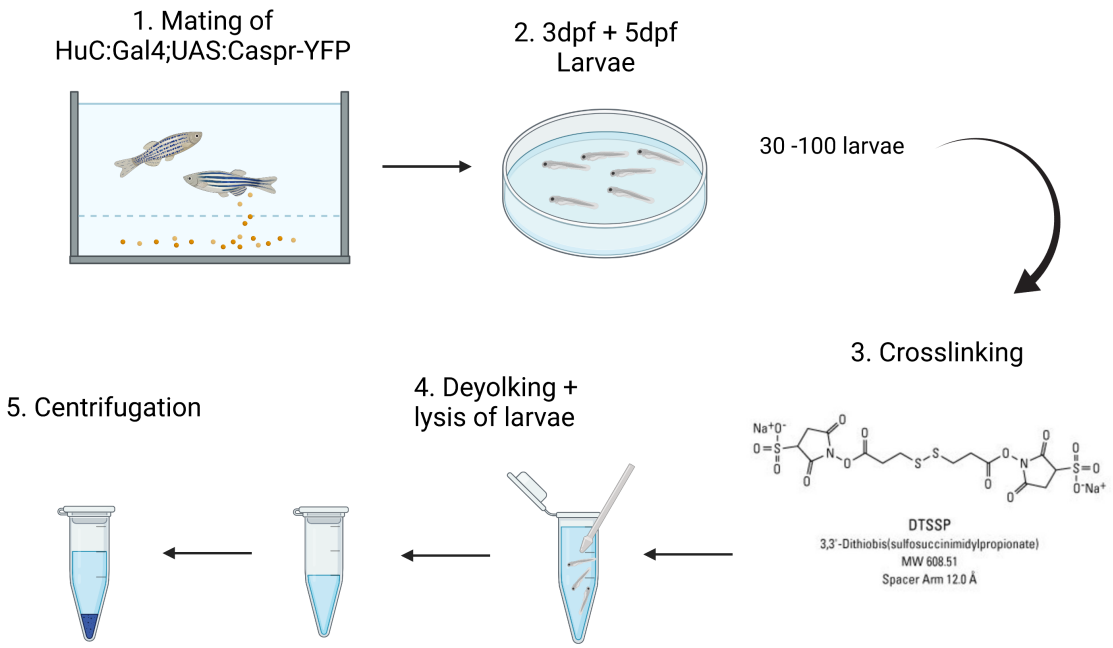

Figure 36: PULLDOWN-APPROACH PART 1 At 3-5 dpf, sorted zebrafish HuC:Gal4;UAS:Caspr-YFP offspring incubate in a cross-linking substance. Then the larvae are deyolked, lysed, and centrifuged. The supernatant should contain the proteins of interest.

After mating, embryos would be sorted for a good green heart expression at 3 dpf. The likelihood of a good Caspr-YFP expression increases with a strong green heart expression. At 3 dpf (early timepoint, when myelination is at the beginning) and 5 dpf (myelination is far developed), 30-100 anesthetized larvae (the number needs to be tested) would incubate in a crosslinking substance (e.g., DTSSP from Sigma or ThermoFisher Scientific) for ∼1hour, depending on substance and protocol, at 28℃. Afterward, larvae would be collected in a 2 mL tube, and the E3 media exchanged for 400 µL deyolking buffer (55 mM NaCl, 1.8 mM KCl, 1.25 mM $NaHCO_3$, protease inhibitor). By pipetting up and down many times, first with a 1000 µL pipette tip, then with a 200 µL tip, the yolk is removed when the solution becomes milky, but the fish still have their full body. The fish would then be spun down, and the deyolking buffer exchanged for 400µL lysis buffer (50

mM Tris, 150 mM NaCl, 1 mM EDTA, 10% Glycerol, 1% Triton-X 100, protease inhibitor). Transfer fish in lysis buffer into a tissue homogenizer (1 mL). Disrupt tissue with homogenizer ($\sim$ 6times up+down+turning). Keep on ice while disrupting the tissue. The solution should be transferred back into a 2 mL tube and incubated on ice for 30 min with vortexing every 5 min. The solution should be clarified by centrifugation (20.000xg (maybe adjust!) for 30 min. at 4℃). The supernatant should be transferred to a fresh 2mL tube. Maybe dilute the supernatant as some Triton might be left.

In the next step, 4 µL of a biotinylated anti-GFP antibody (e.g., GF28R from ThermoFisher Scientific, MBS5400411 from mybiosource.com, or GFP-trap from Chromotek) is added to the supernatant (400µL) (Fig. 37), which is supposed to bind to Caspr-YFP. 100 µL µMACS Streptavidin MicroBeads should be added and shortly mixed by pipetting up and down and inverting. Proteins should then be pulled down according to the manufacturer's protocol. For elution, 150 µL 100 mM Glycine pH 2.5 should be applied directly onto the top of the column matrix. After equilibration, The eluate should drop into 15 µL 1 M Tris pH 8.5. The final elution should contain Caspr-YFP and proteins that interact with it. Measuring the protein concentration and a western blot can clarify if the protocol works successfully. If this is the case, proteomics can be used to identify potential "Mister X" candidates.

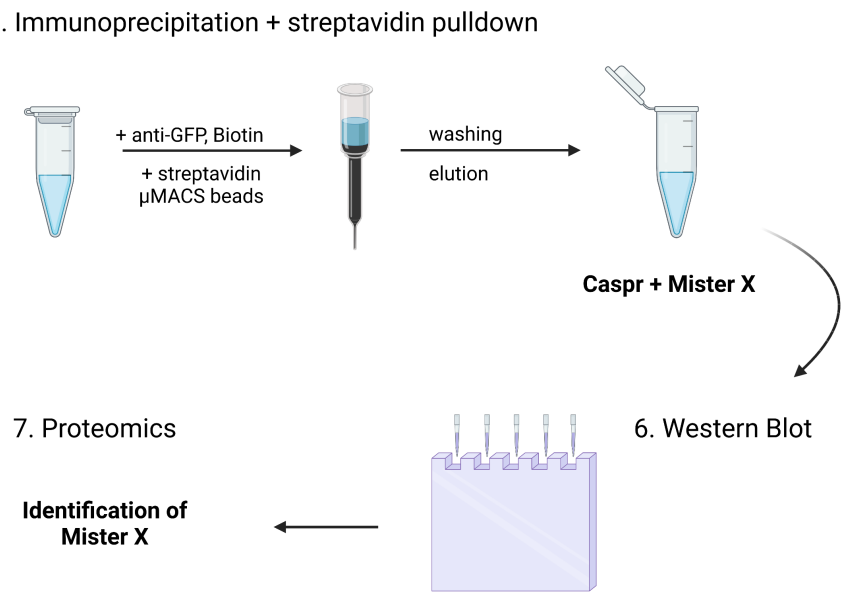

Figure 37: PULLDOWN-APPROACH PART 2 A biotinylated anti-GFP antibody is added to the supernatant. Proteins of interest are pulled down using µMacs Streptavidin MicroBeads. The eluate should contain Caspr-YFP and the interacting protein. This can be clarified by protein measurements, western blot, and proteomics.

II Development of a Zebrafish Line Lacking Major Brain Gangliosides

A reliable approach to test the influence of gangliosides on the distribution of paranodal proteins in the axonal membrane is the use of an animal model which lacks the genes encoding for ganglioside synthesis enzymes. Deleting major brain gangliosides is either achieved by knocking out at least two enzymes that are directly involved in the synthesis of major brain gangliosides (see Fig. 5) or by knocking out one gene at the very beginning of the synthesis pathway. As described in the introduction, some teleost genes are duplicated. Some ganglioside genes took place in the initially described genome duplication and are hence duplicated. This genome duplication increases the number of targeted genes, which would increase the risk of CRISPR off-target effects. Therefore, we chose the second option and targeted a single, non-duplicated gene at the beginning of the synthesis pathway: *ugcg*. The *ugcg* gene encodes for ceramide glucosyltransferase. This enzyme catalyzes the transfer of glucose from UDP-glucose to ceramide. The product of this reaction is glucosylceramide, which is the core segment for synthesizing all glycosphingolipids (GSLs), including the globo-, ganglio-, lacto- and asialo- series [Russo et al., 2018].

Material and Methods

Target Selection and Oligonucleotide Design for DSB-Induction in the Zebrafish genome

Oligonucleotides were designed for targeting the zebrafish *ugcg* gene. Genome sequences for zebrafish (*Danio rerio*) *ugcg* were obtained from the ensembl database (www.ensembl.org/Danio_rerio/, Gene ID: ENSDARG00000058221, Transcript ID: ENSDART00000047954.6) and the corresponding coding sequence (cds) was used for target selection. Targets were chosen in one of the first exons of the targeted gene.

We used a scoring algorithm within chopchop, which utilized the danRer10/GRCz10 genome sequence at that time to reduce off-target matches. Targets were chosen adjacent to a PAM, with a length of 20 nucleotides (nt), a GC content ranging from 45% to 65%, and a restriction site in a range of 2-3 nt around the cutting site. Results were compared with a search in `http://crispr.mit.edu/`. Of the potential candidates found by chopchop, only targets with a score higher than 90 (of 100) within crispr.mit.edu were chosen for final use.

Oligonucleotides of the chosen targets were designed to fit directly into the IDT Alt-R® CRISPR crRNA scaffold. 3 oligonucleotides were designed and ordered from IDT as Alt-R® CRISPR crRNA (Table 19).

DNA Oligonucleotides

DNA oligonucleotides were ordered from Integrated DNA Technologies (IDT, Leuven, Belgium) to target genes in a CRISPR/cas9 manner by integration into the IDT Alt-R® CRISPR crRNA scaffold.

Gene	Name	Target Sequence	Exon #	Direction
ugcg	UGCG #1	GGGCAAGGTACGAGCTCGTC	4	+
ugcg	UGCG #2	CTCGTCTGGATCTGTGACAG	4	+
ugcg	UGCG #3	AAGGTACCGTCCTATAAGCT	2	-

Table 19: OLIGONUCLEOTIDES USED IN THIS DISSERTATION.

Additional Chemicals

Chemical	Manufacturer	Cat No.
Alt-R® CRISPR-Cas9 tracrRNA, 5 nmol	Integrated DNA technologies, Leuven, Belgium	77220763
Alt-R® S.p. Cas9 Nuclease V3, 100 µg	Integrated DNA technologies, Leuven, Belgium	77220764
10 x 2 mL Nuclease Free Duplex Buffer	Integrated DNA technologies, Leuven, Belgium	77220765

Table 20: ADDITIONAL CHEMICALS FOR CRISPR/CAS9 GENE KO GENERATION.

Annealing of Oligonucleotides

RNA oligos (crRNA and tracrRNA) were resuspended in nuclease-free duplex buffer for final concentrations of 10 µM (Table 20). CrRNA and tracrRNA were mixed in equimolar concentrations and diluted in nuclease-free duplex buffer (e.g., 1 µM crRNA, 1 µM tracrRNA, 98 µL buffer). Oligonucleotides were then heated to 95℃ in a thermocycler and slowly cooled down for 1℃ every 1 min until 20℃ was reached. RNA oligonucleotides were then stored at -80° until further usage.

CRISPR/Cas9 Mediated KO Induction

Cas9 working buffer (200 µL 1 M HEPES pH 7.5, 118.2 mg KCl, nuclease-free ddH_2O to 10 mL) was prepared and used to dilute the Cas9 enzyme to a working concentration of 1 µM. Diluted Cas9 enzyme was stored at -80°. Before microinjecting, RNA oligonucleotides and Cas9 protein were carefully thawed on ice and mixed at 1:1 (e.g., 3 µL RNA oligos and 3 µL Cas9). The mix was incubated for 5 min at room temperature to form RNP complexes.

Zebrafish embryos were mated, and embryos were collected as described above. ∼3 nL of the RNA/Cas9 mix was injected in one-cell stage embryos.

KO Detection by RFLP

The genome sequence of interest was amplified using PCR. PCR primers were GGTAAGAAAGTT GGCATCAACC (fwd) and CAGTCCCACCTTCTCCGTC (rev). After using restriction enzymes, which should cut the amplified DNA close to the CRISPR/Cas9 induced insertion/ deletion of nt (indel), the efficiency of the guide was evaluated. Guide#2 turned out to be the most efficient guide (∼70-80% KO generation) and was used to generate F0 *ugcg* depleted zebrafish. The RFLP enzyme for KO detection after UGCG Guide#2 injection was HpyCH4III.

Results and Discussion

After Guide#2 was tested to be the most efficient, this guide was injected into a few egg lays. Some embryos per clutch were PCR tested at 3 dpf. Three clutches with a high indel rate were raised until three months of age. Of 100 fish that were raised to adulthood, ∼25% died during growth. Interestingly, ∼75% of the survived fish seemed to show a phenotype (Fig. 38). However, after PCR analysis of biopsies, the results suggested that a phenotype is not necessarily connected to a *ugcg* genome modification. For example, the impaired fish4 is a wt zebrafish, while the potential wild type fish8 turned out to be a potential *ugcg* KO.

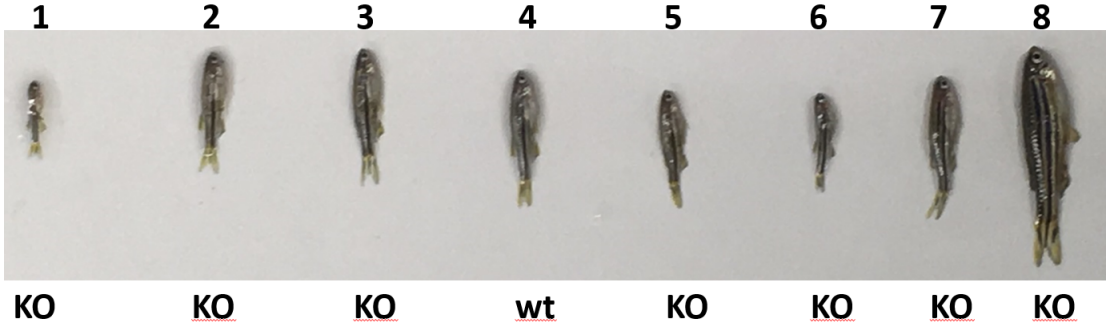

Figure 38: PHENOTYPE OF UGCG GRNA INJECTED FISH AT 3 MONTHS.

To clarify the PCR results and the phenotype, we sent biopsies for sequencing and received surprisingly clean sequencing results (Fig. 39). Unfortunately, all of the genetic deletions that we found were of 6 nt length and, therefore, not a true gene KO. A TIDE analysis, which predicts the most likely indel from -10 to +10 nt of the sequencing data, confirmed these results. The most likely deletion in our sequencing data was -6 nt (44.1%), followed by no change (31.2%) and +10 nt (3.2%). Deletion of two amino acids could still cause a non-functional ceramide glucosyltransferase. However, mice lacking the Ugcg gene were embryonic lethal Yamashita et al. [1999]. Considering the effects of a Ugcg deletion in the mouse model, we conclude that our fish with a genetic *ugcg* modification most likely died during growth. Therefore, deleting 2 amino acids does not or only slightly impair ceramide glucosyltransferase. At three months, the observed phenotype of the F0 generation probably occurred due to problems during injections. We did not follow up with this experiment and did not gain data on, e.g., survival rates of these KO fish. Mice with a globally disrupted *Ugcg* gene die during gastrulation [Yamashita et al., 2005a]. However, a

floxed mouse model with a conditionally disrupted *Ugcg* gene shows a loss in Purkinje cells and behavioral deficits.

By generating a zebrafish line that does not express ceramide glucosyltransferase, we aimed to investigate the role of gangliosides during myelination. Global disruption of the *ugcg* gene would have been essential for our experiments. As a conditional disruption of *ugcg* in zebrafish was not applicable, we dropped the development of this zebrafish line.

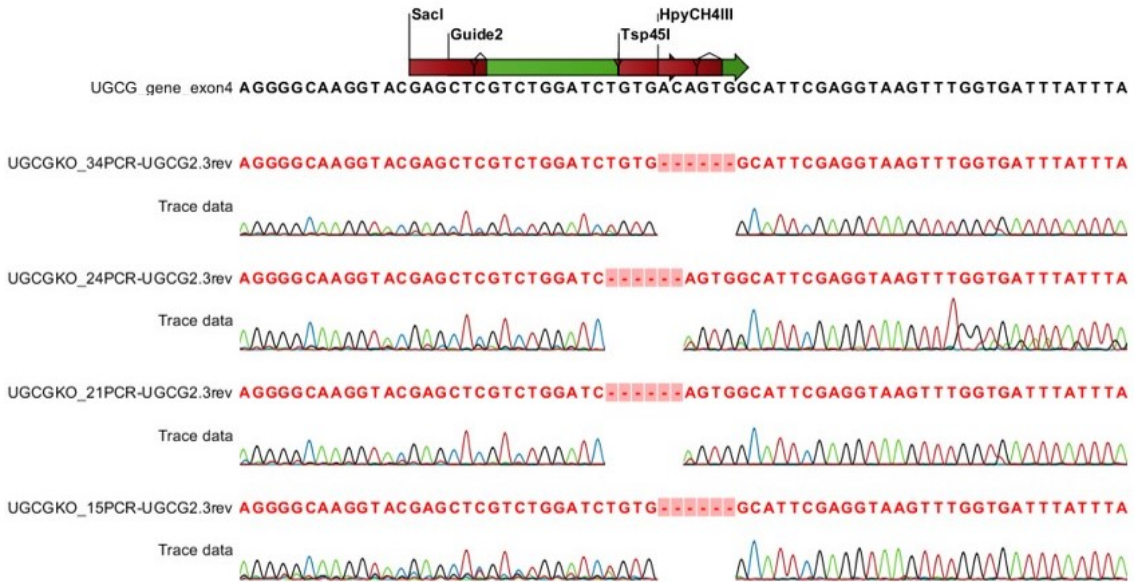

Figure 39: SEQUENCING DATA OF POTENTIAL UGCG KO FISH Upper sequence: UGCG genomic DNA sequence of exon 4; green arrow: guide sequence; red bars: potential restriction sites for enzyme digest. Lower sequences: sequencing results of F0 generation biopsies..

III Ganglioside null mice are severely impaired

Crossing *ST3GAL5* mutant mice [Yamashita et al., 2003] with a mouse line that lacks the *B4GALNT1* gene [Liu et al., 1999] results in a complete loss of all gangliosides [Yamashita et al., 2005b] (*ST3GAL5*$^{-/-}$*/ B4GALNT1*$^{-/-}$, compare chapter 1.3.1 "Gangliosides - Sialic Acid Containing Glycosphingolipids" and Fig. 5).

Ganglioside null mice present with a surprisingly healthy phenotype when they are born, as was reported in previous studies [Yamashita et al., 2005b]. Nevertheless, they develop a severe neurodegenerative phenotype very quickly and die within 1-3 months. A smaller body and brain size, low survival rate, and behavioral deficits have been reported for this genotype [Yamashita et al., 2005b]. Investigation and presentation of this data would have been redundant. However, to document the severity of the phenotype, we present an image of a *ST3GAL5*$^{-/-}$*/ B4GALNT1*$^{-/-}$ compared to a double heterozygous littermate at P12. At this age, they already differ in size by 2 cm (Fig. 40). However, the severity of phenotypes differed between litters and even littermates, with some *ST3GAL5*$^{-/-}$*/ B4GALNT1*$^{-/-}$ not easily identifiable, while others were spotted at first glance.

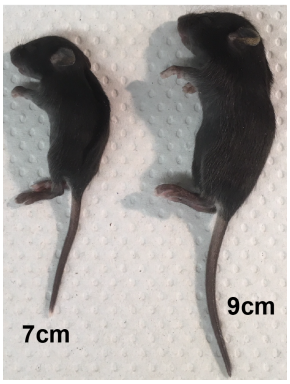

Figure 40: ST3GAL5$^{x/-}$ x B4GALNT1$^{x/-}$ P12 LITTERMATES Two *ST3GAL5*$^{x/-}$ *x B4GALNT1*$^{x/-}$ littermates at P12. The double KO pup on the left side is 2 cm shorter than its double heterozygous littermate on the right side.

IV The Size of an Extracellular Protein Domain is another Measure for Entering the Periaxonal Space

The periaxonal space between the axonal and the oligodendroglial membrane is ∼10-12 nm wide [Pronker et al., 2016]. While GFP has a molecular mass of 26.9 kDa and a cylinder-like structure with a length of 4.2 nm and a diameter of 2.4 nm [Yang et al., 1996a; Ormö et al., 1996], we considered it to be small enough to enter the periaxonal space. However, there is the possibility that proteins cannot enter this cleft simply because of the size of their extracellular domain. We wanted to investigate if big extracellular domains can enter the periaxonal space using a double GFP protein. For this protein, two GFPs were linked with a rigid, α-helical $(EAAAK)_3$ linker (∼3.4 nm in length (calculated by Synlinker). The two extracellular GFPs were also attached to the HS-TM domain by a rigid EAAAK linker (see Fig. 41A). Thus, the protein diameter did not change, but the length increased to ∼11-12 nm and the molecular weight to ∼53.8 kDa. Therefore, the extracellular domain of our double GFP construct should have just the right length to enter the periaxonal space.

The double GFP-TM plasmids were injected, imaged, and analyzed as described above (see section 3.1.6). Single GFP was used as a control.

Both proteins are depleted from the internode in the axonal membrane (see Fig. 41B). Not only did we detect a significant internodal depletion for both proteins (1xGFPp=0.031, 2xGFPp=0.008, we also saw the double GFP protein to be significantly more depleted than the single GFP protein (p=0.046), see Fig. 41C). These results suggest that protein size needs to be considered for sorting into the periaxonal space.

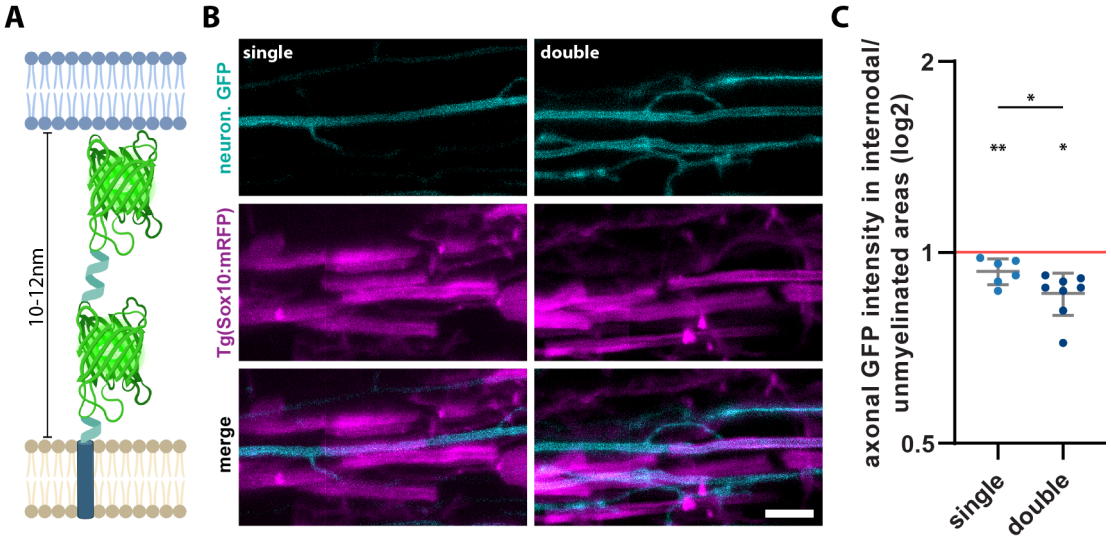

Figure 41: DOUBLE VS. SINGLE MEMBRANE-ASSOCIATED GFP IN ZEBRAFISH A 2xGFP protein structure in periaxonal space: GFP molecules are linked together and to the HS-TM domain with an α helical linker. The protein has about the same length as the width of the periaxonal space. **B** Neuronal expression of double and single GFP attached to the HS-TM domain in the zebrafish spinal cord by using the Gal4;UAS system, together with the neuronal HuC promotor; scale bar 5µm. **C** Graph shows mean ± SD, tested for the difference to 1 by one sample Wilcoxon test, two-sided, 1 = continuous distribution, <1 = internodal depletion, >1 = internodal accumulation; Differences between double and single GFP were tested with Mann-Whitney test, two-tailed; one dot represents mean of measurements in one animal.

V Oligodendroglial Promotor Testing

For a side project, it was necessary to evaluate the efficiency and specificity of different zebrafish promoters for the expression of proteins of interest in oligodendrocytes and myelin. This is not a comprehensive analysis but rather a quick overview of expression patterns. Three different promoters (Olig1(3.2), Sox10, and Myrf) were cloned into an expression vector to drive the expression of membrane-associated PM-GFP (pTol2CG2_olig1(3.2)_PM-GFP, pTol2CG2_Sox10_-PM-GFP, pTol2CG2_Myrf_PM-GFP). They were injected into Tg(Sox10_mRFP) one-cell stage embryos, and their expression efficiency was evaluated at 3 and 5 dpf.

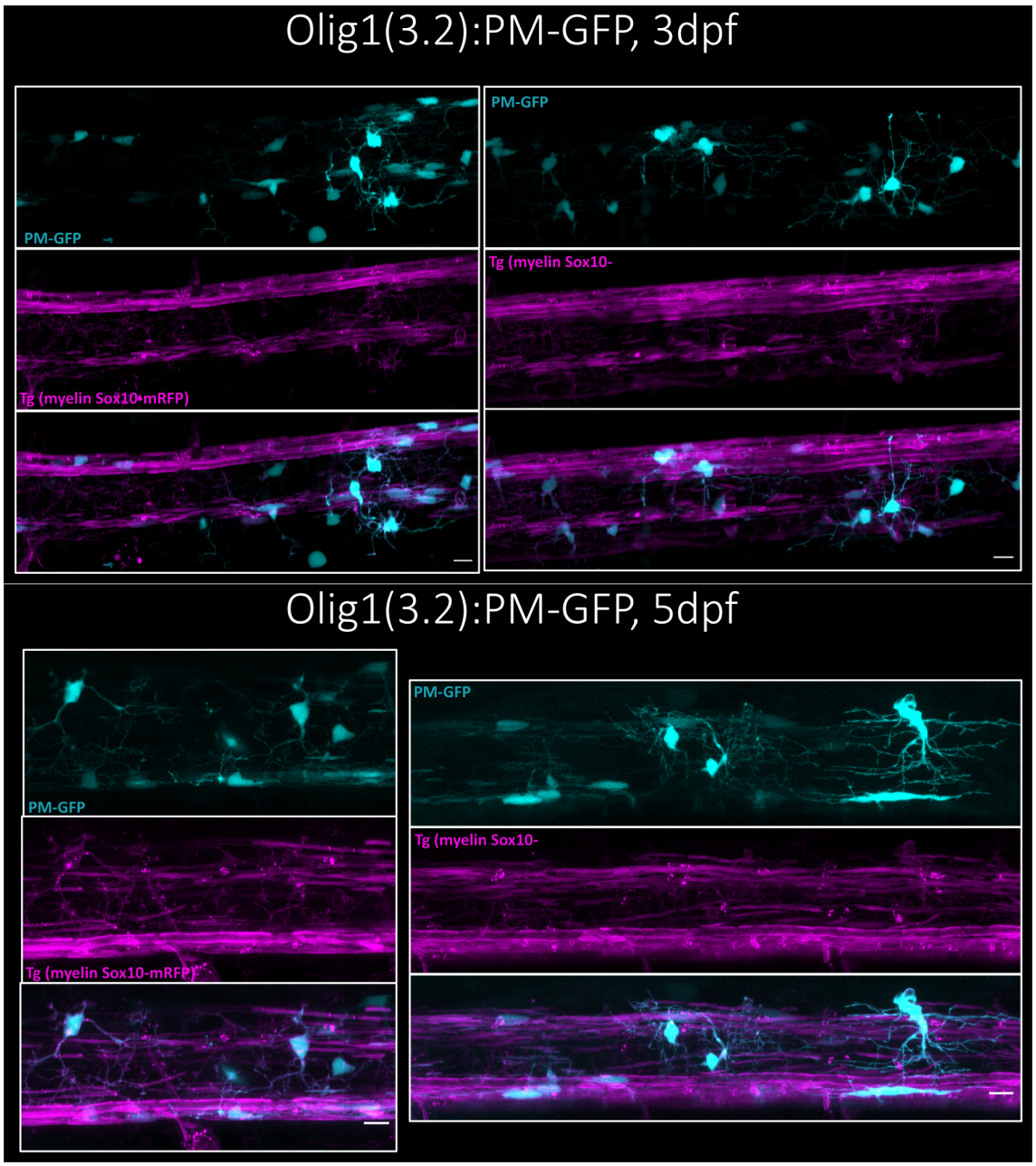

Figure 42: OLIG1(3.2)-DRIVEN GFP EXPRESSION At 3dpf mainly oligodendroglial cell bodies and some neuronal cell bodies are labelled by olig1(3.2)-driven PM_GFP expression. At 5dpf, some sparsely labeled myelin sheaths were detected as well.

Olig1(3.2) seems to drive the expression of PM_GFP from the early stages of myelination. At 3 dpf, it stains oligodendroglial cell bodies (Fig. 42). Unfortunately, some neuronal cell bodies also seem to be labeled. At 5 dpf, we also detected some myelin sheaths, which were GFP-labelled by olig1(3.2)-driven PM_GFP expression. However, most PM_GFP stayed in the cell bodies, and some neuronal cell bodies were stained as well.

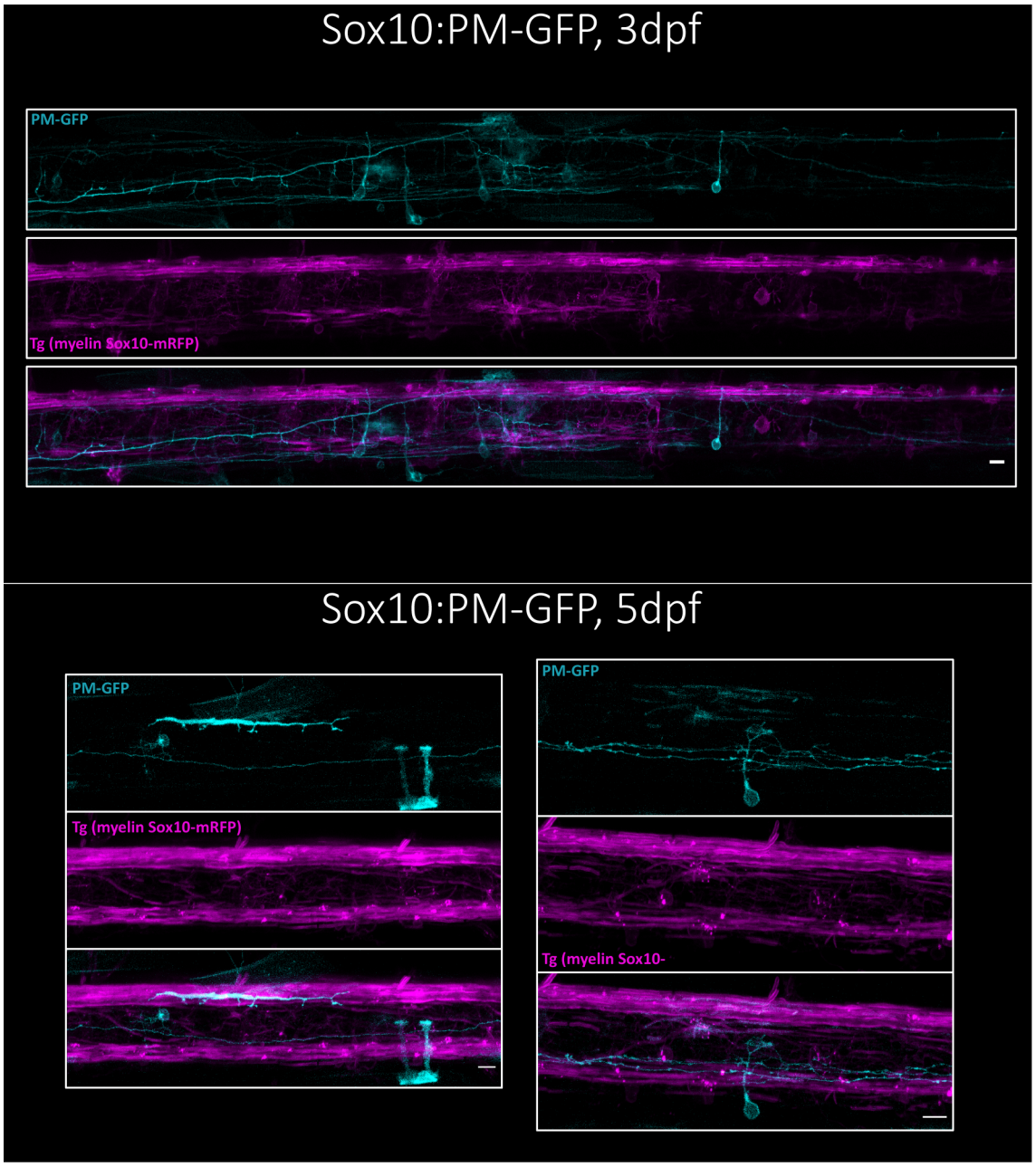

Figure 43: SOX10-DRIVEN GFP EXPRESSION The PM_GFP expression driven by Sox10 was very low. At 3 dpf, we hardly detected labeled oligodendrocytes or myelin sheaths but rather neuronal cell bodies and axons. Only at 5 dpf did we find a few sparsely labeled myelin sheaths..

Tg(Sox10_mRFP) zebrafish give a beautiful myelin signal throughout development. We expected an overlapping expression pattern for Sox10_PM-GFP after injections into Tg(Sox10_mRFP) one-cell stage embryos (Fig. 43). However, the PM_GFP intensity was very low at 3 dpf and did not increase much until 5 dpf. In addition, we mainly found PM_GFP labeled neurons. Only at 5 dpf we detected some sparsely labeled myelin sheaths.

Only the third tested promoter, Myrf, provided an excellent PM_GFP signal (Fig. 44). From early on, oligodendroglial cell bodies and myelin sheaths are strongly labeled. At 5dpf, the Myrf-driven PM_GFP expression mimics the Sox10_mRFP expression.

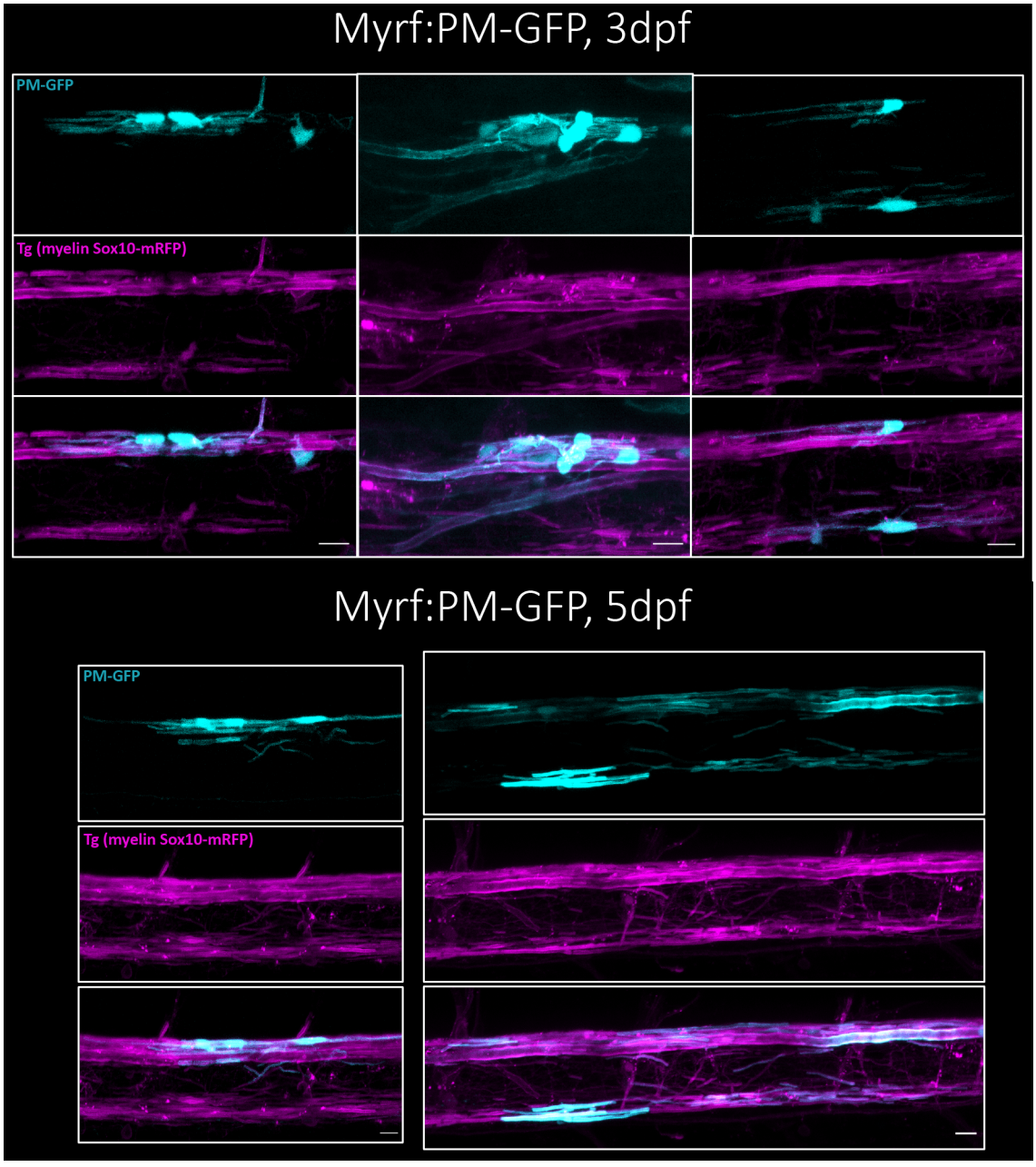

Figure 44: MYRF-DRIVEN GFP EXPRESSION The PM_GFP expression driven by Myrf was very efficient. From 3 dpf on, we found many strongly labeled oligodendroglial cell bodies and myelin sheaths. At 5 dpf, the expression pattern was similar to the expression pattern of the Tg(Sox10_mRFP).

VI Staining for Gangliosides in the Mouse Spinal Cord

Some antibodies binding to gangliosides have been described [Kotani et al., 1992; Ozawa et al., 1992; Vajn et al., 2013b]. Vajn et al. [2013b] analyzed the ganglioside distribution in the adult mouse cerebellum, while Kotani et al. [1995] did the same with the rat cerebellum during development until adulthood. We would not expect to find a difference in the ganglioside distribution between vertebrate species. Indeed, regarding the ganglioside distribution in the adult stage, both labs show similar results [Kotani et al., 1995; Vajn et al., 2013b]. For example, both found GM1 mainly in the white matter tracts, while GD1a and GT1b were mainly detected in the grey matter and only sparsely in white matter tracts. We tested the anti-GD1a and anti-GT1b antibodies of [Kotani et al., 1992; Ozawa et al., 1992], provided by amsbio (AMS.A2507), and followed their staining protocol. To date, the anti-GT1b antibody is not produced anymore. We decided to try another approach that did not permeabilize the tissue additionally. We stained mouse spinal cord tissue of ST3GAL5 x B4GALNT1 double heterozygous or double ko mice with the antibodies. This report is not a comprehensive test but rather a first impression.

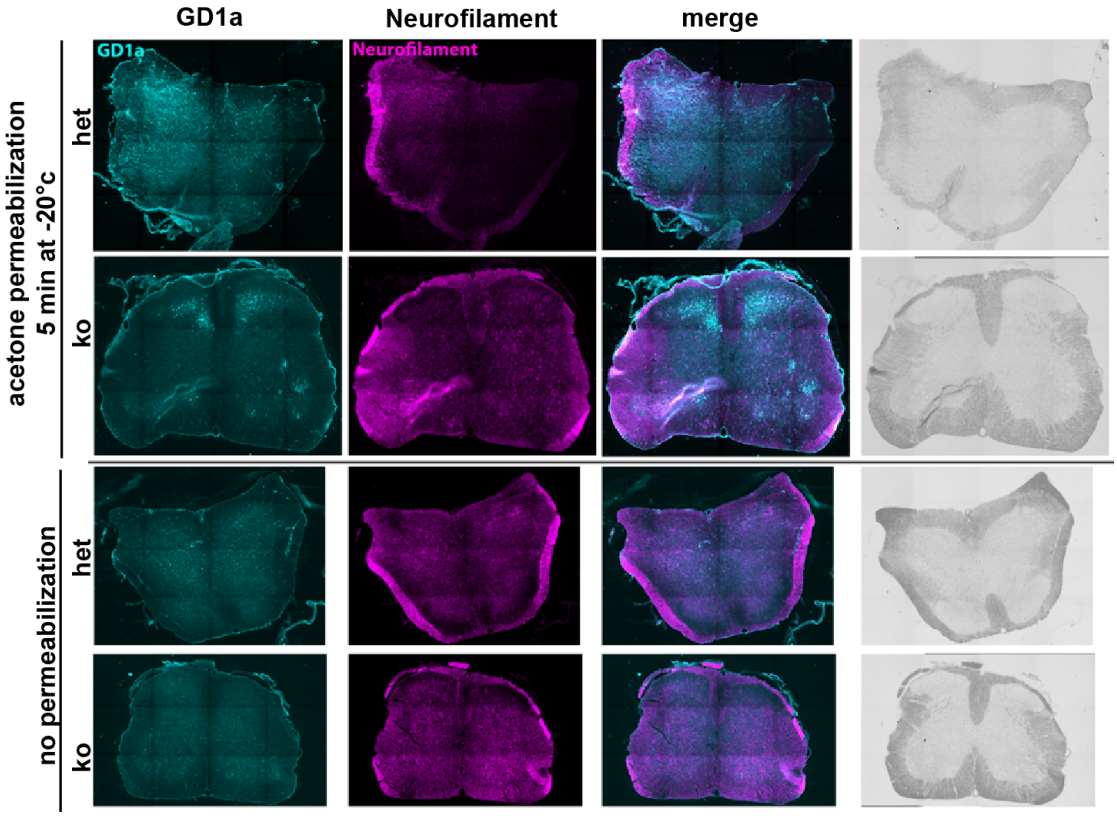

Figure 45: GD1a Staining in Mouse Spinal Cord Staining of spinal cords of P21 ST3GAL5 x B4GALNT1 double heterozygous or double ko mice with anti-GD1a and neurofilament. The tissue was either not permeabilized or by application of -20 ℃ acetone for 5min..

Using the manufacturer's protocol for permeabilization and staining, we detected GD1a in the spinal cord gray matter of ST3GAL5 x B4GALNT1 double heterozygous mice, sparsely in the gray matter of double ko animals (Fig. 45). No permeabilization generated a hardly detectable signal in both genotypes' spinal cord grey matter.

Anti-GT1b antibody staining generated a hardly detectable signal in the spinal cord gray matter of

all genotypes, no matter which permeabilization method was applied (Fig. 46).

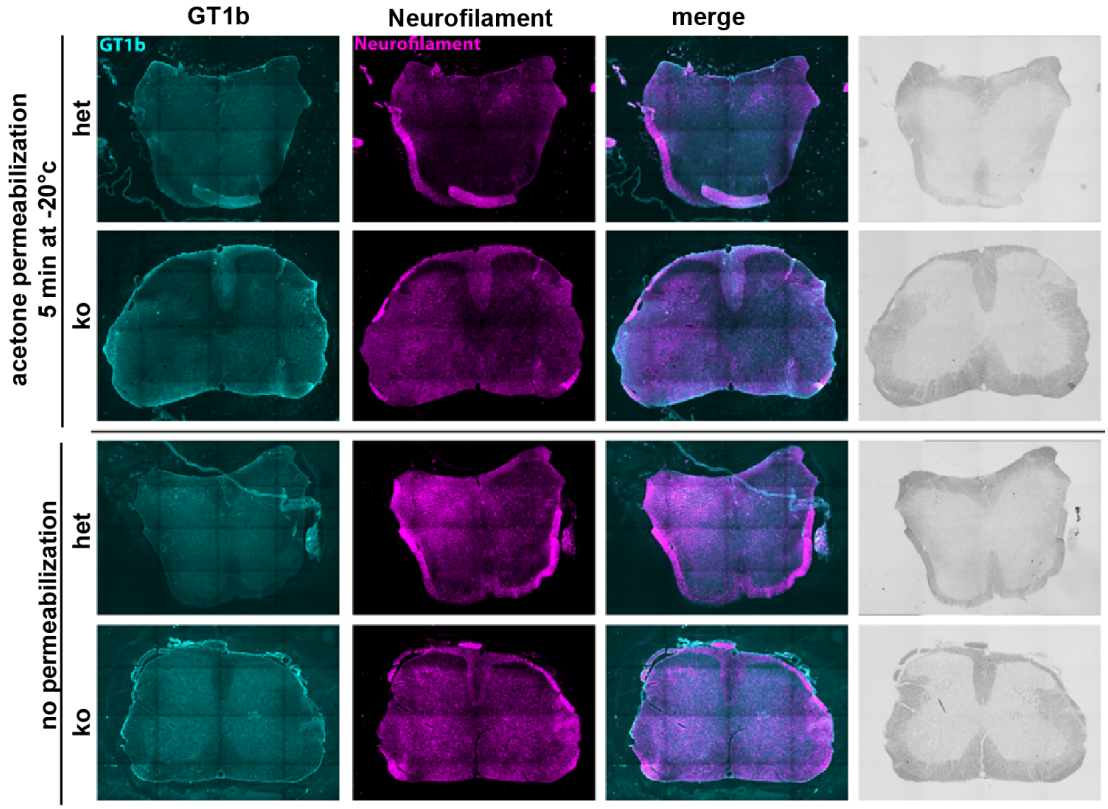

Figure 46: GT1b Staining in Mouse Spinal Cord Staining of spinal cords of P21 ST3GAL5 x B4GALNT1 double heterozygous or double ko mice with anti-GT1b and neurofilament. The tissue was either not permeabilized or by application of -20°C acetone for 5min..

We expected to find GD1 and GT1b mainly in white matter tracts as both gangliosides are interacting with oligodendroglial MAG[Ledeen, 1985; Yang et al., 1996b; Collins et al., 1997; Strenge et al., 1999; Vyas et al., 2002]. However, it has never been actively proposed, but MAG interaction may mask the epitope for the antibodies. Hence, GD1 and GT1b antibodies do not bind these gangliosides. Thus, as was reported by [Kotani et al., 1992; Ozawa et al., 1992], they do not show a signal in the white matter. Our results for GD1a are similar, though not very clear. The anti-GT1b antibody staining was not applicable.

VII *p*-values for Lipidomic Data CNS Axons of Mice

Brain Lipidome in Ganglioside Mice - *p*-values

Condition	Significant?	Adj. *p* Val.
Gangliosides	.	.
.	**GD3 36:1;2**	.
wt vs. het	*	0.0314
wt vs. ko	ns	0.9975
het vs. ko	*	0.0261
.	**GD1 36:1;2**	.
wt vs. het	**	0.0018
wt vs. ko	****	<0.0001
het vs. ko	****	<0.0001
.	**GD1 36:1;2**	.
wt vs. het	ns	0.8584
wt vs. ko	ns	0.1143
het vs. ko	*	0.0320
.	**GT1 36:1;2**	.
wt vs. het	****	<0.0001

Table 21: Brain Lipidome in Ganglioside Null Mice - *p*-values for differences in ganglioside content between age groups. Only significantly different ganglioside species are shown.

Condition	Significant?	Adj. *p* Val.
Lipid	**Species**	.
.	**PC**	.
wt vs. het	*	0.0128
wt vs. ko	ns	0.5179
het vs. ko	ns	0.3122
.	**PE**	.
wt vs. het	**	0.0033
wt vs. ko	***	0.0009
het vs. ko	ns	0.7503
.	**PS**	.
wt vs. het	****	<0.0001
wt vs. ko	****	<0.0001
het vs. ko	ns	0.9166

Table 22: Brain Lipidome in Ganglioside Null Mice - *p*-values for differences in lipid species content between age groups. Only significantly different lipid species are shown.

Condition	Significant?	Adj. *p* Val.
Chain	**Length**	.
.	**DAG**	.
wt vs. het	**	0.0024
wt vs. ko	ns	0.2104
het vs. ko	ns	0.1433
.	**LPE**	.
wt vs. het	ns	>0.999
wt vs. ko	**	0.0024
het vs. ko	***	0.0006
.	**PA**	.
wt vs. het	****	<0.0001
wt vs. ko	****	<0.0001
het vs. ko	ns	>0.999
.	**PC O-**	.
wt vs. het	****	<0.0001
wt vs. ko	****	<0.0001
het vs. ko	ns	>0.999

Table 23: Brain Lipidome in Ganglioside Null Mice - *p*-values for differences in the average fatty acid carbon chain length between age groups. Only lipid species with significantly different chain lengths are shown.

Condition	Significant?	Adj. *p* Val.
Double	**Bonds**	.
.	**LPE**	.
wt vs. het	ns	0.2894
wt vs. ko	*	0.0380
het vs. ko	ns	0.5323
.	**PC O-**	.
wt vs. het	***	0.0008
wt vs. ko	****	<0.0001
het vs. ko	ns	0.6288

Table 24: Brain Lipidome in Ganglioside Null Mice - *p*-values for differences in in saturation levels between age groups. Only lipid species with significantly different number of double bonds are shown.

Optic Nerve Lipidome in Ganglioside Mice - *p*-values

Condition	Significant?	Adj. *p* Val.
Gangliosides	.	.
.	**GD1 36:1;2**	.
wt vs. het	****	<0.0001
wt vs. ko	****	<0.0001
het vs. ko	****	<0.0001
.	**GD1 38:1;2**	.
wt vs. het	ns	0.3143
wt vs. ko	****	<0.0001
het vs. ko	****	<0.0001

Table 25: Optic Nerve Lipidome in Ganglioside Null Mice - *p*-values for differences in ganglioside content between age groups. Only significantly different ganglioside species are shown.

Condition	Significant?	Adj. *p* Val.
Lipid	**Species**	.
.	**PC**	.
wt vs. het	**	0.0032
wt vs. ko	ns	0.5113
het vs. ko	ns	0.0942
.	**PC O-**	.
wt vs. het	*	0.0260
wt vs. ko	ns	0.7718
het vs. ko	ns	0.1657
.	**PE O-**	.
wt vs. het	***	0.0007
wt vs. ko	ns	0.2616
het vs. ko	ns	0.0938
.	**PS**	.
wt vs. het	****	<0.0001
wt vs. ko	****	<0.0001
het vs. ko	ns	0.2191

Table 26: Optic Nerve Lipidome in Ganglioside Null Mice - *p*-values for differences in lipid species content between age groups. Only significantly different lipid species are shown.

Condition	Significant?	Adj. *p* Val.
Chain	**Length**	.
.	**PA**	.
wt vs. het	ns	0.0844
wt vs. ko	***	0.0001
het vs. ko	ns	0.1141

Table 27: Optic Nerve Lipidome in Ganglioside Null Mice - *p*-values for differences in the average fatty acid carbon chain length between age groups. Only lipid species with significantly different chain lengths are shown.

Condition	Significant?	Adj. *p* Val.
Double	**Bonds**	.
.	**DAG**	.
wt vs. het	***	0.0006
wt vs. ko	***	0.0006
het vs. ko	ns	>0.999

Table 28: Optic Nerve Lipidome in Ganglioside Null Mice - *p*-values for differences in in saturation levels between age groups. Only lipid species with significantly different number of double bonds are shown.

Brain Lipidome During Development - *p*-values

Condition	Significant?	Adj. *p* Val.
Gangliosides	.	.
.	**GD1 36:1;2**	.
P12 vs. P21	*	0.0215
P12 vs. adult	****	<0.0001
P21 vs. adult	****	<0.0001
.	**GD1 36:2;2**	.
P12 vs. P21	****	<0.0001
P12 vs. adult	****	<0.0001
P21 vs. adult	****	<0.0001
.	**GD1 38:1;2**	.
P12 vs. P21	***	0.0009
P12 vs. adult	*	0.0129
P21 vs. adult	ns	0.07089
.	**GT1 36:1;2**	.
P12 vs. P21	****	<0.0001
P12 vs. adult	****	<0.0001
P21 vs. adult	ns	0.0685
.	**GT1 36:2;2**	.
P12 vs. P21	*	0.0283
P12 vs. adult	**	0.0011
P21 vs. adult	ns	0.5637
.	**GT1 38:1;2**	.
P12 vs. P21	ns	0.0557
P12 vs. adult	***	0.0007
P21 vs. adult	ns	0.3326
GT1	**-OAc 36:1;2**	.
P12 vs. P21	ns	0.9963
P12 vs. adult	*	0.0295
P21 vs. adult	ns	0.2110

Table 29: Brain Lipidome During Development - *p*-values for differences in gangliosides between age groups. Only signif. diff. species shown.

Condition	Significant?	Adj. *p* Val.
Lipid	**Species**	.
.	**Chol**	.
P12 vs. P21	****	<0.0001
P12 vs. adult	****	<0.0001
P21 vs. adult	ns	0.1051
.	**HexCer**	.
P12 vs. P21	***	0.0007
P12 vs. adult	****	<0.0001
P21 vs. adult	ns	0.5055
.	**PC**	.
P12 vs. P21	****	<0.0001
P12 vs. adult	****	<0.0001
P21 vs. adult	****	<0.0001
.	**PE O-**	.
P12 vs. P21	****	<0.0001
P12 vs. adult	****	<0.0001
P21 vs. adult	**	0.0035
.	**PS**	.
P12 vs. P21	ns	0.1787
P12 vs. adult	****	<0.0001
P21 vs. adult	****	<0.0001

Table 30: Brain Lipidome During Development - *p*-values for differences in lipid species content between age groups. Only significantly different lipid species are shown.

Condition	Significant?	Adj. *p* Val.
Chain	**Length**	.
.	**CL**	.
P12 vs. P21	****	<0.0001
P12 vs. adult	****	<0.0001
P21 vs. adult	****	<0.0001
.	**HexCer**	.
P12 vs. P21	****	<0.0001
P12 vs. adult	****	<0.0001
P21 vs. adult	ns	0.1208
.	**LPC**	.
P12 vs. P21	ns	0.1625
P12 vs. adult	****	<0.0001
P21 vs. adult	***	0.0003
.	**LPE**	.
P12 vs. P21	ns	0.1625
P12 vs. adult	***	0.001
P21 vs. adult	ns	0.1208
.	**LPE O-**	.
P12 vs. P21	ns	0.1625
P12 vs. adult	****	<0.0001
P21 vs. adult	****	<0.0001
.	**PA**	.
P12 vs. P21	****	<0.0001
P12 vs. adult	****	<0.0001
P21 vs. adult	ns	>0.999
.	**PC**	.
P12 vs. P21	***	0.001
P12 vs. adult	****	<0.0001
P21 vs. adult	ns	0.1208
.	**PC O-**	.
P12 vs. P21	***	0.001
P12 vs. adult	****	<0.0001
P21 vs. adult	****	<0.0001
.	**PE O-**	.
P12 vs. P21	ns	0.1625
P12 vs. adult	***	0.001
P21 vs. adult	ns	0.1208
.	**PG**	.
P12 vs. P21	****	<0.0001
P12 vs. adult	****	<0.0001
P21 vs. adult	****	<0.0001
.	**PS**	.
P12 vs. P21	***	0.001
P12 vs. adult	****	<0.0001
P21 vs. adult	****	<0.0001
.	**SM**	.
P12 vs. P21	***	0.001
P12 vs. adult	****	<0.0001
P21 vs. adult	ns	0.1208
.	**Sulf**	.
P12 vs. P21	****	<0.0001
P12 vs. adult	****	<0.0001
P21 vs. adult	****	<0.0001

Table 31: Brain Lipidome During Development - *p*-values for differences in the average fatty acid carbon chain length between age groups. Only lipid species with significantly different chain lengths are shown.

Condition	Significant?	Adj. *p* Val.
Double	**Bonds**	.
.	**CL**	.
P12 vs. P21	*	0.0122
P12 vs. adult	****	<0.0001
P21 vs. adult	ns	0.2656
.	**DAG**	.
P12 vs. P21	ns	0.3203
P12 vs. adult	*	0.0122
P21 vs. adult	****	<0.0001
.	**LPC**	.
P12 vs. P21	ns	>0.999
P12 vs. adult	*	0.0399
P21 vs. adult	*	0.0238
.	**LPE**	.
P12 vs. P21	ns	>0.999
P12 vs. adult	**	0.005
P21 vs. adult	**	0.0037
.	**LPE O-**	.
P12 vs. P21	ns	0.3203
P12 vs. adult	*	0.0122
P21 vs. adult	ns	0.2656
.	**PC O-**	.
P12 vs. P21	ns	0.9885
P12 vs. adult	****	<0.0001
P21 vs. adult	****	<0.0001
.	**PE O-**	.
P12 vs. P21	****	<0.0001
P12 vs. adult	****	<0.0001
P21 vs. adult	****	<0.0001
.	**PG**	.
P12 vs. P21	****	<0.0001
P12 vs. adult	****	<0.0001
P21 vs. adult	****	<0.0001
.	**PS**	.
P12 vs. P21	****	<0.0001
P12 vs. adult	****	<0.0001
P21 vs. adult	****	<0.0001
.	**Sulf**	.
P12 vs. P21	ns	0.1957
P12 vs. adult	***	0.0007
P21 vs. adult	ns	0.0768

Table 32: Brain Lipidome During Development - *p*-values for differences in in saturation levels between age groups. Only lipid species with significantly different number of double bonds are shown.

Optic Nerve Lipidome During Development - *p*-values

Condition	Significant?	Adj. *p* Val.
Gangliosides	.	.
.	**GD1 34:1;2**	.
P12 vs. P21	**	0.004
.	**GD1 36:1;2**	.
P12 vs. P21	****	<0.0001
P12 vs. adult	****	<0.0001
P21 vs. adult	****	<0.0001
.	**GD1 36:2;2**	.
P12 vs. P21	****	<0.0001
.	**GT1 36:1;2**	.
P12 vs. P21	****	<0.0001
P12 vs. adult	****	<0.0001
P21 vs. adult	**	0.0074
.	**GT1 38:1;2**	.
P12 vs. P21	ns	0.1988
P12 vs. adult	*	0.0139
P21 vs. adult	ns	0.5044

Table 33: Optic Nerve Lipidome During Development - *p*-values for differences in ganglioside content between age groups. Only significantly different lipid species are shown.

Condition	Significant?	Adj. *p* Val.
Lipid	**Species**	.
.	**Chol**	.
P12 vs. P21	**	0.0033
P12 vs. adult	****	<0.0001
P21 vs. adult	****	<0.0001
.	**HexCer**	.
P12 vs. P21	ns	0.2128
P12 vs. adult	ns	0.0549
P21 vs. adult	***	0.0003
.	**PA**	.
P12 vs. P21	ns	0.9572
P12 vs. adult	ns	0.0514
P21 vs. adult	*	0.0248
.	**PC**	.
P12 vs. P21	****	<0.0001
P12 vs. adult	****	<0.0001
P21 vs. adult	****	<0.0001
.	**PE O-**	.
P12 vs. P21	****	<0.0001
P12 vs. adult	****	<0.0001
P21 vs. adult	****	<0.0001
.	**Sulf**	.
P12 vs. P21	ns	0.4717
P12 vs. adult	**	0.0036
P21 vs. adult	ns	0.0922

Table 34: Optic Nerve Lipidome During Development - *p*-values for differences in lipid species content between age groups. Only significantly different ganglioside species are shown.

Condition	Significant?	Adj. *p* Val.
Chain	**Length**	.
.	**DAG**	.
P12 vs. P21	****	<0.0001
P12 vs. adult	****	<0.0001
P21 vs. adult	ns	0.7874
.	**LPC**	.
P12 vs. P21	*	0.0255
P12 vs. adult	***	0.0004
P21 vs. adult	ns	0.3875
.	**LPE**	.
P12 vs. P21	*	0.0255
P12 vs. adult	***	0.1221
P21 vs. adult	ns	0.7874
.	**LPE O-**	.
P12 vs. P21	ns	0.3875
P12 vs. adult	*	0.0255
P21 vs. adult	ns	0.3875
.	**PC**	.
P12 vs. P21	**	0.0037
P12 vs. adult	***	0.0004
P21 vs. adult	ns	0.7874
.	**PC O-**	.
P12 vs. P21	ns	0.1221
P12 vs. adult	****	<0.0001
P21 vs. adult	***	0.0004
.	**SM**	.
P12 vs. P21	***	0.0004
P12 vs. adult	***	0.0004
P21 vs. adult	ns	>0.999
.	**Sulf**	.
P12 vs. P21	*	0.0255
P12 vs. adult	***	0.0004
P21 vs. adult	ns	0.3875

Table 35: Optic Nerve Lipidome During Development - *p*-values for differences in the average fatty acid carbon chain length between age groups. Only lipid species with significantly different chain lengths are shown.

Condition	Significant?	Adj. *p* Val.
Double	**Bonds**	.
.	**DAG**	.
P12 vs. P21	****	<0.0001
P12 vs. adult	*	0.0315
P21 vs. adult	*	0.0473
.	**LPC**	.
P12 vs. P21	****	<0.0001
P12 vs. adult	****	<0.0001
P21 vs. adult	ns	0.7539
.	**LPE O-**	.
P12 vs. P21	ns	0.2518
.	**PA**	.
P12 vs. P21	ns	0.1389
P12 vs. adult	****	<0.0001
P21 vs. adult	****	<0.0001
.	**PC O-**	.
P12 vs. P21	ns	0.2518
P12 vs. adult	***	0.0003
P21 vs. adult	*	0.0473
.	**PE**	.
P12 vs. P21	ns	0.7058
P12 vs. adult	*	0.0473
P21 vs. adult	ns	0.2518

Table 36: Optic Nerve Lipidome During Development - *p*-values for differences in in saturation levels between age groups. Only lipid species with significantly different number of double bonds are shown.

VIII Makro for Quantifying axonal signal intensity

20171220_Quantify_internodes.ijm

My former colleague Ioannis Alexopoulos and me developed a Fiji/ImageJ macro to semi-automatically measure the intensity in single axons before, behind and under a myelin sheath. This macro enables the user to choose the axonal measuring area manually. The axonal thickness is adjustable (see Fig.**??**A). The output of the macro gives, among other values, the mean intensity in the measured area.

```
*******************************************************************************
Author Dr. Ioannis K. Alexopoulos
The author of the macro reserves the copyrights of the original macro.
However, you are welcome to distribute, modify and use the program under
the terms of the GNU General Public License as stated here:
(http://www.gnu.org/licenses/gpl.txt) as long as you attribute proper
acknowledgement to the author as mentioned above.
This program is distributed in the hope that it will be useful,
but WITHOUT ANY WARRANTY; without even the implied warranty of
MERCHANTABILITY or FITNESS FOR A PARTICULAR PURPOSE. See the
GNU General Public License for more details.
*******************************************************************************
Macro Description
This macro is used to measure the length and the intensities of
axons in myelinated (internodes) versus non-myelinated regions.
/

// Create dialog, create save folders, and select file(s) to process
 Dialog.create("Internode analysis");
Dialog.addCheckbox("Analyse single image container file", true);
Dialog.addCheckbox("Load ROI of interest", false);
Dialog.addCheckbox("Load maximum projections", false);
Dialog.addString("Name of saving folder: ", "_Results");
Dialog.addNumber("Set the line selection width (pixels)", 10);
Dialog.addNumber("The axonal signal is in channel", 1);
Dialog.addNumber("The myelin signal is in channel", 2);
Dialog.show();

// Variables of Dialog
 single_file=Dialog.getCheckbox();
LOAD_ROI=Dialog.getCheckbox();
LOAD_MAX=Dialog.getCheckbox();
save_folder=Dialog.getString();
line_width=Dialog.getNumber();
axonal_ch=Dialog.getNumber();
myel_ch=Dialog.getNumber();
sep = File.separator;

if (single_file)
{
Filelist=newArray(1);
```

```
Filelist[0] = File.openDialog("Select a file to proccess...");
SourceDir=File.getParent(Filelist[0]);
Filelist[0]=File.getName(Filelist[0]);
}else
{
SourceDir = getDirectory("Choose source directory");
Filelist=getFileList(SourceDir);

}
// Remove Folders from Filelist array
 tmp=newArray();
for(k=0;k<Filelist.length;k++)
{
if (!File.isDirectory(SourceDir+"/"+Filelist[k]))
{
tmp = Array.concat(tmp,Filelist[k]);
}
}
Filelist=tmp;
if(LOAD_ROI)
{
LARGE_ROI_PATH = getDirectory("Select the folder containing the ROIs");
}
if(LOAD_MAX)
{
MAX_PATH = getDirectory("Select the folder containing the maximum projections");
}

new_folder=SourceDir + sep + save_folder;
File.makeDirectory(new_folder);
File.makeDirectory(new_folder+ sep +
"MaximumProjections");
File.makeDirectory(new_folder+ sep + "ROIs");
File.makeDirectory(new_folder+ sep + "Measurements");
setBatchMode(true);

for (k=0;k<Filelist.length;k++)
{
if(!endsWith(Filelist[k], sep))
{
run("Bio-Formats Macro Extensions");
Ext.setId(SourceDir+sep+Filelist[k]);
Ext.getSeriesCount(SERIES_COUNT);
FILE_PATH=SourceDir + sep + Filelist[k];

SeriesNames=newArray(SERIES_COUNT);
myel_mean=newArray(SERIES_COUNT);
myel_mod=newArray(SERIES_COUNT);
myel_min=newArray(SERIES_COUNT);
myel_max=newArray(SERIES_COUNT);
myel_median=newArray(SERIES_COUNT);
myel_len=newArray(SERIES_COUNT);
```

```
unmyel1_mean=newArray(SERIES_COUNT);
unmyel1_mod=newArray(SERIES_COUNT);
unmyel1_min=newArray(SERIES_COUNT);
unmyel1_max=newArray(SERIES_COUNT);
unmyel1_median=newArray(SERIES_COUNT);
unmyel1_len=newArray(SERIES_COUNT);

unmyel2_mean=newArray(SERIES_COUNT);
unmyel2_mod=newArray(SERIES_COUNT);
unmyel2_min=newArray(SERIES_COUNT);
unmyel2_max=newArray(SERIES_COUNT);
unmyel2_median=newArray(SERIES_COUNT);
unmyel2_len=newArray(SERIES_COUNT);

for (i=0;i<SERIES_COUNT; i++)
options="open=["+ FILE_PATH + "] " + "autoscale color_mode=Default view=Hyperstack stack_order=XYCZT " + "se-
ries_"+d2s(i+1,0);
run("Bio-Formats Importer", options);
FILE_NAME=File.getName(FILE_PATH);
Ext.setSeries(i);
Ext.getSeriesName(SERIES_NAMES);
SeriesNames[i]=SERIES_NAMES;
if(endsWith(Filelist[k], ".lif"))
{
SAVE_NAME=Filelist[k]+"_"+SERIES_NAMES;
}else
{
SAVE_NAME=File.nameWithoutExtension;
}
getDimensions(width, height, channels, slices, frames);
rename(SAVE_NAME);
Stack.setChannel(axonal_ch);
run("Cyan");
Stack.setChannel(myel_ch);
run("Magenta");
if(LOAD_MAX)
{
open(MAX_PATH+sep +"MAX_"+SAVE_NAME+".tif");
}else
{
setBatchMode("show");  Stack.setDisplayMode("composite");
waitForUser("Please inspect the z-stack and after clicking OK \n select the slices to project");
Dialog.create("Give the slices numbers to project");
Dialog.addMessage("Do a maximum projection: ");
Dialog.addNumber("From slice", 1);
Dialog.addNumber("...to slice", slices);
Dialog.show();
setBatchMode("hide");
low_z=Dialog.getNumber();
high_z=Dialog.getNumber();
run("Z Project...", "start="+low_z+" stop="+high_z+" projection=[Max Intensity]");
```

```
}
rename("MAX_"+SAVE_NAME);
selectWindow(SAVE_NAME);
close();
run("Set Measurements...", "mean modal min median redirect=None decimal=3");
Stack.setChannel(axonal_ch);
run("Green");
Stack.setChannel(myel_ch);
run("Magenta");
setTool("polygon");
if(LOAD_ROI)
{
roiManager("Open", LARGE_ROI_PATH + sep + "ROI_"+SAVE_NAME+".zip");
}else
{
setBatchMode("show");
Stack.setDisplayMode("composite");
if(channels>2)
{
Stack.setActiveChannels("110");
}
setLineWidth(line_width);  setTool("freeline");
roiManager("reset");
waitForUser("Please draw a line over an unmyelinated region and press OK");
roiManager("Add");
waitForUser("Please draw a line over an unmyelinated region and press OK");
roiManager("Add");
waitForUser("Please draw a line over a myelinated region and press OK");
roiManager("Add");
setBatchMode("hide");
}
run("Clear Results");
roiManager("Select", 2);
roiManager("Set Line Width", line_width);
Stack.setChannel(axonal_ch);
run("Measure");
myel_mean[i]=getResult("Mean", 0);
myel_mod[i]=getResult("Mode", 0);
myel_min[i]=getResult("Min", 0);
myel_max[i]=getResult("Max", 0);
myel_median[i]=getResult("Median", 0);
myel_len[i]=getResult("Length", 0);
run("Clear Results");

roiManager("Select", 0);
roiManager("Set Line Width", line_width);
Stack.setChannel(axonal_ch);
run("Measure");
unmyel1_mean[i]=getResult("Mean", 0);
unmyel1_mod[i]=getResult("Mode", 0);
unmyel1_min[i]=getResult("Min", 0);
unmyel1_max[i]=getResult("Max", 0);
```

```
unmyel1_median[i]=getResult("Median", 0);
unmyel1_len[i]=getResult("Length", 0);
run("Clear Results");

roiManager("Select", 1);
roiManager("Set Line Width", line_width);
Stack.setChannel(axonal_ch);
run("Measure");
unmyel2_mean[i]=getResult("Mean", 0);
unmyel2_mod[i]=getResult("Mode", 0);
unmyel2_min[i]=getResult("Min", 0);
unmyel2_max[i]=getResult("Max", 0);
unmyel2_median[i]=getResult("Median", 0);
unmyel2_len[i]=getResult("Length", 0);
run("Clear Results");

saveAs("tif", new_folder+ sep + "MaximumProjections" + sep +"MAX_"+SAVE_NAME);
roiManager("save", new_folder+ sep + "ROIs" + sep +"ROI_"+SAVE_NAME+".zip")
run("Clear Results");
run("Close All");
roiManager("reset");
}

// Calculate % of myelination and microglia infiltration, fix and save table of results
for (i=0;i<SERIES_COUNT; i++)
{
setResult("Label", i, SeriesNames[i]);
setResult("Myelinated Area-Length[um]", i, myel_len[i]);
setResult("Myelinated Area-Mean Intensity", i, myel_mean[i]);
setResult("Myelinated Area-Min Intensity", i, myel_min[i]);
setResult("Myelinated Area-Max Intensity", i, myel_max[i]);
setResult("Myelinated Area-Modal Intensity", i, myel_mod[i]);
setResult("Myelinated Area-Median Intensity", i, myel_median[i]);
setResult("Unmyelinated Area1-Length[um]", i, unmyel1_len[i]);
setResult("Unmyelinated Area1-Mean Intensity", i, unmyel1_mean[i]);
setResult("Unmyelinated Area1-Min Intensity", i, unmyel1_min[i]);
setResult("Unmyelinated Area1-Max Intensity", i, unmyel1_max[i]);
setResult("Unmyelinated Area1-Modal Intensity", i, unmyel1_mod[i]);
setResult("Unmyelinated Area1-Median Intensity", i, unmyel1_median[i]);
setResult("Unmyelinated Area2-Length[um]", i, unmyel2_len[i]);
setResult("Unmyelinated Area2-Mean Intensity", i, unmyel2_mean[i]);
setResult("Unmyelinated Area2-Min Intensity", i, unmyel2_min[i]);
setResult("Unmyelinated Area2-Max Intensity", i, unmyel2_max[i]);
setResult("Unmyelinated Area2-Modal Intensity", i, unmyel2_mod[i]);
setResult("Unmyelinated Area2-Median Intensity", i, unmyel2_median[i]);
}
saveAs("Results", new_folder+ sep + "Measurements" + sep +Filelist[k]+".txt");
}
}
setBatchMode(false);
```

IX Nucleotide Sequences Used in this Dissertation

Sequences of IDT gBlocks gene fragments

GFP-GPI

actcaatgaGGTACCACCATGattccagaggccttccagcccagagccatgaagcacaccacc accgtcctgatgctcgcgctgtcctcccgcttttggtcggt-
gtgtgctATGGTGAGCAAGGGCG AGGAGCTGTTCACCGGGGTGGTGCCCATCCTGGTCGAGCTGGACGGCGACGTA
AACGGCCACAAGTTCAGCGTGTCCGGCGAGGGCGAGGGCGATGCCACCTACGG CAAGCTGACCCTGAAGTTCATCT-
GCACCACCGGCAAGCTGCCCGTGCCCTGGCC CACCCTCGTGACCACCCTGACCTACGGCGTGCAGTGCTTCAGC-
CGCTACCCCGA CCACATGAAGCAGCACGACTTCTTCAAGTCCGCCATGCCCGAAGGCTACGTCCA GGAGCGCAC-
CATCTTCTTCAAGGACGACGGCAACTACAAGACCCGCGCCGAGGT GAAGTTCGAGGGCGACACCCTGGTGAACCG-
CATCGAGCTGAAGGGCATCGACTT CAAGGAGGACGGCAACATCCTGGGGCACAAGCTGGAGTACAACTACAACAGCCA
CAACGTCTATATCATGGCCGACAAGCAGAAGAACGGCATCAAGGTGAACTTCAA GATCCGCCACAACATCGAGGACG-
GCAGCGTGCAGCTCGCCGACCACTACCAGCA GAACACCCCCATCGGCGACGGCCCCGTGCTGCTGCCCGACAAC-
CACTACCTGAG CACCCAGTCCGCCCTGAGCAAAGACCCCAACGAGAAGCGCGATCACATGGTCCT GCTGGAGTTCGT-
GACCGCCGCCGGGATCACTCTCGGCATGGACGAGCTGTACAA GGGTGGAGGTGGATCAggagctgtcgcacaagtgcgcat-
cacaggttcggctccggctccggctctgg cctcggctctgctgctgctgccgctcctctggactctgatgctctgaGAGCTCactcaatga

GFP-HA-TM

actcaatgaGGTACCACCATGGCCATCATCTACCTCATACTGTTGTTTACAGCAGTGCGCGGAA TGGTGAGCAAGGGC-
GAGGAGCTGTTCACCGGGGTGGTGCCCATCCTGGTCGAG CTGGACGGCGACGTAAACGGCCACAAGTTCAGCGT-
GTCCGGCGAGGGCGAGGG CGATGCCACCTACGGCAAGCTGACCCTGAAGTTCATCTGCACCACCGGCAAGC TGC-
CCGTGCCCTGGCCCACCCTCGTGACCACCCTGACCTACGGCGTGCAGTGC TTCAGCCGCTACCCCGACCACATG
AAGCAGCACGACTTCTTCAAGTCCGCCATGCCCGAAGGCTACGTCCAGGAGCG CACCATCTTCTTCAAGGACGACG-
GCAACT ACAAGACCCGCGCCGAGGTGAAGTTCGAGGGCGACACCCTGGTGAACCGCATC GAGCTGAAG GGCATC-
GACTTCAAGGAGGACGGCAACATCCTGGGGCACAAGCT GGAGTACAACTACAACAGCCACAACGTCTATATCATGGC-
CGACAAGCAGAAGA ACGGCATCAAGGTGAACTTCAAGATCCGCCACAACATCGAGGACGGCAGCGTG CAGCTCGC-
CGACCACTACCAGCAGAACACCCCCATCGGCGACGGCCCCGTGCT GCTGCCCGACAACCACTACCTGAGCACCCA
GTCCGCCCTGAGCAAAGACCCCA ACGAGAAGCGCGATCACATGGTCCTGCTGGAGTTCGTGACCGCCGCCGGGATC
ACTCTCGGCATGGACGAGCTGTACAAGGGTGGAGGTGGATCAATGGGGGTCTA CCAGATCCTGGCCATTTACGCTACA
GTTGCAGGAAGTCTTAGCTTGGCTATTA TGATGGCCGGCATTTCGTTCTGGATGTGCTCTAACGGCTCTCTGCAGT-
GCCGCA TTTGCATTTGAGAGCTCactcaatga

GFP-Herpes-TM

actcaatgaGGTACCACCATGGCCATCATCTACCTCATACTGTTGTTTACAGCAGTGCGCGGAA TGGTGAGCAAGGGC-
GAGGAGCTGTTCACCGGGGTGGTGCCCATCCTGGTCGAGCTGGACGGCGA CGTAAACGGCCACAAGTTCAGCGT-
GTCCGGCGAGGGCGAGGGCGATGCCACCTACGGCAAGCTG ACCCTGAAGTTCATCTGCACCACCGGCAAGCTGC-
CCGTGCCCTGGCCCACCCTCGTGACCACCC TGACCTACGGCGTGCAGTGCTTCAGCCGCTACCCCGACCACATG
AAGCAGCACGACTTCTTCAA GTCCGCCATGCCCGAAGGCTACGTCCAGGAGCGCACCATCTTCTTCAAGGACGACG-
GCAACTAC AAGACCCGCGCCGAGGTGAAGTTCGAGGGCGACACCCTGGTGAACCGCATCGAGCTGAAGGGCA TC-
GACTTCAAGGAGGACGGCAACATCCTGGGGCACAAGCTGGAGTACAACTACAACAGCCACAA CGTCTATATCATGGC-
CGACAAGCAGAAGAACGGCATCAAGGTGAACTTCAAGATCCGCCACAAC ATCGAGGACGGCAGCGTGCAGCTCGC-
CGACCACTACCAGCAGAACACCCCCATCGGCGACGGCC CCGTGCTGCTGCCCGACAACCACTACCTGAGCACCC
AGTCCGCCCTGAGCAAAGACCCCAACGA GAAGCGCGATCACATGGTCCTGCTGGAGTTCGTGACCGCCGCCGGG
ATCACTCTCGGCATGGAC GAGCTGTACAAGGGTGGAGGTGGATCAATGGGGGTCTACCAGTGGGTCGGCATCGGC
ATAGGCG TTTTGGCCGCTGGCGTCCTCGTAGTGACTGCAATCGTATACGTGGTGAACGGCTCTCTGCAGTG CCG-
CATTTGCATTTGAGAGCTCactcaatga

GFP-PM

actcaatgaGGTACCACCatgggttgtaaaaaatccaagttggatggtgaccaaaatggatgtg tgcttgaaccagtgaacGGTGGAGGTGGATCAATG-
GTGAGCAAGGGCGAGGAGCTGTTCACCGG GGTGGTGCCCATCCTGGTCGAGCTGGACGGCGACGTAAACGGC-
CACAAGTTCAGCGTGTCCGGC GAGGGCGAGGGCGATGCCACCTACGGCAAGCTGACCCTGAAGTTCATCTGCAC-
CACCGGCAAGC TGCCCGTGCCCTGGCCCACCCTCGTGACCACCCTGACCTACGGCGTGCAGTGCTTCAGCCGCTA
CCCCGACCACATGAAGCAGCACGACTTCTTCAAGTCCGCCATGCCCGAAGGCTACGTCCAGGAG CGCACCATCTTC
TTCAAGGACGACGGCAACTACAAGACCCGCGCCGAGGTGAAGTTCGAGGGCG ACACCCTGGTGAACCGCATCGAGCT-
GAA GGGCATCGACTTCAAGGAGGACGGCAACATCCTGGG GCACAAGCTGGAGTACAACTACAACAGCCACAACGTC-
TATATCATGGCCGACAAGCAGAAGAAC GGCATCAAGGTGAACTTCAAGATCCGCCACAACATCGAGGACGGCAGCGT-
GCAG CTCGCCGACC ACTACCAGCAGAACACCCCCATCGGCGACGGCCCCGTGCTGCTGCCCGACAACCACTAC-
CTGAG CACCCAGTCCGCCCTGAGCAAAGACCCCAACGAGAAGCGCGATCACATGGTCCTGCTGGAGTTC GTGAC-
CGCCGCCGGGATCACTCTCGGCATGGACGAGCTGTACAAGTGATAAGAGCTCactcaat ga

2xGFP-Herpes-TM part1

actcaatgaGAAGCAGCTGCGAAGGAGGCTGCCGCGAAAGAGGCTGCAGCGAAGATGGTGAGCA AGGGCGAGGAGCT-
GTTCACCGGGGTGGTGCCCATCCTGGTCGAGCTGGACGGCGACGTAAACGG CCACAAGTTCAGTGTGTCCGGT-
GAGGGTGAAGGCGATGCTACCTACGGTAAGCTGACCCTGAAG TTCATCTGCACCACAGGTAAGCTGCCTGTGCCATG-
GCCTACCCTCGTGACCACCCTGACCTACG GCGTGCAGTGCTTCAGCCGCTACCCCGACCACATGAAGCAGCACGACT
TCTTCAAGTCCGCCAT GCCCGAAGGCTACGTCCAGGAGCGCACCATCTTCTTCAAGGACGACGGCAACTACAAGAC-
CCGC GCCGAGGTGAAGTTCGAGGGCGACACCCTGGTGAACCGCATCGAGCTGAAGGGCATCGACTTCA AGGAG-
GACGGCAACATCCTGGGGCACAAGCTGGAGTACAACTACAACAGCCACAACGTCTATAT CATGGCCGACAAGCAGAA-
GAACGGCATCAAGGTGAACTTCAAGATCCGCCACAACATCGAGGAC GGAAGCGTACAGCTCGCTGACCACTACCAGCA-
GAACACCCCAATCGGCGACGGCCCAGTGCTGC TGCCCGACAACCACTACCTGAGCACCCAGTCCGCCCTGAGCAAA-
GACCCCAACGAGAAGCGCGA TCACATGGTCCTGCTGGAGTTCGTGACCGCCGCCGGGATCACTCTCGGCATGGAC-
GAGCTGTAC AAGGAAGCCGCTGCTAAAATGGGGGTCTACCAGTGGGTCGGCATCGGCATAGGCGTTTTGGCCG CTG-
GCGTCCTCGTAGTGACTGCAATCGTATACGTGGTGAACGGCTCTCTACAGTGCCGCATTTG CATTTGAGAGCTCCAGCT
TTTGTTCCCTTT

2xGFP-Herpes-TM part2

ACTCACTATAGGGCGAATTGGGTACCACCATGattccagaggccttccagcccagagccatgaa gcacaccaccaccgtcctgatgctcgcgct-
gtcctcccgcttttggtcggtgtgtgctATGGTG AGCAAGGGCGAGGAGCTGTTCACCGGGGTGGTGCCCATCCTGGTCGAGCTG-
GACGGCGACGTAA ACGGCCACAAGTTCAGTGTGTCCGGTGAGGGTGAAGGCGATGCTACCTACGGTAAGCTGACCCT
GAAGTTCATCTGCACCACAGGTAAGCTGCCTGTGCCATGGCCTACCCTCGTGACCACCCTGACC TACGGCGTGCAGT-
GCTTCAGCCGCTACCCCGACCACATGAAGCAGCACGACTTCTTCAAGTCCG CCATGCCCGAAGGCTACGTCCAGGAGCG-
CACCATCTTCTTCAAGGACGACGGCAACTACAAGAC CCGCGCCGAGGTGAAGTTCGAGGGCGACACCCTGGTGAAC-
CGCATCGAGCTGAAGGGCATCGAC TTCAAGGAGGACGGCAACATCCTGGGGCACAAGCTGGAGTACAACTACAACAGC-
CACAACGTCT ATATCATGGCCGACAAGCAGAAGAACGGCATCAAGGTGAACTTCAAGATCCGCCACAACATCGA GGACG-
GAAGCGTACAGCTCGCTGACCACTACCAGCAGAACACCCCAATCGGCGACGGCCCAGTG CTGCTGCCCGACAAC-
CACTACCTGAGCACCCAGTCCGCCCTGAGCAAAGACCCCAACGAGAAGC GCGATCACATGGTCCTGCTGGAGTTCGT-
GACCGCCGCCGGGATCACTCTCGGCATGGACGAGCT GTACAAGGAGGCAGCAGCGAAGGAAGCAGCAGCGAAA-
GAGGCTGCAGCGAAGATactcaatga

X Plasmid Maps of newly Generated Expression Plasmids

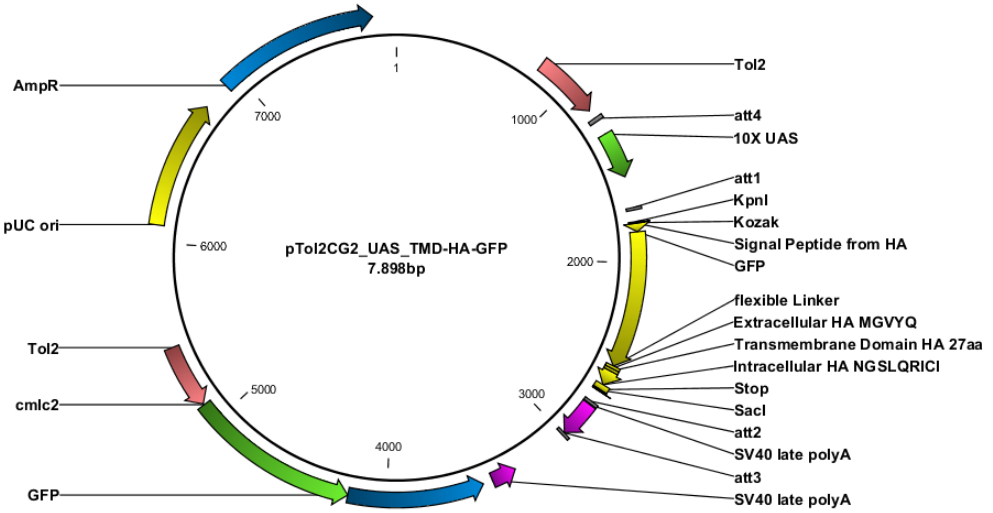

Figure 47: pTol2CG2_UAS_TMD-HA-GFP.

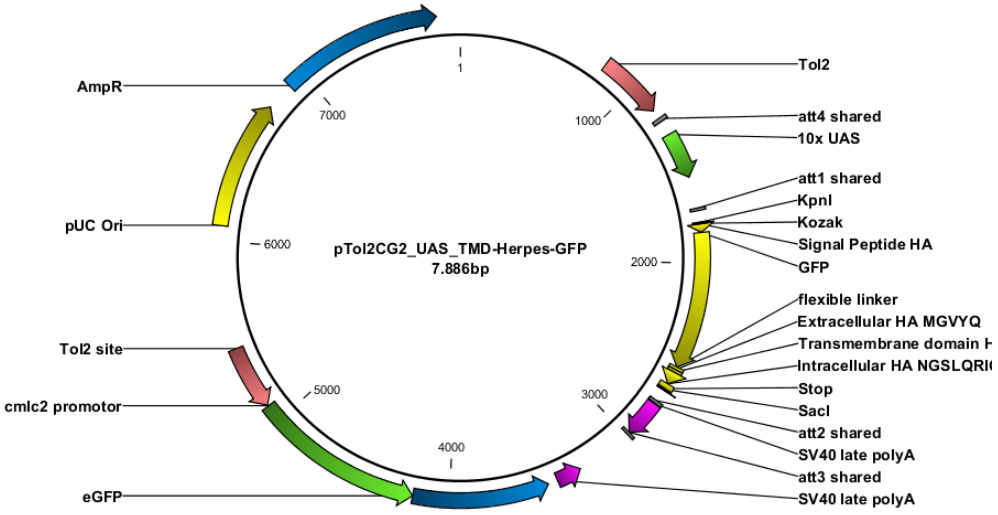

Figure 48: pTol2CG2_UAS_TMD-Herpes-GFP.

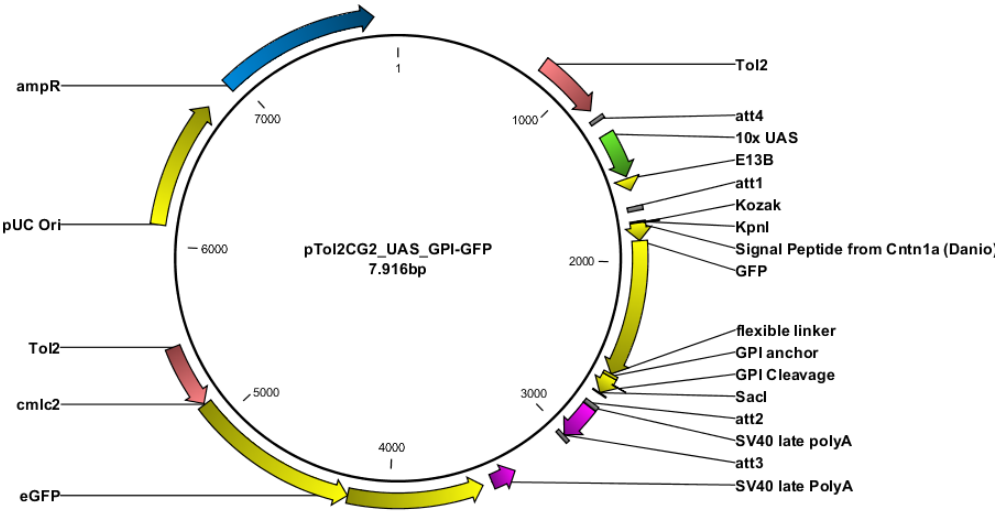

Figure 49: pTol2CG2_UAS_GPI-GFP.

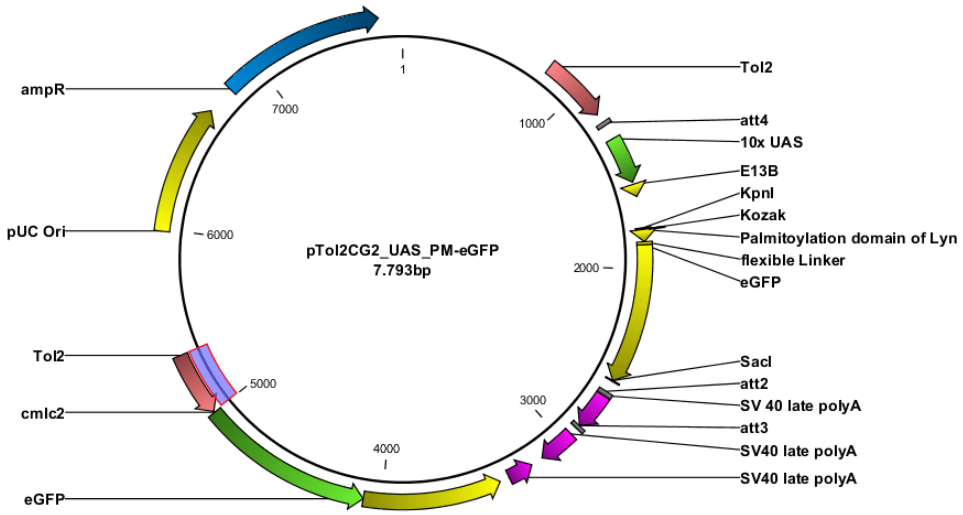

Figure 50: pTol2CG2_UAS_PM-eGFP.

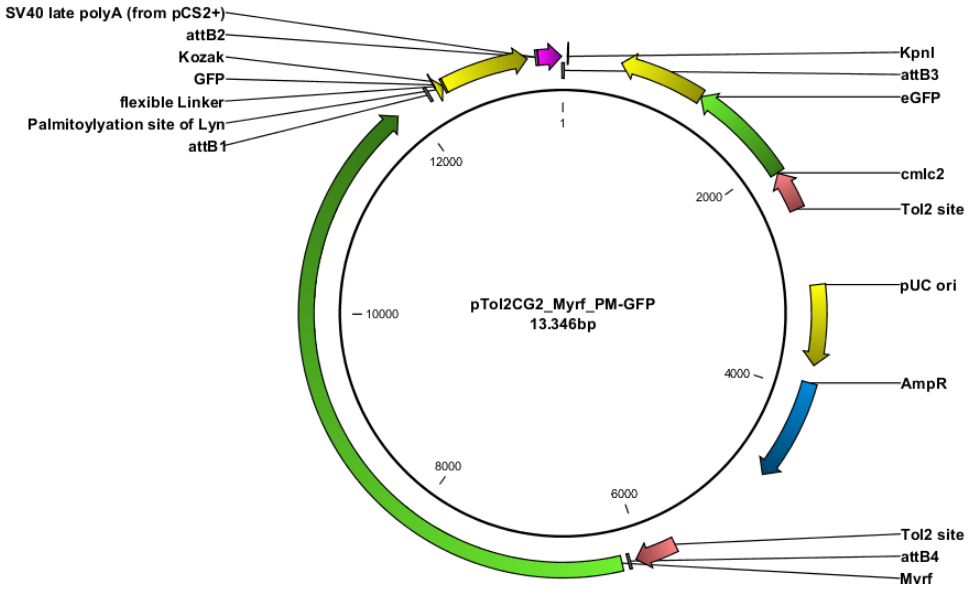

Figure 51: pTol2CG2_Myrf_PM-GFP.

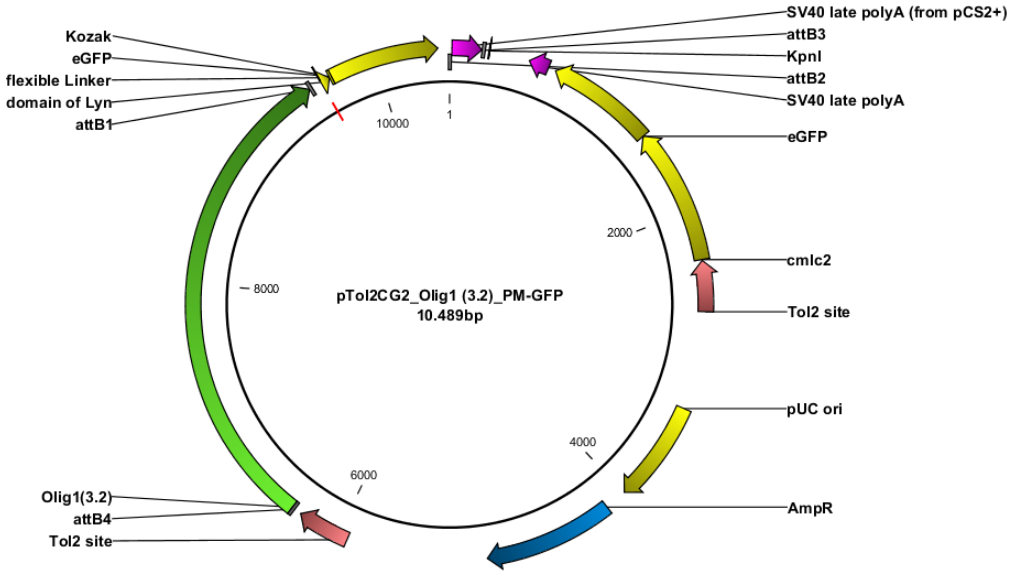

Figure 52: pTol2CG2_Olig1(3.2)_PM-eGFP.

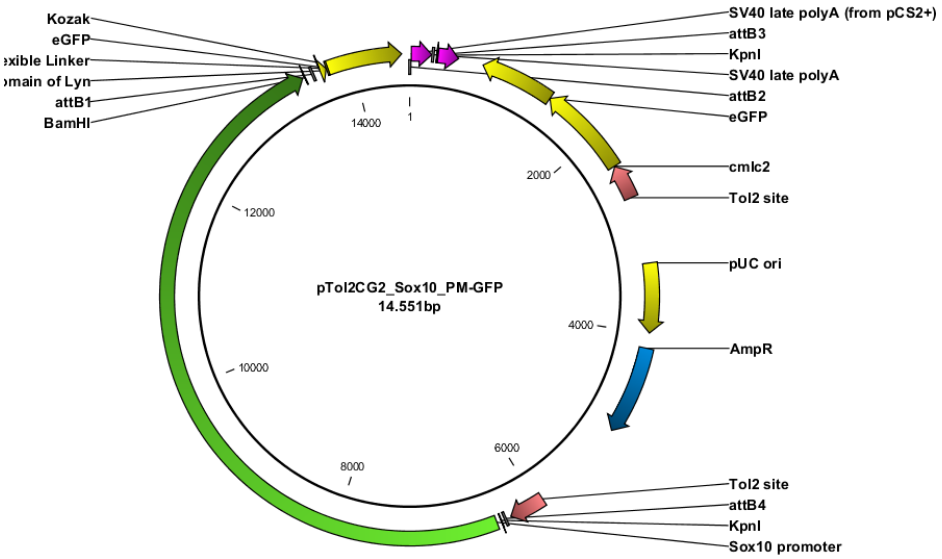

Figure 53: pTol2CG2_Sox10_PM-GFP.

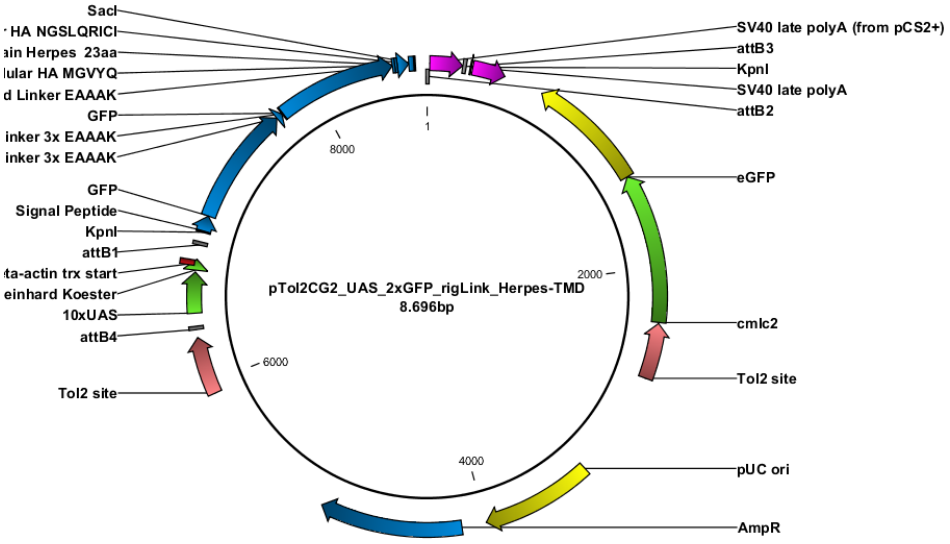

Figure 54: pTol2CG2_UAS_2xGFP_rigLink_Herpes-TMD.

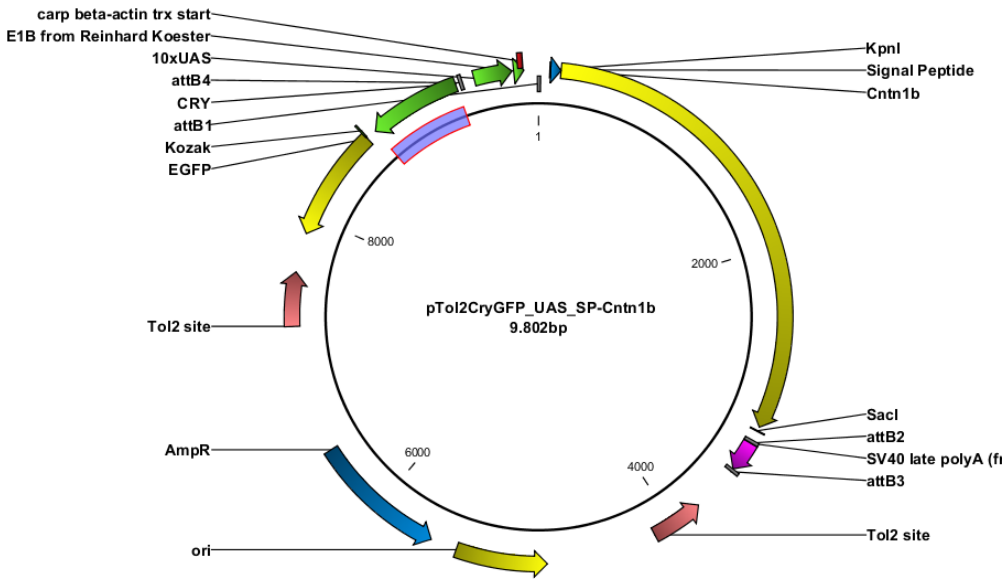

Figure 55: pTol2CryGFP_UAS_SP-Cntn1b.